Republic of Iraq
Ministry of Higher Education and Scientific Research
University of Babylon
College of Materials Engineering
Department of Metallurgical Engineering

Modification of Niobium Alloy for Surgical Implants Applications

A Thesis

Submitted to the Department of Metallurgical Engineering College of Materials Engineering / University of Babylon in Partial Fulfillment of the Requirements for the Degree of Philosophy of Doctoral of Sciences in Metallurgical Engineering

By

Salih Jawad Hamza AL-Nafie

(MSc. Materials Engineering)

Supervised by

Prof.Dr. Haydar H. J. Jamal Al Deen

2022A.D *1443A.H*

بِسْمِ اللَّهِ الرَّحْمَنِ الرَّحِيمِ

﴿نَرْفَعُ دَرَجَاتٍ مَنْ نَشَاءُ وَفَوْقَ كُلِّ ذِي عِلْمٍ عَلِيمٍ﴾

صَدَقَ اللَّهُ الْعَلِيّ الْعَظِيم

سورة يوسف (76)

Supervisors Certificate

We certify that this thesis entitled **" Modification of Niobium Alloy for Surgical Implants Applications"** is prepared by (Salih Jawad Hamza) under our supervision at the Department of Metallurgical Engineering / College of Materials Engineering / University of Babylon in partial fulfillment of the requirements for the degree of Ph.D. of Science in Materials Engineering/Metallurgical.

Name of supervisor:
Prof.Dr. Haydar H. J. Jamal Al Deen
Date: / / 2022

الخلاصة :

النيوبيوم معدن جذاب بشكل عام ويعتبر من المعادن التي تمتلك توافق حيوي جيد.

يكون من المعادن المقاومة للتأكل الجيدة كونه يمتلك سطح خامل للغاية ويكون ذات خواص ميكانيكيه محدودة مما يؤثر على التطبيقات لعنصر النيوبيوم . يؤدي اضافه عناصر اخرى الى تحسين الخواص الميكانيكية تشكل سبيكة (Nb-1%Zr)واحده من اكثر المواد تنوعا من حيث تعدد الاستخدامات ويتم ذالك تحسين الخصائص (البيولوجية والبنيه المجهرية وخواص الميكانيكية والكهروكيميائية) تستخدم هذه السبائك على نطاق واسع في التطبيقات الطبية الحيوية وذلك بسبب خصائصها مثل معامل مرونة منخفض والتوافق الحيوي ومقاومه التأكل بشكل افضل من السبائك الاخرى .يعتمد زياده التطبيقات بسبب تحسين الخواص الميكانيكية والبيولوجية والكهروكيميائية للسبائك ذات الاساس(Nb-1%Zr)بعد اضافه6-5.0 جرمانيوم .تم انتاج تلك السبائك بطريقه متلو رجيا المساحيق في قالب من الفولاذ المقاوم للصدأ وتم اجراء عمليه التلبيد عند درجه 1200درجه مئوية لمده 5 ساعات .اجراء اختبار X-RD للتعرف على الاطوار المتكونة و استخدام المجهر الضوئي لمعرفة البنيه المجهرية بعد التلبيد حيث تم الحصول على محلول جامد (Nb) وجد عند زياده نسبيه عنصر الجرمانيوم نلاحظ تحسين في خواص الصلادة مقاومه التأكل مقاومه الانضغاط ومقاومه البلاء وكذلك الخواص البيولوجية ونقصان معدل تحرر الايونات مقارنه مع السبيكة الأساسية .والتي تستخدم في المزروعات الجراحية .

الصلادة تحسنت بمقدار (34.43%) عند اضافة الجرمانيوم مقارنه مع السبيكة الاساس وكذألك اتحسن الخواص (مقاومة البلا و معامل المرونة ومقاومة الانضغاط

)(93.18%)،(84.04%)، (79.10 %) بالتعاقب وأيضا تحسن مقاومة التأكل لتكون (39%).

Dedication

. To my father and mother.

. To my brothers and sisters.

. To my supervisor.

. To my friends.

. With my love

and respect.

Acknowledgment

In the name of Allah, the Most Gracious, the Most Merciful

First and above all, I praise **ALLAH**, the almighty for providing me this opportunity and granting the capability to proceed this project.

I would like to express my deepest appreciation to my supervisor **Prof.Dr. Haydar H. J. Jamal Al Deen** for giving me their valuable guidance, support and undivided attention throughout the completion of my project.

I would like to extend my gratitude to the Dean of the University of Babylon College of Materials Engineering Department of Metallurgical Engineering , Head of Metal Engineering Department and all the staff for their great efforts.

I would like to warmly thank and gratitude my father and mother for their assistance, encouragement and support during the period of preparing this work.

I want to express my deepest thanks to the staff and laboratories of the Technology University , Materials Engineering Department.

I greatly thankful to all our well-wishers, classmates and friends for their inspiration and help.

Finally, I would like to thank all the staffs of the workshop Materials Engineering Department lab.

Abstract

Niobium is a particularly attractive metal for application as a biomaterial, due to the highly inert and unreactive nature of its surface. However, mechanical property limitations have restricted the use of the material in this field. (Nb-1%Zr) alloy forms one of the most versatile (multipurpose) materials in processing, microstructure, biological, electrochemical, and mechanical properties. These alloys are widely used in biomedical applications, mainly replacing stiff fabrics due to their properties, such as lower modulus of elasticity, high biocompatibility, and better corrosion resistance than other alloys. This work focuses on recent developments of electrochemical, biological and mechanical properties of (Nb-1%Zr) based alloys, where germanium additions were made by different percautages (0.5-6) wt.% for biomedical applications. Alloys were produced using a powder metallurgy method in a steel mold, then sintered at 1200 °C for 5 hours. The effect of germanium element additives was investigated using X-ray diffraction, and mechanical properties (Brinell hardness, compression, elastic modulus, and wear); electrochemical properties (Open circuit potential (OCP)- time measurement, Potentiodynamic polarization, ion release); and biological properties (Antibacterial, MTTS Test, Simulated body fluid) was investigated. It is found that increasing germanium content results decrease the porosity. However, the increasing content of germanium particles improves the hardness, compressive strength, and wear resistance. Germanium contrast, the wear resistance decreased by increasing the applied loads for all alloying elements content. The results show that, the alloy that content at (0.5-6) wt.% germanium particles relatively have high mechanical and wear properties as compared with the base alloy, and it could be considered

suitable because of high corrosion resistance in biomedical applications, mainly in surgical implant.

In comparison with the base alloy, the hardness, improved by (34.43**%)** with the addition of (6%) Germanium at (650Mpa) compaction pressure, the wear resistance, elastic modulus, and compression strength enhanced by (93.18**%**), (84.04**%**) and (**79.10%**) respectively. Furthermore, the corrosion resistance enhanced by (**39%**).

List of Contents.

List of Figures.

List of Tables.

List of symbols and abbreviations

Symbols	Meaning	Units
BCC	Body center cubic	
$E_{corr.}$	Corrosion potential	mv
$I_{corr.}$	Corrosion current	
XRD	X-Ray Diffraction	
T	Temperatures	
P	Density	g/cm^3 or Kg/m^3
$i_{cor.}$	Corrosion Current Density	A/cm^2
Mv	Millivolt	
LOM	Light Optical Microscope	
OCP	Open-Circuit Potential	µv

XRF	X-Ray Fluorescent	
Wt.	Weight Percentage	
CR	Corrosion Rate	
E	Modulus o elastic	GPa
L	Length	mm
P	Porosity	
P	Load	N
S	Strain	
T	Time	Min. or hr.
MTT	Dimethy -thiazol-diphenyl-tetrazolium bromide	
MDCK	Madian darpy canine kidney	

الخطأ	التصحيح
Hank	Hank's solution
Nitinol	Alloy of (Nb-1%Zr-xGe)
Recommendation	Recommendation for future work
MTT	Dimethy -thiazol-diphenyl-tetrazolium bromide
MDCK	Madian darpy canine kidney
تسلسل الفقره= 1.4	1.5
the radius of Ge=1.659µm	1.22µm
Polarization curve= Current(µA)	Log current density(µA/cm^2)
توجد بعض الفقرات بالاطروحة بخطوط غامقة	

Chapter One……Introduction

1. Introduction

1.1 General Veiw

Advances in materials science and technology have also had significant impact on the medical field, such that a variety of metallic materials found utility as implant materials owing to their biocompatibility, formability, and high strength [1-4]. However, despite the utility of metallic materials of high strength in many implants, cases of implant failure due to metal fatigue and fracture have been reported [4-6].

In such an incident, not only the treatment is unsuccessful, but also infection and other severe consequences may prevail, making an urgent surgical intervention inevitable. Since the severity of all the whispered consequences depends on how the fracture of the implant takes place, understanding the fracture, and in particular, impact behavior of implant materials emerges as an important aspect of implant design, especially when designing implants using new materials [4-6].

Niobium-Zirconium (Nb-Zr) alloys constitute a good example to this case, such that they have recently been forwarded as candidate materials to be utilized in implants [7-9]. Both constituents of these alloys have been separately proven to be biocompatible, and they have received considerable attention from researchers working in the biomaterials field due to the superior corrosion resistance they exhibit [7-9]

Recent works on this material have demonstrated that an excellent combination of mechanical properties, high strength, and good fatigue resistance can be obtained in Nb-Zr alloys upon introduction of an ultrafine-grained (UFG) microstructure [10-13]

For implant materials, in addition to resistance against corrosion induced by the chemically aggressive human body environment, mechanical performance related parameters, such as high strength,

improved fatigue resistance, and fracture toughness, are also important, especially considering loading conditions that can sometimes become intense [14-17]. For instance, sudden impact loads prompted by falling, jumping, or other causes may lead to serious injuries and bone fractures in various body parts, such as hip or knee joints, or dental implants [18-22]. Thus, understanding the impact response is crucial for a potential implant material for guaranteeing the safety and satisfactory mechanical performance of the implant during service [4-6].

The impact performance of a material is mainly dictated by its microstructural parameters, such as grain boundaries, grain size, precipitates and delaminations, and its ductile-to-brittle transition temperature (DBTT) [23-25]. Another important parameter influencing the impact response is the texture of the material, and in particular, the distribution of grain boundary misorientation angles (GBMAs), which becomes of significant importance in UFG materials; High-angle grain boundaries hinder or slow down crack propagation by constituting evenmore effective barriers against dislocation motion, leading to improved fracture toughness and lower DBTT values [24-28]. In addition to significantly influencing the crack propagation behavior under impact loading, texture of an alloy also defines its degree of anisotropy, which dictates the relative slip activity in each grain [29], and thereby the overall deformation response of a material [30,31].

Anisotropy attains even higher priority in the design of implants to replace bone tissue as the bone itself possesses a high degree of anisotropy [32,33]. Thus, to mimic bone tissue as closely as possible, and thereby ensure a mechanical behavior similar to that of the bone under all possible loading conditions, and especially impact loading, an implant material with a similar anisotropy to that of the bone should be targeted [18-22].

1.2 Biomaterials

Degeneration ,contusion and sickness require the repair by the surgical operations. This demands change the skeletal parts that include knees, hips, finger joints, elbows, vertebrae, teeth and another bodily pivotal organs kidney, heart, skin. Biomaterials which fulfill the particular function of the living materials when substitute them [34].

The National Institute of Health (NIH) defines biomaterial as: any material other than a drug, can be used to treat or replacement or support living tissue or organ, these materials may be combined and synthetic or nature in origin [35].

The biomaterials science studies the physical, mechanical and chemical properties of substances in addition to response of host tissue to biomaterial applications. So it deals with knowledge of interaction of living tissue with nonliving substances [36].

The success of biomaterials in human body rely on agents as material characteristics, design, and biocompatibility as well as factors do not depend on engineer, but on the mechanism using from the surgeon, the health of patient and state, and the activity of patient [37].

According to time there are three types of implants :

1. Short term implants are objected in very short time in contact with living tissue, as needles, scalpels and the other surgical tools.
2. Medium term implants are objected to remain for a limited time in contact

with living tissue as tissue scaffolds for skin alteration and reconstruction.

3. Long term implants are objected to remain always in contact with living tissue as bone, joint replacements, implanted sensors for blood glucose, dental prostheses, stents, heart valves and heart pacemakers.

Mainly two risks must be avoided for this type are bacterial colonization and wear [38].

1.3 The Main Properties of Niobium:

Niobium belongs to the group of metals having a high melting point, corrosion resistant, has good ductility at room temperature, consists of gray color, and acquires blue color when exposed to air for a long period [44,45].

The niobium is resistant to corrosion due to the formation of an oxide film on its surface, when combined have multiple oxidation states, in which the +5 is the most common state. In ambient temperature conditions, does not react with hydrogen, air, water, or acids, except hydrofluoric acid and its mixture with nitric acid. On the other hand, under the effect of the temperature, increase Nb reacts with most non-metallic and generates products that are non-stoichiometric and interstitial elements. Under these conditions, it is also resistant to attack by molten bases [44,45].

Nb is characterized by having only one stable isotope, which has the crystalline structure in the form of body centered cubic (BCC). The physical and mechanical properties of the Nb are influenced by the purity of the metal, so even small quantities of interstitial impurities may promote degradation of the properties of the metal. The main impurities of Nb products in accordance with specifications of the American Society for Testing and Materials (ASTM), are oxygen, nitrogen, hydrogen, carbon, iron, molybdenum and tungsten [45,46].

The physico-chemical properties of niobium are similar to tantalum, implying an occurrence together in nature, so that it becomes difficult their separation. One of the methods consists in the hydrometallurgy process known by the use of (Methyl Isobutyl Ketone), under acidic conditions. This procedure allows the isolation of niobium pentoxide

(Nb_2O_5) which can be reduced by using aluminum, known as aluminothermic process which generates niobium and aluminum oxide [45,46].

Its high melting point permits its use as a component of various alloys [47-49]. With only 8.57 grams per cubic centimeter, the density of niobium is only about half that of tantalum, one of the lightest of refractory metals. Also, it has a higher strength to weight ratio compared to metals titanium, nickel, vanadium and zirconium. This is an important industrial, where weight is an important factor in the industrial use of the property Nb [45-49].

The Nb presents high and higher values for the mechanical properties compared to ferrous metals in general, such as tensile strength and modulus of elasticity. Also, there is very low electrical resistivity of Nb, compatible to other refractory metals. Moreover, its thermal conductivity increases directly with the increase in temperature, as well as most metals [47-49].

1.4 Niobium Zerconium Alloy

Nb and Zr are desirable elements for the use in biological systems and biomedical applications thanks to their biocompatibility, resistance to corrosion, mechanical integrity and ionic cytotoxicity [50,51].

Nb-Zr alloys can be processed via multiple routes, but the longstanding challenge is to develop improved microstructures that possess attractive properties. These alloys show a positive heat of mixing that has a magnitude that ranges from (6-17)kJ/ mol [52-55]. Thus, conventional processing might not be suitable for these alloys and the use of non-equilibrium processing techniques for the development of the underlying microstructures gained considerable attention in recent years [56].

Mechanical alloying (**MA**) is one of the non-equilibrium processing techniques that is capable of producing alloys with improved properties, despite its simplicity. It consists of repeated cold welding, fracturing and re-welding of powder particles in a high-energy ball mill [57]. In this technique, phase diagram restrictions do not apply, and non-equilibrium phases are achieved. To date, only little attention was given to the use of (**MA**) to produce alloys made up of immiscible Zr and Nb [57].

Other elements were considered in the design and development of biomaterials, which included Ni and Cr. Nevertheless, Ni is showing low biocompatibility while Cr has concerns over its genotoxicity [55]. On the other hand, Zr and Nb meet the criteria for biomaterials in terms of biocompatibility, resistance to corrosion, mechanical considerations, and ionic cytotoxicity [55]. Both niobium and zirconium are highly passivating metals and it was proven that the amount of released metallic ions from Nb-Zr alloy into physiological media is small (<0.3 mg /L) [58-59].

In particular, the addition of Zr was found to result in a high level of blood compatibility when used as implants and leads to better corrosion resistance due to the formation of a stable oxide surface layer. However, little work was done to unravel the possible utilization of Nb-Zr alloys as biomedical implants and to adequately assess their properties [60].

1 .4 Aims of this Work

The aim of this work is to study the effect of trace addition of Ge on some properties of biomedical (Nb -1%Zr) alloy for using in surgical implants applications. This aim can be summarized by the following steps :

1. Different percentages of Ge (0.5 - 6)% will be added to the base alloy.
2. In order to investigate the effect of Ge on (Nb -1%Zr) alloy, several

tests were needed to be made which are mechanical test (hardness, compression, and wear); microstructure characterization (XRD , XRF,SEM and light optical microscope); chemical tests (ion release, antibacterial and MTT-based cytotoxicity); and electrochemical test (open circuit and polarization).

Chapter Two……Theoretical Part

2 .1 Introduction

This chapter is presenten and discussed will cover a general view about (Nb-1%zr) alloy used in implants; it will also cover the microstructure of metals and its alloys. There will also be a brief look at the phase diagram of (Nb-1%zr)and (Nb-Ge) alloys. There will be a focus on the types (Nb-1%Zr) alloys, their chemical compositions which will include biomaterials, mechanical properties ,biological properties and electrochemical properties. There will be a focus on the applications of the (Nb-1%Zr) alloy and the crucial element in the study (Germanium). Then there will be a detailed focus on the (Nb-1%Zr) alloy processing, powder metallurgy, blending and mixing of the powders, compacting and sintering. There will be a great focus on the corrosion behavior towards the end of this chapter which will cover the types of corrosion etc. Then joints and implants. There will be some concentration on the wear properties. Finally, the end of this chapter will cover up some of the recent research and studies about (Nb-1%Zr) alloys in general.

2 .2 General View

Implants are manufactured from many types of materials, involving metals, polymers, ceramics and their composites. Among these materials, metals are an important group. Stainless steel, (Co-Cr-Mo) alloys and Titanium alloys are the trendy metals used in orthopedics (Bones) applications. The selection of alloys for a particular application has contingent on a type of design standards, involving biocompatibility, resistance to corrosion, tensile strength, fatigue strength, young modulus, wear resistance, processing and also costs [61].

In metallic biomaterials, corrosion is the undesirable chemical reaction of metal with its environment. Tissue fluid in the human body

contains proteins, water, dissolved oxygen and other various ions including hydroxide and chloride. As a result, the human body possess an extremely aggressive environment for metals used in implantation. So, the resistance of corrosion of a metal implant is main requirement of its biocompatibility. Table (2.1) show the mechanical properties of selected metallic biomaterials including niobium.

Nb and Zr are desirable elements for the use in biological systems and biomedical applications thanks to their biocompatibility, resistance to corrosion, mechanical integrity and ionic cytotoxicity [63,64]. Nb–Zr alloys can be processed via multiple routes, but the longstanding challenge is to develop improved microstructures that possess attractive properties. These alloys show a positive heat of mixing that has a magnitude that ranges from 6 to 17 kJ mol^{-1} [65-68]. Thus, conventional processing might not be suitable for these alloys and the use of non-equilibrium processing techniques for the development of the underlying microstructures gained considerable attention in recent years [69].

Table (2.1): Mechanical properties of selected metallic biomaterials including niobium [71].

Material	Tensile strength (MPa)	0.2% Yield strength (Mpa)	Elongation %	Elastic Modulus (GPa)
316L	595	275	60	193
Nb	195	105	25	103
Nb-1%Zr	241	138	20	68.9
Ti	240-331	170-241	30	102.7
Ti-6Al-4V	900-993	830-924	14	113.8

2.3 Phase Diagram

2.3.1 (Nb-Zr) Alloy

The (Nb-1%Zr) base alloys have been a biomedical attention e.g., surgical and dental implants, etc. This is because of their exceptional wear resistance and corrosion resistance [72].

According to Thermo-Calculation, the 5 phases below are existed in the (Nb-1%Zr), figure (2.1).

• *βZr, Nb)* Composition wt.% Nb (*0 t0 100*)

•*(αZr)* Composition wt.% Zr

• ***Metastable phase***

(a) Changes from p6/mmm to p3ml with increasing Nb content

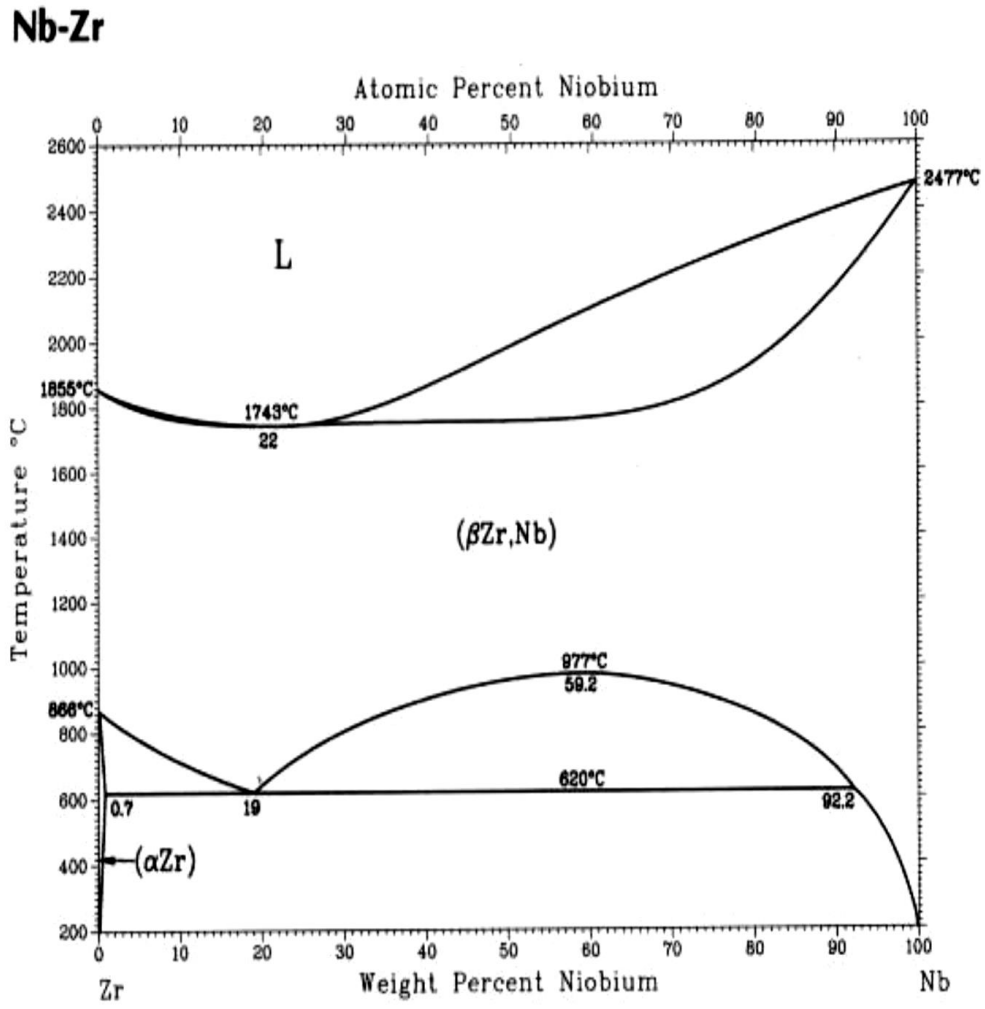

Figure (2.2): Phase Diagram of (Nb-Zr) Alloy [72].

Table (2.2): Phases existed in the (Nb-Zr) **[72]**

Phase	Composition wt.%Nb	Person Symbol	Space Group
(βZr, Nb)	*0 t0 100*	*cl2*	*Im3m*
(αZr)	*0 to 0.7*	*hp2*	*$P6_3/mmc$*
Metastable phase			
(i)	…	*hp3*	*(a)*
(a) Changes from p6/mmm to p3ml with increasing Nb content			

2.3.2 (Nb-Ge) Alloy

The (Nb-Ge) base alloys have been an enormous commercial and biomedical attention e.g., surgical and dental implants, etc. because of their biocompatibility, exceptional wear and corrosion resistance [72].

According to Thermo-Calculation, the 5 phases below are existed in the (Nb-Zr), figure (2-2).

• sold solution (Nb)

•β

• Nb_5Ge_3

• $NbGe_2$

• *(Ge)*-rich body-centered cubic (BCC) phase.

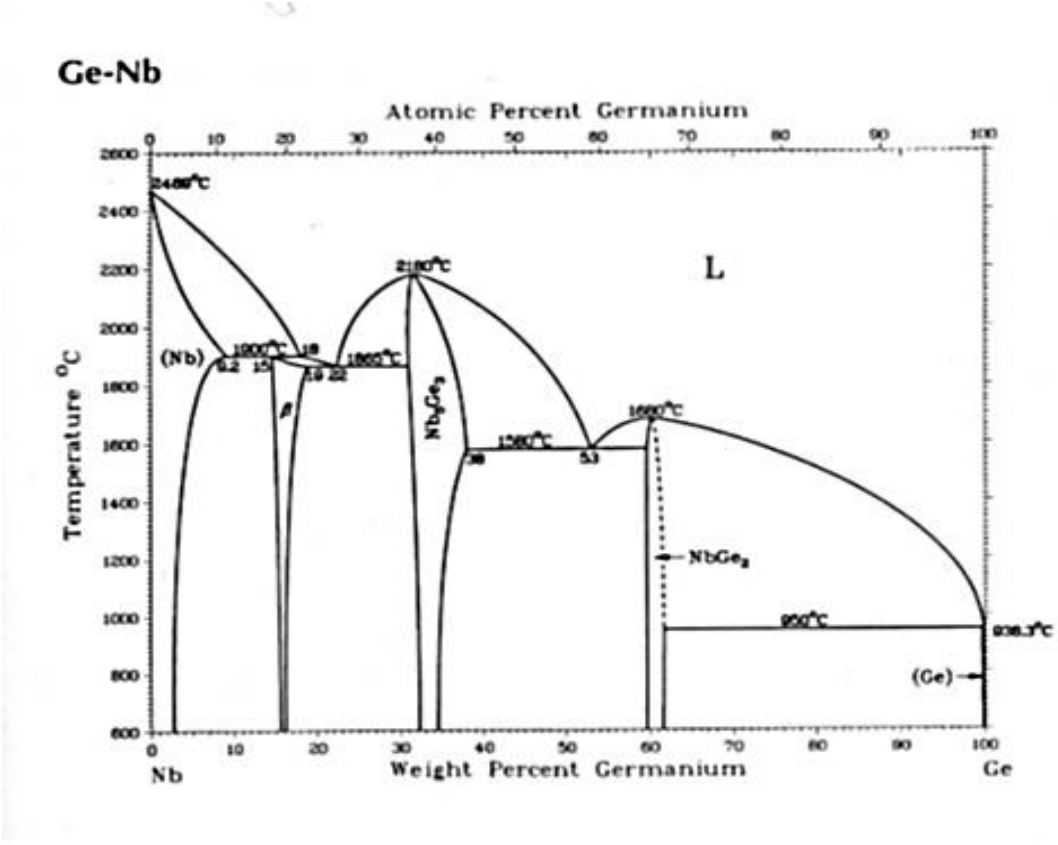

Figure (2.3): Phase Diagram of (Nb-Ge) Alloy [72].

Table (2.3): Phases existed in the (Nb-Ge) **[72]**

Phase	Composition wt.%Ge	Person Symbol	Space Group
(Nb)	*0 to 9.2*	*cl2*	*Im3m*
B	*15 to 19*	*cp8*	*Pm3n*
Nb_5Ge_3	*32 to 38*	*t/32*	*I4/mcm*
$NbGe_2$	*~61.0*	*hp9*	$P6_222$
(Ge)	*100*	*cF8*	*Fd3m*

2.3.3 Solid Solution Alloys

A solid solution occurs when we alloying two metals and they are completely soluble in each other. If a solid solution alloy is viewed under a microscope only one type of crystal can be seen just like a pure metal. Solid solution alloys have similar properties to pure metals but with greater strength but are not good electrical conductors [73].

2.3.3.1 Substitutional Solid Solution

The name of this solid solution tells you exactly what happens as atoms of the parent metal (or solvent metal) are replaced or substituted by atoms of the alloying metal (solute metal). In this case, the atoms of the two metals in the alloy, are of similar size. Here we see the black atoms have been replaced or substituted by the white atoms in Figure below [73].

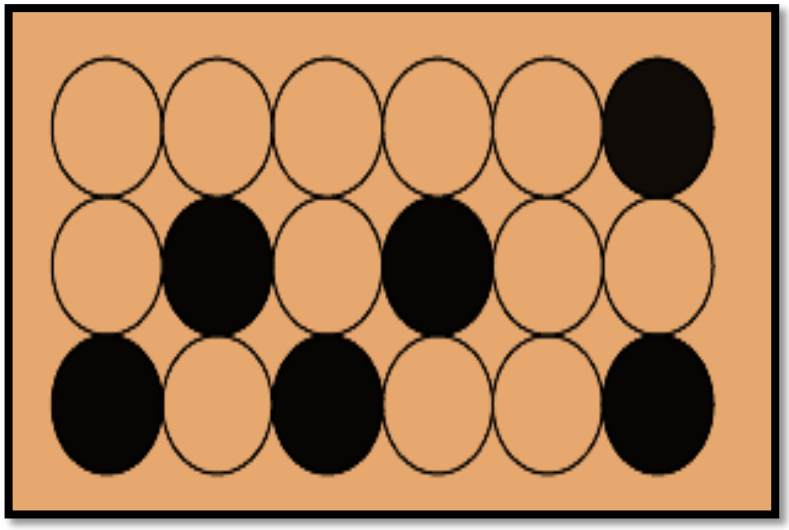

Figure (2.3): Substitutional Solid Solution [73].

2.3.3.2 Interstitial Solid Solution

In interstitial solid solutions the atoms of the (parent or solvent metal) are bigger than the atoms of the (alloying or solute metal). In this case, the smaller atoms fit (sit) into interstices (i.e., spaces between the larger atoms). The smaller atoms are small enough to fit into the spaces between the larger solvent atoms. Shown in figure below [73].

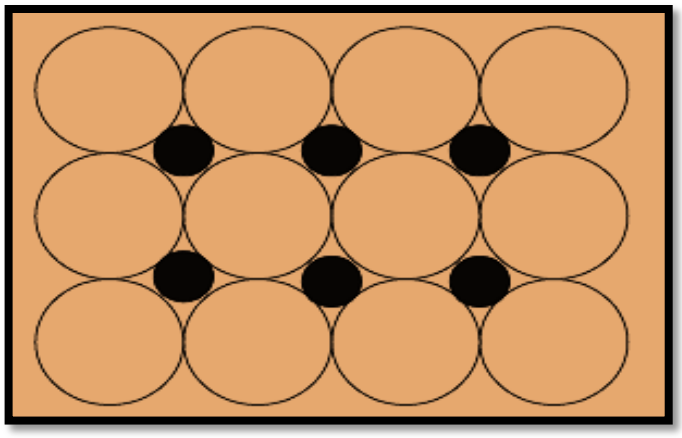

Figure (2.4): Interstitial solid solution [73].

In both substitutional and interstitial solid solutions, the overall atomic structure is virtually unchanged. Examples of solid solution

alloys include (Copper-Nickel), (Gold-Silver) all whom has an **FCC** [73].

2.4 Applications

The following are the application areas of niobium:

1. Production of high-temperature resistant alloys and special stainless steel.
2. Optics.
3. Superconductors.
4. Super alloys.

Niobium compounds such as niobium carbide are used in cutting tools. Other compounds such as lithium niobate are used in electro ceramics. Niobium-tin alloys are used as superconducting magnets. Niobium is used in stainless steel alloys that are used in nuclear reactors, missiles, jets, pipelines, cutting tools and welding rods [74].

The main applications of biomaterials can be classified into the categories below:

-Cardiovascular medical devices (stents, grafts and etc.)

-Orthopedic and dental applications (implants, tissue engineered scaffolds and etc.)

-Ophthalmologic applications (contact lenses, retinal prostheses and etc.)

-Bio electrodes and biosensors •

-Burn dressings and skin substitutes •

-Sutures •

-Drug delivery systems

Figure (2.5): Applications areas of Nb [74].

2.5 Metals which are added

2.5.1 Zirconium

Zirconium is a chemical element with the symbol Zr and atomic number 40. The name zirconium is taken from the name of the mineral zircon (the word is related to Persian Zr (zircon; zar-gun, "gold-like" or "as gold")), the most important source of zirconium [72]. It is a lustrous, grey-white, strong transition metal that closely resembles hafnium and, to a lesser extent, titanium. Zirconium is mainly used as a refractory and opacifier, although small amounts are

used as an alloying agent for its strong resistance to corrosion. Zirconium forms a variety of inorganic and organometallic compounds such as zirconium dioxide and zirconocene dichloride, respectively. Five isotopes occur naturally, four of which are stable. Zirconium compounds have no known biological role [72].

2.5.2 Germanium

Germanium is a chemical element with the symbol Ge and atomic number 32. It is a lustrous, hard-brittle, grayish-white metalloid in the carbon group, chemically similar to its group neighbor's silicon and tin. Pure germanium is a semiconductor with an appearance similar to elemental silicon. Like silicon, germanium naturally reacts and forms complexes with oxygen in nature [72].

Because it seldom appears in high concentration, germanium was discovered comparatively late in the history of chemistry. Germanium ranks near fiftieth in relative abundance of the elements in the Earth's crust. In 1869, Dmitri Mendeleev predicted its existence and some of its properties from its position on his periodic table, and called the element ekasilicon. Nearly two decades later, in 1886, Clemens Winkler found the new element along with silver and sulfur, in an uncommon mineral called argyrodite. Although the new element somewhat resembled arsenic and antimony in appearance, the combining ratios in compounds agreed with Mendeleev's predictions for a relative of silicon. Winkler named the element after his country, Germany. Today, germanium is mined primarily from sphalerite (the primary ore of zinc), though germanium is also recovered commercially from silver, lead, and copper ores [72].

Elemental germanium is used as a semiconductor in transistors and various other electronic devices. Historically, the first decade of

semiconductor electronics was based entirely on germanium. Presently, the major end uses are fiber-optic systems, infrared optics, solar cell applications, and light-emitting diodes (LEDs). Germanium compounds are also used for polymerization catalysts and have most recently found use in the production of nanowires. This element forms a large number of organogermanium compounds, such as tetraethylgermanium, useful in organometallic chemistry. Germanium is considered a technology-critical element [72].

Germanium is not thought to be an essential element for any living organism. Some complex organic germanium compounds are being investigated as possible pharmaceuticals, though none have yet proven successful. Similar to silicon and aluminium, naturally-occurring germanium compounds tend to be insoluble in water and thus have little oral toxicity. However, synthetic soluble germanium salts are nephrotoxic, and synthetic chemically reactive germanium compounds with halogens and hydrogen are irritants and toxins [72].

2.6 Powder Metallurgy

2.6.1 Basic Steps in Powder Metallurgy Technique:

The fabrication of parts by using powder metallurgy technique includes several steps shown in figure (2.6) below, which consists of blending and mixing of powders, compaction, sintering, and other secondary finishing processes **[76].**

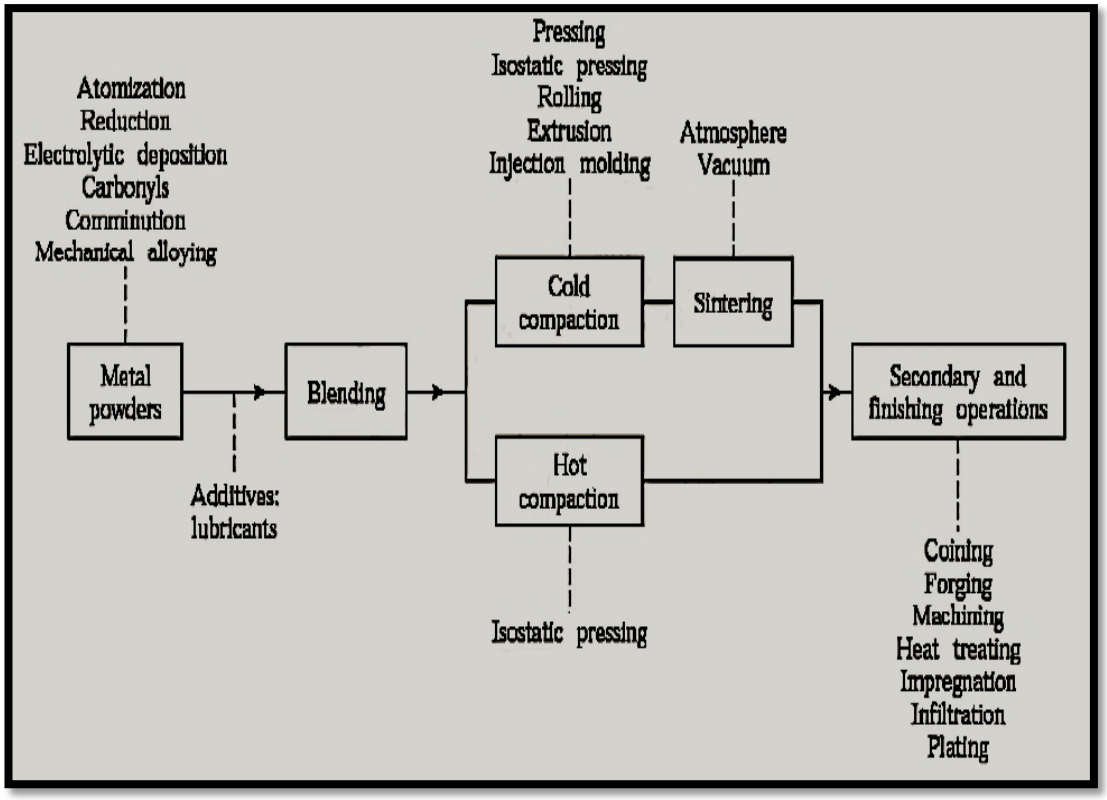

Figure (2.6): Basic steps in the Powder Metallurgy process [76].

2.6.2 Blending and Mixing of Powders:

Blending is a process of thorough intermingling of powders of the same components or material, whilst **mixing** described the intermingling of powders of several or more different materials. The mixing process is very desirable in the preparation of alloys from primary powders. Material additives such as lubricates or binders are commonly added in both kinds of processes so as to facilitate powder pressing to achieve the

Required green strength and controlling the porosity in the final product. The mixing process of material powders is very complex operation which depends on the mass movement of one powder component within that of another powder component. This movement is depending on the powder materials, particle shape, particle size, and surface conditions. Mixing process may be either dry or wet mixing. Wet mixing by adding alcohol, benzene, glycerin or acetone as a liquid

medium in sufficient amount so as to bring the powder to the coherency of a thin paste, is utilized to produce a homogeneous mixture of powder particles. When the mixing process achieved, benzene or acetone is removed during the mixing in air or in a controlled oven up to 50ºC **[77, 78].**

The mixing process is used to produce a homogeneous distribution of powders and controlling the characteristics of product powder. It must produce a homogenous and uniform mixture in the least possible time. The mixing time may be differing from a few minutes to 24 hours or even some days depending on the results desired. High mixing time leads to work hardening of particles; thus it must be avoided **[77, 78].**

2.6.3 Die Compaction:

The initial stage used for shaping lose powders into a desired form product and adequate strength for additional handling is called cold compaction process. It is mainly achieved via unidirectional compaction in a mold or to a lesser extent via cold isostatic pressing (CIP). There were some other specialized techniques of compaction processes such as injection molding and explosive compaction. The pressure utilized to produce green compact of the component depends on the material and the characteristics of the powder. The compacting operation should be designed in order to the press will be regularly distributed in the affected region **[79].**

In the initial pressing stage, the particles are rearranged leading to a superior packing material. The raising of pressure reduces the porosity of green compact and provides better packing material. The high pressure leads to deformation of individual particles and some cold welding takes place between the particles which provides some strength to the green compact. The compaction of the green compact is not

regular because the friction of the wall. This problem can be reduced through utilizing lubricants and applying a load from top and bottom at the same time. The mold design is very essential factor in order to allow the green compact ejected after compaction. Therefore, the obtained geometry by using unidirectional compaction way is limited **[79, 81].**

Figure (2.7): Die compaction utilized for preparing samples.

2.6.4 Sintering:

Sintering is the operation in which the green compact formed from powder materials are thermally treated at temperatures less than the melting temperature of the base component so as to increase the strength of the green compact when the particles bonded with each other **[77].** When a green compact is heated in an isolated atmosphere to a temperature under the melting temperature of the base component, a

densification of the powder takes place by elimination of pores leading to increase the mechanical strength of a sintered product **[81].**

At the level of a microscopic scale, cohesion between powder particles occurs as a necks form and grow at the contact particles region. The temperature required for Aluminium composite sintering is commonly about 600°C **[81].** Sintering process conducted at a temperature in the range of (**0.7- 0.9**) of the absolute melting point of the base metal in a multi component powder system. During sintering process, the physical, chemical and metallurgical effects of the different powder are interacting at the same time **[75].**

For sintering process, the driving force is the reduction in surface energy of the powder. It can be increased by adding reactive elements or adding components that become liquid at the sintering temperature. This way called as liquid phase sintering process. One more option is by applying an external pressure during the sintering process. This way called as pressure sintering. Sintering process efficiency is usually affected by some factors such as sintering temperature, sintering time, the properties of the protective atmosphere, the green compact density, powder particles size and powder particle shape **[80, 81].** Figure (2.8) shows these two cases in a schematic binary phase diagram **[80].**

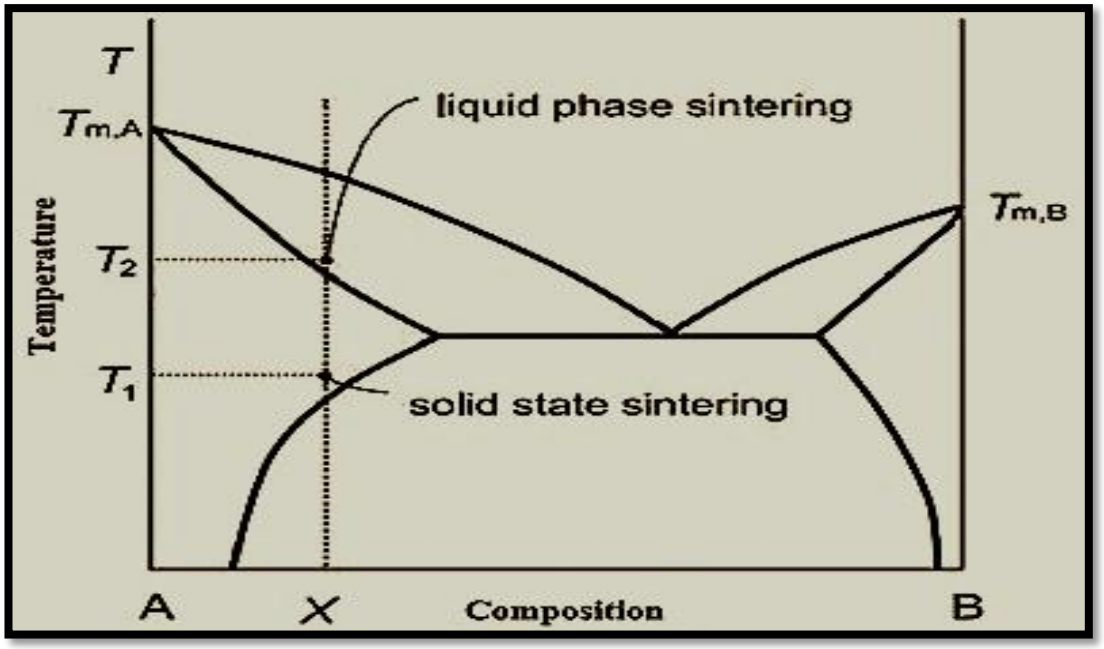

Figure (2.8): Schematic phase diagram with sintering areas [80].

Liquid phase sintering process occurs in three steps. At the beginning the liquid phase wets the particles, leading to rearrange the particles and to a rapid densification. Secondly, the small particles dissolve and re-precipitate on larger particles. Finally, traditional solid phase sintering takes place **[81].**

Solid state type of sintering process can be divided into four interrelating stages, involves:

1. The particles of powder materials are bonded to form necks.

2. Alteration the geometry of pores, and shrinking the compact.

3. Pores isolation via grain growth and elimination of the remainder porosity **[81].**

The driving force of solid-state sintering process is the difference in free energy or chemical potential between the free surface of the particles and contact points of linked particles **[80].** Figure (2.9) shows the stages of solid-state sintering process.

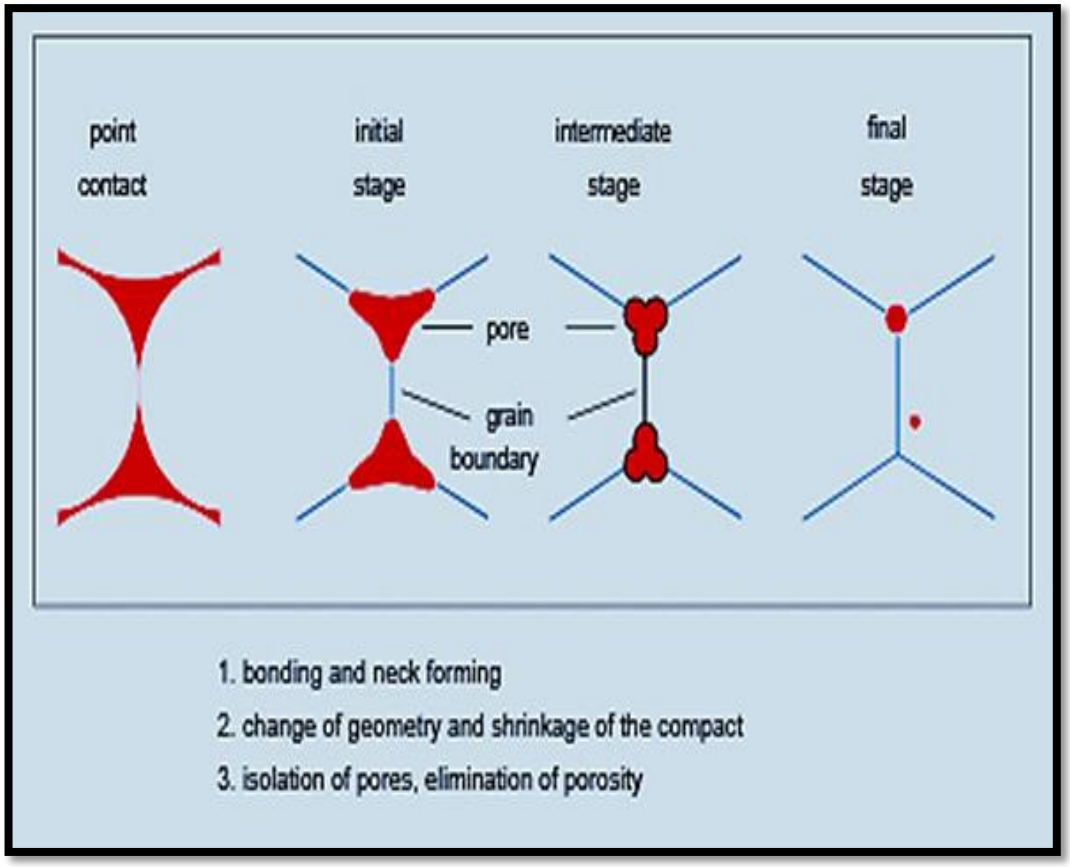

Figure (2.9): Powder consolidation, solid state sintering **[80].**

2.7 Corrosion

2.7.1 Types of Corrosion

The diagram on the following page illustrates the main types of corrosion which will be discussed in this chapter.

2.7.1.1 Uniform Corrosion

This corrosion results from the continual shifting of anode and cathode regions of the surface of a metal in contact with the electrolyte and leads to a nearly uniform corrosive attack on the entire surface. An example of such corrosion is the rusting of steel plate in seawater [82].

If the rate of metal loss is known, allowances can be made in design and maintenance to accommodate the corrosion. Although it is

termed uniform corrosion, it is characterized by the average surface loss [82].

2.7.1.2 Galvanic Corrosion

When two different metals are exposed to a corrosive environment, an electrical potential difference will exist. If the two metals are electrically connected, the more active metal will become the anode in the resulting galvanic cell and its corrosion will be increased. An example of such a corrosion cell is the use of steel bolts to hold copper plates together Not all galvanic corrosion is detrimental. Zinc coated steel, or galvanizing, is used to protect steel, not because the steel is resistant to corrosion, but because the zinic, being anodic to the steel, corrodes preferentially. Hence, the steel is protected catholically by making any exposed areas of steel into cathodes [83].

It is generally good practice not to use dissimilar metals unless it is necessary, but if it is, the following precautions should be used:

Attempt to electrically isolate the metals.

Use protective coatings on the metal surface(s), generally the cathode Catholically protect the less noble metal. Put corrosion inhibitors into the system.

Use design in which anodic part may be replaced easily.

Keep out moisture.

Use metals that are close to one another in the galvanic series.

Design so that the anode/cathode area ratio is high.

Use design allowances to account for the corrosion.

2.7.1.3 Crevice Corrosion

Crevice corrosion is a localized attack which occurs when crevices, formed by lapped joints, or areas of partial shielding, are exposed to corrosive environments. Such resulting cells are referred to as concentration cells. Two common cases are oxygen cells and metal-ion cells. Oxygen concentration cells occur when the shielded area becomes depleted in oxygen and the area acts as an anode relative to the oxide region. As illustrated , the corrosion becomes quite rapid because of the small shielded area as compared to the unshielded area. Do not get confused with the concentration polarization that we previously discussed. In the case of an oxygen cell, we have an oxygen "gradient" that forces the formation of the anode and cathodes with respect to the oxygen levels. oxygen cell, we have an oxygen "gradient" that forces the formation of the anode and cathodes with respect to the oxygen levels [83].

The initial driving force of such corrosion is the oxygen cell. The continued growth is fostered by the accumulation (often caused by the same factors that produced the low oxygen level) of acidic, hydrolyzed salts within the crevice. Alloys, such as 18-8 stainless steels, are subjected to oxygen cell crevice corrosion [83].

Metal-ion cells are formed mainly with copper alloys. The shielded area accumulates corrosion products and becomes cathodic to the regions outside of the crevice where corrosion products are kept washed away. The figure below illustrates this type of concentration cell.

Another example of metal-ion cell corrosion occurs when relative speeds of electrolyte over the metal surface are greater at one point than at another, thus resulting in metal-ion crevice corrosion. A good example is where a disc of metal is rotating at high speed in seawater. Corrosion occurs near the edge where linear velocities ($v=\omega r$) are the highest and

the metal-ion concentration is low (since the ions are repeatedly swept away). The high velocity, higher than in regions closer to the hub of the disc, sweeps away the metal-ions, thus forming anode regions. At the center of the disc, where velocities are lower, the metal acts as a cathode and is protected (Do not confuse this with the discussion on "immunity" from corrosion where the low ion concentration was one of the entering arguments. That was an equilibrium concentration. In this case, metal ions continue to form because we can't reach an equilibrium concentration). However, the two concentration cells corrode at different regions of the crevice. The oxygen cell corrodes under the shielded area while the metal-ion cell corrodes outside of the area. As stated before, the initial driving force behind the corrosion is either the oxygen or the metal-ion cell. Its continued growth is governed by the accumulation of corrosion products, calcareous deposits, and salts within the crevice [83].

2.7.1.4 Pitting Corrosion

Pitting is an extremely localized attack that eventually results in holes in the metal. It is one of the most destructive and insidious forms of corrosion. Basically, the alloys subject to pitting are those that rely on an oxide film for protection, such as stainless steels. The initiation of a pit can be the result of any of the following [84]:

a) Chemical attack, such as ferrous chloride or aerated seawater on stainless steel.

b) Mechanical attack such as an impact or scratching that removes small areas of the protective film.

c) Crevice corrosion resulting from tiny deposits on the surface, especially in stagnant seawater.

Some theories state that pitting is just a special case of crevice corrosion.

2.7.1.5 Selective Leaching Dealloying

Selective Leaching corrosion results from areas of a metal surface being different metallurgically from other, adjacent areas. Brass, for example, is an alloy with zinc and copper in a "solid solution". It can corrode with the zinc being selectively removed from the alloy, leaving behind the copper. It makes the alloy porous and compromises its mechanical properties. In brass it may be identified when its yellow natural color turns reddish or coppery in appearance. It is helpful to add a small amount of tin to the alloy to prevent dealloying. Such selective leaching is known as "dezincification". Cast irons can corrode in such a matter that the iron is selectively corroded away, leaving behind a soft graphite layer. This is referred to as "graphitization". Other examples are referred to as dealuminification, denickelification, decobaltification, etc. where the terms refer to the metallic element that is selectively corroded away.

The mechanism of selective leaching has been explained as follows for a brass alloy:

A. the brass corrodes

B. the zinc ions stay in solution

C. the copper plates back on as a solid layer

The problem with this theory is that the corrosion occurs even under high electrolyte flow velocities when one would surmise that the copper ion would be swept away before they could plate out.

A second theory, again for brass, is that the zinc corrodes preferentially, leaving behind copper in a lattice structure. A corrosion process in which the less noble metal in an alloy is attacked preferentially and replaced in the matrix by cathodic products. The most common example of this occurs with brass and is termed dezincification.

In the dezincification of brass, the zinc in the alloy's matrix is attacked and copper remains [84].

2.7.1.6 Erosion-Corrosion

Erosion-Corrosion results from a high velocity electrolyte flow whose abrasive action accelerates the corrosion. This corrosion is especially severe when the electrolyte contains solids in suspension. The effect is to remove a protective oxide from the film surface, thus exposing fresh alloy to corrode. Erosion-Corrosion could be thought of as pitting on a much larger scale.

There is, in fact, a limit to what electrolyte velocities can be tolerated by specific metals. Coppernickel alloys are selected for seawater service based on their resistance to erosion-corrosion (amongst other requirements). This table illustrates these limitations [84].

2.7.1.7 Stress-Corrosion-Cracking (S.C.C.)

Stress-corrosion-cracking occurs with specific alloys under the following threshold conditions [84]:

a) Specific corrosive environment solution composition

b) Minimum tensile stress levels

c) Temperature

d) Metal composition

e) Metal structure

Some examples of SCC are the brass and stainless-steel alloys. Specific brass alloys will crack in ammonia containing environments when a minimum threshold tensile stress is reached. Stainless steel alloys do not crack in ammonia environments, but will crack in chloride solutions.

The interplay of the conditions leading to SCC is not well understood. It is believed that the corrosion causes a pit or surface discontinuity to form on the metal which then functions to act as a stress concentrator. The presence of a minimum threshold tensile stress, coupled with the corrosion, causes the crack to propagate. Additionally, during the initial corrosion, the tensile stresses could cause the protective films on the surface to rupture, thereby exposing the metal to the corrosive environment.

This particularly dangerous corrosion type can be the result of environmental factors or cyclic stresses. The following are the major types of cracking attack:

Corrosion fatigue - the accelerated failure of a metal which undergoes cyclic loading due to its presence in a corrosive environment.

Stress corrosion cracking (SCC) - the corrosion induced cracking which occurs in alloys under high tensile stress. The cracks start on the surface and go inward. It should be noted that the stress can be the result of cold working, forming, or external loading.

Hydrogen embrittlement - the loss in ductility of a metal due to the saturation of atomic hydrogen in the grain boundaries. It occurs at local cathodic sites and is aggravated by stress and compounds such a hydrogen sulfide [85].

Liquid metal cracking - metals subjected to simultaneous tensile stress and certain molten metals can undergo this type of cracking. It is most common in mercury/copper alloy systems. Stress corrosion cracking [from Jones (1996)].

2.7.1.8 Intergranular Corrosion

On a microscopic level, metals and their alloys have small, distinguishable regions called grains. Within an individual grain the

orientation of the atomic arrangement (called a lattice) is the same. Individual grains have different orientations and the boundary between the grains is called the grain boundary. Normally, grain boundaries are no more reactive in corrosion than the grain itself. Under certain conditions, however, the grain boundaries are altered from the grain itself by impurities and/or enrichment (or depletion) of one of the alloying elements.

Heat treatment and welding can lead to changes metal composition which may incite intergranular corrosion. In severe cases, intergranular corrosion can lead to a marked decrease in mechanical properties and can, in extreme cases, turn the metal into a pile of individual grains.

One of the most common examples of intergranular corrosion occurs in stainless steels. During welding of the alloy, or heating in the temperature range of 950 · F to 1450 · F, the alloy becomes sensitized or susceptible to intergranular corrosion as illustrated in Figure 26. The chromium carbide (Cr23C6) is not soluble in this temperature range and preciptates out of the grain into the grain boundary. As a result, the area of the grain adjacent to the grain boundary is depleted of the chromium and becomes anodic to the rest of the grain and to the grain boundary. The corrosion of this depleted grain boundary area is very severe and occurs in environments and acids where the alloy would not normally corrode. The simplest solution to the stainless steel intergranular corrosion problem is to cast alloys with carbon contents below 0.03%. (This prevents the formation of the chromium carbide and the chromium stays in solution) [85].

2.7.1.9 Fretting

A rapid localized attack which occurs on mated surfaces under load when a small amount of slip is allowed to occur. It is often observed on bearings, shafts, and gears in mounted in vibrating machinery. Not only is mechanical damage of the surface possible, but the protective surface film of the metal is also removed. This in turn hastens electrochemical corrosion processes [85].

2.7.1.10 Biological corrosion

Biological organisms can play a major role in metal attack. This attack is usually categorized in the following two headings:

Microbially induced corrosion (MIC) - aerobic and anaerobic bacteria and other microorganisms contain enzymes and can produce metabolites which accelerate corrosion. This can manifest itself in pitting type corrosion of the metal surface.

Macrofouling effects - barnacles, oysters, and other macrofoulers produce by-products that are often acidic and can accelerate corrosion. These organisms also create crevices at their attachment points that can lead to crevice corrosion [86].

2.7.1.11 Stray current corrosion

Corrosion can be accelerated by the action of electrical currents entering a metal from some external source such as a generator or a battery and leaving the metal to continue its flow in whole or part through the seawater electrolyte. As an example of stray current corrosion, consider the bilge pump illustrated below. The electrical connections were made such that the current found a path from the pump and its through-hull connection to the seawater and back through the propeller shaft and engine to the battery [86].

2.7.2 Corrosion Behavior of (Nb-1% Zr) Base Alloy

The corrosion resistance of the implant alloy is a very important determinant of its biocompatibility. The nature of the environment and the surface treatments has a marked influence on corrosion [86].

Nb and Zr are desirable elements for the use in biological systems and biomedical applications thanks to their biocompatibility, resistance to corrosion, mechanical integrity and ionic cytotoxicity [86, 87].

Advances in materials science and technology have also had significant impact in the medical field, such that a variety of metallic materials found utility as implant materials owing to their biocompatibility, formability, and high strength [88-91]. However, despite the utility of metallic materials of high strength in many implants, cases of implant failure due to metal fatigue and fracture have been reported [91-93]. In such an incident, not only the treatment is unsuccessful, but also infection and other severe consequences may prevail, making an urgent surgical intervention inevitable. Since the severity of all the aforementioned consequences depends on how the fracture of them plant takes place, understanding the fracture–and in particular, impact – behavior of implant materials emerges as an important aspect of implant design, especially when designing implants using new materials. Niobium–zirconium (NbZr) alloys constitute a good example to this case, such that they have recently been forwarded as candidate materials to be utilized in implants [94-96]. Both constituents of these alloy shave been separately proven to be biocompatible, and they have received considerable attention from researchers working in the biomaterials field due to the superior corrosion resistance they exhibit [94-96].

The corrosion resistance of the alloy can be improved by the formation of protective film on the surface, in (Nb-1% Zr) alloy the protective layer mainly consists of NbO. The formation of NbO inactive thin layer on the surface is extremely important for enhancing the corrosion resistance of (Nb-1% Zr), while releasing of ions from (Nb-1% Zr) surface is the main reason of lowering corrosion resistance and biocompatibility [96].

2.8 (Nb-1% Zr) Wear Property

Wear is harm to surface, in general involving gradual lack of material, because of relative motion between two surfaces [58]. The wear process may rupture the protective oxide film inherently present on the alloy's surface, which can lead to accelerat attack in the presence of a corrosive medium. Furthermore, in certain applications the generation of wear debris is a critical concern [59].

2.8. Friction and Wear

Friction and wear occur when two surfaces undergo sliding or rolling under load. Friction is a serious cause of energy dissipation, where wear is the main cause of material wastage. Suitable materials are selected for mating bodies and/or solid/liquid lubrication, is used to control friction and hence reduce the wear rate at which the mating surface degrades. In order to make the best choice of material for certain conditions, a deeper understanding of these two processes (friction and wear) is necessary **[17, 18].**

Friction is the resistance to relative motion of contacting bodies. The degree of friction is expressed as a coefficient of friction, which is expressed as the ratio of force required to initiate or sustain relative motion, to the normal force that presses the two bodies together. Two

modes of friction may occur; sliding friction or rolling friction. The friction between sliding surfaces (*sliding friction*) is due to the combined effects of adhesion between flat surfaces, ploughing by wear particles and hard asperities, and asperity deformation. Rolling friction is a complex phenomenon because of its dependence on so many factors, including inconsistent sliding (called slip) during rolling, and energy losses during mixed elastic and plastic deformations. Rolling friction may be classified into two types, one in which large tangential forces are transmitted (one example, the traction drives and driving wheels of an automobile), and another in which small tangential forces are transmitted, often referred to as free rolling show the figure schematic of fatigue wear, due to the formation of surface and subsurface cracks as shown in figure (2.10) **[17, 18].**

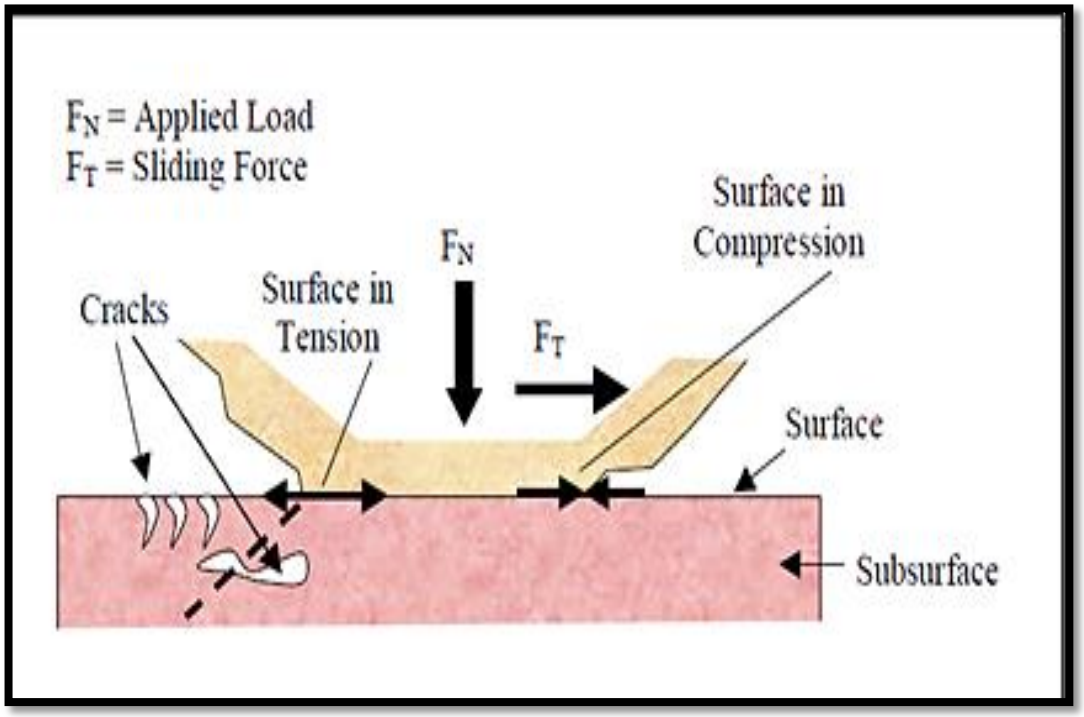

Figure (2.10): Schematic of fatigue wear, due to the formation of surface and subsurface cracks [17].

Wear is a process of removal of material from one or both of two solid surfaces in solid state contact, occurring when two solid surfaces

are in sliding or rolling motion together **[17]**. The rate of removal is generally slow, but steady and continuous some wear mechanical.

Studying the mechanisms of wear is very important so as to design materials which are favorable for wear reduction [58]. Wear mechanisms generally can be grouped into six generic types:

2.8.1 Mechanisms of Wear

1. Adhesive Wear

Adhesive wear results through the surface interaction and welding of the asperities junctions at the sliding contact. This mechanism of wear is influenced by the kind of bonding (ionic, covalent, metallic and Vander vales) in the contact junction. The weaker part of the materials in contact is removed and transferred to the counter surface, if the bond in the junction is stronger than the bond in the bulk. Surface removal results in a rough appearance and a large volume of worn material, hence severe wear **[97].** Adhesive wear is often called galling or scuffing, where interfacial adhesive junctions lock together as two surfaces slide across each other under pressure. As normal pressure is applied, local pressure at the asperities become extremely high. Often the yield stress is exceeded, and the asperities deform plastically until the real area of contact has increased sufficiently to support the applied load. In the absence of lubricants, asperities cold-weld together or else junctions shear and form new junctions. This wear mechanism is not only destrosed the sliding surfaces, but the generation of wear particles which cause cavitation and can lead to the failure of the component. An adequate supply of lubricant resolves the adhesive wear problem occurring between two sliding surfaces as shown in figure (2.11) **[97]**.

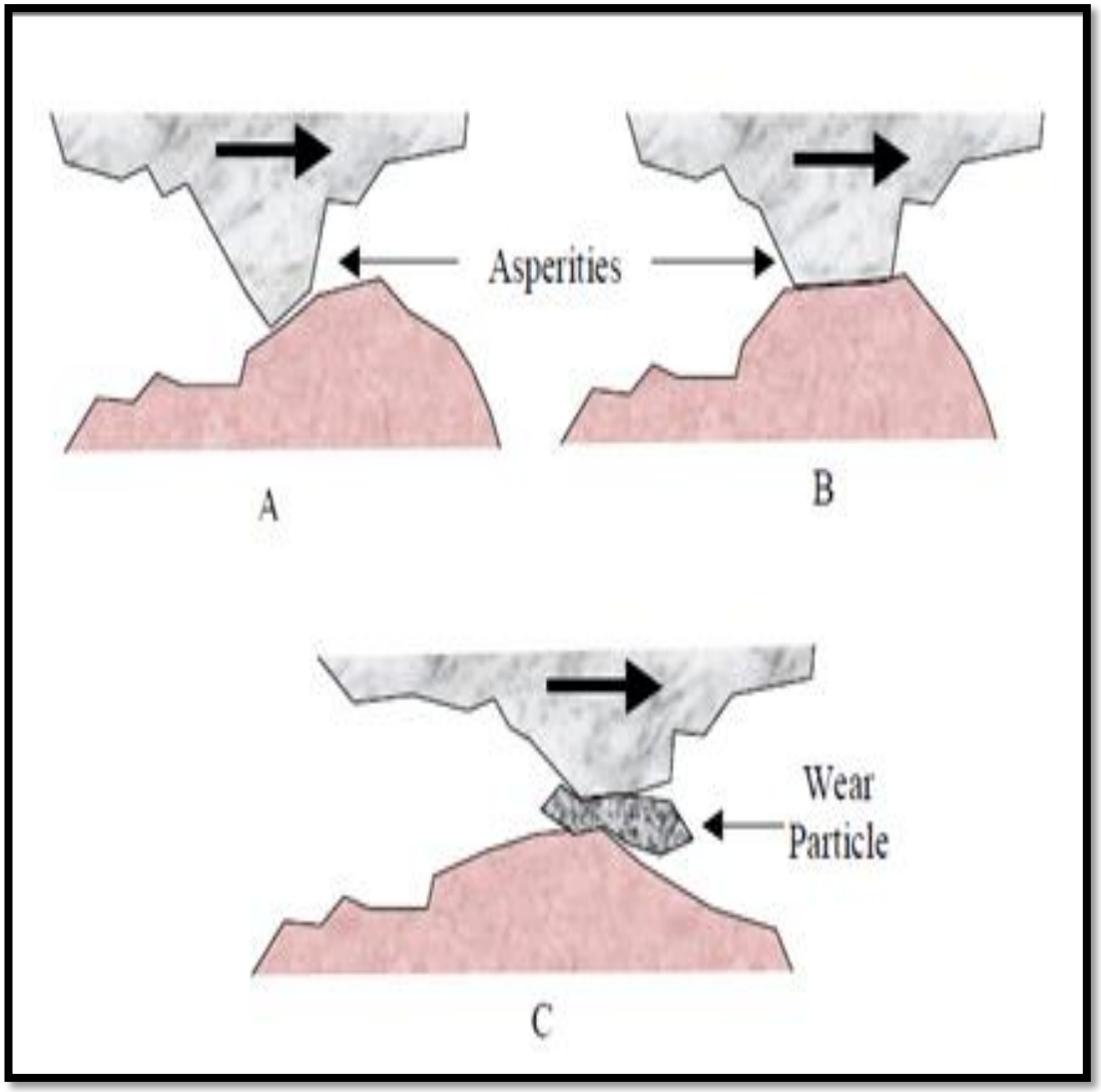

Figure (2.11): Schematic of generation of a wear particle as a result of adhesive wear process **[97].**

2. Delamination Wear

The debris is plates, the length to the thickness is ten times caused by forming and fracture such as cylinder in internal combustion machining may occur in abrasive wear. It is seen that the ductility increases strength of material against delimitation [97].

3. Fatigue Wear

Fatigue wear: wear debris is generated by cyclic loading of the contact. This mechanism can be recognized by the formation of crack and flaking of surface material [97].

4. Erosive Wear

The impingement of solid particles, or small drops of liquid or gas often cause what is known as erosion of materials and components. Solid particle impact erosion has been receiving increasing attention especially in the aerospace industry. Examples include the ingestion of sand and erosion of jet engines and of helicopter blades. The response of engineering materials to the impingement of solid particles or liquid drops varies greatly depending on the class of material, materials properties (dependent on thermal history, exposure to previous stresses or surface tensions), and the environmental parameters associated with the erosion process, such as impact velocity, impact angle, and particle size / type. Movement of the particle stream relative to the surface and angle of impingement both have a significant effect on the rate of material removal **[97]** as shown in Figure **(2,12).**

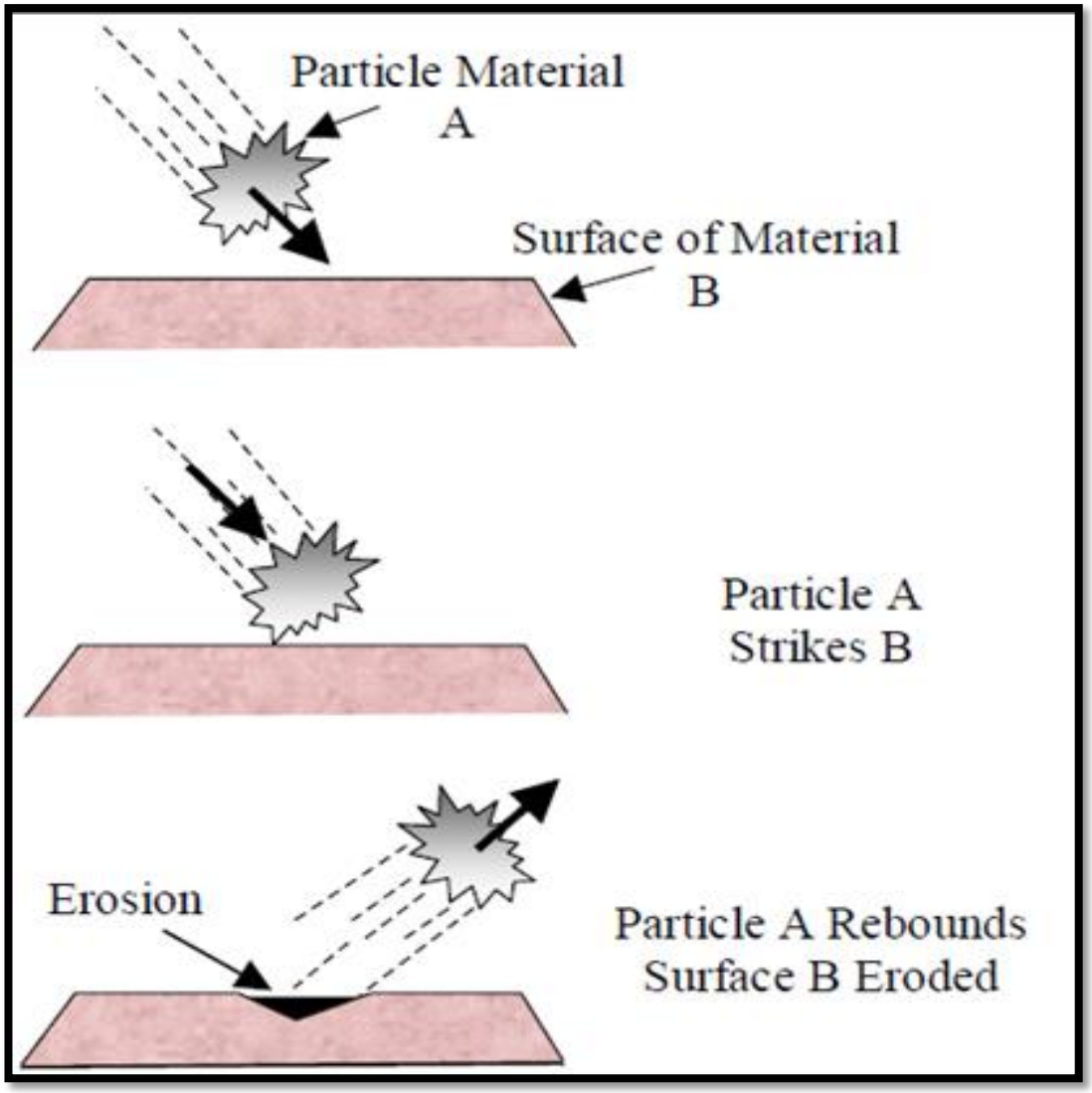

Figure (2.12): Schematic of erosive wear **[97].**

5. Tribochemical Wear

Tribochemical wear results from the removal of reaction products/layers formed in situ from the contacting surface.

6. Abrasive Wear

The material removal by hard particles sliding between two surfaces is in relative motion. The surface deforms plastically and grooves are produced in the surface **[97]**. More than one type of mechanism can be involved in a wear situation. Also, these individual

mechanisms can interact sequentially to form a more complex wear process. However, one mechanism generally is the controlling and primary mechanism. The relative importance or occurrence of individual mechanisms can change with changes in tribosystem parameters. Therefore, materials can exhibit transitions in wear behavior as a result of changes in other operational parameters, such as load, velocity, and friction **[97]**. Abrasive wear occurs when material is removed from one surface by another harder material, leaving hard particles of debris between the two surfaces. It can also be called scratching, gouging or scoring depending on the severity of wear. Abrasive wear occurs under two conditions **[97, 98]**:

1. Two body abrasion; In this condition, one surface is harder than the other rubbing surface. Examples in mechanical operations are grinding, cutting, and machining.

2. Three body abrasion; In this case a third body, generally a small particle of grit or abrasive, lodges between the two softer rubbing surfaces, abrades one or both of these surfaces as shown in figure(2.13) below abrasion in the micro-scale.

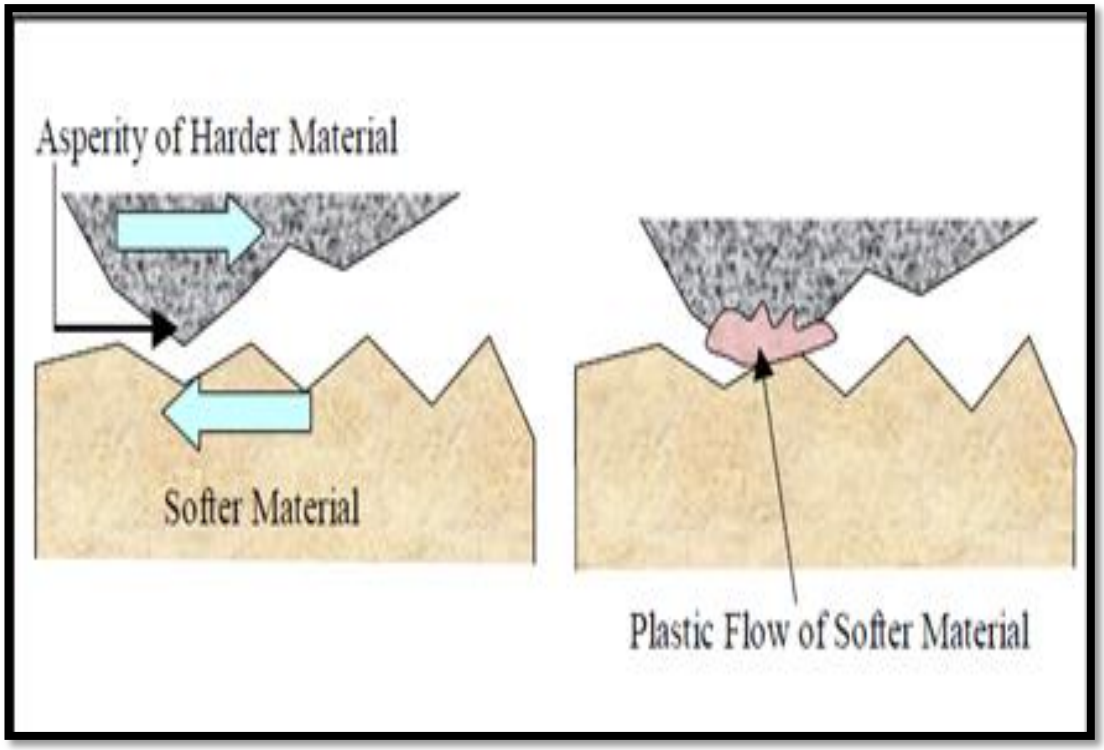

Figure (2.13): Abrasion in the micro-scale **[97].**

2.9 Contact angle and wettability

The topic of wetting has received tremendous interest from both fundamental and applied points of view. It plays an important role in many industrial processes, such as oil recovery, lubrication, liquid coating, printing, and spray quenching [99–104]. In recent years, there has been an increasing interest in the study of superhydrophobic surfaces, due to their potential applications in, for example, self-cleaning, nanofluidic, and electrowetting [105–110]. Wettability studies usually involve the measurement of contact angles as the primary data, which indicates the degree of wetting when a solid and liquid interact. Small contact angles (<90°) correspond to high wettability, while large contact angles (>90°) correspond to low wettability, as shown in figure (2.14). This paragraph will begin with an introduction of the fundamental science behind wetting and contact angle phenomena, followed by a comprehensive description of the various techniques used

to measure contact angles, as well as their applications and limitations in terms of the geometric forms of solid samples. Most of the techniques can be classified into two main groups: the direct optical method and the indirect force method. Calculations based on measured contact angle values yield an important parameter-the solid surface tension, which quantifies the wetting characteristics of a solid material.

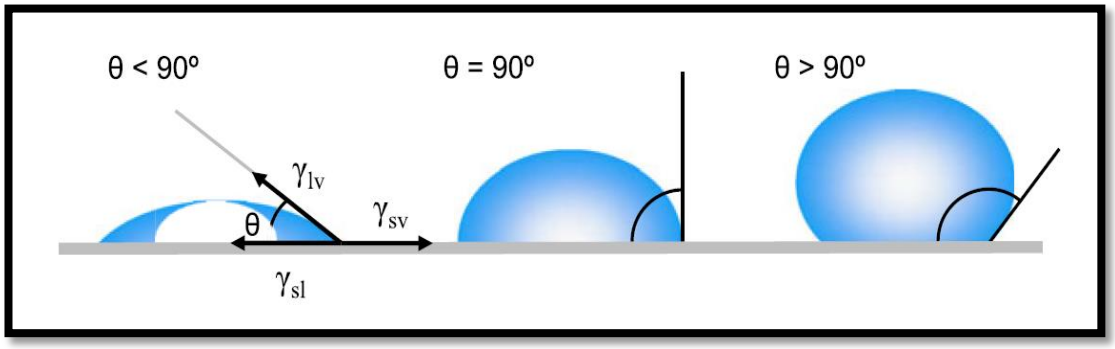

Figure (2.14): Illustration of contact angles formed by sessile liquid drops on a smooth homogeneous solid surface [110].

2.10 Elastic modulus

The modulus of elasticity or (Young's modulus) E is a material property, that describes its stiffness and is therefore one of the most important properties of solid materials. Mechanical deformation puts energy into a material [111]. The energy is stored elastically or dissipated plastically. The way a material stores this energy is summarized in stress-strain curves. Stress is defined as force per unit area and strain as elongation or contraction per unit length When a material deforms elastically, the amount of deformation likewise depends on the size of the material, but the strain for a given stress is always the same and the two are related by Hooke´s Law (stress is directly proportional to strain) [112]:

$$\sigma = E \cdot \varepsilon$$

where σ is stress [MPa]
E modulus of elasticity [MPa]
ε strain [unitless or %]

From the Hook's law, the modulus of elasticity is defined as the ratio of the stress to the strain [113]:

$$E = \frac{\sigma}{\varepsilon} \quad [MPa]$$

Stress is not directly measurable. We can calculate it from different formulas for different types of the loading (tension, flexural stress,) Strain is defined as the change of the length divided by the original (initial) length [114]:

$$\varepsilon = \frac{\Delta l}{l_0} = \frac{l_1 - l_0}{l_0} \quad [unitless\ or\ \%]$$

where Δl is change of the length [m]
l_1 length after elongation [m]
l_0 original (initial) length [m]

2.11 Biological (MTT-Based Cytotoxicity Assays)

2.11.1 Cell line and Maintenance

The Madin-Darby Canine Kidney (MDCK) cells are a model mammalian cell line purchased from LONZA Biologics (Slough, UK).

2.11.1.1 Cells thawing

One cryotube of the frozen cells was taken from the fluid nitrogen bank and thawed in a 37 ºC water bath. The vial evacuated from the water some time recently the ice floccule broken down totally, wiped

with 70% ethanol. Without pause, the cell suspension substance of the vial pipetted under laminar stream cabinet into a 15 ml sterile plastic centrifuge tube containing 10 ml of pre-warmed development medium. Centrifugation was done at 800 rpm for 10 min and the supernatant was suctioned and emptied. The cells pellet was re-suspended into 5ml warm new development media with 10% fetal bovine serum (FBS) and exchanged into 25 ml measure cell culture carafe brooded at 37C˚ and the development media supplanted on another day [115].

2.11.1.2 Subculture of cell line

After the cells became confluent as monolayer, subculture was done according to Uysal et al. protocol (Uysal et al., 2018) as follows [115]:

1. Cultures were viewed using an inverted microscope to evaluate the degree of confluence and confirm the non-appearance of bacterial and parasitic contamination.

2. The consumed medium removed.

3. The cell monolayer was washed with phosphate buffer saline (PBS) without Ca_2+, Mg_2+ using a volume equivalent to half the volume of culture medium. This wash step was repeated if the cells were known to adhere strongly.

4. Trypsin- EDTA was pipetted into the washed cell monolayer using 1ml per 25cm2 of surface area. Flask was rotated to cover the monolayer with trypsin.

5. Flask returned to the incubator and left for 2-10 minutes.

6.The cells were examined using an inverted microscope to ensure that all the cells are detached and floating. The side of the flasks may be gently tapped to release any remaining attached cells.

7. The required number of cells was transferred to a new labeled flask containing pre-warmed medium.

8. The cell line was incubated at 37C°.

9. This process was repeated as demanded by the growth characteristics of the cell line.

2.11.1.3 Harvesting of cells

Harvesting is a technique that uses the proteolytic enzyme trypsin, to detach and disaggregate the adherent monolayer cells from the bottom of the culture vessel. This procedure was performed whenever the cells need to be harvested for passage and cell count and it include the following steps [115]:

1. When the cell growth became as a monolayer and before the exponential phase, the medium was aspirated and discarded.

2. The cells then washed with 3ml of warm PBS solution.

3. About 1ml of warm trypsin EDTA solution was added to cover the monolayer, and with gentle rocking of the flask dish 4-5 times to flood the monolayer.

4. The flask dish was incubated at 37°C until the cell monolayer was detached.

5. Once the cells detached, the flask was removed from incubator and complete separation of the cells was done by rocking the flask from side to side.

6. The cells were gently pipetted up and down to disrupt cell clumps into single cells.

7. Cells were examined by inverted microscope and re-suspended into the desired number in a growth medium with 5-10% FBS, which was used to inactivate trypsin.

8.The cells were sub cultured into two flasks or cultured on culture plate. (Uysal et al., 2018)

2.12 Literature Review

in 2001 James A. Davidson, etal.,. the present invention is a medical implant or device fabricated, in any manner, from a niobium (Nb)-titanium (Ti)-zirconium (Zr)-Molybdenum (Mo) alloy (NbTiZrMo alloy). The implant or device has components at least partially fabricated from a metal alloy comprising a) between about 29 and 70 weight percent Nb; b) between about 10 and 46 weight percent Zr; c) between about 3 and 15 weight percent Mo; and a balance of titanium. The inventive alloy provides for a uniform beta structure which is corrosion resistant, and can be readily processed to develop high-strength and low-modulus, with the ability for conversion oxidation or nitridization surface hardening of the medical implant or device [116].

In 2006 Carlos Kleber Z. Andrade* and Rafael O. Rocha, in this review, recent applications of these versatile reagents in organic synthesis, including our own results, will be disclosed. Niobium catalysts generally possess a good Lewis acidity and have received increased attention in recent years. The applications of niobium pentachloride as Lewis acid in organic synthesis have been recently reviewed. Since then, there has been an increasing number of examples on the use of niobium catalysts inorganic reactions such as Biginelli reactions, Friedel-Crafts acylation and Sakurai-Hosomi reactions of acetals, Knoevenagel condensation, acetylation of alcohols and phenols, among others. Also,

chiral niobium complexes have been reported to give high enantiomeric excesses in asymmetric Mannich-type reactions [117].

In 2007G. Zorn etal., a new low modulus Ti-Nb alloy with low elastic modulus and excellent corrosion resistance is currently under consideration as a surgical implant material. The usefulness of such materials can be dramatically enhanced if their surface structure and surface chemistry can be controlled. This control is achieved by attaching a self-assembled monolayer (SAM) based on 11-chloroacetyl-1-undecylphosphonic acid, CAUDPA, to the surface and immobilization of a peptide to the monolayer. The SAM is characterized by Fourier Transform Infrared Spectroscopy (FTIR) and X-ray Photoelectron Spectroscopy (XPS) at two different takeoff angles. The CAUDPA molecules were covalently bonded on the substrate in a configuration in which the phosphoric group turns toward the Ti45Nb while the acetyl chloride end group tail turns to the topmost surface. In such configuration sequential in situ reaction is possible by exchange between the chloride and a biological molecule. Such biological molecule is the arginine-glycine-aspartic acid-cysteine, RGDC, small amino acid sequence present in many molecules of the extracellular matrix. Preliminary cell culture in-vitro result shows an improvement of the response of osteoblast cells to Ti45Nb after the peptide immobilization [118].

In 2011 René Olivares-Navarrete, etal., Niobium coatings deposited by magnetron sputtering were evaluated as a possible surface modification for stainless steel (SS) substrates in biomedical implants. The Nb coatings were deposited on 15 mm diameter stainless steel substrates having an average surface roughness of 2 μm. To evaluate the biocompatibility of the coatings three different in vitro tests, using human alveolar bone derived cells, were performed: cellular adhesion,

proliferation and viability. Stainless steel substrates and tissue culture plastic were also studied, in order to give comparative information. No toxic response was observed for any of the surfaces, indicating that the Nb coatings act as a biocompatible, bio-inert material.

Cell morphology was also studied by immune-fluorescence and the results confirmed the healthy state of the cells on the Nb surface. X-ray diffraction analysis of the coating shows that the film is polycrystalline with a body centered cubic structure. The surface composition and corrosion resistance of both the substrate and the Nb coating were also studied by X-ray photoelectron spectroscopy and potentiodynamic tests. Water contact angle measurements showed that the Nb surface is more hydrophobic than the SS substrate [119].

In 2013 Qiang Li, and etal., For spinal-fixation applications, implants should have a high young's modulus to reduce spring back during operations, though a low young's modulus is required to prevent stress shielding for patients after surgeries. In the present study, Ti–29Nb–13Ta–4.6Zr alloy (TNTZ) with a low young's modulus was modified by adding Cr to obtain a higher deformation-induced young's modulus in order to satisfy these contradictory requirements. Two newly designed alloys, TNTZ–8Ti–2Cr and TNTZ–16Ti–4Cr, possess more stable b phases than TNTZ. These alloys consist of single phases and exhibit relatively low young's moduli of <65 GPa after solution treatment. However, after cold rolling, they exhibit higher young's moduli owing to a deformation-induced x-phase transformation. These modified TNTZ alloys show significantly less spring back than the original TNTZ alloy based on tensile and bending loading–unloading tests. Thus, the Cr-added TNTZ alloys are beneficial for spinal-fixation applications [120].

In 2019 Rodrigo Sacramento da Silva, and Alexandre Antunes Ribeiro, characterized Titanium-35Niobium (Ti-35Nb) surface modified by controlled chemical oxidation. Ti-35Nb (wt.%) substrates were processed by powder metallurgy. The powders were mechanically mixed, uniaxially cold pressed and sintering at whatmean. Then, the sintered substrates were immersed in a solution consisting of equal volumes of concentrated H_2SO_4 and 30% aqueous H_2O_2 for 4 hours at room temperature under continuous agitation. Sample characterizations were performed by scanning electron microscopy, profilometry, contact angle measurement, X-ray diffraction, and X-ray photoelectron spectroscopy. The results showed that the samples exhibited a microporous structure with micro-roughness on surface, and the β-Ti phase was stabilized by complete Nb atoms diffusion in Ti matrix. In addition, the chemical treatment successfully modified the Ti-35Nb surface with micropore formation and enhancement of hydrophilic feature and TiO_2 and Nb_2O_5 layer, which can improve the biocompatibility of TiNb alloy implants [121].

In 2020 Oleg Mishchenko etal developed a Zr-Ti-Nb system with a low young modulus suitable for biomedical application, including orthopedics and dental implantology. Two diferent charges were used for new alloy production with melting in a vacuum-arc furnace VDP-1 under atmospheric control (argon + helium) with a non-consumable tungsten electrode and a water-cooled copper crystallizer. Post-treatment included a forging-rolling process to produce a bar suitable for implant production. SEM with EDX and the mechanical parameters of the new alloy were evaluated, and a cell culture experiment provided a biocompatibility assessment. The chemical composition of the new alloy can be represented as 59.57-19.02-21.41 mass% of Zr-Ti-Nb. The mechanical properties are characterized by an

extremely low young modulus—27,27 GPa for the alloy and 34.85 GPa for the bar. The different master alloys used for Zr-Ti-Nb production did not affect the chemical compound and mechanical parameters so it was possible to use affordable raw materials to decrease the final price of the new product. The cell culture experiment demonstrated a full biocompatibility, indicating that this new alloy can be used for dental and orthopedics implant production [122].

In 2008 Lee, S. H., et al focused on the significant improvement in mechanical properties of biomedical Co Cr Mo alloys with combination of N addition and Cr enrichment. An examination of a Ni free Co, Cr and Mo alloy under as cast condition was done by means of tensile tests and microstructure observations. The findings of the observation shows that the solubility of N in CoCrMo alloys increases with increasing Cr content from 29 to 34 mass %. This result suggests that there is a significant improvement in mechanical properties such as yield stress, tensile stress and fracture elongation. Also, the increasing amount of Cr content has also contributed to the improved mechanical properties[123].

In 2008 Oksiutaa, Z., et al focused on CoCr Mo based composite which is reinforced with bioactive glass. This study used a powder metallurgy technology to produce a porous CoCr Mo based composite bioactive glass. The results show that the microstructure, mechanical and corrosion properties of composite materials are significantly affected by the addition of bioglass to the alloy as well as rotary cold repressing and heat treatment of sintered specimens in comparison with pure porous alloys. Also, the addition of bioglass obtained a higher corrosion resistance, hardness and yield strength even though the powder metallurgy samples were in a passive state[124].

In 2008 Krishna, B. V., et al looked at functionally graded, hard and wear resistant of CoCrMo alloy. The alloy was coated on Ti-6A14V alloy with a metallurgical sound interface using a laser engineering net shaping. The findings showed that addition of CoCrMo alloy onto the surface of Ti_6A1_4V alloy showed major increase in the surface hardness without any intermetallic phases in the transition area. The study also investigated human osteoblast cells (cultured) to test the coatings of vitro biocompatibility. Based on vitro biocompatibility CoCrMo alloy concentration increases in the coating. It reduces the number of live cells after 14 days of culture on the coating compared with base Ti-6A1-4V alloy. However, the coated samples constantly showed better bone cell increase than 100% CoCrMo alloy[125].

In 2008 Dourandish, M., et al looked at the sintering biocompatible CoCrMo alloy manufactures stepwisely for porosity-graded composite structures. These composite structures provide strength at the core and a porous layer for the tissue growth. To evaluate the process two grades of gas atomized CoCrMo powder with an average particle size of 19 and 63 micro m was used. The microstructural of the sintered specimens was evaluated. The findings showed an intermediate sintering temperature of 1280C° and argon can be used in developed of the porosity graded composite layers can be produced e.g., a relative dense core (5% porosity) with a porous layer (33% porosity) [126].

In 2009 Songur, M., et al investigated the electrochemical corrosion properties of metal alloys used in orthopaedic implants. The study investigated 316 stainless steel, CoCrMo and Ti6A14V alloys in simulated body conditions at 37C° by using Tafel Plots, mixed potential and electrochemical impedance spectroscopy. The results show that the Ti6A14V has the highest corrosion resistance followed by CoCrMo alloy. The best pairs of alloys for galvanic corrosion with the minimum

galvanic potential and current values were Ti6A14V_CoCrMo, as the mixed potential theory and Tafel method suggests. The study accomplished that the most suitable material for implant applications in the human body is Ti6A14V[127].

In 2010 Giacchi, J. V., et al concentrated on the resulting microstructures rising from samples poured under manufactured environmental situations of three different types Co, Cr and Mo alloys and these were. An alloy built up from commercial purity constituents, a remelted alloy and a certified alloy for comparison. An optical microscopy with a colorant etchant was used to identify the current phases and scanning electron microscopy. The result illustrates the cast microstructure of Co_fcc dendritic matrix with a existence of a secondary phase such as (M23C6) carbides precipitated at grain boundaries and interdendritic zones. In this type of alloys these precipitates are the main strengthening mechanism[128].

In 2010 Kamardan, M. G., et al focused mainly on the sintering temperature effect to the shrinkage behavior of cobalt chromium alloy of powder metallurgy technique. Several tests were conducted to determine several effects such as: compression and hardness test, the rate of shrinkage measurement, the bulk density and porosity percentage measurement and micro structural study. The findings revealed that the increasing of sintering temperature has caused a reduction of Co_Cr. This has resulted to the reduction of the pore volume and therefore increased its density and in combination with that the strength and the hardness of Co and Cr was also increased[129].

In 2010 Rodrigues, W. C., et al focused on powder metallurgical processing of Co, 28%Cr, 6%Mo for dental implants: physical, mechanical and electrochemical properties. This study examined the powder metallurgical production of a CoCrMo alloy for

dental implants in conventional parameters. The study investigated the achievement of the applications of these parameters an alloy with enough green density, low porosity after sintering, considerable hardness and impulsively passive behavior in the ringer solution. The results show that the physical, mechanical and electrochemical properties of the alloy are affected by a small variation of the sintering temperature with comparison of samples with different sintering temperatures[130].

In 2011 Do rz ń ki, L. A. studied the relationship between cobalt content on hardness and chromium content on corrosion resistance on the basis of base cobalt alloys Co, Cr, Mo used in prosthodonita. The investigation was to choose five base cobalt alloys with different concentration of cobalt and additions. In order to test the hardness microhardness Fm ARS 900 Future TECH with load 1 kg was used. Corrosion resistance test were carried out at room temperature and use of Volta PGP201 system for electrochemical tests. The examinations were made in water centre which simulated artificial saliva environment. The findings of the study showed that the cobalt content in Co, Cr, Mo alloys in one of the possible parameters which influence on hardness. The highest value of hardness was obtained for alloy with the highest Co content. Chromium content in one of the most important factors which influence on corrosion resistance, due to that alloy with the highest Cr content characterized the higher re-passivation potential[131].

In 2012 Adzali, N. M. S., et al reviewed the works carried out in the field of composite metal alloys that are reinforced with ceramic with special reference to their mechanical properties, corrosion and bioactivity behavior. The review was from the point of microstructure, mechanical properties, corrosion and bioactivity behavior. This was obtained by the composite metal alloys added with ceramic for biomedical applications. The research investigation shows

that those composites can be good alternative materials for biomedical applications. It also found that the ceramic is an additive which can increase the mechanical properties, reduce the corrosion rate and increase the formation of an appetite layer on the surface, which provides improved protection for the based metal alloys matrix"[132].

In 2012 Patel, B., et al. "looked at metal on metal hip replacement and it focused on two typically manufactured alloys (ASTM F75 and ASTM F1537) and a spark plasma sintered alloy were evaluated for their microstructure, tribological performance and the release of metallic content. The spark plasma sintering is a powder processing technique that utilizes electric current Joule heating to produce high heating rates to sinter powders to form an alloy. The results showed that the SPS alloy with oxides and not carbides in its microstructure had the superior hardness, which caused in the lowest wear and friction coefficient with lower amount of chromium and molybdenum detected from the wear remains compared to ASTM F75 and ASTM F1537. The results also showed that the wear debris in size and size distribution of the SPS alloy was significantly small which indicate the material that exhibits good performance and more favorable as compared to the present conventional cobalt based alloys used in orthopedics[133].

In 2012 Mischler, S., and Munoz, A. I. [133] evaluated previous studies and experiments that concentrated on the degradation of the CoCrMo alloys using the existing tribocorrosion concept. Tribocorrosion is a sub-discipline of tribology and corrosion that recently made significant progress in mechanistic understanding and modeling. The findings of this study showed a clear key role for the electromechanical phenomena on the tribological behavior of biomedical Co, Cr and Mo alloy implants. The results also show that the wear accelerated corrosion

due to the mechanical removal of the passive film during sliding is a major contribution to the overall degradation[133].

In 2013 LiU, R., et al "studied the surface modification of a medical grade Co-Cr-Mo alloy by low temperature plasma surface alloying with nitrogen and carbon. The study aimed to improve the hardness, wear resistance and corrosion resistance of alloy (Co-Cr) by plasma surface alloying with nitrogen and with both (carbon and nitrogen) at low temperatures (300 and 400 C°). The results showed that the optimized treatment environment have produced very promising surface layers on CCr alloy for biomedical applications"[135].

In 2013 Daud, Z. C., et al "focused on the corrosion behavior of powder metallurgy of Co-Cr-Mo alloy. The powders were first blended with binder using rotation mill and compacted using uniaxial cold press to a pellet shape and then sintered at two sintering temperatures (1300C° 1350C°) with 90 minutes of sintering time. An immersion test was carried out in a water bath with maintain temperature at 37C° for 90 days. The results show that the sample sintered at 1350C° has the lowest mpy results after 90 days immersed in 0.9% sodium chloride[136].

In 2014 Muna, K. A., et al "focused on the corrosion resistance properties of CoCrMo alloy which was immersed in artificial saliva at 37±1 C°. The surface of the specimen was analyzed before and after the immersion using an optical microscope. In order to test the corrosion resistance, an electrochemical measurement by polarization was performed. The findings of the study show that the galvanic corrosion demonstrated that the CoCrMo [136] .

In 2015 Mantrala, K. M., et al "concentrated on laser engineered net shaping. Co Cr Mo alloy samples fabricated a laser based additive manufacturing technology have been subjected to heat treatment to study the influence on microstructure, wear and corrosion properties.

The study used an L9 orthogonal array o Taguchi method and then the samples were solutionised at 1200C° for 30, 45 and 60 min followed by water quenching. The heat-treated samples were evaluated for their microstructure, hardness, and wear and corrosion resistance after conducting aging treatment at 815 and 830C° for 2, 4 and 6 hr. The results showed that an analysis of variance and relational analysis on the experimental data revealed that the samples were subjected to solution treatment for 60 min, without aging; demonstrate best combination of hardness, corrosion resistance and wear resistance[138].

In 2015 Sabine, W. and Bojan, M. investigated the relationship between the microstructure, mechanical factors and stent design which is commercially available in cobalt-chromium stents were investigated with concentration on different inhomogeneous plastic deformation due to crimping and dilation. The results of the investigation showed that features material related deformation behavior with mainly primary slip was recognized to be responsible for the particular properties of Co Cr stents[139].

Chapter Three……..……Experimental Part

3.1 Introduction:

In this chapter, the experimental setup; techniques and equipment; preparation of mold; preparation of Niobium-1%Zirconium alloy, and the effect of Germanium content on alloy; and mechanical, chemical, electro-chemical and physical tests, will be presented.

3.2 Materials and Apparatuses:

3.2.1 Basic Powder:

In this research the materials powders used to prepare Nb-1%Zr-xGe alloys are listed in Table (3.1) with average particle size, purity and the original ingredients from HWNANO- company in China.

Table (3.1): Materials powder utilized in this study with their average particle size.

Powder	Average particle size (μm)	Purity %
Niobium	10	99.95
Zirconium	12.20	98.25
Germanium	0.818	99.97

3.2.2 Apparatuses:

The apparatuses used in this study are**:**

1. Drying furnace type (PRODIT s.a.s. via asti, 59-10026 santena (torino) Italy).

2. Sensitive balance type ENTRIS224- 1S (Sartorius Lab Instruments GmbH & Co, KG, Goettingen, Germany).

3. Stainless steel mold specially designed and built to prepare the samples.

4. Hydraulic compacting machine (CARVER) type (1569 MORRIS STREET, WABASH, INDIANA U.S.A 46992-0544, (260) 563-755).

5. Electrical argon furnace.

6. Grinding and polishing device type (Metallographic lapping/ polishing machine, MTI Corporation, model UNI POL-820).

7. Optical microscope type (Electronic Eyepiece, model YJEYE01, resolution of 1280 (H) *1024 (V), China).

8. X-ray instrument (XRD) type SHIMADZU Lab X XRD - 6000 (Japan).

9. Laser particle size analyzer (model: better size 2000).

10. Brinell hardness test device type

11. Top planetary ball mill mixer (Bench – Top Planetary Automatic Ball Mill).

12. Turning machine type (ZMM-Sliven/Bulgaria)

13. Wear test machine, Microtest S.A type (C/Valle de Tobalina, 1028021 – Madrid (Spain)).

14. Potentiostat.

3.3 Program of the Current Study:

To study the effect of weight fraction of Germanium particles on microstructure, physical, chemical and mechanical properties such as wear and hardness on Niobium-1%Zerconium alloy, samples coded in table (3.2) below. Code **B** refers to Niobium-1%Zerconium alloy, while digits refer to germanium content. Figure (3.1) shows the program of the experimental work.

Table (3.2): Samples Prepared for this study.

Sample Code	Parameters					
	Germanium Content (%)	**Particle Size (μm)**	**Mixing Time (hr.)**	**Compaction Pressure (Mpa)**	**Sintering Temp. (℃)**	**Sintering Time (hr.)**
B	**0%**	0.818	**5**	**650**	**1200**	**5**
B_1	**0.5%**					
B_2	**1%**					
B_3	**1.5 %**					
B_4	**2%**					
B_5	**2.5%**					
B_6	**3%**					
B_7	**3.5%**					
B_8	**4%**					
B_9	**4.5%**					
B_{10}	**5%**					
B_{11}	**5.5%**					
B_{12}	**6%**					

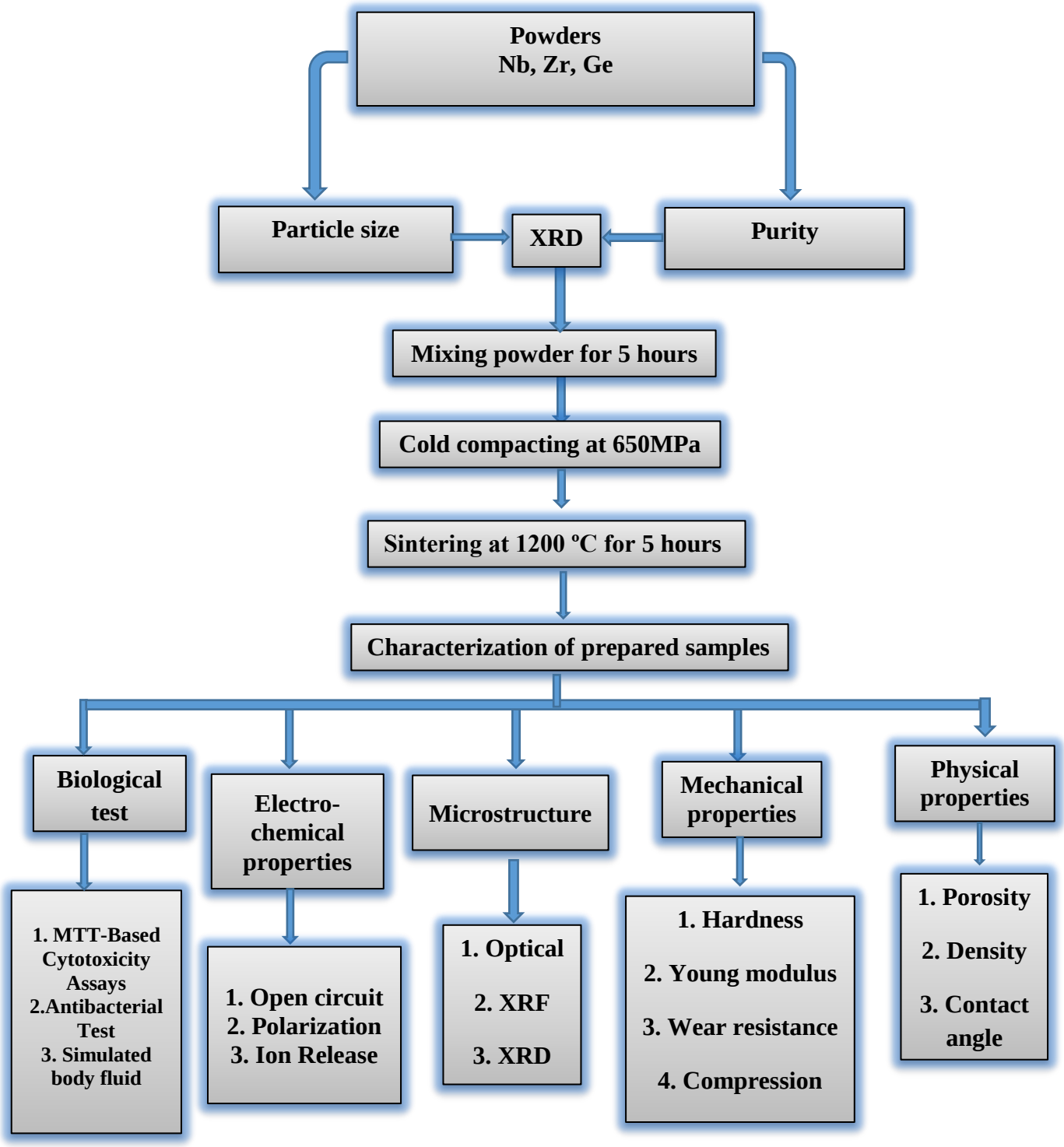

Figure (3.1): Flowchart of experimental work.

3.3.1 Particle Size Analyzer

The average particles size was calculated using better size 2000 laser particles size analyzer shown in fig. (3.2).

3.3.2 Samples Preparation

Powder metallurgy technique was used to prepare the samples. The procedure includes mixing, compacting and sintering.

3.3.2.1 Powder Weight

Sensitive Balance type (L220S– D) with (± 0.0001 accuracy) Germany origin was used to weight each type of powders before mixing

3.3.2.2 Mixing of Metal Powders

The weighted powders have been wetly mixed by using planetary automatic ball mill shown in figure (3.4), steel balls with different diameter have been used and Ethanol has been added as a mixing medium of wet mixing. The mixing process was being carried out for 5 hours.

3.3.2.3 Powder Compacting

In this step, (3.5 g) of powder mixture has been compacted by using electric hydraulic press to produce a disk sample with dimension of 13 mm in diameter and 3mm thickness, the compacting pressure was 650MPa and holding time was 2 minutes. Graphite used as a lubricant to reduce the friction during the pressing process.

3.3.2.4 Sintering

The sintering process has been carried out under Argon conditions by using electrical argon furnace that showed in Figure (3.6). In this stage, samples compacts are sintered after compaction stage by raising the temperature of the samples to **(1200℃)** for **(5 hours)** and let it cool down inside the furnace till the temperature of the samples drops up to room temperature. Thereafter, the samples will be ready for testing. Figure (3.7) shows the program of the sintering process.

Figure (3.6): Electrical argon furnace.

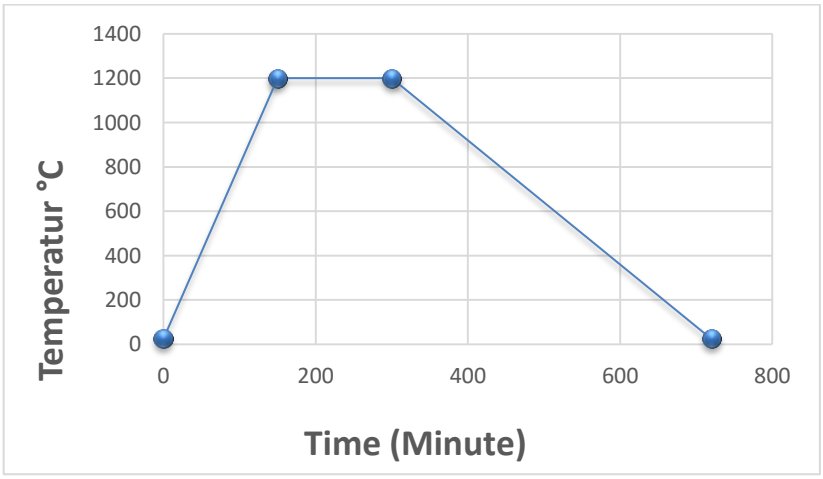

Figure (3.7): The program of the sintering process.

3.4 Preparation of Specimens for The Testing

All samples after sintering process were grinded by using (180, 400, 600, 800, 1000,1200,1500,2000) grit silicon carbide papers, then polished with diamond past to get a bright mirror finish for the final step.

Etching was made at room temperature; Table (3.3) illustrated the chemical composition of the etching solution [86]. After etching process, the specimens were washed with water and dried.

Table (3.3): Chemical Composition of Etching Solution [86]

No.	Constituent	ml.
1	HF	5
2	HNO_3	25

3.4.1 Microstructure Characterization

3.4.1.1 X- Ray Diffraction Analysis

The test of X-ray diffraction analysis utilized for each element powder used in this study separately, and for Nb alloy after sintering then compare the results with standard charts. In this test, the speed used was (6 deg. /min.), the step was (0.02 deg.), and the angle from (20-80) deg. with copper (Cu) target, wave with length (1.54060) Angstrom, the voltage of (40 KV), and the current used was (30 mA). The analysis of pure Niobium, Zirconium and Germanium powder have been done in Babylon university/college of engineering materials, department of ceramics and construction materials. Figure (3.8) shows the XRD device used for this testing.

Figure (3.8): X-ray diffraction (XRD) analyzer device.

3.4.1.2 Light Optical Microscope (LOM)

Involved identification of the phases, shape and grain size are some characteristics of grain boundaries. Each of these has distinct characteristics. The microstructure evaluated with (100x, 200x and 400x) magnification using Olympus microscope manufactured by Japan.

3.4.1.3 X-Ray Fluorescent Analysis (XRF)

Handheld (XRF) analyzer type (DS-2000) American, is used to explain the chemical composition for powders and alloys, Figure (3.9) shows image of machine.

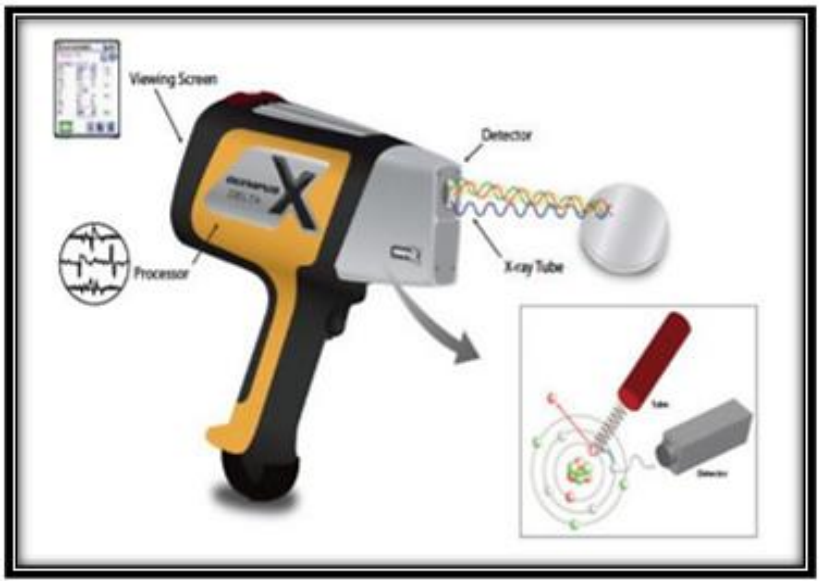

Figure (3.9): X-Ray Fluorescent Analysis (XRF)

3.4.2 Mechanical tests

3.4.2.1 Macro-hardness Measurement

Macro-hardness Brinell tester showed in the following Figure is used to measure the hardness of the specimens with (31.25) kg as applying weight and the incubation time was (10 sec) in state applied weight and

diameter (2.5mm). Three reading for each specimen had been taken and the average value used to analysis the behavior of the alloys.

Figure (3.10): Wilson Hardness Machine.

3.4.2.2 Elastic Modules

The elastic modulus, the intrinsic nature of materials, is determined by the bonding force among the atoms. This bonding force is associated with the crystal structure and the distances among the atoms, which can significantly affect alloying addition, heat treatment, and porosity. Elastic deformation behavior investigations are essential for understanding the mechanical reaction of biomedical materials [37]. This elastic module measures material rigidity which can be determined using the longitudinal and transverse velocity values in the following equations [38].

$$\nu = \frac{1 - 2\left(\frac{V_T}{V_L}\right)^2}{2 - 2\left(\frac{V_T}{V_L}\right)^2}$$

$$E = \frac{V_L{}^2 \rho(1+\sigma)(1-2\sigma)}{(1-\sigma)}, \quad \text{……. (3.1)}$$

where ν is the Poisson's ratio,

VT is shear (Transverse) velocity (m/s),

VL is the longitudinal velocity (m/s),

E: elastic modulus (GPa),

ρ: density (kg/m3).

3.4.2.3 Dry Sliding Wear Test

Before wear test, the specimens were dried at (100 C°) for (2 h) and cooling in the furnace, this process had been done by using vacuum drying furnace, then the samples are saved in well- knit boxes with silica gel material to keep them completely dry.

The dry sliding wear are studied by using pin on disk concept using (400 rpm) and constant radius (4mm) with different sliding distance and the loads were (20N and 25N). The specimens is weighted before test using (0.0001) accuracy electric balance. After a period of time (5, 10, 15, 20 and 25 min) the specimens test is weighted and the dry sliding wear rate had determined according to Equation (3.2). The wear instrument that was used in this work as showed in Figure (3.11). The test method had been covered according to ASTM G 99[88]. The following equation was used to determine wear rate [88]

$$Wear\ rate = \frac{weight\ loss\ (g)}{\rho(\frac{g}{cm^3})} \qquad \text{…… (3.2)}$$

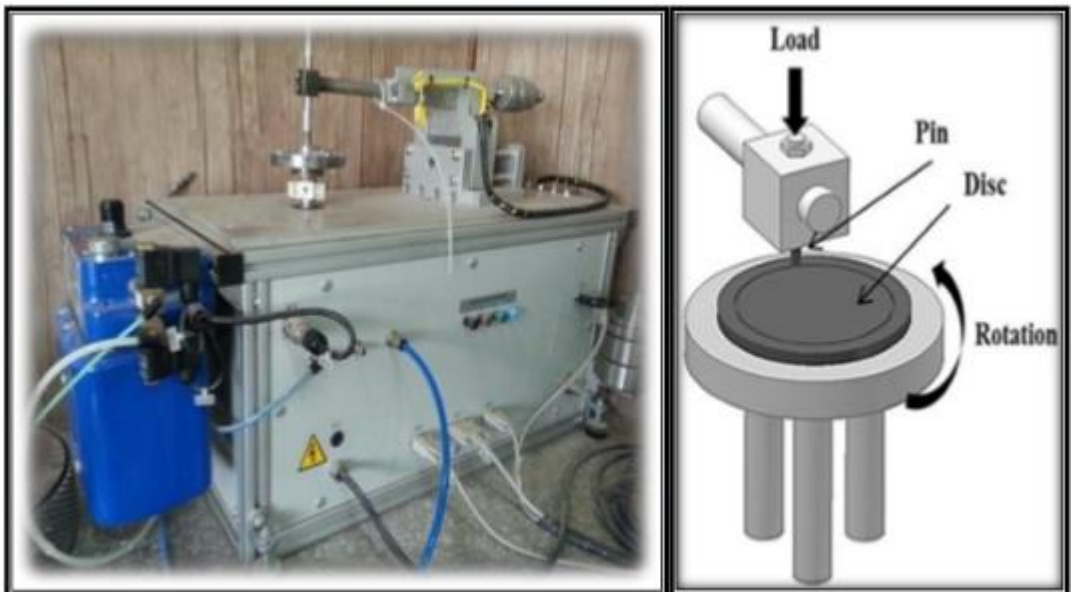

Figure (3.11): Dry Sliding Wear Machine

3.4.2.4 Compressive Strength Test:

The capability of a materials or structures to resist loads is called compressive strength. It can be measured via plotting applied force against deformation in testing machine. It is the main value for design of structure. In this test, specimens were prepared in dimensions (10mm x 20 mm). The test was run at a constant loading speed of 0.5mm/min. The compressive strength is calculated by using the following equation:

Compressive strength (MPa.) = Max force(N)/Cross section Area (mm^2) .... (3.3)

This test was conducted using samples for compression test used in the search after sintering so as to know the stress that fail specimens of the alloy listed and comparing between them. The test was conducted in Babylon University - College of Materials Engineering –metallurgical Dept. using device type (computer control electronic universal testing machine-model: WDW-200, serial NO. W1124) as shown in Figure (3.12). Maximum load capacity of (200 KN) and the pulling speed (0.5 mm / min.).

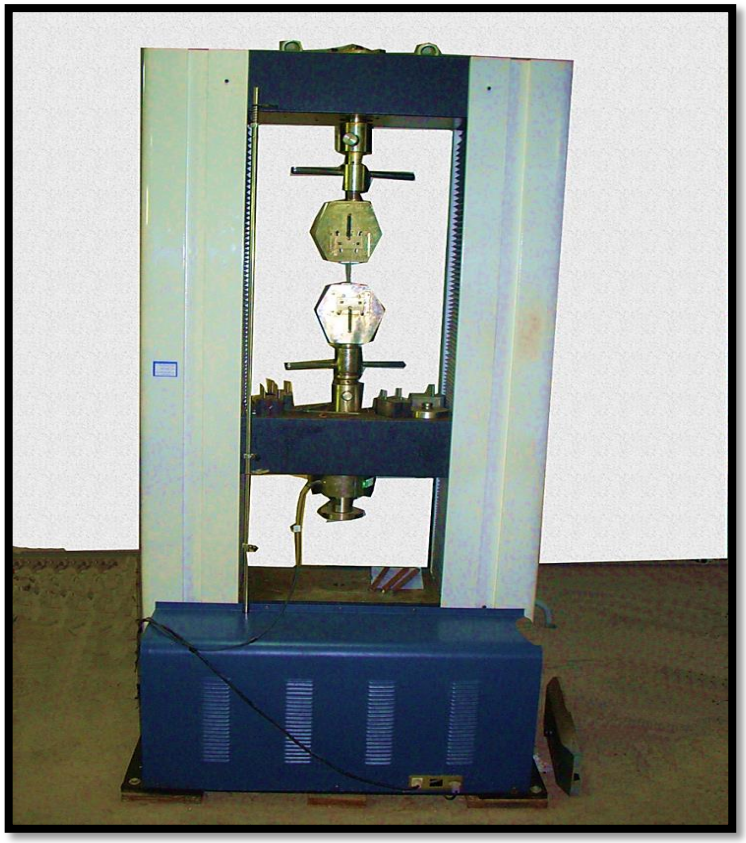

Figure (3.12): Universal testing device.

3.4.3 Electro-chemical Tests

Two types of corrosion tests have been accomplished an open Circuits Potential (OCP) - time measurements, and potentiodynamic polarization have been used as the technique for evaluating corrosion parameters for all alloys tested. One specimen from each alloy type have been prepared for each test. The dimensions of the specimen have been prepared for the test are (13) mm in diameter and (4) mm in thickness. Prior to tests, the exposed surface of each specimen has been ground flat using emery paper up to 2500 grit and polished with diamond past of 3 μm particle size. The specimens have been degreased with ethyl alcohol and dried under an air stream. Electrical connections have been made using pregnant fastened to the unpolished surface of each specimen. The electrolyte solution used in corrosion tests was applied in natural saliva

and hank solution that has composition is shown in Table (3.4). The pH solution was 6.8 and 7.2 for synthetic saliva and Hank's solution respectively at 37 ºC temperature **[**85].

Table (3.4): Chemical composition of synthetic saliva [85] Hank's solution (g/l) and Hank's solution(g/L) [85]

No.	Components	Synthetic saliva (g/l)	Components	Hank's solution (g/l)
1	NaCl	0.4	NaCl	8
2	KCl	0.4	$CaCl_2$	0.14
3	CaCl2.2H2O	0.906	KCl	0.4
4	$NaH_2PO_2.2H_2O$	0.69	$NaHCO_3$	0.35
5	Na2S.9H2O	0.005	Glucose	1
6	Urea	1	MgCl2.6H2O	0.1
7	/	/	Na2HPO4.2H2O	0.06
8	/	/	KH2PO4	0.06
9	/	/	MgSO4.7H2O	0.06

3.4.3.1 Open Circuit Potential (OCP)

The experimental arrangement for the measurement of open circuit potential is shown in Figure (3.13). It shows a schematic drawing describing the experimental situation. A 400 ml capacity glass electrolytic cell is used. The tests were carried out with the specimens immersed in a solution of artificial saliva and Hank's solution. The potential of the working electrode (specimen) is measured with respect to a Standard Calomel Electrode (SCE). A voltmeter is connected

between the working electrode and the reference electrode. For each specimen, one hours open circuit potential, EOC, measurement was performed. The first record was taken immediately after immersion then the voltage was monitored for the interred period of test at an interval of five minute.

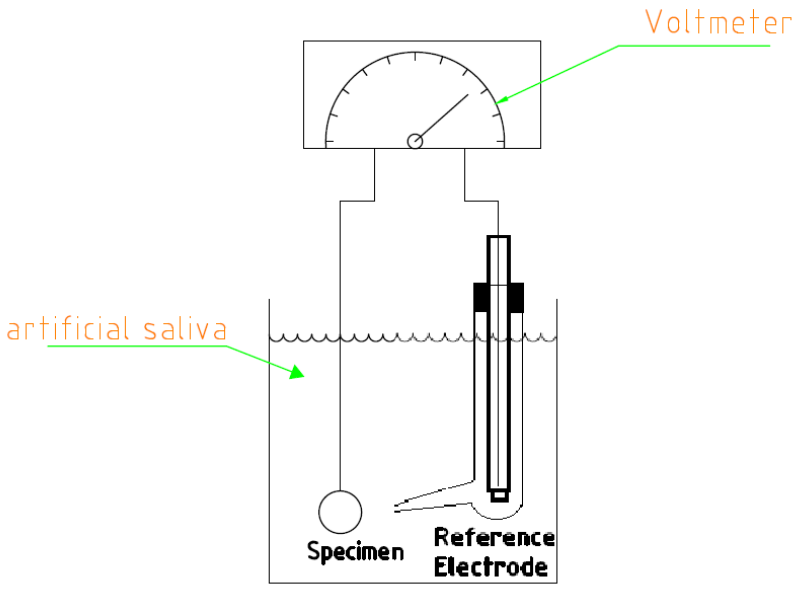

Figure (3.13): Illustrates a schematic drawing describes the experimental situation

3.4.3.2 Linear Polarization

Polarization tests have been performed by using electrochemical standard cell which containing working electrode, auxiliary electrode (Pt. electrode) and reference electrode (SCE) carried out in synthetic saliva and hank according to the American Society for Testing and Materials (ASTM) **[86].** Polarization experiments have been conducted in potentiostate type (Winking M Lab 200). When the specimen reaches the constant potential, potentiodynamic polarization has been started from an initial potential of 250 mV below the open circuit potential and the scan has been continued up to 250 mV above the open circuit potential. The specimens have been scanned in the positive direction at a

sweep rate of 0.4mV/s and the current has been reported with respect to potential. Figure (3.14) shows the electrochemical system used**.**

The corrosion potentials (E_{corr}) and corrosion current density (I_{corr}) are obtained as a result of the test and then the corrosion rate measurement is obtained by using the following equation [86]: -

$$\boldsymbol{Corrosion\ Rate\ (mpy) = \ [\![(0.13\ icor.(E.W))/\rho]\!]} \quad \textbf{……..(3.4)}$$

Where:

E.W: equivalent weight (g/eq.)

ρ: density (g/cm^3)

i_{corr}: current density ($\mu A/cm^3$)

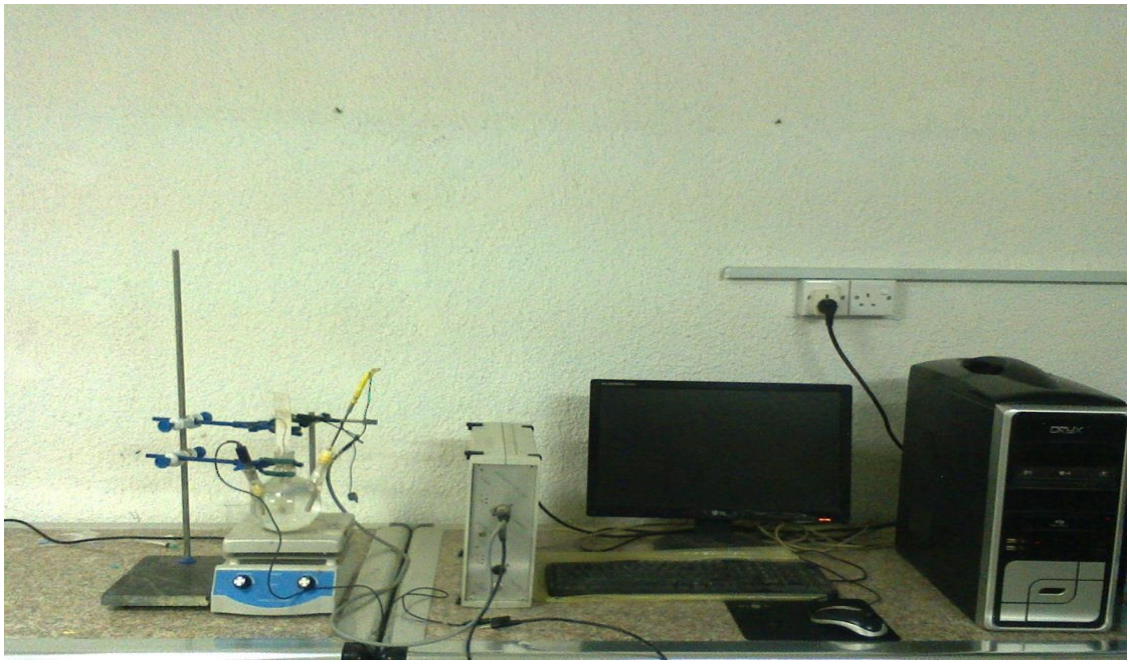

Figure (3.14): The electrochemically system.

3.4.3.3

Ion Release Test The test was conducted in the laboratory (Kufa Office / for Scientific Qualification Services), where the alloys of the elements were placed for (30) day at 37± 1˚C, immersion alloys in a solution of artificial saliva and hank's solution**.**

The investigation of metal ion release of the prepared specimens with and without additions the defect mercury ion release in vitro by immersing in artificial saliva and Hank's solution. The test of static immersions is recognized in agreement with the currently specified JIS T- 0304 standards for metallic biomaterial **[87]**. Specimens are immersed in plastic containers with 50mL of solution (artificial saliva and Hank's solution) for (30) days in glass chamber. Specimens are immersed in small containers, where these containers are kept in glass chamber to keep the temperature at 37±1 ˚C.

Assessing the metal ion (Nb) concentrations by Atomic Absorption flame as shown in Figure (3.15).

Figure (3.15). Atomic Absorption Flame**.**

3.4.4 Biological test

3.4.4.1 MTT-Based Cytotoxicity Assays

MDCK cell line was seeded with different type of (1-13) in 12-well plates for incubation period of 24 hr at 37C°. The cytotoxicity was assessed by MTT assays as follow:

Procedure (Meerloo et al; 2011):

1- At the end of the incubation period, the medium was removed from the wells and then the cells were washed with PBS. A blank control was carried to assess unspecific formazan conversion.

2- A volume of 1.2 ml of MTT solution (5 mg/ ml) was added to 10.8 ml medium to obtain final concentration of 0.5 mg/mL. Then, 200 µl of the resulting solution was added in each well.

3- The plate was incubated for 3 hours at 37°C until intracellular purple formazan crystals were visible under the inverted microscope.

4- The supernatant was removed and 100 µl DMSO was added in each well to dissolve the resultant formazan crystals.

5- The plate was incubated at room temperature for 30 minutes until the cells have lysed and purple crystals have dissolved.

6- Absorbance was measured by a microplate reader at 570 nm.

The absorbance reading of the blank must be subtracted from all samples. Absorbance readings from test samples must then be divided by those of the control and multiplied by 100 to give percentage cell viability or proliferation. Absorbance values greater than the control indicate cell proliferation, while lower values suggest cell death or inhibition of proliferation. Percent of cell viability or percent of inhibition was calculated by the following formula:

$$\% \text{ viability} = (AT - AB) / (AC - AB) \times 100\% \quad \text{…….(3.5)}$$

Where:

AT = Absorbance of treated cells (drug).

AB = Absorbance of blank (only medium).

AC = Absorbance of control (untreated)

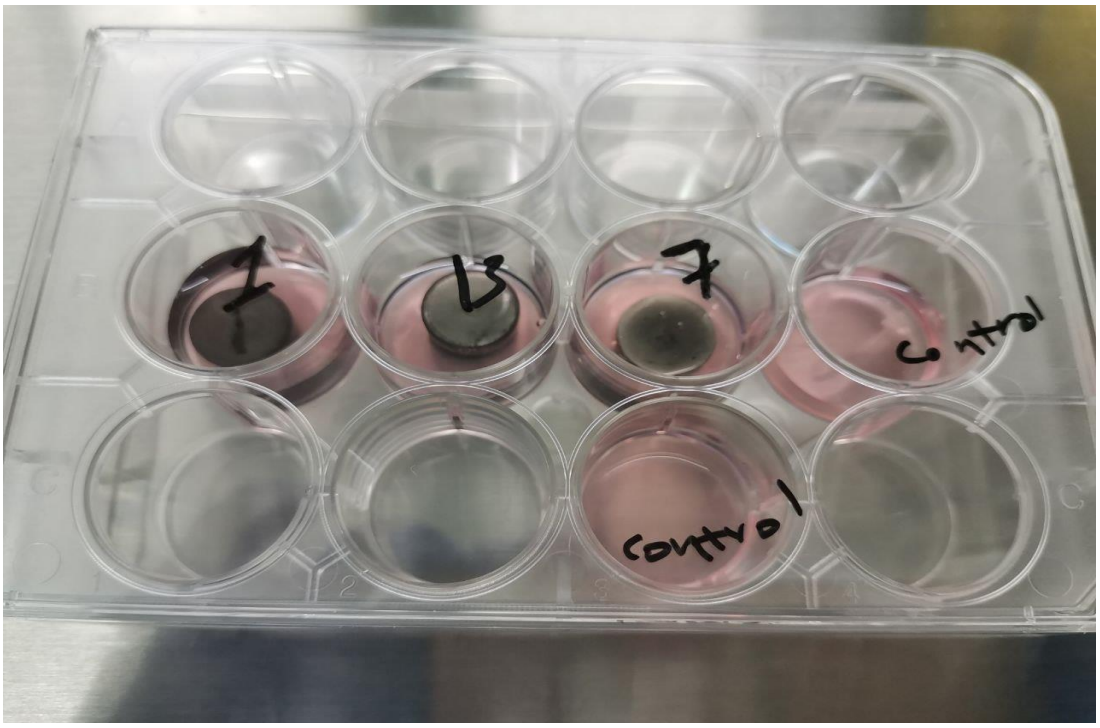

Figure (3.16): The samples were placed in a plate of 12 wells.

1. Normal cells of Madian Darpy Canine Kidney (MDCK) were seeded in 25ml flask, followed by an incubation at a temperature of 37°C, and 5% CO2 over 24 hr.

2.After 24hrs, the MDCK cell line (5x104 cells/ml) was implanted with samples in 12 micro-titer plate, in a final volume of 2ml of complete culture medium per well, as in Figure (3.16).

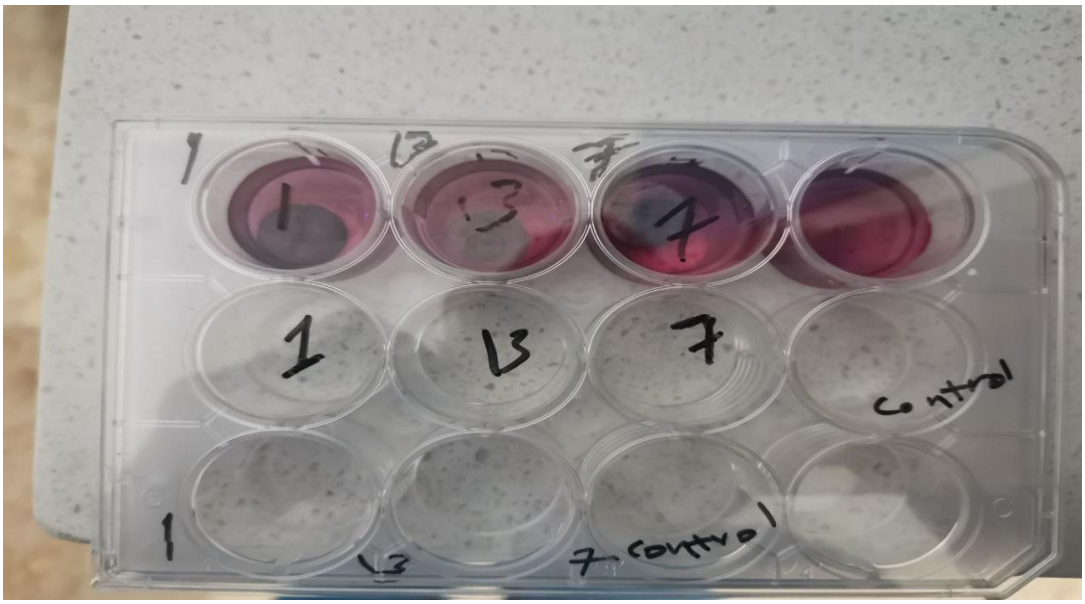

Figure (3.17): The plate after addition of cell line and before incubation.

The plate incubation took place at a temperature of 37°C, and 5% CO_2 for 24 hrs, as shown in figure (3.17).

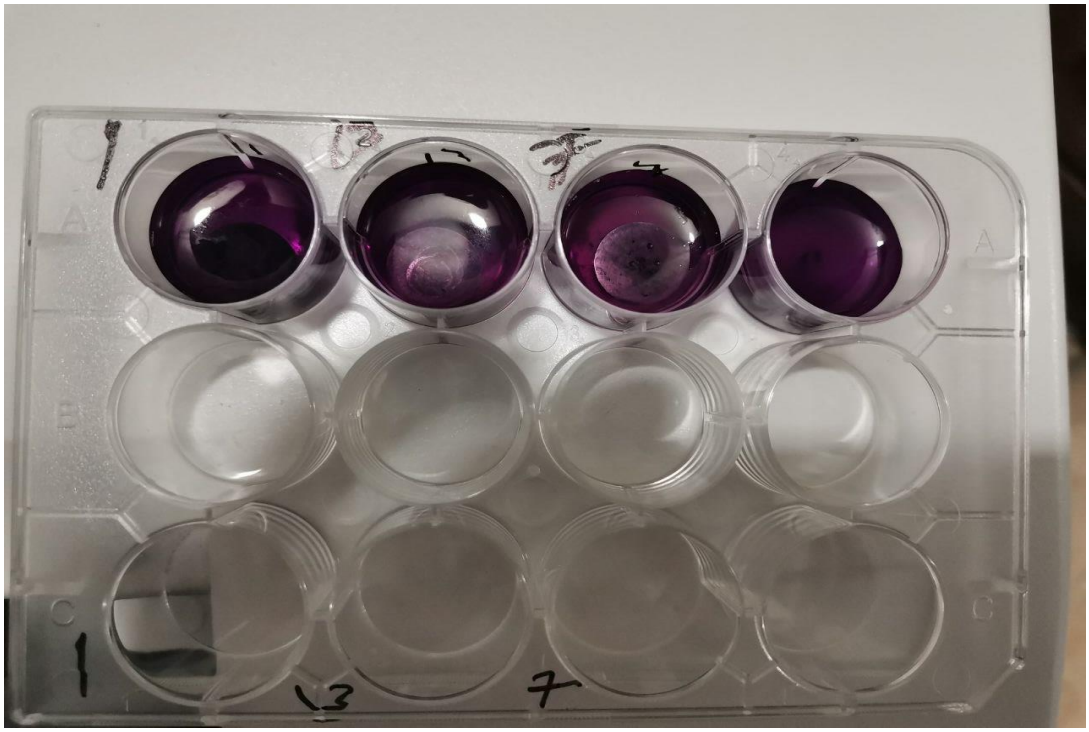

Figure (3.18): The plate after 24h of incubation.

After exposure, 200 µl of the MTT solution had been added to every well. Further incubation of the place occurred at 37°C, 5% CO2 over 4 hours as in figure (3.18).

3.The media were carefully removed and 5ml of soluble solution dimethyl sulfoxide (DMSO) was added per well for 30 min 0., as in figure (3.19).

4.The absorbance was determined using an Elisa reader at a wavelength of 570 nm at the Pharmacology College- University of Babylon as shown in Figure (3.20). The data of optical density (OD) was subjected to statistical analysis for calculating the cell viability for cell line, through the following equation:

$$\text{Cell viability (\%)} = \frac{\text{OD of test}}{\text{OD of control}} \times 100\% \quad \text{.....(3.6)}$$

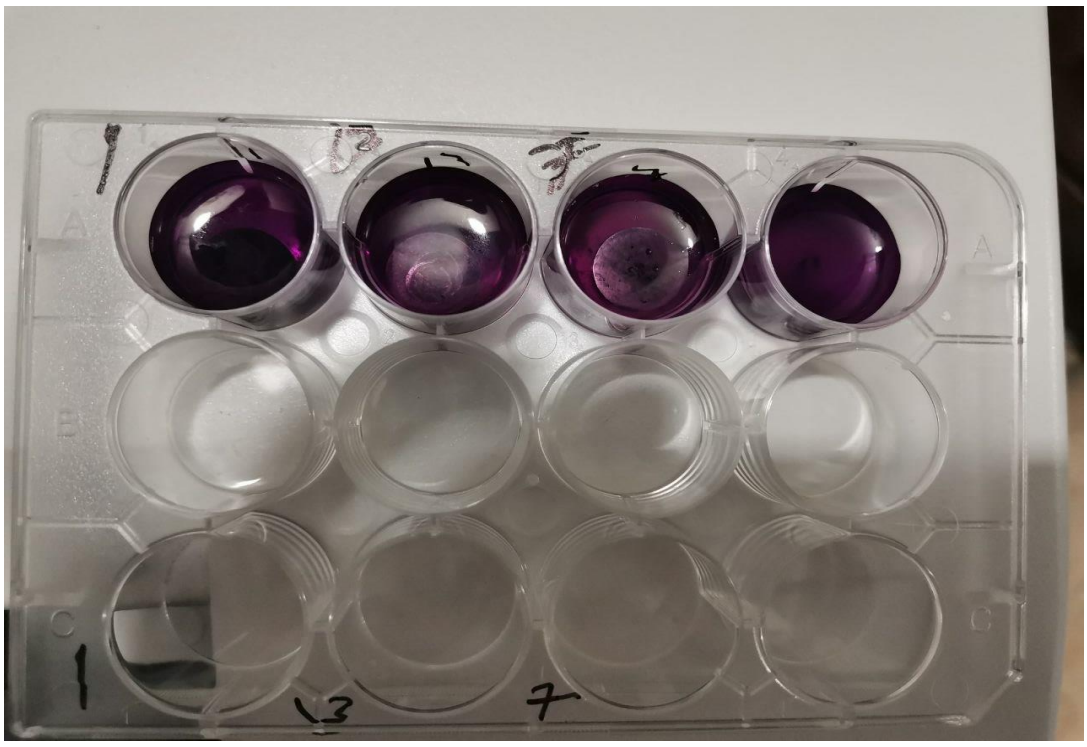

Figure (3.19): The plate after half hour DMSO

Figure (3.20): Elisa reader.

3.4.4.2 Antibacterial Test

When biomaterials especially metallic implants are used inside the human body, they are exposed to types of bacteria that cause infections in the adjacent living cells to the metallic implant. Therefore, it must be known if there are bacteria present or not on (Nb-1%Zr-xGe) substrate. Then 0.5 ml of the solution was taken and placed in another petri dish to be incubated for 24 h at 37 C° at College of Girls science / University of Babylon.

3.4.4.3 Simulated body fluid

Dipping Examination, the body's analogues solution A group of salts is prepared as in the table (3.5) and dissolved in distilled water in an amount of (1) liter and at room temperature and at (7.2-7.4) PH. For a period of three weeks. and before that, the XRD of the metal is examined, and after the immersion process for a period of three weeks, the XRD is examined.

Table (3.5): Chemical composition of simulated body fluid.

Items	Description	Quantity (gm/l)
1	**NaCl**	**8.036**
2	**KCl**	**0.225**
3	**$CaCl_2$**	**0.293**
4	**$NaHCO_3$**	**0.352**
5	**K_2HPO_4**	**0.230**
6	**$MgCl_2.6H_2O$**	**0.311**
7	**$NaSO_4$**	**0.072**

3.4.5 Physical Tests:

3.4.5.1 Contact Angle Test

Contact angle inspection device measure the angle of contact between the liquid (Distilled water) and solid (Nb-1%Zr-XGe) alloys substrate to know the wettability of the electrolyte to the surface of the base sample as shown in figure (3.21). This test done at college of Material engineering /University of Babylon.

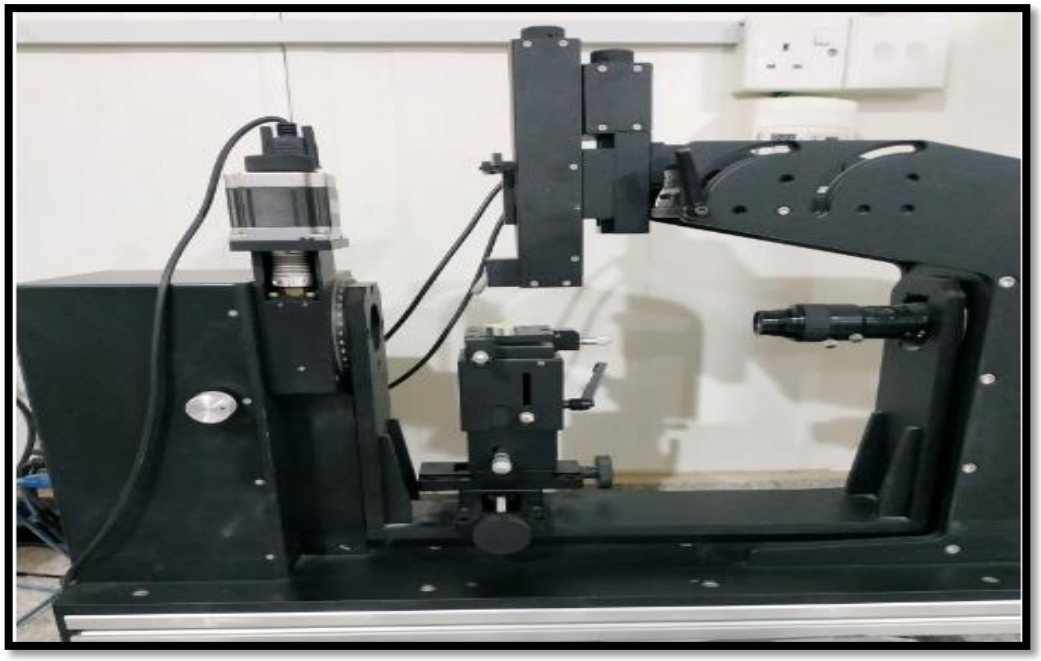

Figure (3.21): Contact Angle Inspection Device.

Chapter Four

Results and Discussion

4 .1 Introduction

This chapter is presenten and discussed the experimental results which include the properties related to the samples that were prepared by powder metallurgy technique. The porosity of the sintering samples, microstructure examination that done by light optical microscope and SEM, phase's analysis that done by XRD technique, mechanical tests (hardness, elastic modulus, compression, and wear), electrochemical tests (open circuit, polarization, and ion release), contact angle, biological tests (antibacterial, MTT test, and simulated body fluid) .

4.2 Particle Size Analysis

The particle size of (Nb,Zr, & Ge) powders have been analyzed. The results are shown in figure (4.1).

The average particle size for powder materials are shown in table (4.1).

Table (4.1): Average Particle Size for Materials.

Material (powder)	Average particle size(μm)
Nb	10
Zr	12.20
Ge	0.818

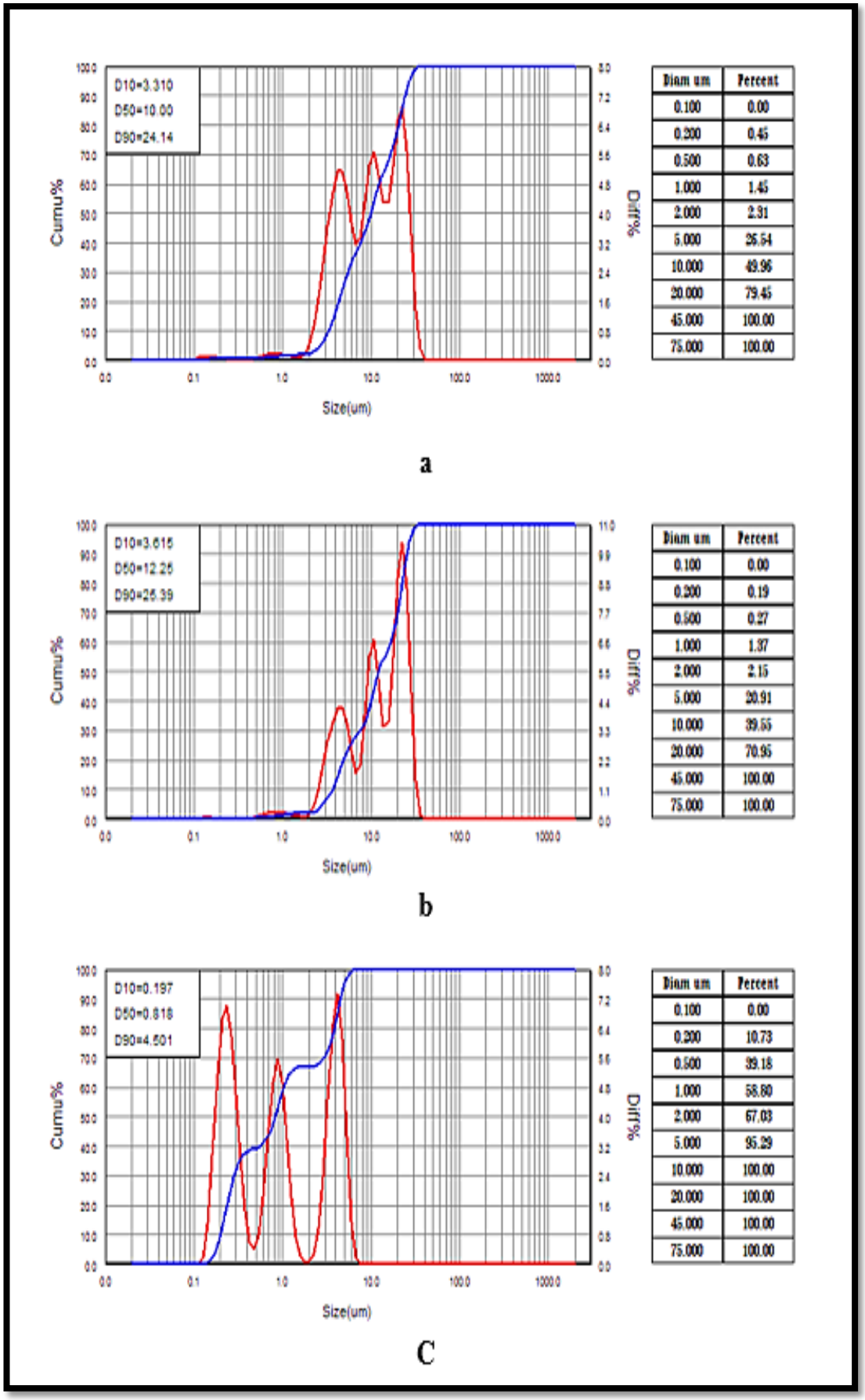

Diam um	Percent
0.100	0.00
0.200	0.45
0.500	0.63
1.000	1.45
2.000	2.31
5.000	26.64
10.000	49.96
20.000	79.45
45.000	100.00
75.000	100.00

Diam um	Percent
0.100	0.00
0.200	0.19
0.500	0.27
1.000	1.37
2.000	2.15
5.000	20.91
10.000	39.55
20.000	70.95
45.000	100.00
75.000	100.00

Diam um	Percent
0.100	0.00
0.200	10.73
0.500	39.18
1.000	58.80
2.000	67.03
5.000	95.29
10.000	100.00
20.000	100.00
45.000	100.00
75.000	100.00

Figure (4.1): Particles Size Analysis (a)Nb, (b)Zr, and (c)Ge.

4.3 Microstructure Charecterization.

4.3.1 X-Ray Diffraction (XRD)

X-Ray diffraction test was done for pure powders as shown in figures (4.2),(4.3), & (4.4).

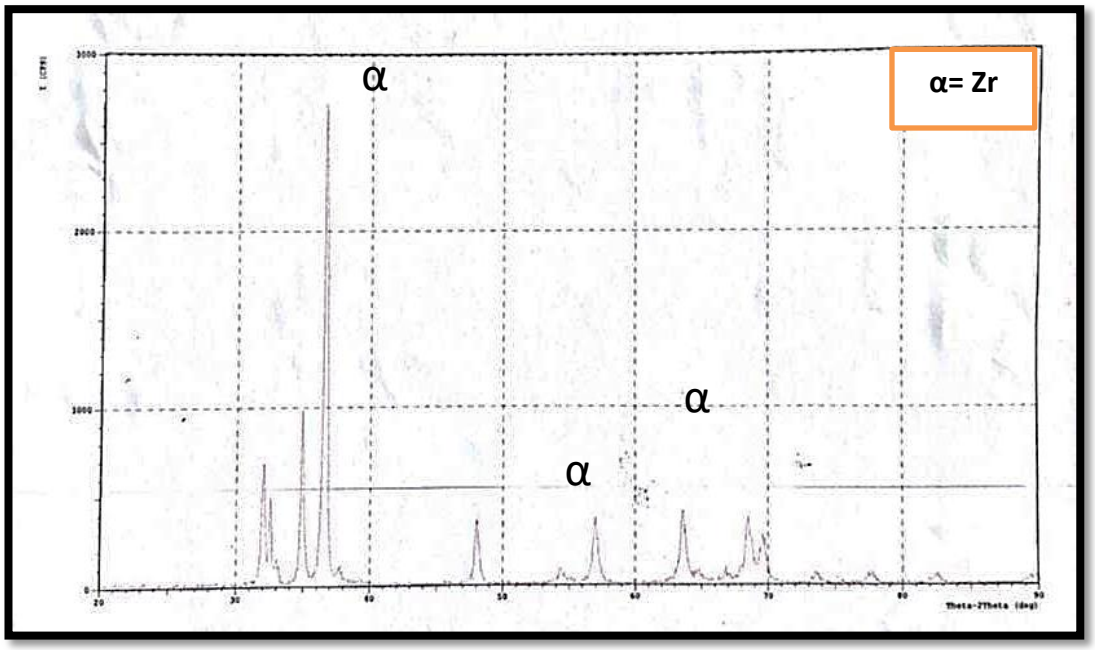

Figure (4.2): XRD Patterns for Zr Powder.

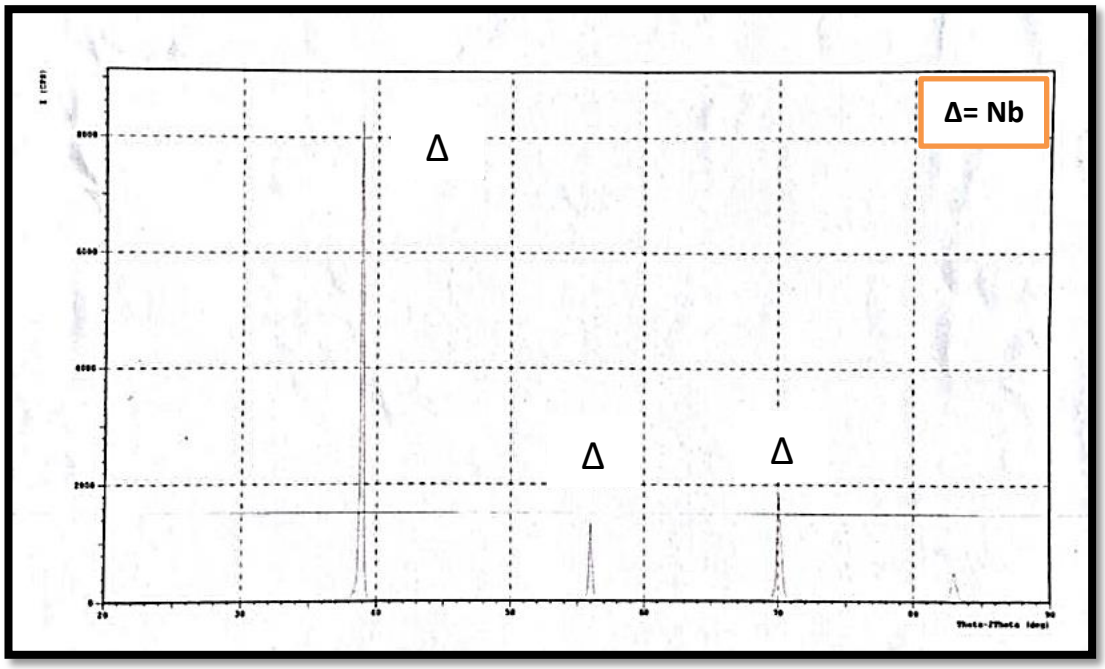

Figure (4.3): XRD Patterns for Nb Powder.

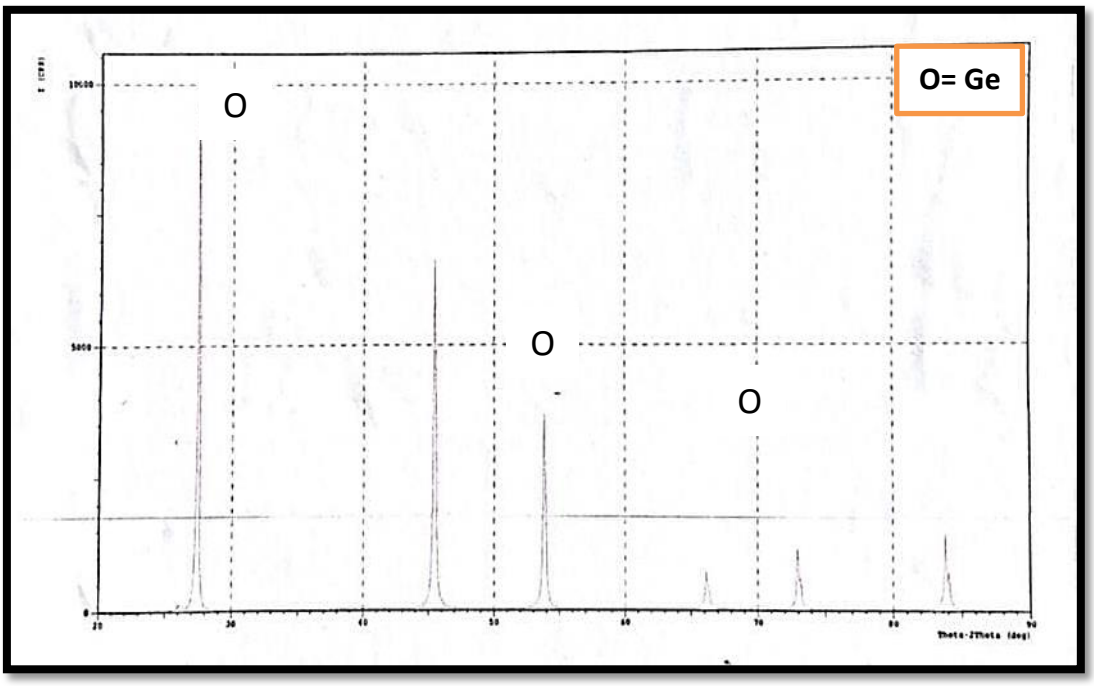

Figure (4.4): XRD Patterns for Ge Powder.

The XRD patterns for green compact (Nb-1%Zr-xGe) alloy show no phases other than Nb, Zr and Ge because no phase transformation takes place during the compacting process.

Phase transformation is diffusion process and needs a high temperature to occur. Figures (4.5), (4.6), and (4.7) show the XRD patterns for (Nb-1%Zr-xGe) alloy after sintering at 1200 °C for 5hr under argon. It can be observed that all Nb, Zr and Ge transformed to solid solution of (Nb).

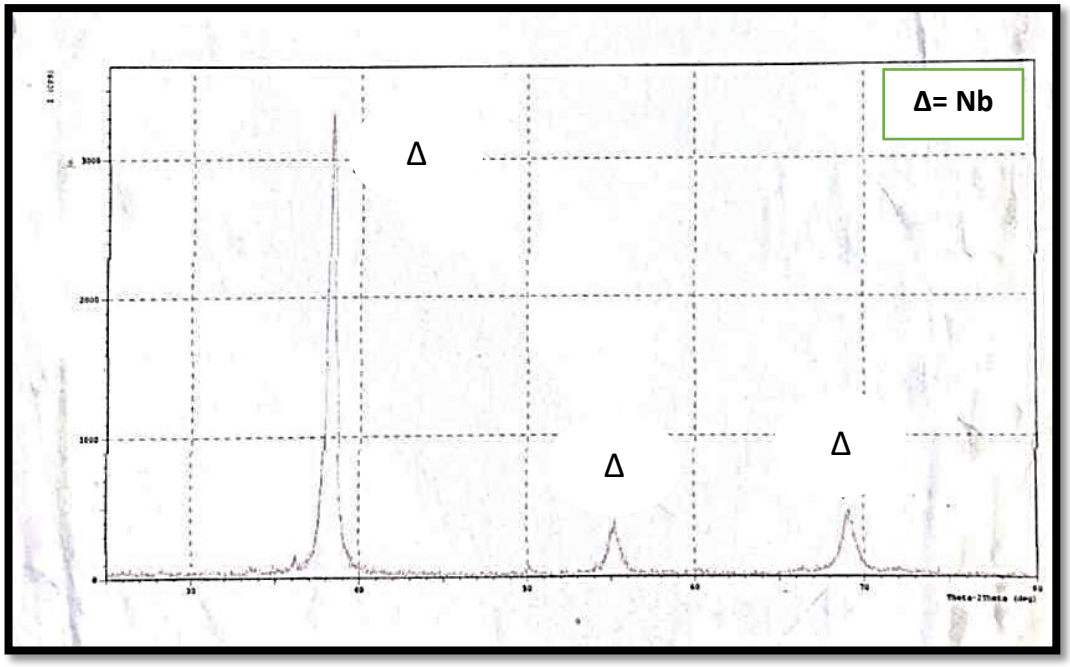

Figure (4.5): XRD Patterns for Base Alloy (Nb-1%Zr) After Sintering Process.

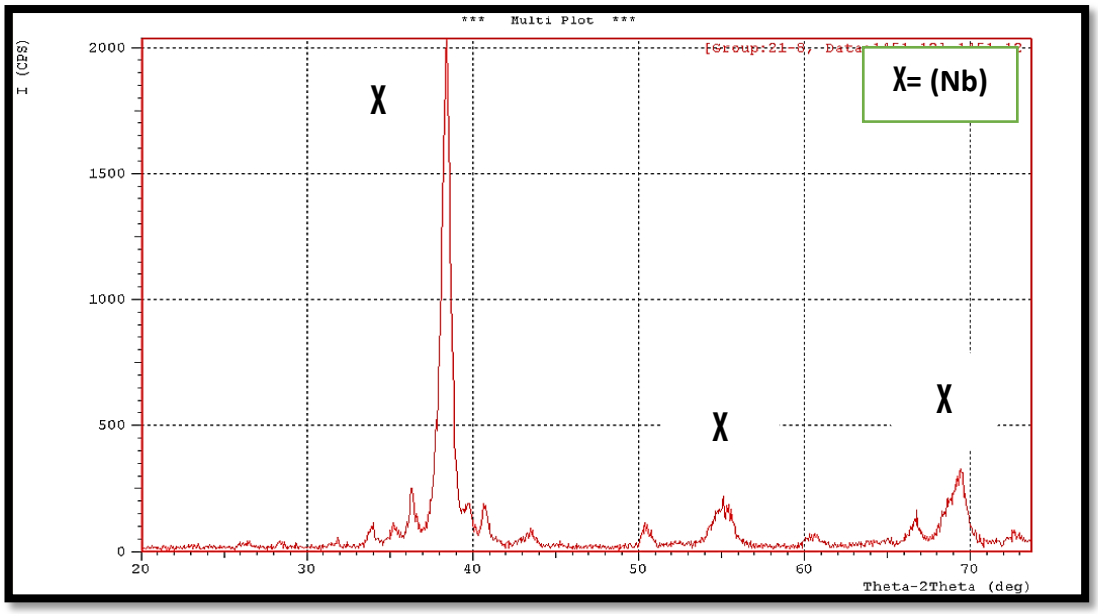

Figure (4.6): XRD Patterns for Alloy (Nb-1%Zr-5.5%Ge) After Sintering Process.

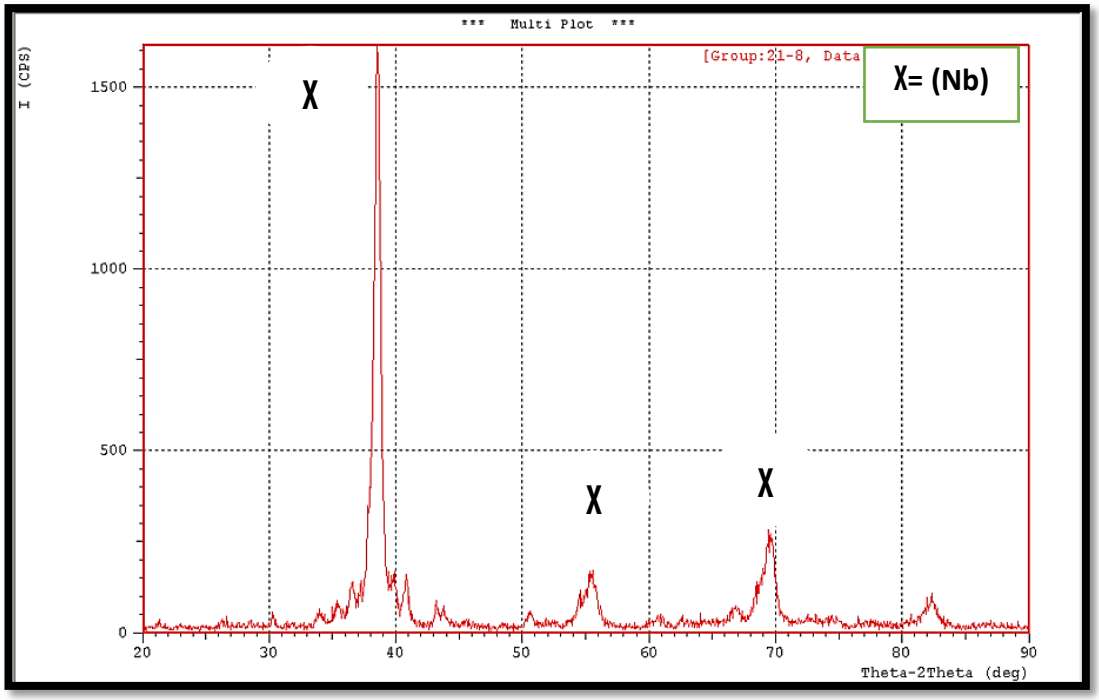

Figure (4.7): XRD Patterns for Alloy (Nb-1%Zr-6%Ge) After Sintering Process.

4.3.2 Light Optical Microscope (LOM)

To reveal the microstructure of prepared specimens, LOM techniques have been used.

Figures [(4.8)-(4.20)] show the microstructure of etched alloys after sintering process with and without additions at 400X magnification. It is clearly shown that, the utilization of the powder metallurgy technique of alloys leads to get a homogeneous distribution of the strengthening phase in the matrix which may enhance wear and mechanical properties of the alloys.The microstructure illustrates the formation of substitution solid solution (Nb) from germanium and niobium atoms, leading to an increase in hardness of the alloy, as well as leads to an improvement in the mechanical properties of the alloy with increasing the percentage of germanium.

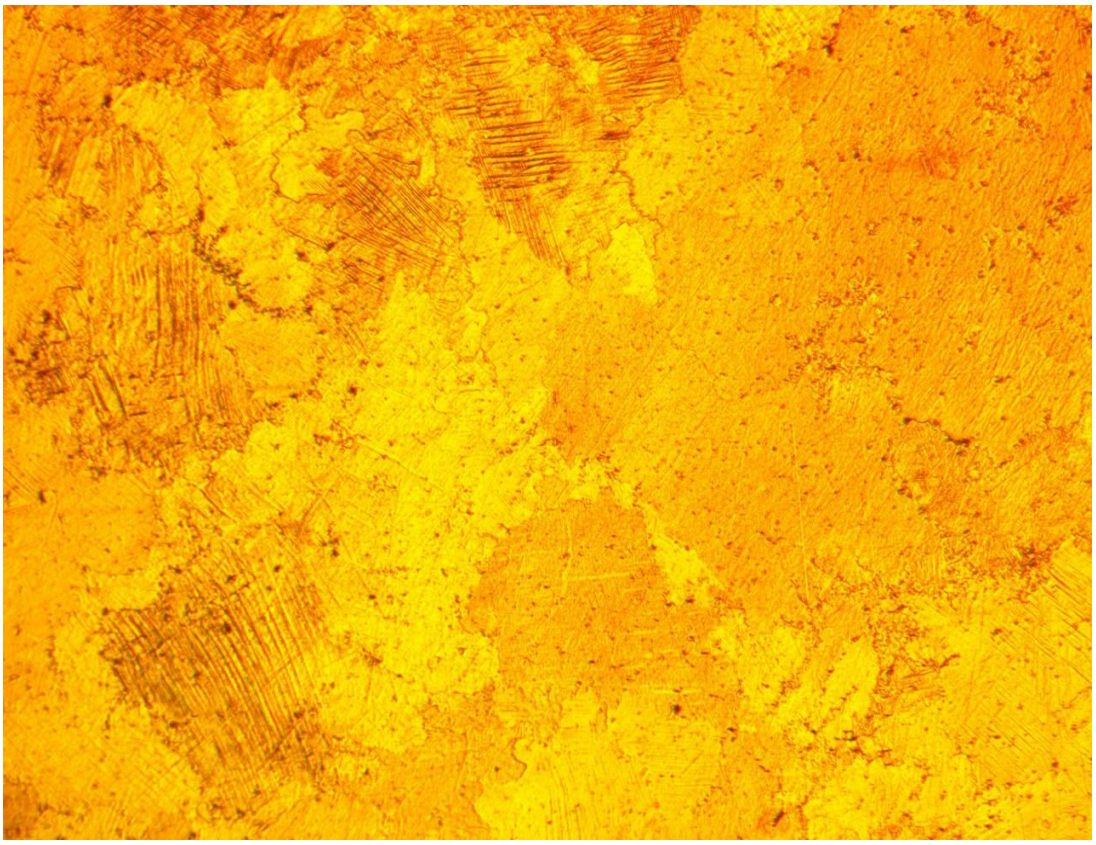

Figure (4.8): Microstructure of etched base alloys after sintering process at 400X magnification.

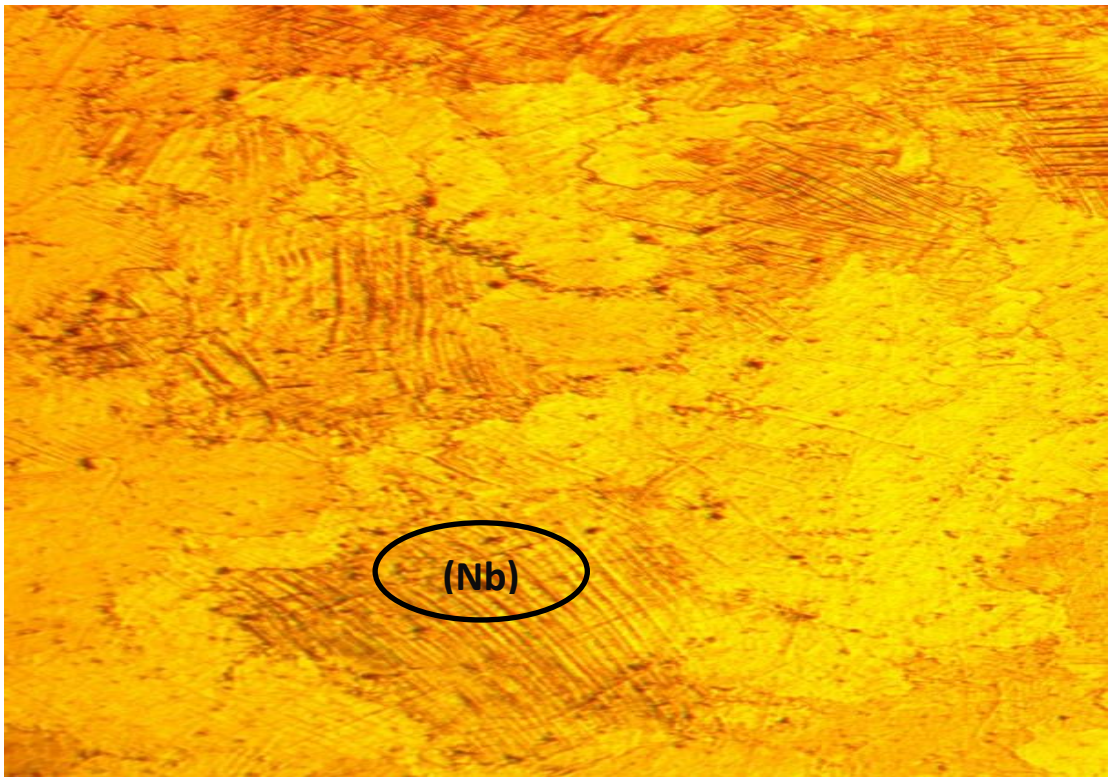

Figure (4.9): Microstructure of etched alloys after sintering process with 0.5wt.% Ge at 400X magnification.

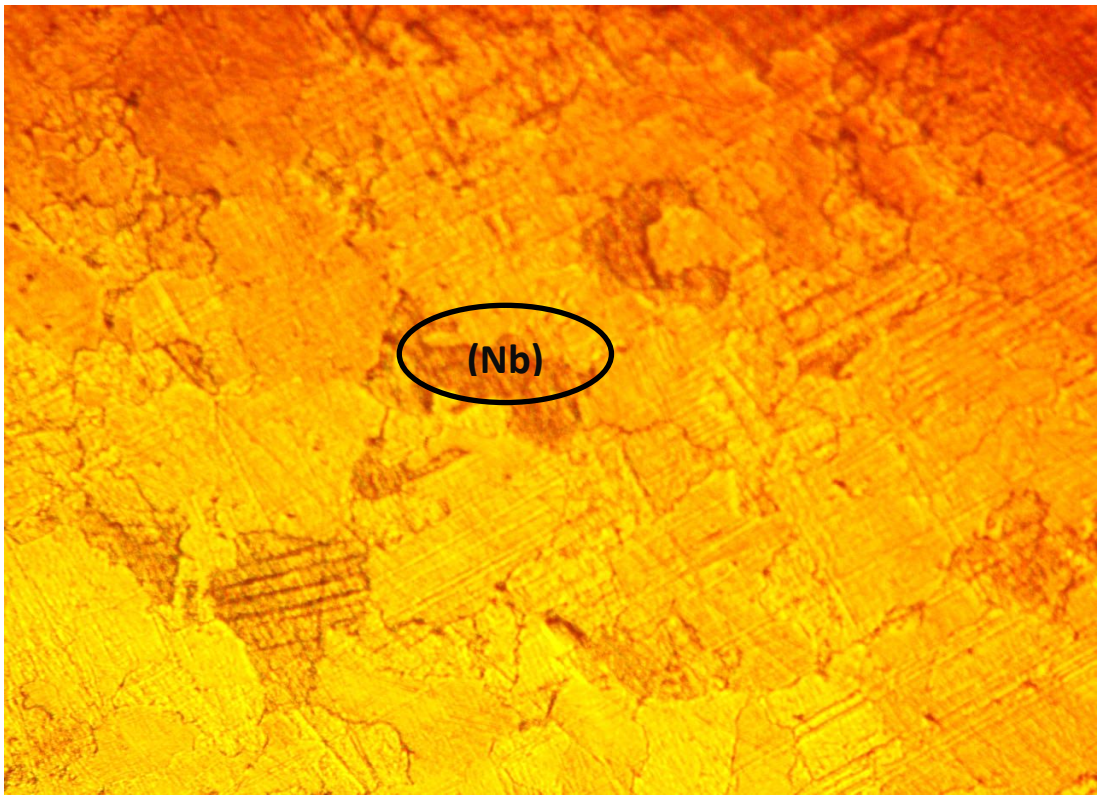

Figure (4.10): Microstructure of etched alloys after sintering process with 1wt.% Ge at 400X magnification.

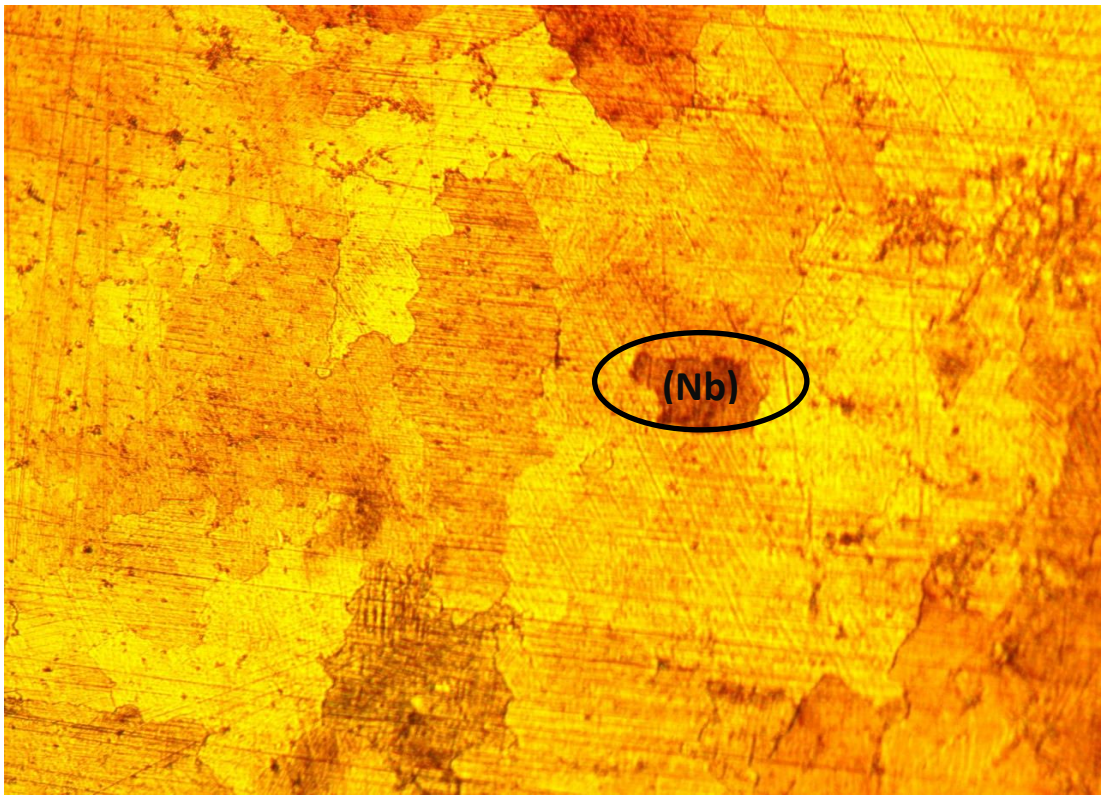

Figure (4.11): Microstructure of etched alloys after sintering process with 1.5wt.% Ge at 400X magnification.

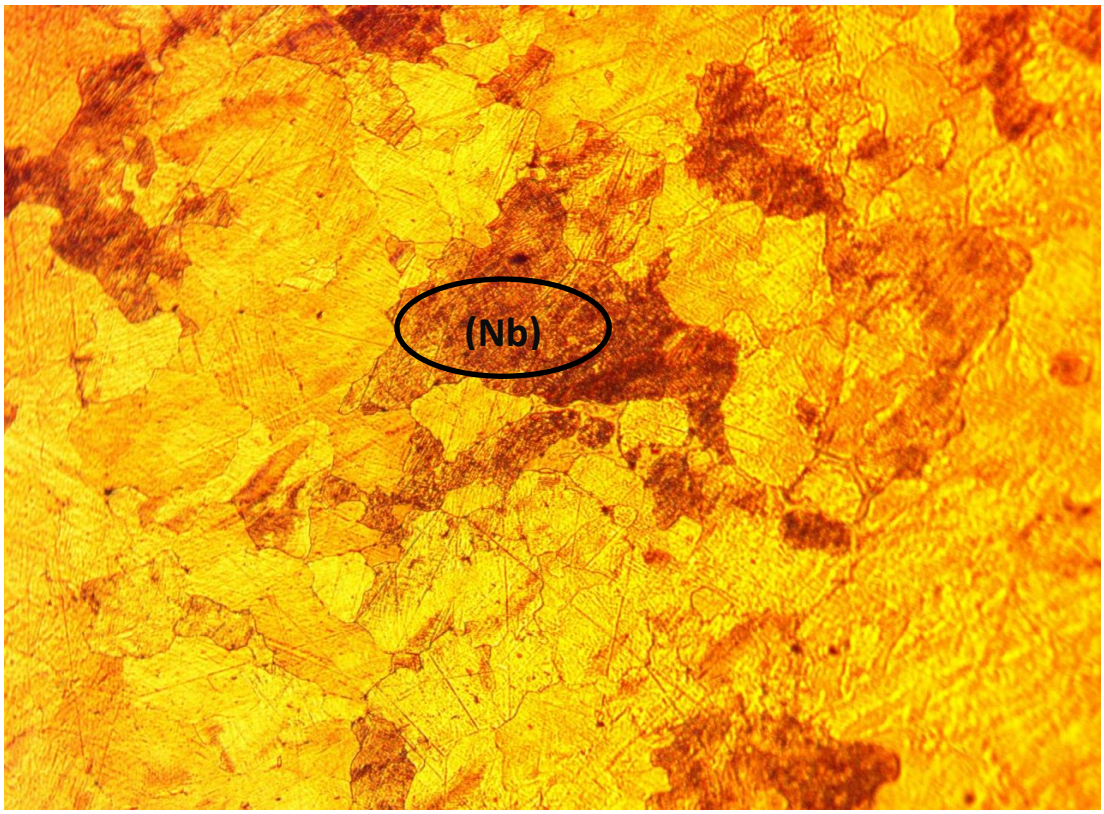

Figure (4.12): Microstructure of etched alloys after sintering process with 2wt.% Ge at 400X magnification.

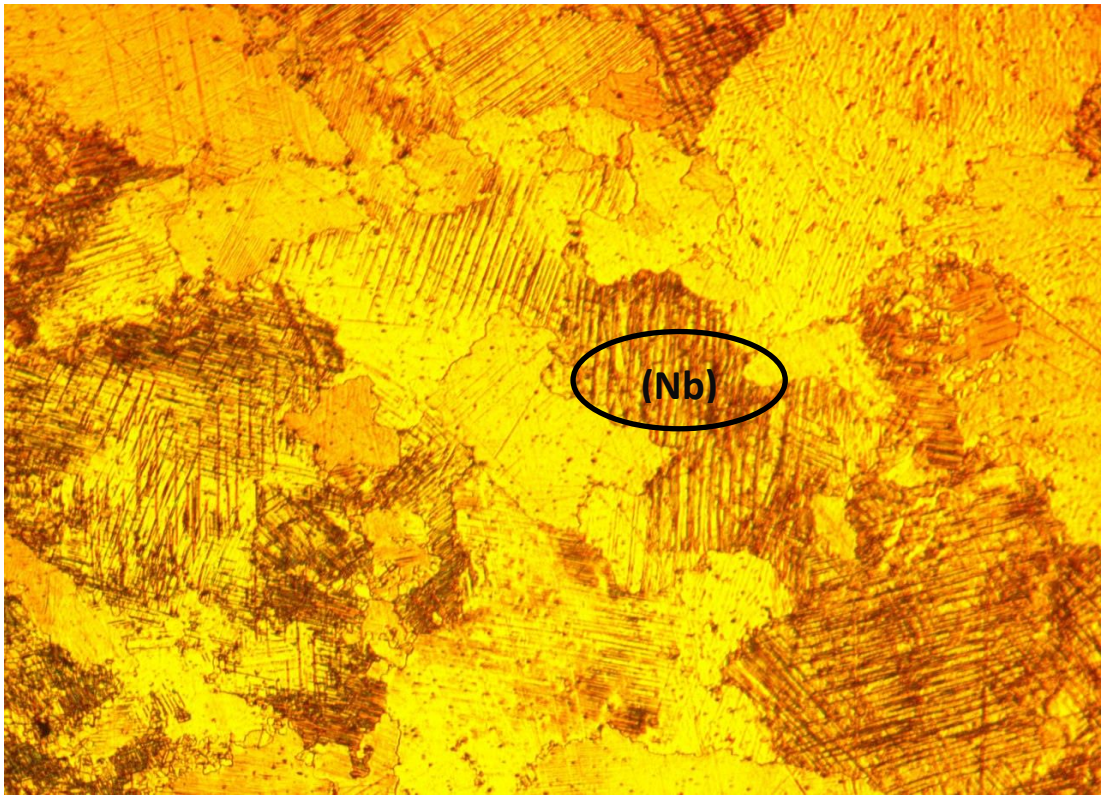

Figure (4.13): Microstructure of etched alloys after sintering process with 2.5wt.% Ge at 400X magnification.

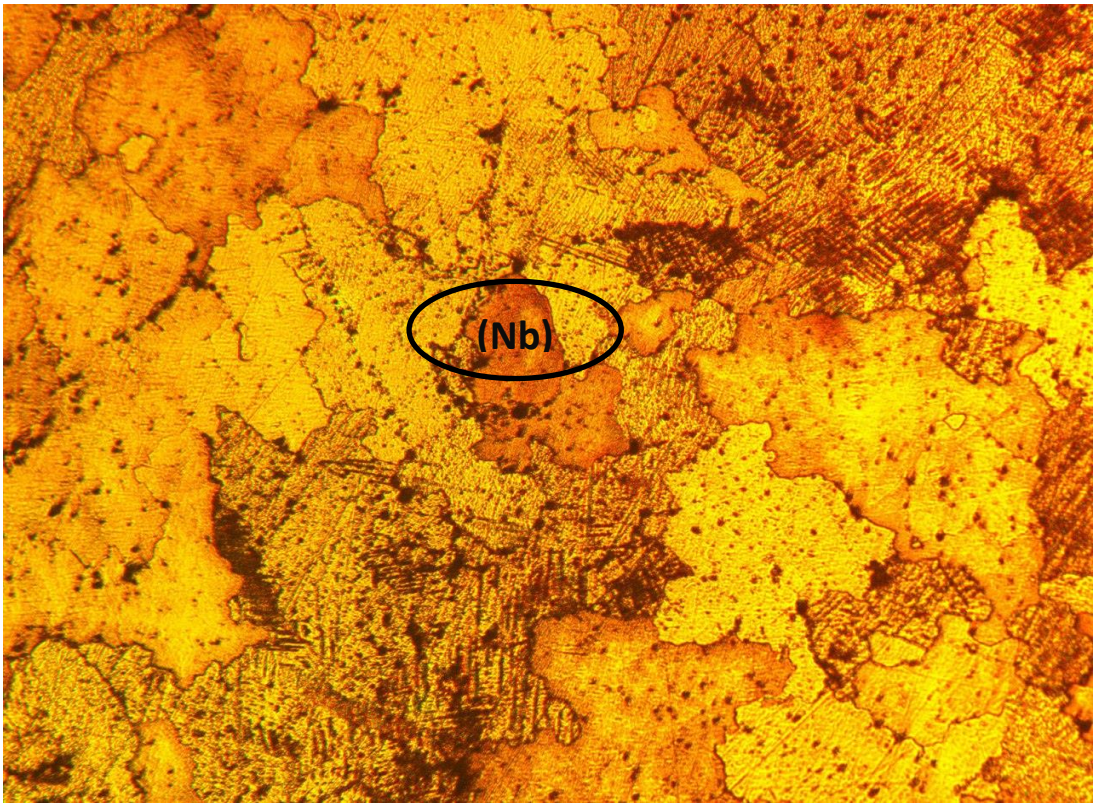

Figure (4.14): Microstructure of etched alloys after sintering process with 3wt.% Ge at 400X magnification.

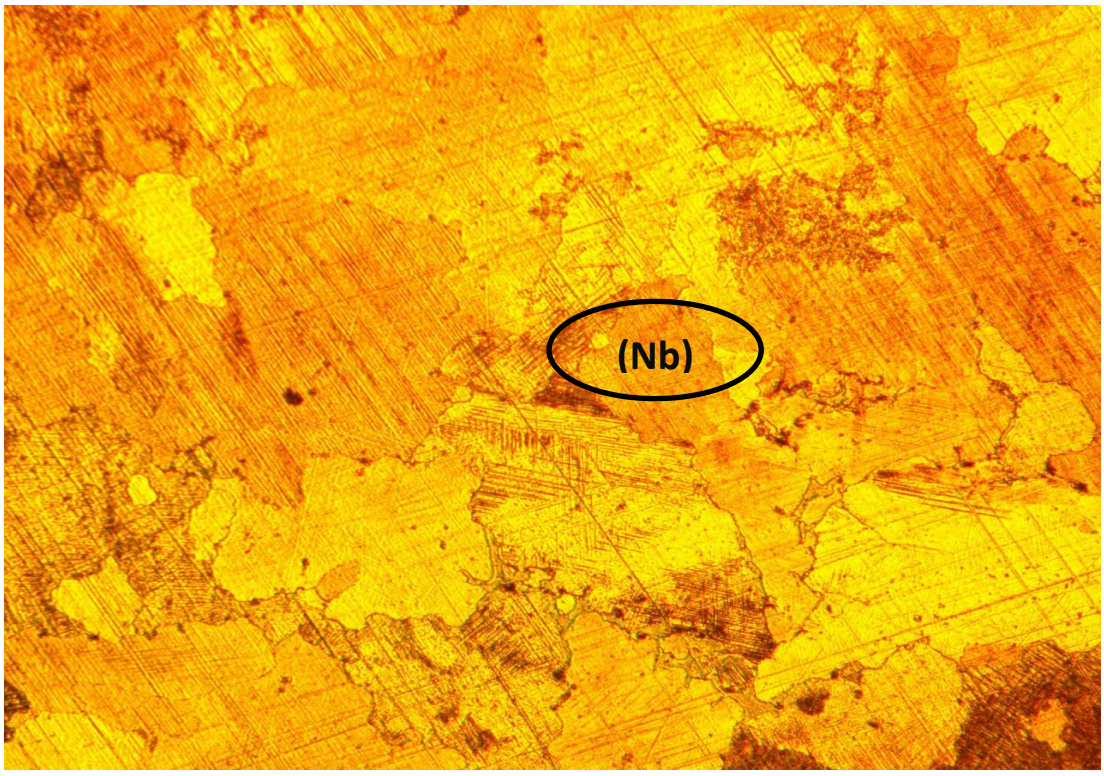

Figure (4.15): Microstructure of etched alloys after sintering process with 3.5wt.% Ge at 400X magnification.

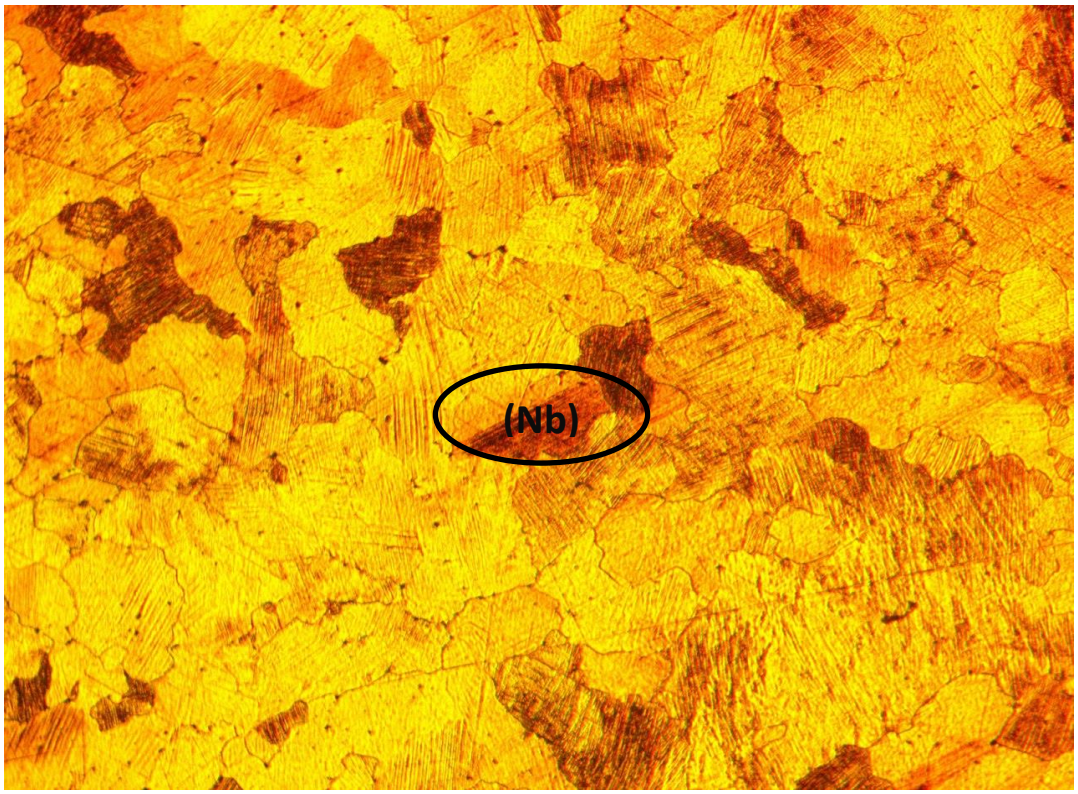

Figure (4.16): Microstructure of etched alloys after sintering process with 4wt.% Ge at 400X magnification.

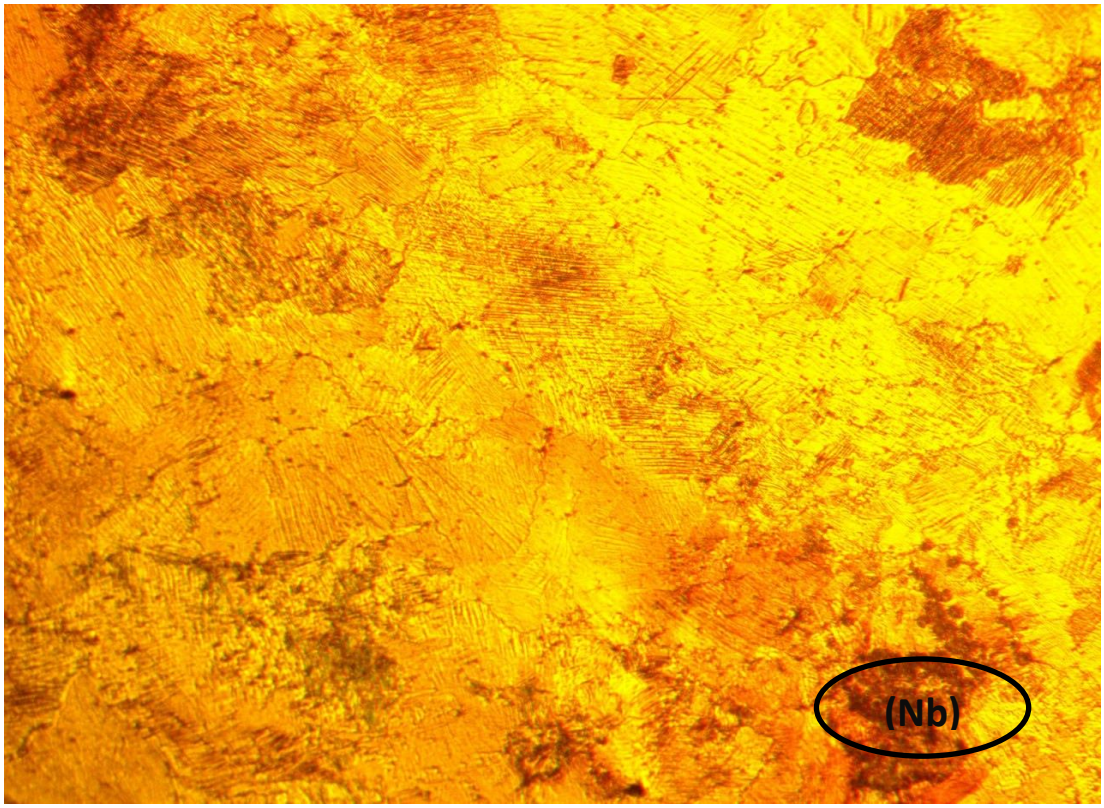

Figure (4.17): Microstructure of etched alloys after sintering process with 4.5wt.% Ge at 400X magnification.

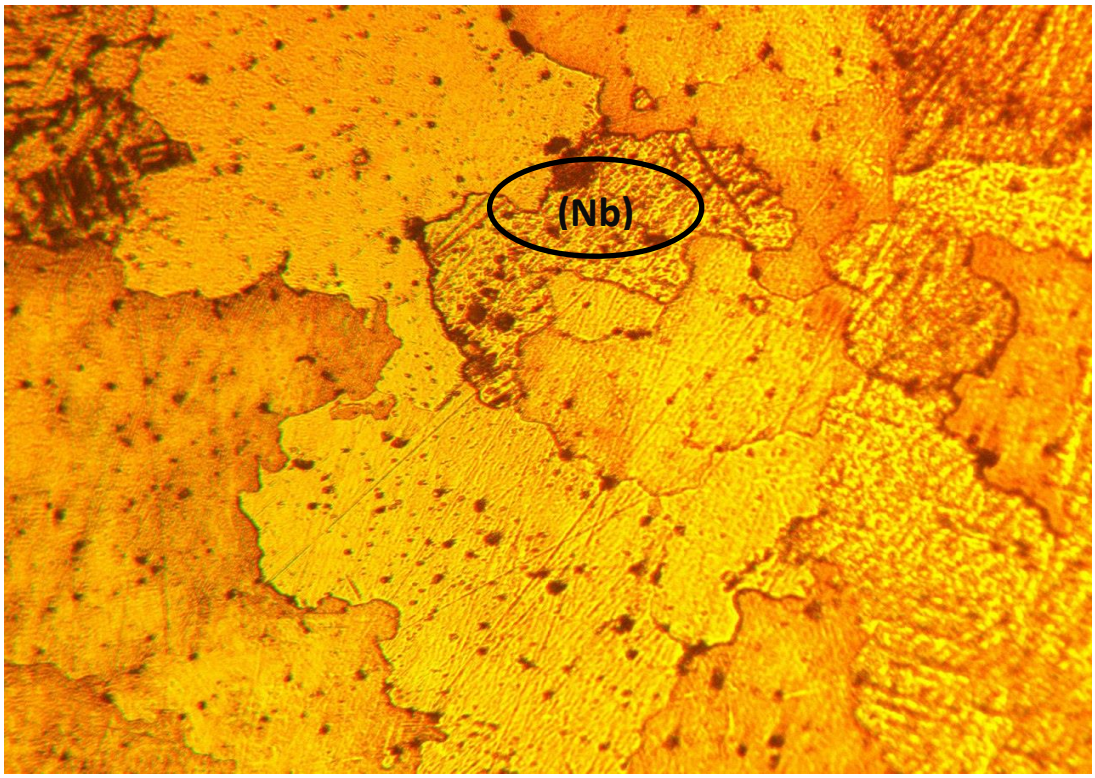

Figure (4.18): Microstructure of etched alloys after sintering process with 5wt.% Ge at 400X magnification.

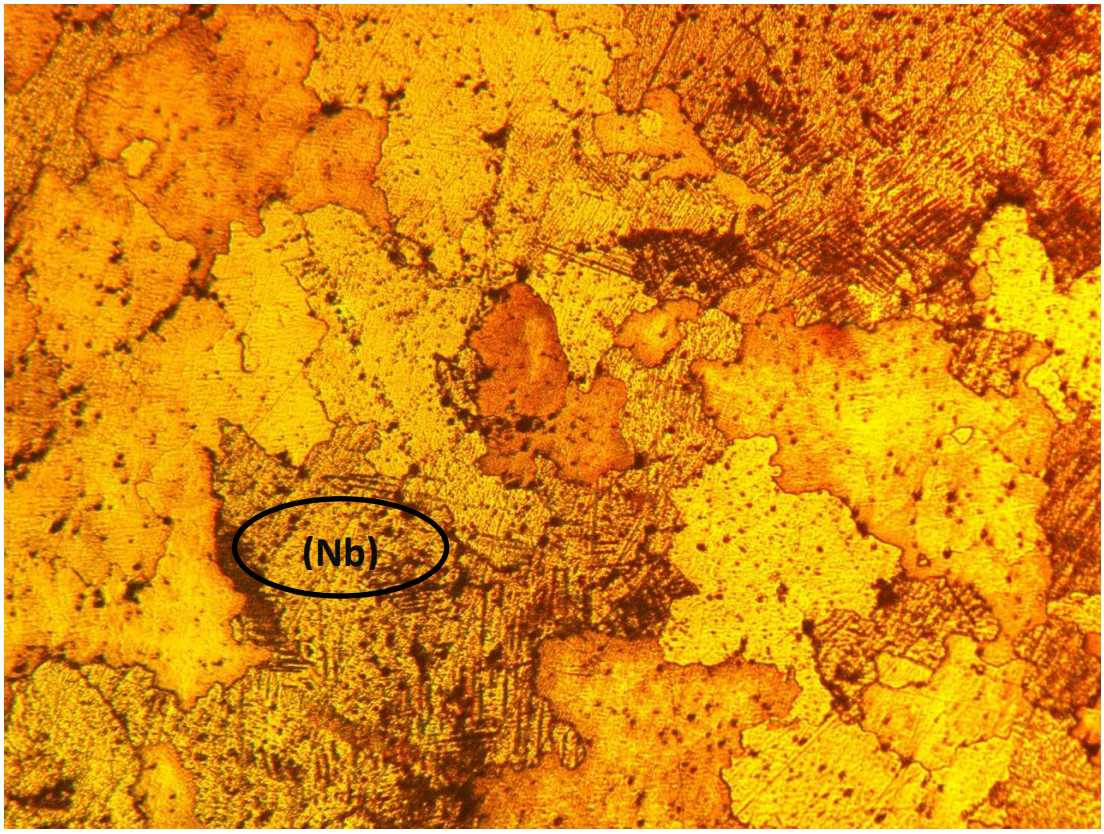

Figure (4.19): Microstructure of etched alloys after sintering process with 5.5wt.% Ge at 400X magnification.

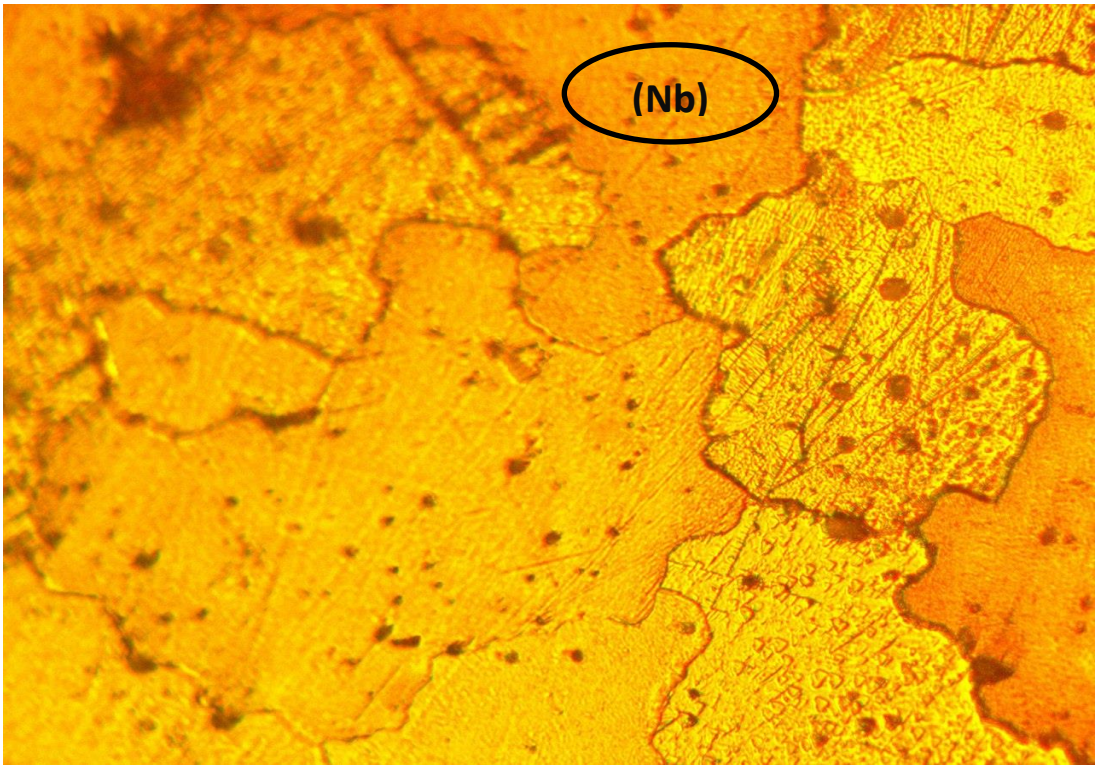

Figure (4.20): Microstructure of etched alloys after sintering process with 6wt.% Ge at 400X magnification.

4.4 Effect of Compacting Pressure on Green Density

Figure (4.21) shows that when the compacting pressure increases, the green density increases too until it reaches a certain limit at which any further increase in the pressure has no or little effect on its value. So the preferred pressure was determined as 650 MPa for all the samples prepared in the present study.

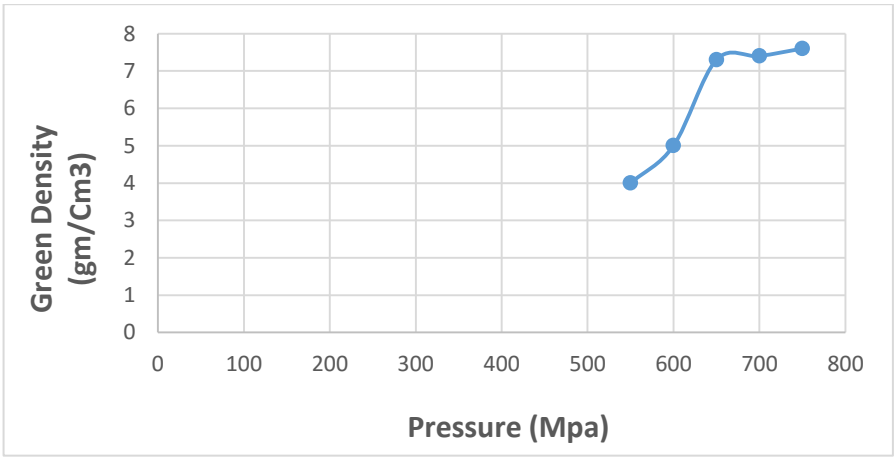

Figure (4.21): Green Density Vs Pressure.

4.5 Physical Properties Tests:

4.5.1 Porosity of Sintered Alloys

The porosity of all sintered alloys was measured after sintering process at 1200 ºC for 5 hours, and the effect of Ge on the porosity has been shown in figure (4.22). There is a decreasing in the porosity values after sintering process. The porosity decreasing with increasing Ge content due to solid solution formation of Germanium in Neobium and in addition to the thermal expansion coefficient of Germanium is lower than that of Neobium. So, the thermal shrinkage will not be found when cooling, and the increasing Germanium addition led to decreasing porosity percent in Neobium alloy.

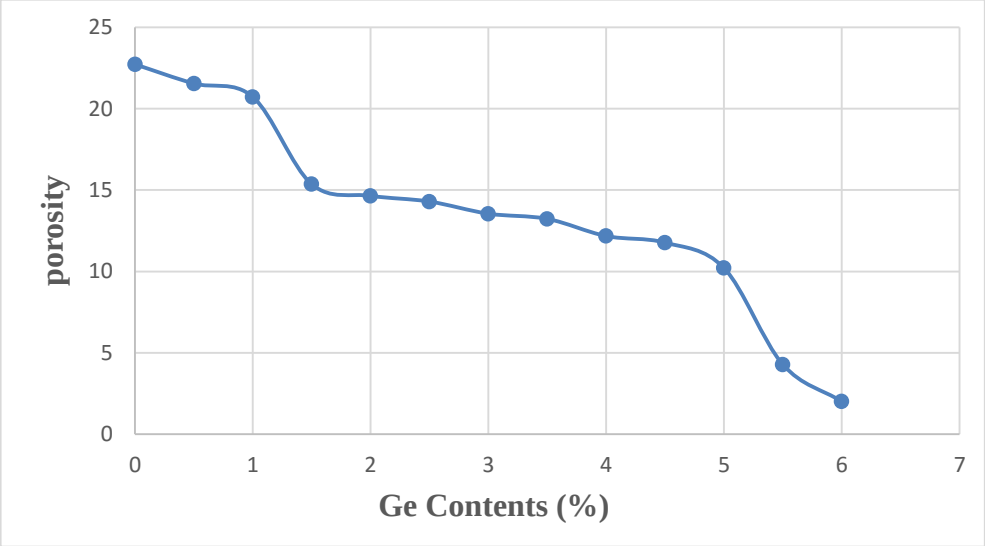

Figure (4.22): Effect of Ge Content on the Porosity for (Nb-1%Zr) Alloys.

4.5.2 Density of Sintered Alloys

The density of all sintered alloys was measured after sintering process at 1200 ºC for 5 hours, and the effect of Ge on the density has been shown in figure (4.23). There is an increasing in the density values after sintering process. The density of Nb alloys increase with increasing Germanium content as aresult of reduction in porosity percent.

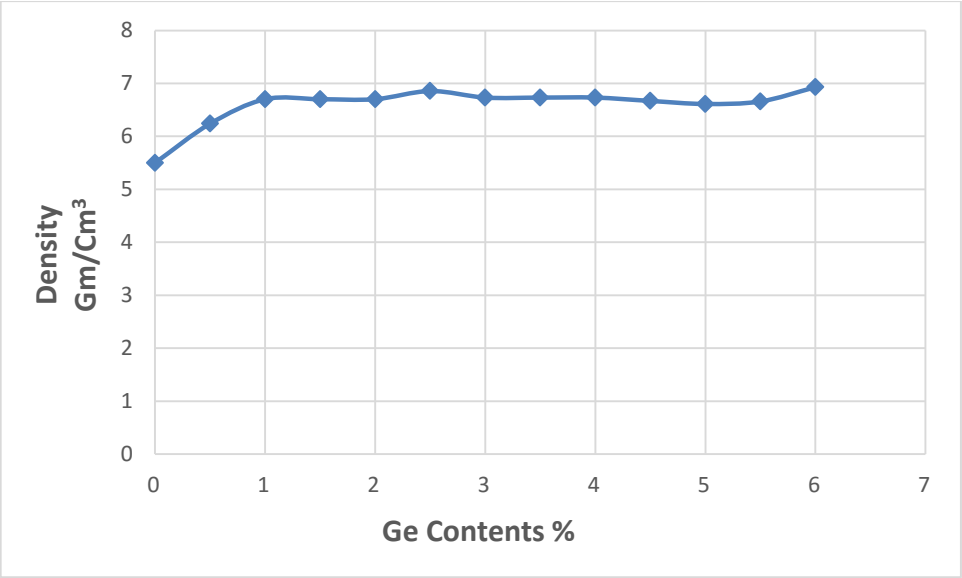

Figure (4.23): Effect of Ge Content on the density for (Nb-1%Zr) Alloys.

4.5.3 Contact Angle Test

When the percentage of germanium increases, the contact angle decreases, and this means that the wettability increases, which leads to an increase in the bonding between body tissues and the implanted alloy and reduction of time required for healling.

From table (4.2) which is shown the variation of contact angles improvement with germanium contents, we notic that there where an increament in improvement percentagre with increasing germanium content, because of Germanium addition led to increase surface tension of surface alloy according to the following equation:

Table (4.2): Values of contact angles according to Ge contents.

Sample	Value of Contact Angle	Improvement (%)	Contact Angle
Base	**45.794**	**/**	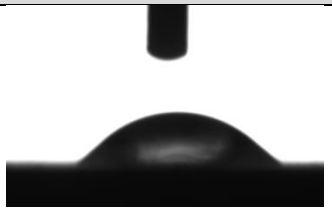
o.5% Ge	**45.657**	**0.30**	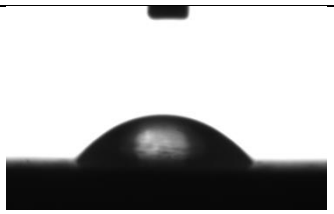
1% Ge	**42.239**	**7.76**	
1.5% Ge	**41.624**	**9.11**	
2% Ge	**39.528**	**13.68**	
2.5% Ge	**38.701**	**15.49**	
3% Ge	**35.43**	**22.63**	
3.5% Ge	**35.057**	**23.45**	
4% Ge	**34.007**	**25.74**	
4.5% Ge	**30.583**	**33.22**	
5% Ge	**29.509**	**35.56**	
5.5% Ge	**23.477**	**48.73**	
6% Ge	**18.168**	**60.33**	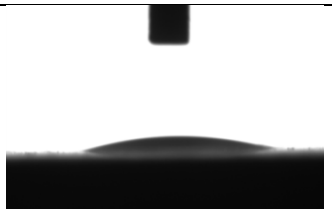

4.6 Mechanical Tests

4.6.1 Hardness

The hardness of Neobium alloy and Nb-1%Zr-xGe specimens was measured by using Brinlle hardness test. Figure (4.24) shows the effect of Germanium addition on the hardness, it can be seen that the hardness of base alloy (Nb-1%Zr) (212 Kg/mm^2) rised with Germanium addition, when Germanium content increased the hardness increased too, it can be attributable to solid solution strengthening, the maximum improvement percentage was for 6% Germanium (285 Kg/mm^2, 34.43%), as shown in table (4.3).

Table (4.3): Improvement percentage in hardness according to Ge contents.

Ge%	HB	Improvement (%)
0	212	/
0.5	223	5.19
1	230	8.49
1.5	245	15.57
2	265	25.00
2.5	268	26.42
3	270	27.36
3.5	274	29.25
4	278	31.13
4.5	280	32.08
5	281	32.55
5.5	283	33.49
6	285	34.43

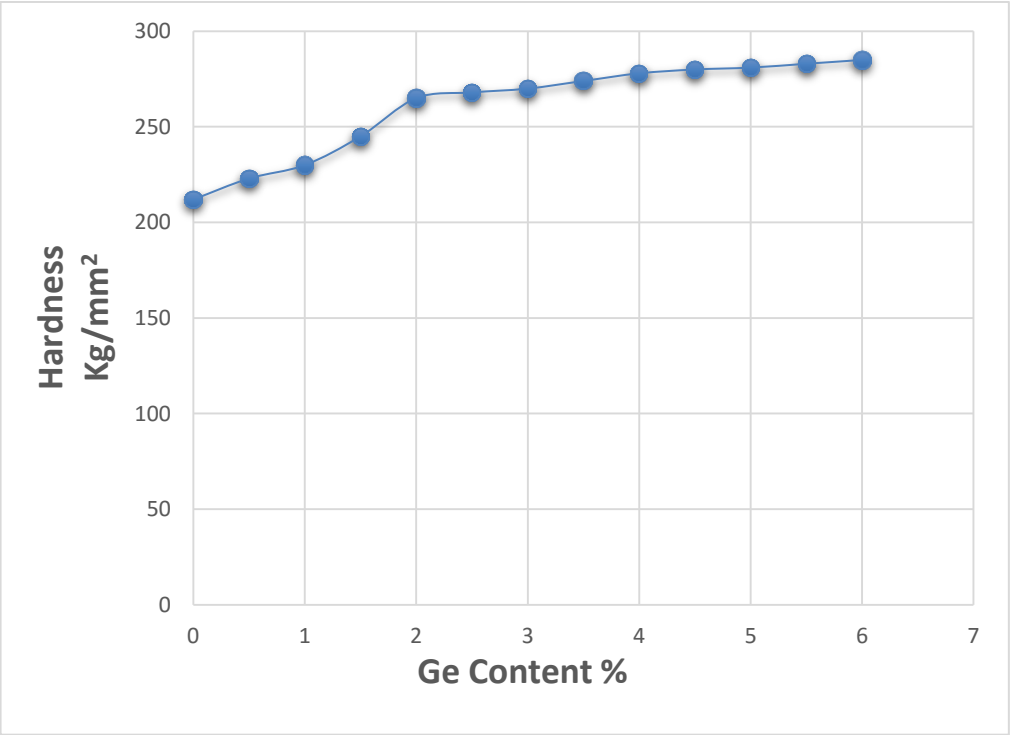

Figure (4.24): Effect of Ge on Hardness.

4.6.2 Compressive Strength:

The compression strength results obtained from stress-strain diagram for Neobium base alloy and for that with Germanium addition are shown in figure (4.25).

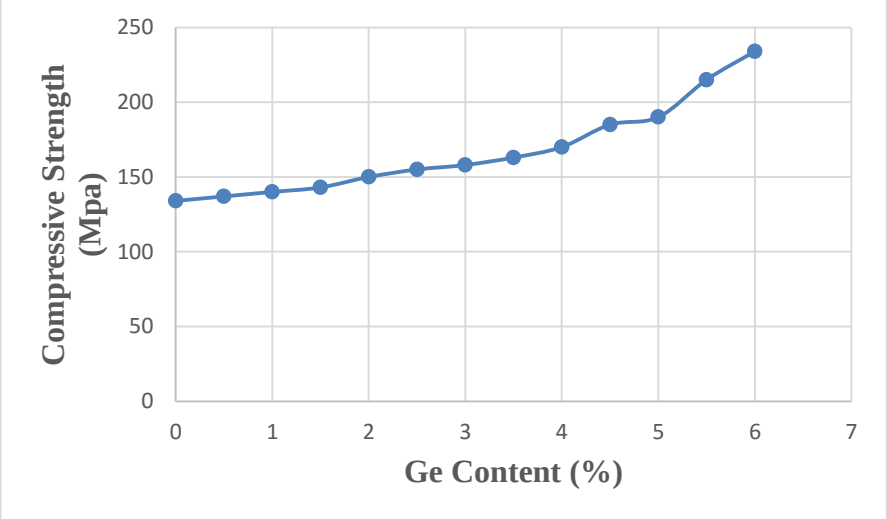

Figure (4.25): Effect of Ge on Compressive strength.

The compressive strength of the base alloy (134Mpa) increased with increasing Germanium contain until reaches (234Mpa) at 6% Germanium achieving improvement percentage of (79.1%), which is attributable to the Germanium addition led to solid solution strengthening and with Germanium content increasing porosity percent decreases, where the porosity is positively related to the materials resistance to compressive. Table (4.4) shows the compressive strength, porosity percentage and improvement percentage for alloys used.

Table (4.4): Compressive strength, porosity, and improvement Vs Germanium contents.

Ge%	Porosity %	Compressive Strength (Mpa)	Improvement in Compressive Strength %
0	25.96	134	/
0.5	22.17	137	2.24
1	20.85	140	4.48
1.5	18.78	143	6.72
2	16.4	150	11.94
2.5	15.2	155	15.67
3	13.45	158	17.91
3.5	13.23	163	21.64
4	11.77	170	26.87
4.5	10.23	185	38.06
5	8.32	190	41.79
5.5	5.5	215	60.45
6	4.28	234	79.10

4.6.3 Elastic Modules

The elastic properties can be determined, and the results are shown in Table (4.4).

Table (4.5): Elastic modulus of the prepared alloys.

Ge%	Elastic Modulus (GPa)	Improvement %	Ge%	Elastic Modulus (GPa)	Improvement %
0	70.33	/	3.5	28.36	59.67
0.5	69.231	1.56	4	26.93	61.70
1	64.74	7.94	4.5	24.33	65.40
1.5	62.654	10.91	5	20.615	70.68
2	43.27	38.47	5.5	14.87	78.85
2.5	36.45	48.17	6	11.22	84.04
3	33.81	51.92	/	/	/

It is observed that the elastic modulus decreases with the increase in the content of Germanium; this decrease can be explained as follows: While the atomic radii of Nb (1.4615 nm) and Zr (1.39 nm), the radius of Ge (1.659 nm) [39]. Obeying Vegard's law (linear rule of the mixture), the assembly of Ge atoms leads to an expansion of the host lattice and, therefore, a linear increase of the lattice parameter of the bcc phase, and this increment will lead to a weaker bonding force between the adjusted atoms [40]. On the other hand, for the phases of Nb alloys, the **(Nb)** phase has the lowest elastic modulus [36]. However, the decreased porosity of the prepared Nb-1%Zr alloys increases with the Germanium contents, leading to the elastic modulus decrease, as shown in table (4.2). Combining the phase compositions (**(Nb)** phase) and porosity that reached 25.96%, these are the primary reasons for decreasing the elastic modulus of the porous Nb-1%Zr alloys with increasing Germanium

contents. The decrease in the elastic modulus of Nb alloy makes it more suitable for surgical implant applications due to decreasing the stress-shielding effect, which negatively affects the bone tissues [41].

4.6.4 Wear Test

All spesimens with 12.8 mm diameter are subjected to wear test under various loads (20 & 25 N) for different time (5, 10, 15, 20 & 25) minets at room temperature , the results are shown in figures [(4.26)-(4.33)].

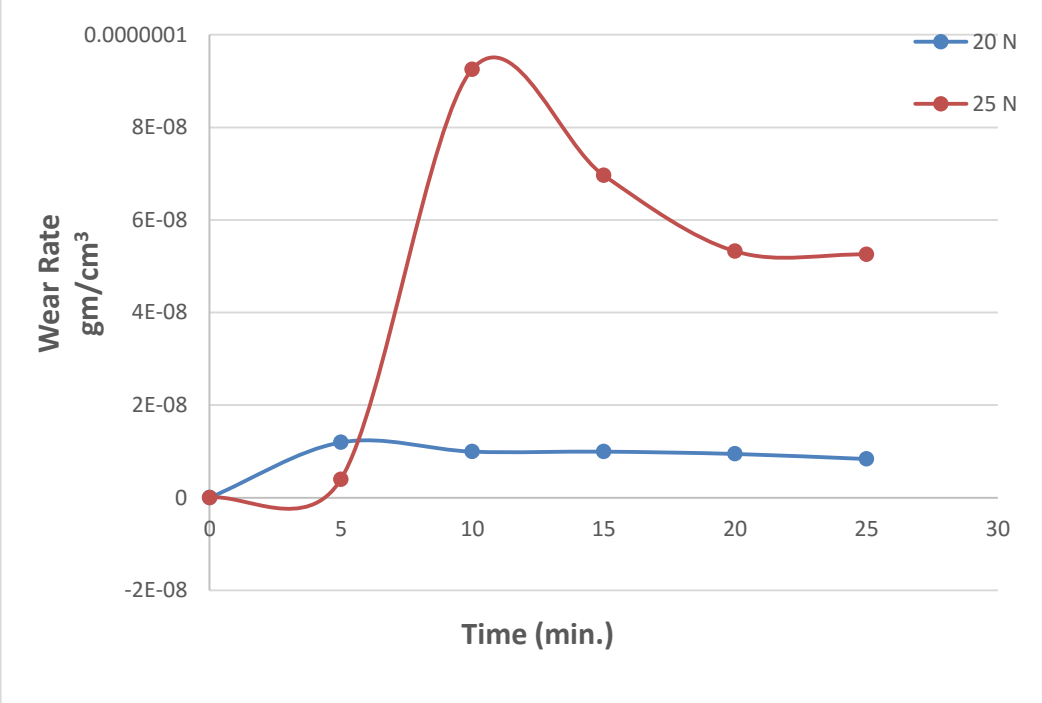

Figure (4.26): Wear Rate Vs Time for Base Alloy Under (20 & 25)N.

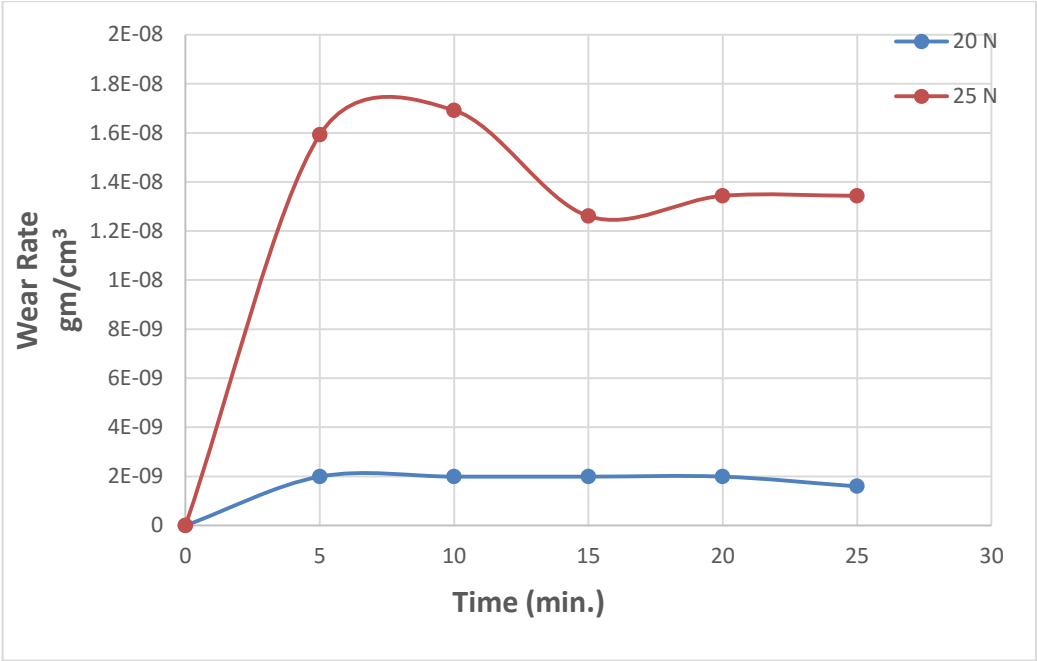

Figure (4.27): Wear Rate Vs Time for (Nb-1%Zr-0.5%Ge)Alloy Under (20 & 25)N.

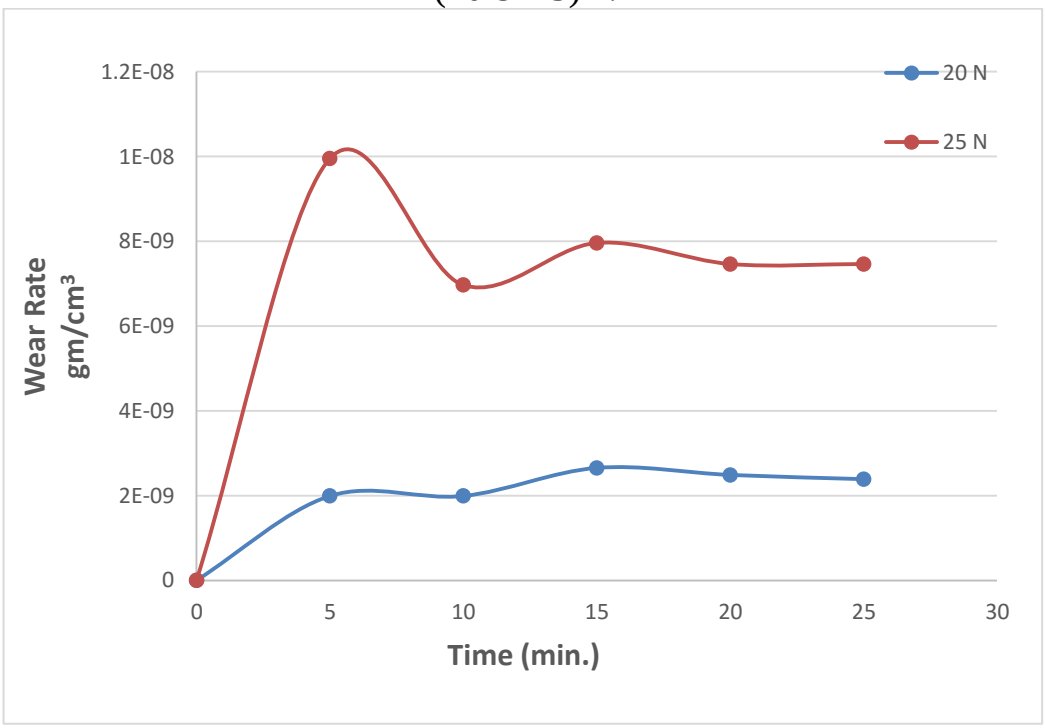

Figure (4.28): Wear Rate Vs Time for (Nb-1%Zr-1%Ge)Alloy Under (20 & 25)N.

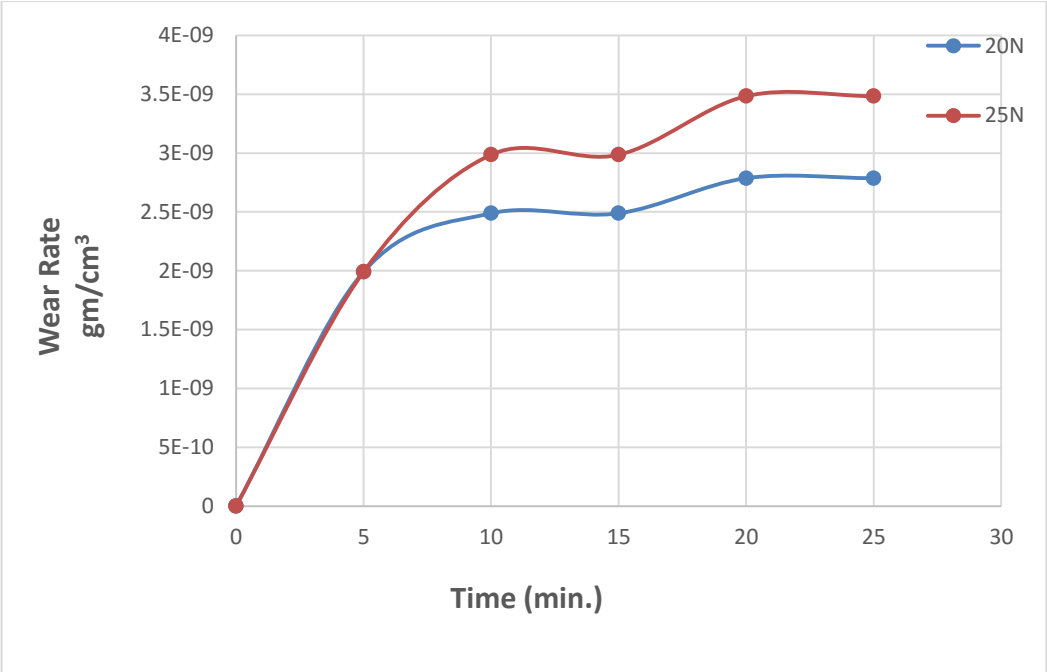

Figure (4.29): Wear Rate Vs Time for (Nb-1%Zr-1.5%Ge)Alloy Under (20 & 25)N.

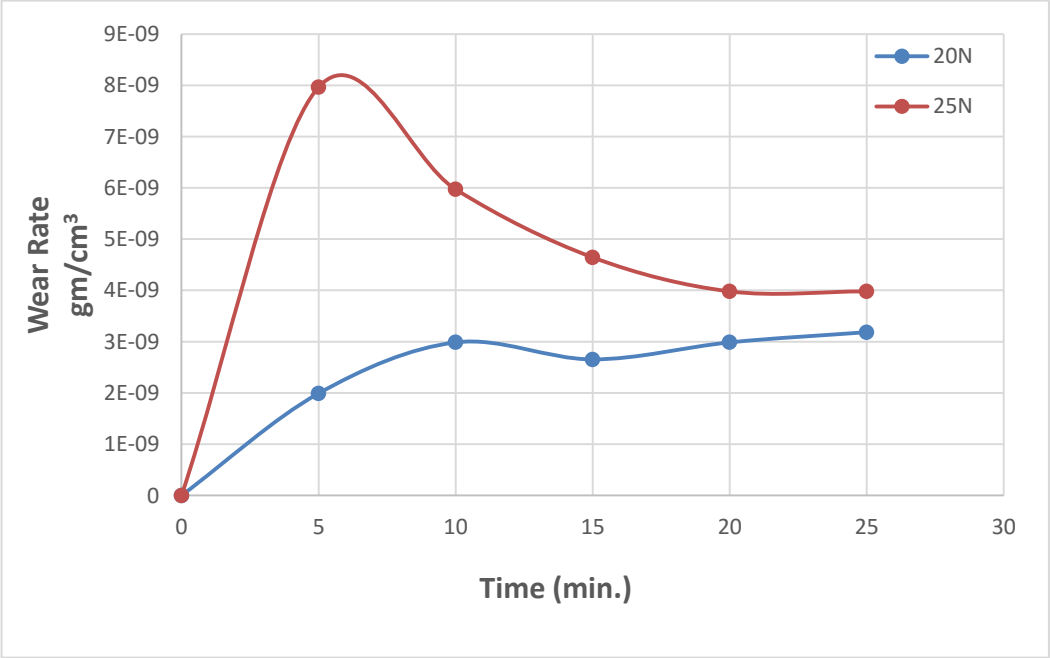

Figure (4.30): Wear Rate Vs Time for (Nb-1%Zr-2%Ge)Alloy Under (20 & 25)N.

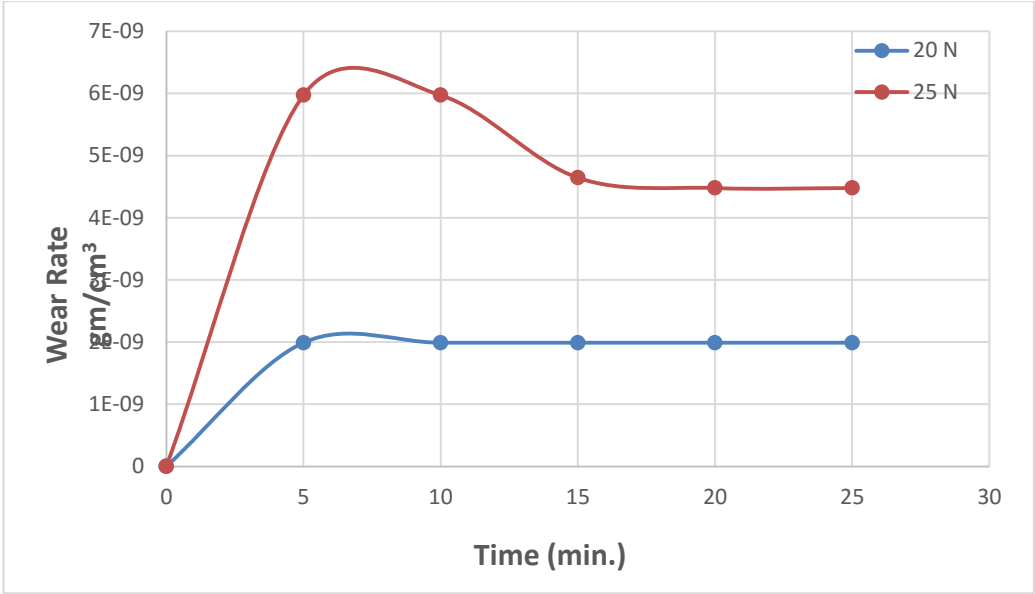

Figure (4.31): Wear Rate Vs Time for (Nb-1%Zr-5%Ge)Alloy Under (20 & 25)N.

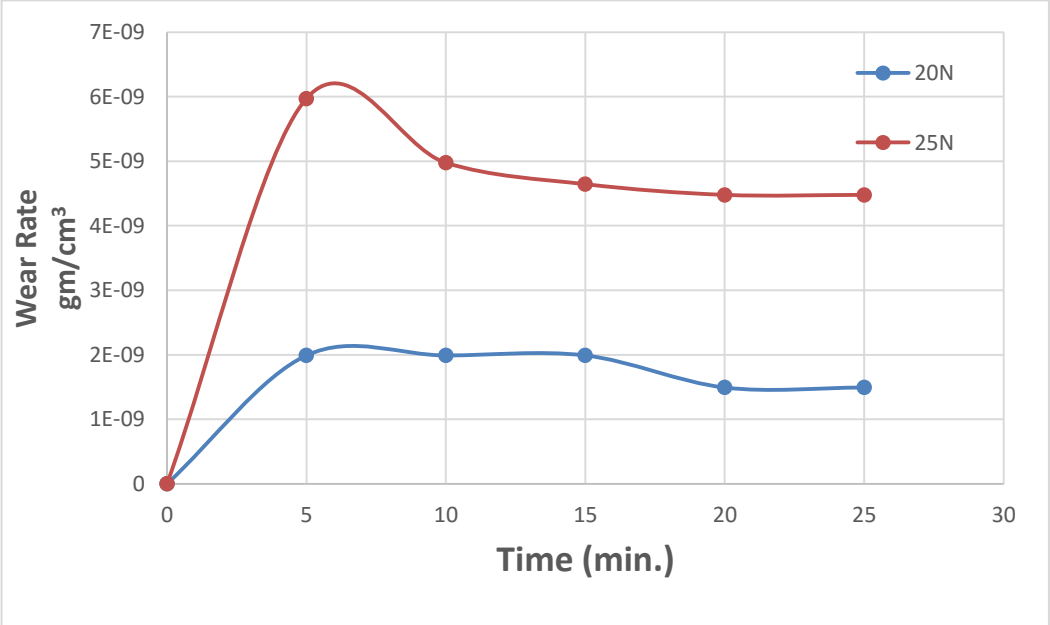

Figure (4.32): Wear Rate Vs Time for (Nb-1%Zr-5.5%Ge)Alloy Under (20 & 25)N.

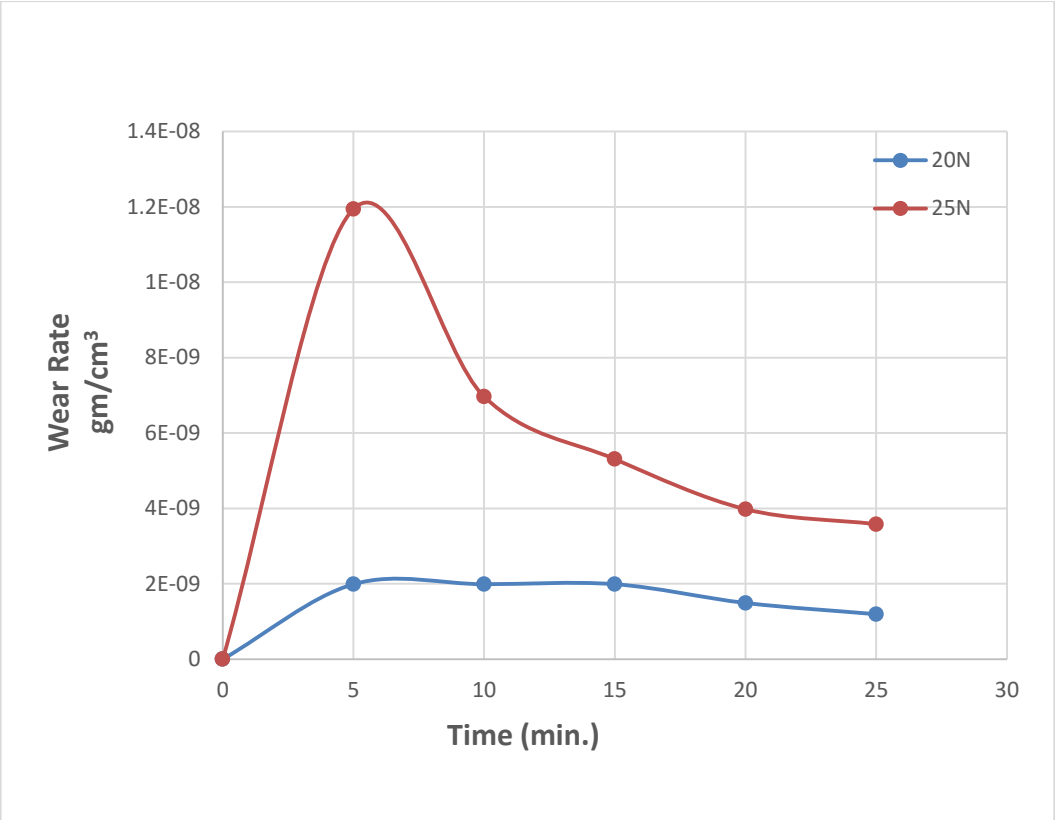

Figure (4.33): Wear Rate Vs Time for (Nb-1%Zr-6%Ge)Alloy Under (20 & 25)N.

Figures [(4.26)-(4.33)], show the effect of Ge addition on the wear resistance, it can be seen that the wear resistance increases with increasing addition percentage of Ge, which can be attributable to the solid solution hardening (Nb) from germanium and niobium which led to increasing hardness of all alloys with germanim contents. Table (4.5) shows the improvement percentage in wear resistance of the base alloy (Nb-1%Zr) with respect to the addition of Ge. We notice from the above figures that when loads (20N and 25N) are applied, the wear rate at (25N) is greater than that of (20N) because of increasing friction coefficient when the wear rate for base alloy is ($1.6 * 10^{-8}$, $5.254 * 10^{-8}$) gm/cm^3 at (20N & 25N) respectively. The wear rate at (25N) starts to increase until it reaches its highest value and then gradually decreases until it stabilizes reaching the steady state, the reason for the increase in the wear rate is because the resistance is less on the surface for easy

removal of the convexity and concavity layers until reaching stability indicating to reach friction coefficient the steady state.

Figures [(4.26)-(4.33)] wear rate vs time for all alloys under various loads and various time , it can be noted that wear rate for all alloys under 25N is higher than 20N, this because of the increasing of friction at the surface as the load increase [92]. Ge addition, increasing of wear rate with time of all specimens because of increasing friction time which leads to remove more material from the surface [93].

The effect of Ge content on wear rate of [B1-B13] under constant load (25N) and constant time (25min), it can be noted that the wear rate decreases with increasing Ge content, the wear rate of 0.5% Germanium alloy is ($1.34*10^{-8}$ mm^3) compare to that of base alloy ($5.254 *10^{-8}$ mm^3) which is achived improvement percentage of (74.43%). The wear resistance improvement increases with increasing Germanium content until reach (93.18%) at 6% Germanium, which is attributable to increasing (Nb) hardness due to solid solution strengthening, this reduction in wear rate return to Ge addition which increases hardness. The effect of Germanium content on wear rate is shown in figure (4.34).

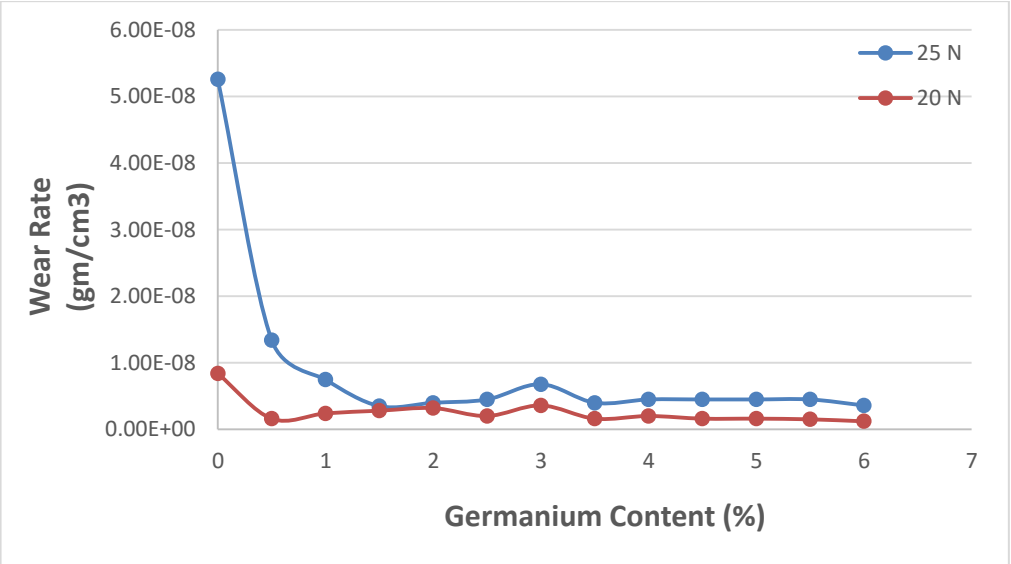

Figure (4.34): The effect of Germanium content on wear rate

Table (4.6): Wear Rate and Improvement Percentage% at (20N & 25N).

Seq.	Alloy	Wear Rate gm/cm^3		Improvement % at 25N
		At 20N	At 25N	
1	Base (Nb-1%Zr)	8.36E-09	5.25478E-08	/
2	(B+0.5%Ge)	1.59E-09	1.34E-08	74.43
3	(B+1%Ge)	2.39E-09	7.46417E-09	85.80
4	(B+1.5%Ge)	2.79E-09	3.48328E-09	93.37
5	(B+2%Ge)	3.18E-09	3.98089E-09	92.42
6	(B+2.5%Ge)	1.99E-09	4.4785E-09	91.48
7	(B+3%Ge)	3.58E-09	6.76752E-09	87.12
8	(B+3.5%Ge)	1.59E-09	3.98089E-09	92.42
9	(B+4%Ge)	1.99E-09	4.4785E-09	93.18
10	(B+4.5%Ge)	1.59E-09	4.4562E-09	93.18
11	(B+5%Ge)	1.59E-09	4.4435E-09	93.18
12	(B+5.5%Ge)	1.49E-09	4.4380E-09	91.48
13	(B+6%Ge)	1.19E-09	3.5828E-09	93.18

4.7 Electrochemical Tests

4.7.1 Open circut potential (OCP) - time measurement

The OPC-time was meseared with respect to SCE for all alloys in Hank's solution and artificial sliva at 37±1 ºC. The time period was from 0 upto 60 minuts with interval 5 minuts were potential reported. Tables (4.5) and (4.6) show the open circut potential and improvement percentage for alloys. Figures [(4.35)-(4.60)] show the OCP throughout time, Figure (4.35) shows that the potential fall two the negative direction until reach the constant value (293 mV) the potential drop with time indicates to the dissolution is greater than the deposition that occurs

on the surface of specimen. When Germanium alloying element is added to the base alloy it is clear that OCP value rise towords the positive direction indicating to that the deposition reaction is greater than desolution reaction, after certain time the potential reach the constant value due to the equilibrium between the dissolution and decomposition achiving improvement percentage upto (97.28%) for 6% Germanium in Hank solution (104.05%) for 6% Germanium in synthetic sliva, make the Neobium alloy more noble.

Table (4.7): Corrosion resistance imrovment with respect to Ge content in Hank's solution.

Ge Content (%)	Eoc. (mV)	Improvment (%)
0	-295	/
0.5	-140	60
1	-125	65.42
1.5	-118	57.62
2	-102	52.54
2.5	-90	69.49
3	-50	95.59
3.5	-16	96.94
4	-15	94.91
4.5	-13	83.05
5	-11	94.57
5.5	-9	95.59
6	-8	97.28

Table (4.8): Corrosion resistance imrovment with respect to Ge content in synthetic artificial Saliva.

Ge Content (%)	Eoc (mV)	Improvment (%)
0	-148	/
0.5	-102	31.08
1	-83	43.91
1.5	-68	54.05
2	-53	64.18
2.5	-50	66.21
3	-18	87.83
3.5	-15	89.86
4	-13	91.21
4.5	-9	93.91
5	-8	94.59
5.5	-6	95.94
6	6	104.05

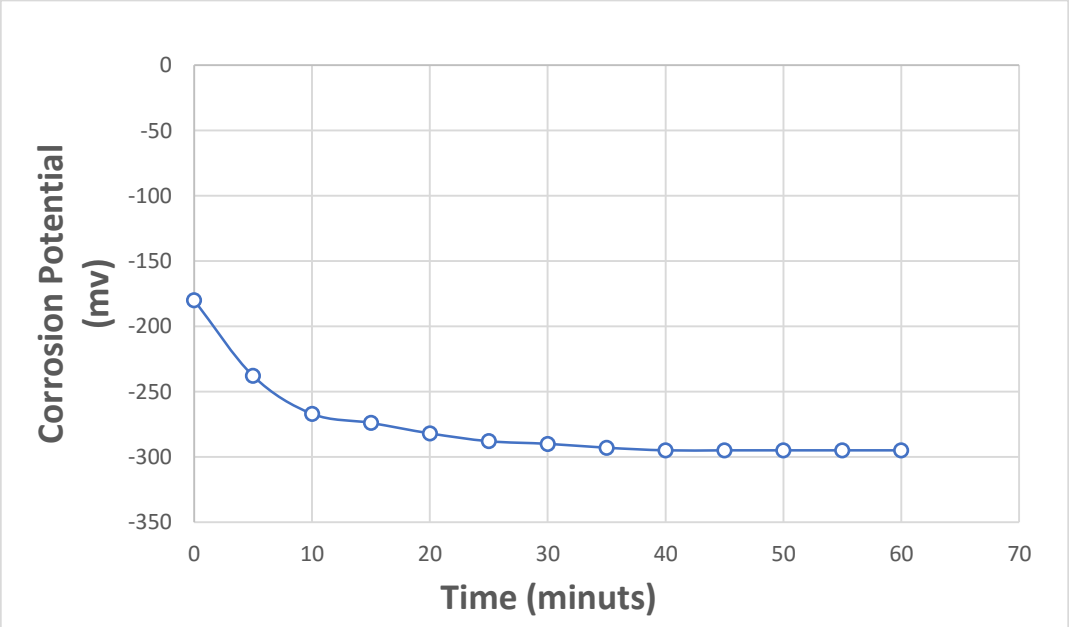

Figure (4.35): The corrosion potential Vs time for (Nb-1%Zr) Alloy for Hank's solution.

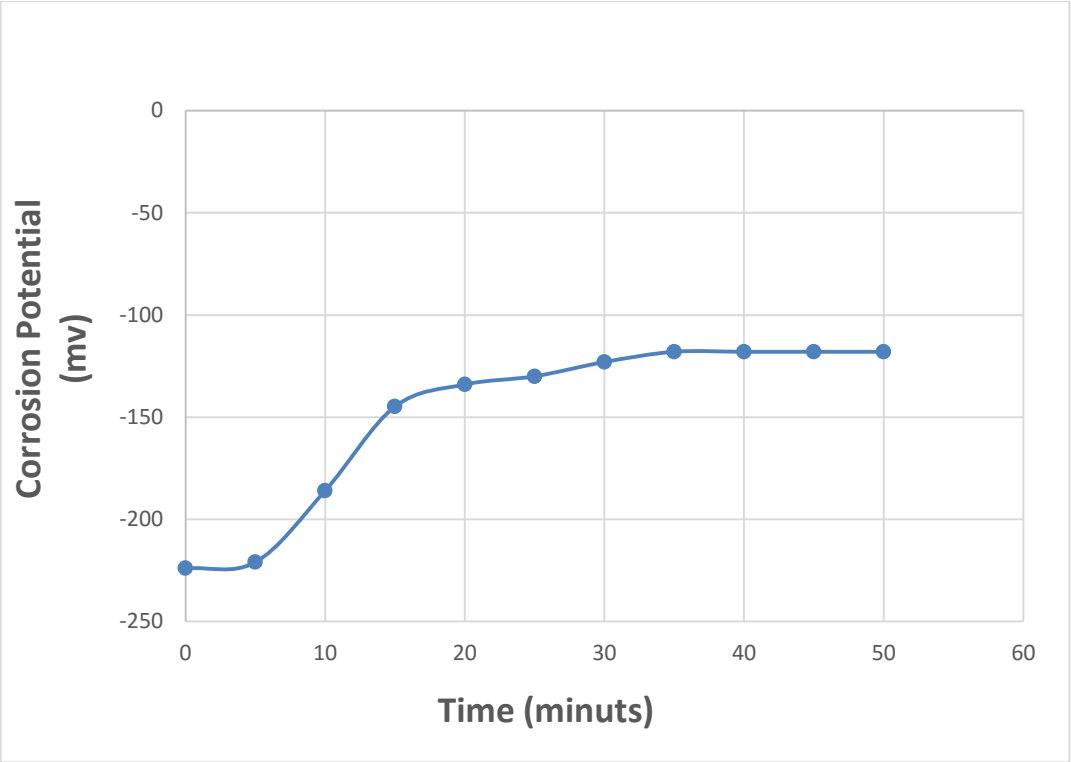

Figure (4.36): The corrosion potential Vs time for (Nb-1%Zr-0.5%Ge)Alloy for Hank's solution.

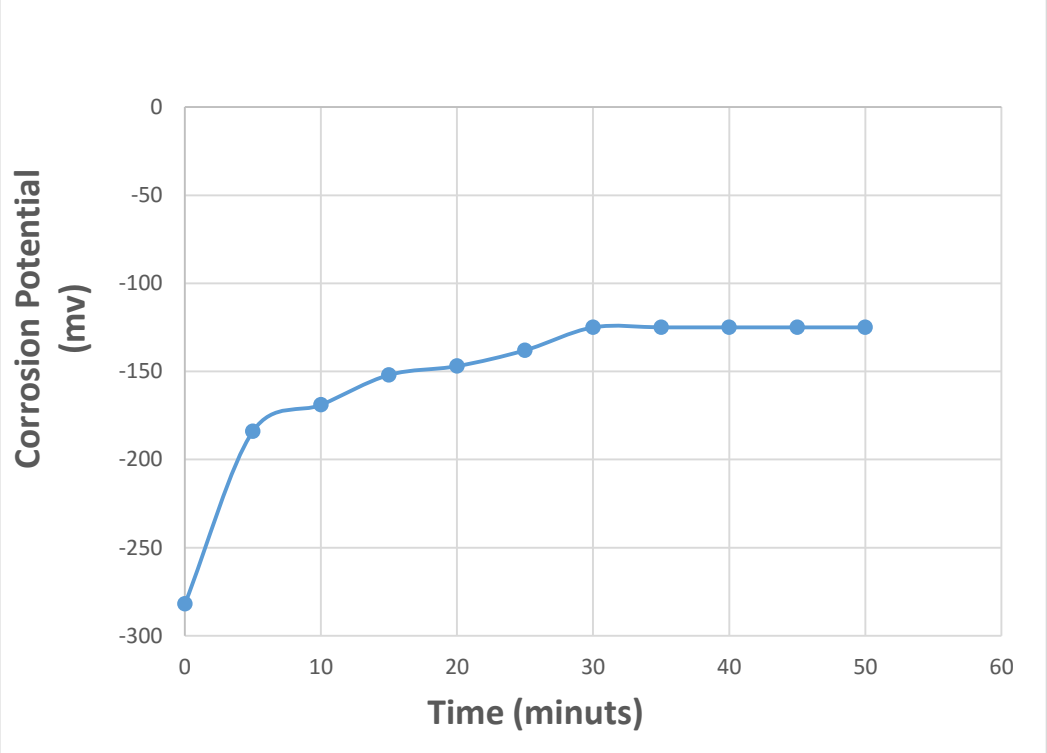

Figure (4.37): The corrosion potential Vs time for (Nb-1%Zr-1%Ge)Alloy for Hank's solution.

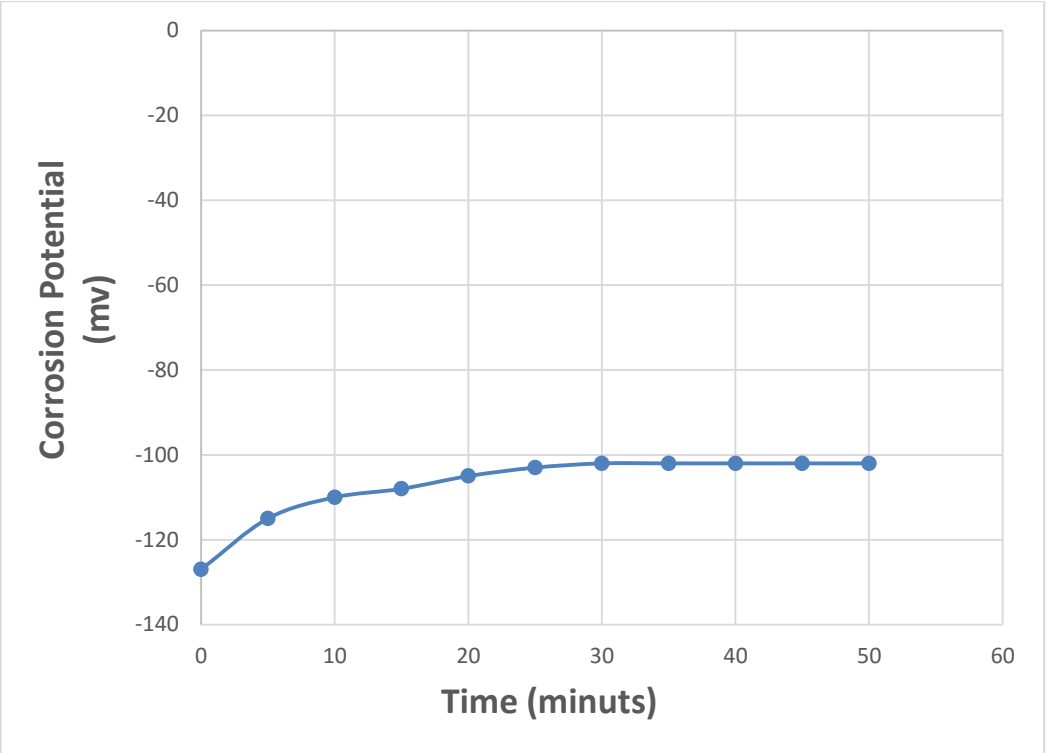

Figure (4.38): The corrosion potential Vs time for (Nb-1%Zr-1.5%Ge)Alloy for Hank's solution.

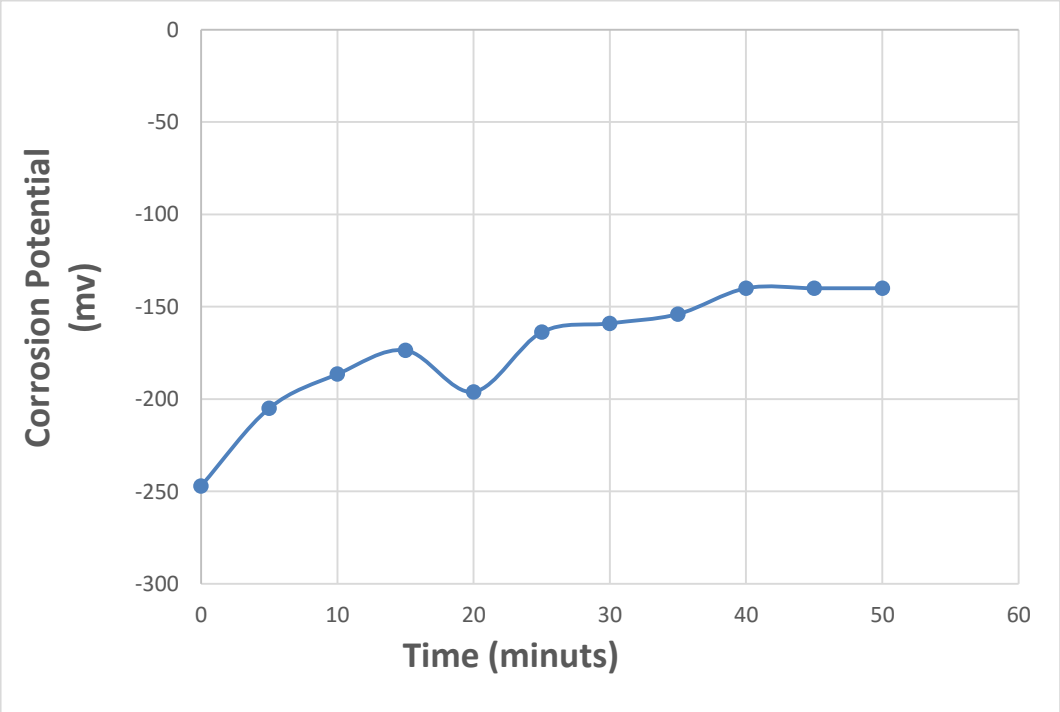

Figure (4.39): The corrosion potential Vs time for (Nb-1%Zr-2%Ge)Alloy for Hank's solution.

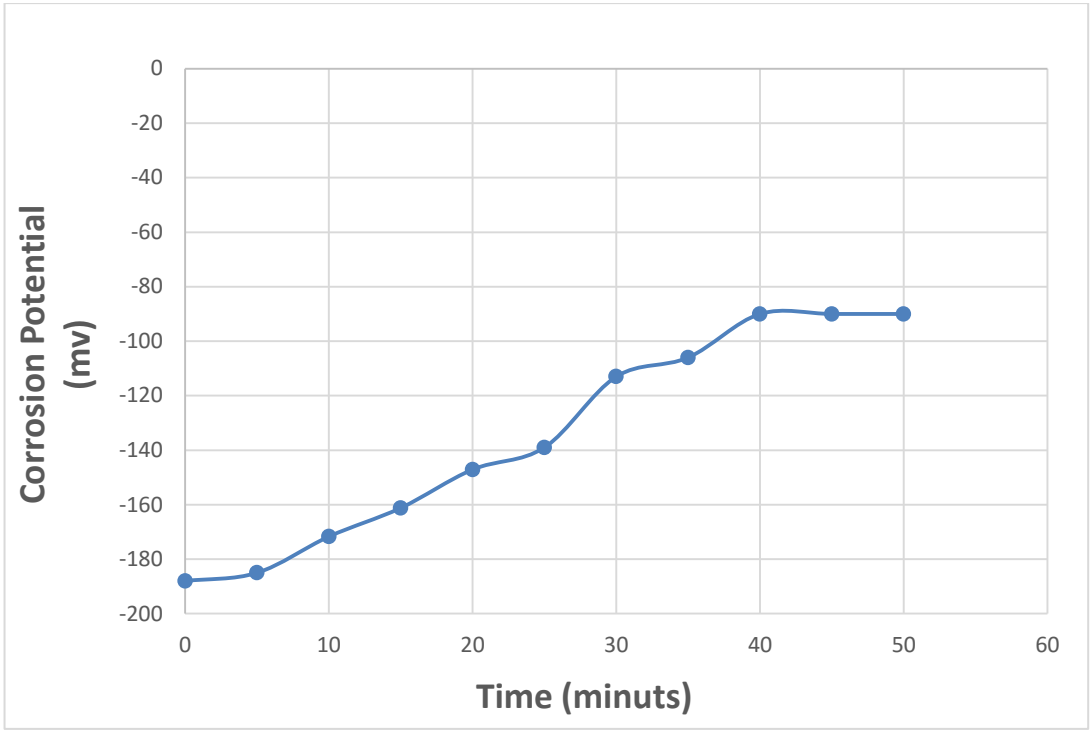

Figure (4.40): The corrosion potential Vs time for (Nb-1%Zr-2.5%Ge)Alloy for Hank's solution.

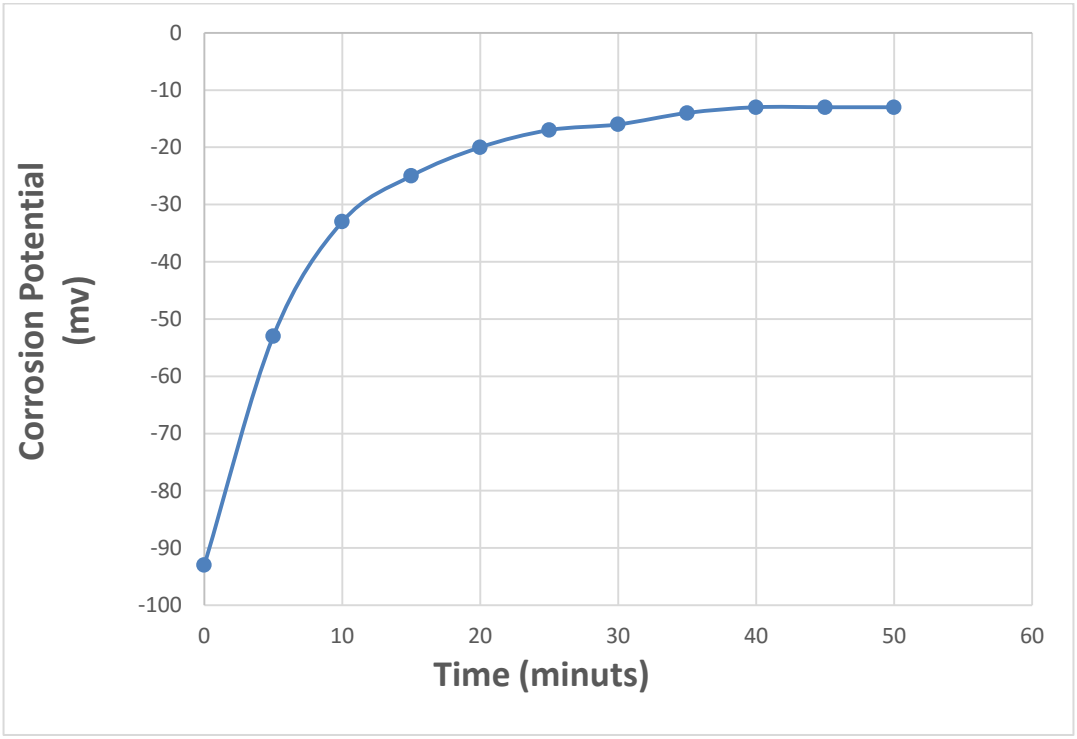

Figure (4.41): The corrosion potential Vs time for (Nb-1%Zr-3%Ge)Alloy for Hank's solution.

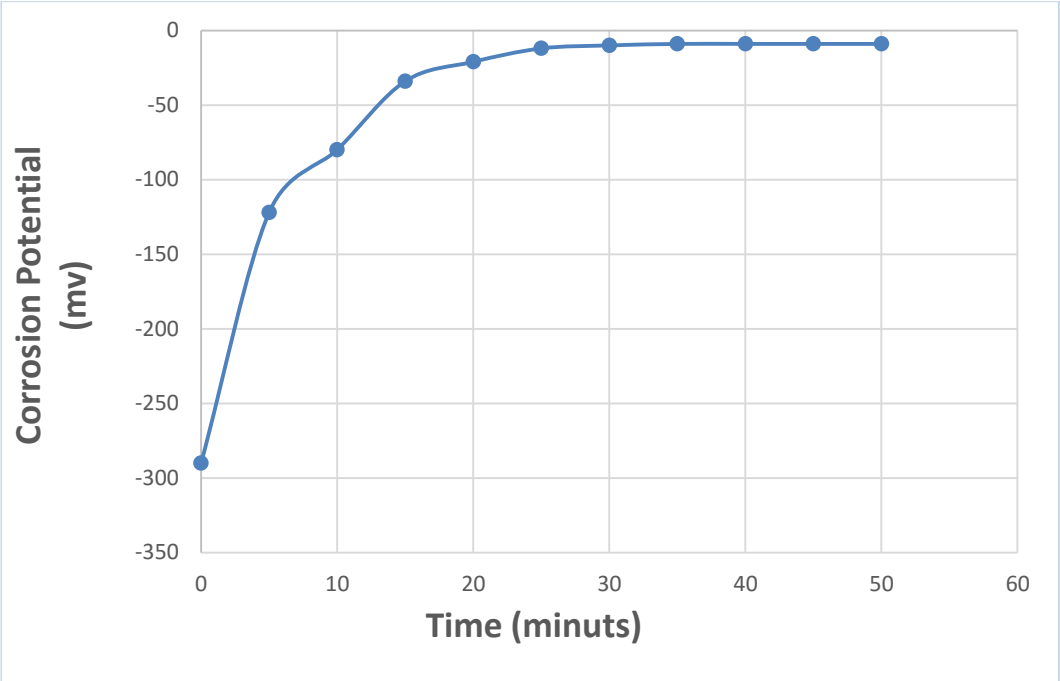

Figure (4.42): The corrosion potential Vs time for (Nb-1%Zr-3.5%Ge)Alloy for Hank's solution.

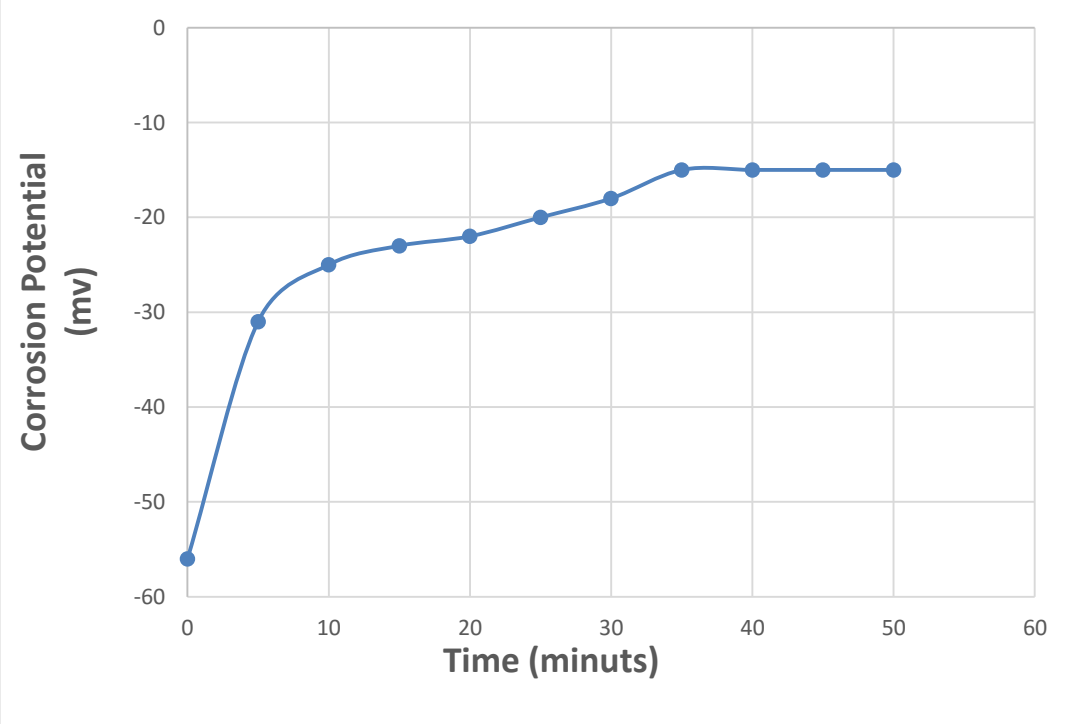

Figure (4.43): The corrosion potential Vs time for (Nb-1%Zr-4%Ge)Alloy for Hank's solution.

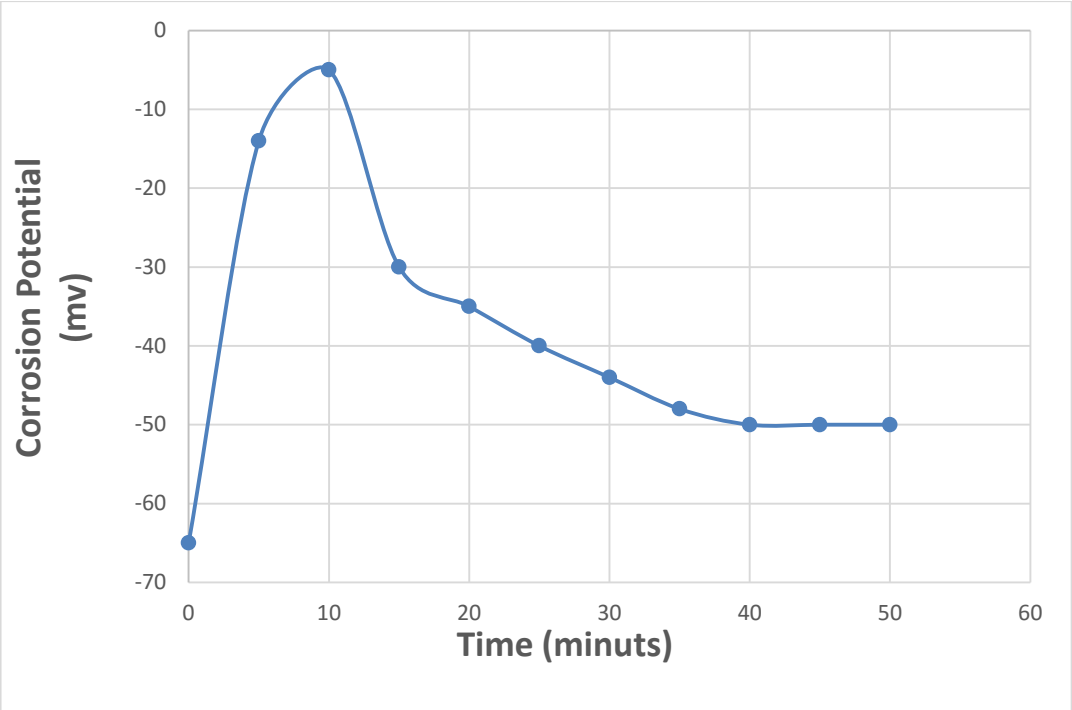

Figure (4.44): The corrosion potential Vs time for (Nb-1%Zr-4.5%Ge)Alloy for Hank's solution.

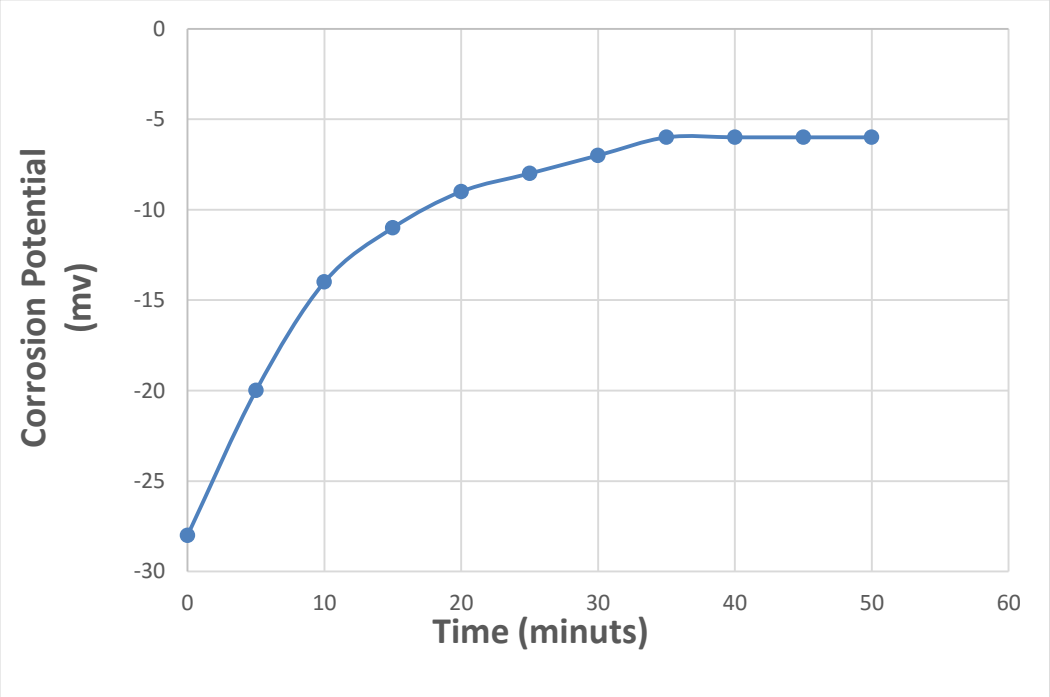

Figure (4.45): The corrosion potential Vs time for (Nb-1%Zr-5%Ge)Alloy for Hank's solution.

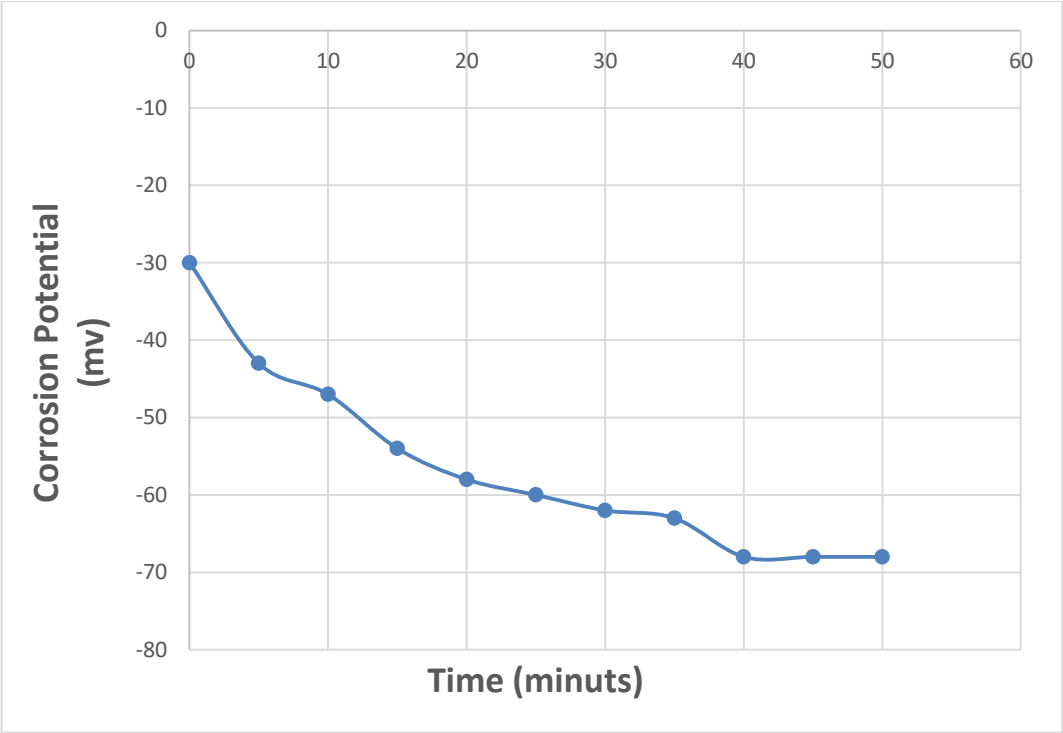

Figure (4.46): The corrosion potential Vs time for (Nb-1%Zr-5.5%Ge)Alloy for Hank.

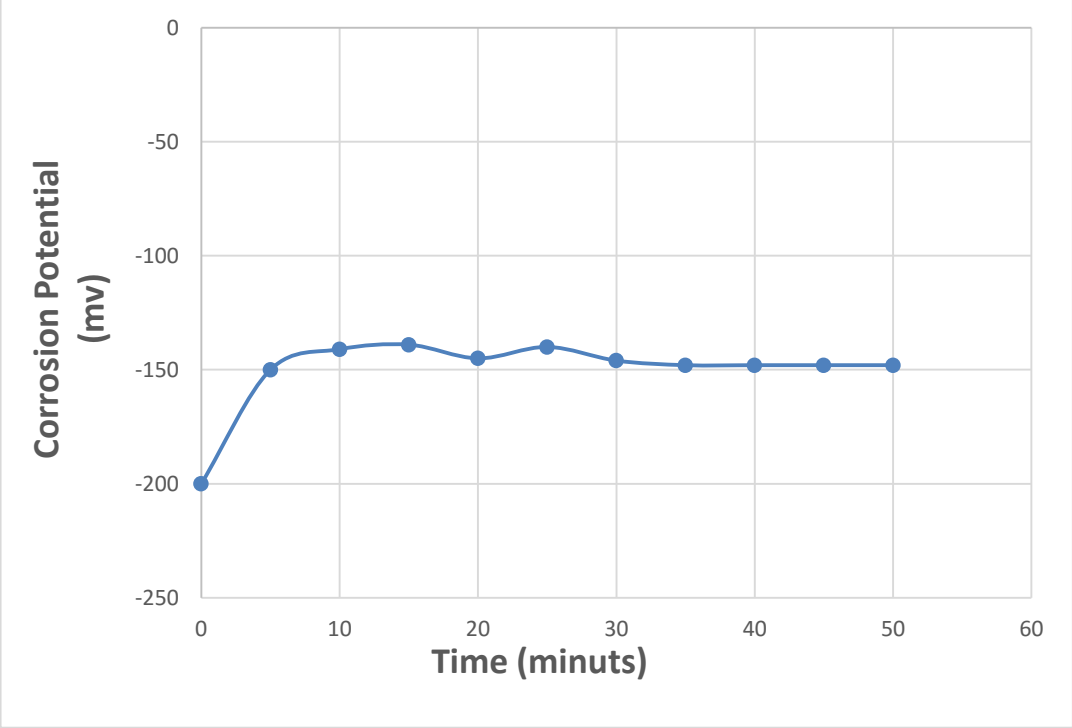

Figure (4.47): The corrosion potential Vs time for (Nb-1%Zr-6%Ge)Alloy for Hank.

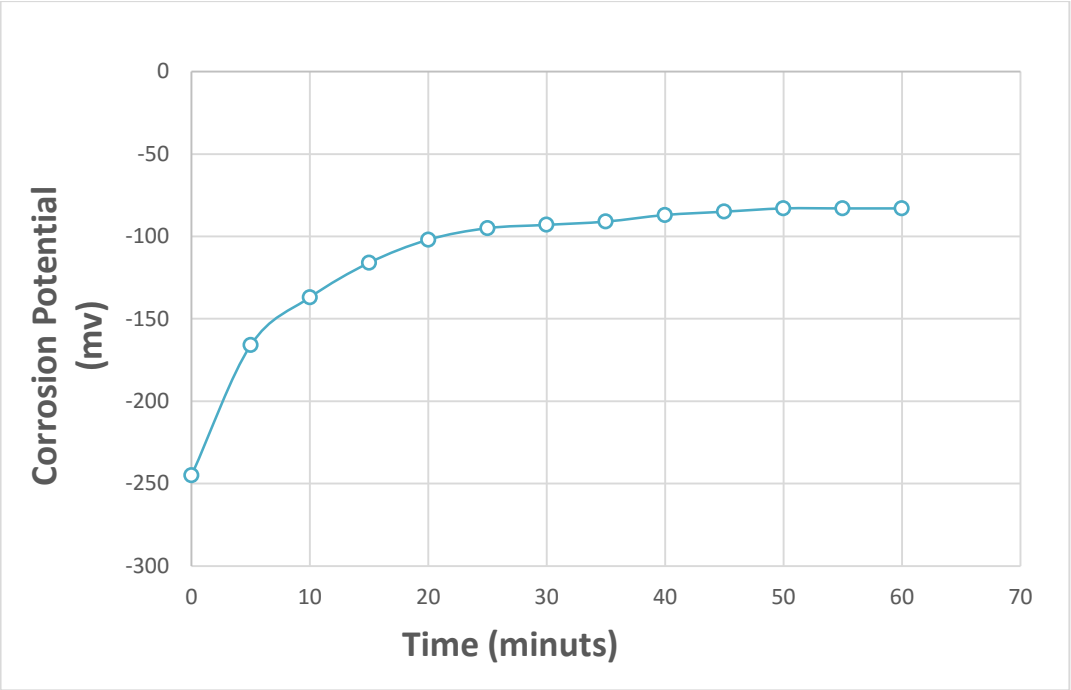

Figure (4.48): The corrosion potential Vs time for (Nb-1%Zr)Alloy for Saliva.

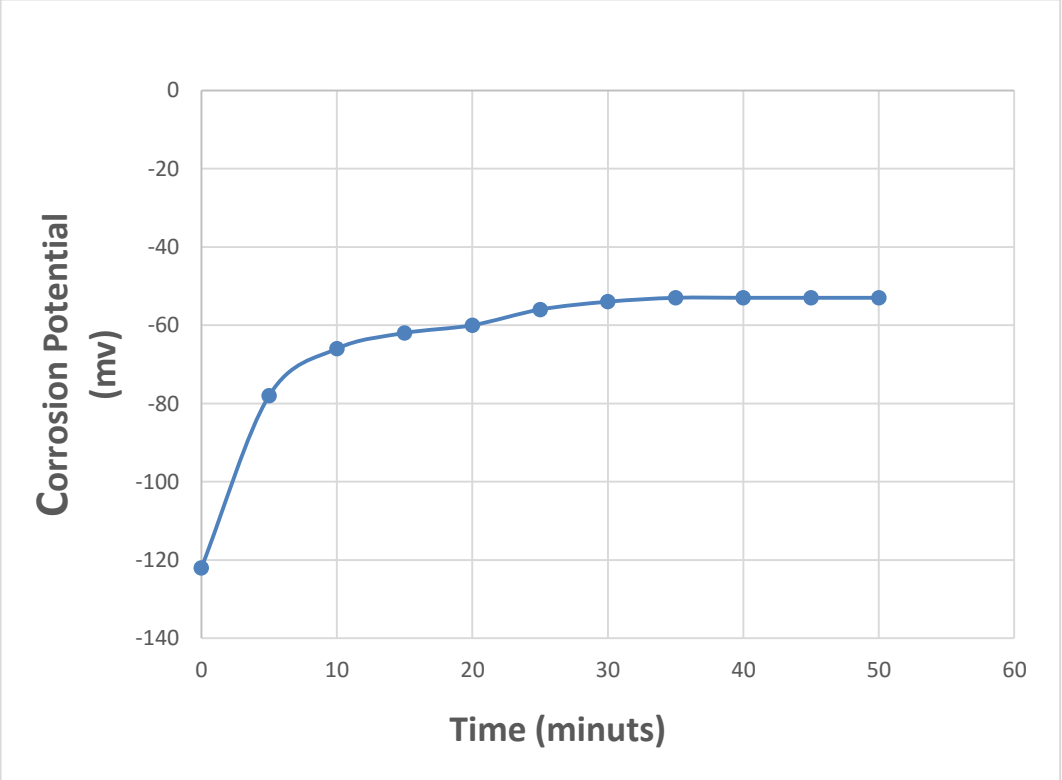

Figure (4.49): The corrosion potential Vs time for (Nb-1%Zr-0.5%Ge) Alloy for Saliva.

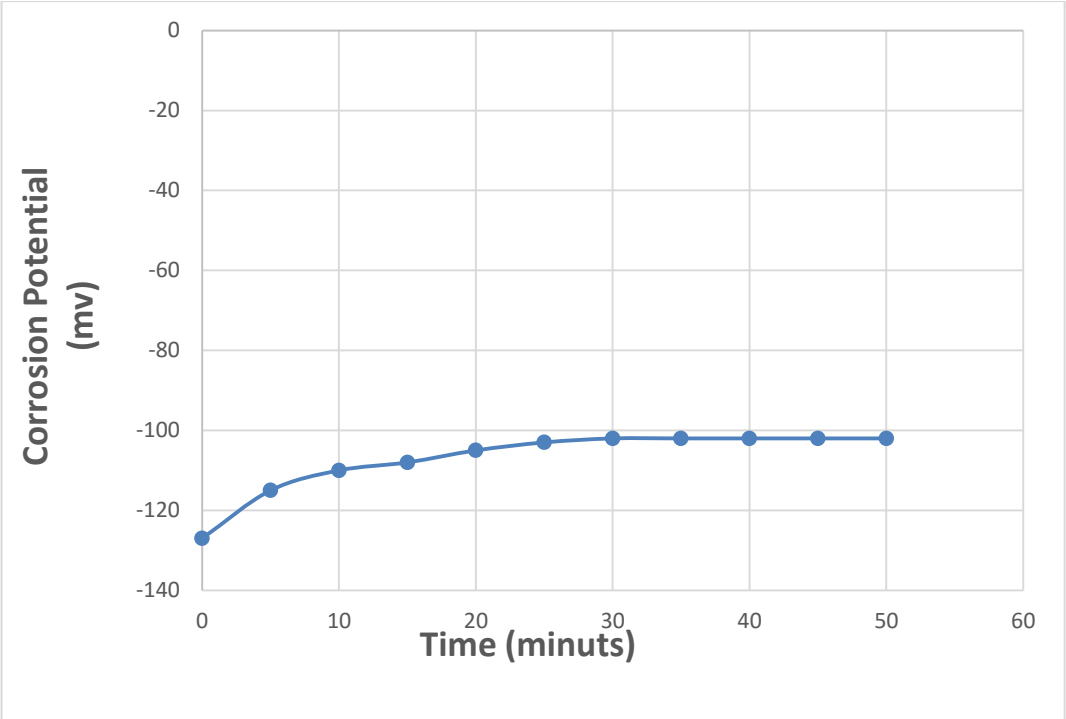

Figure (4.50): The corrosion potential Vs time for (Nb-1%Zr-1%Ge) Alloy for Saliva.

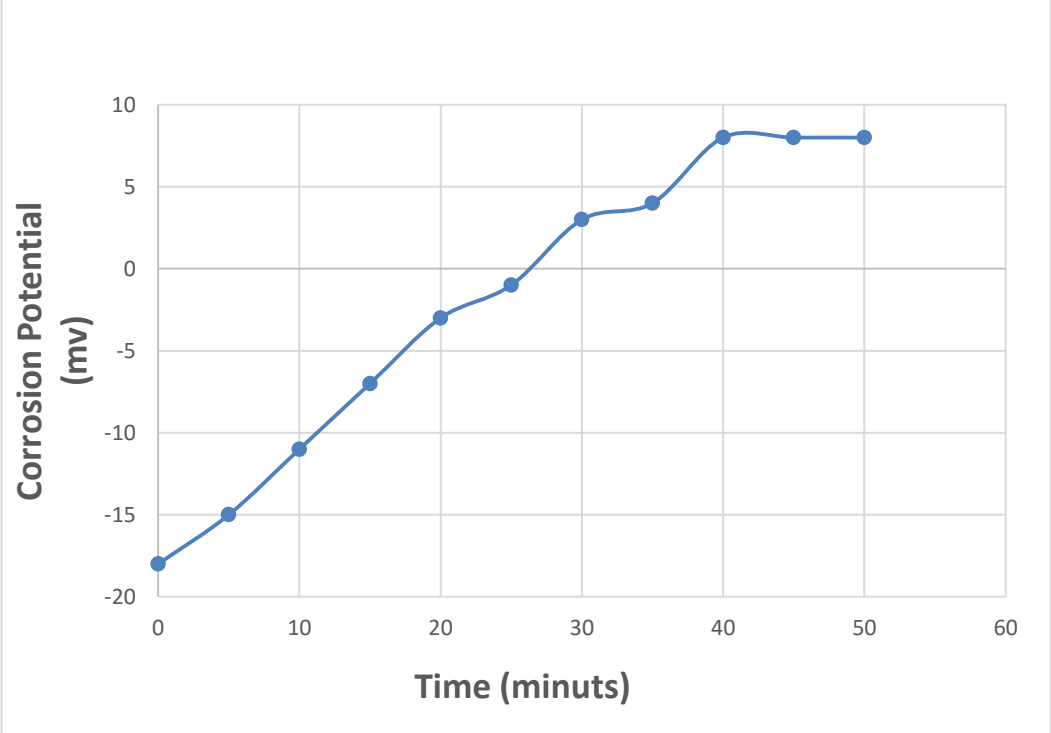

Figure (4.51): The corrosion potential Vs time for (Nb-1%Zr-1.5%Ge) Alloy for Saliva.

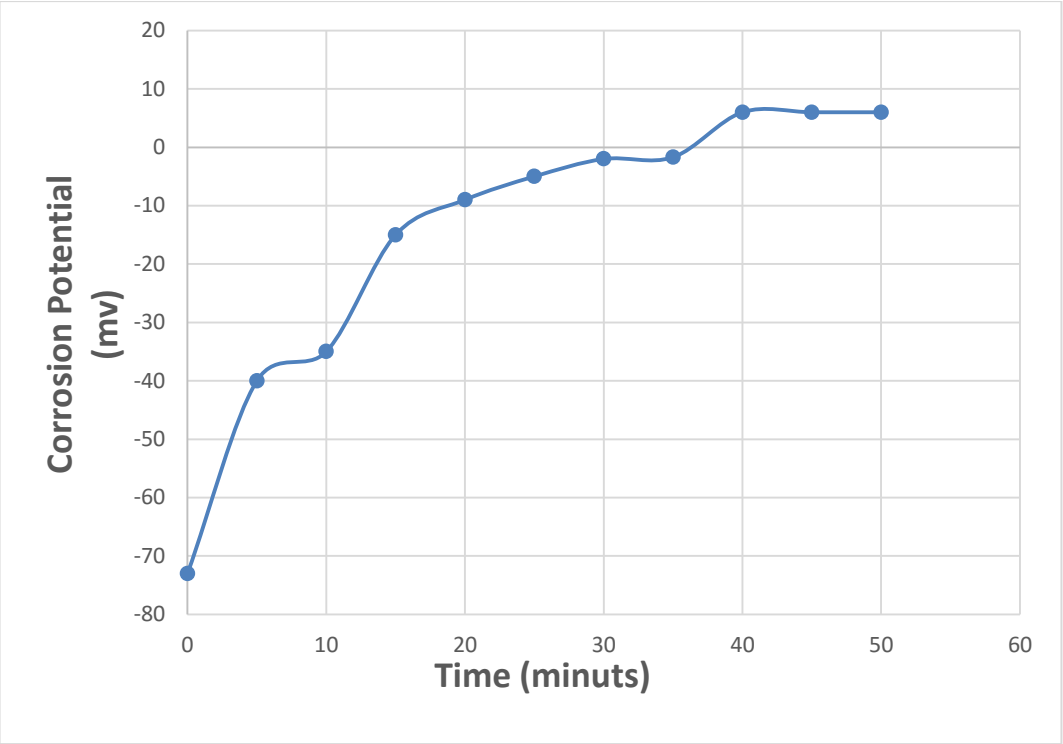

Figure (4.52): The corrosion potential Vs time for (Nb-1%Zr-2%Ge) Alloy for Saliva.

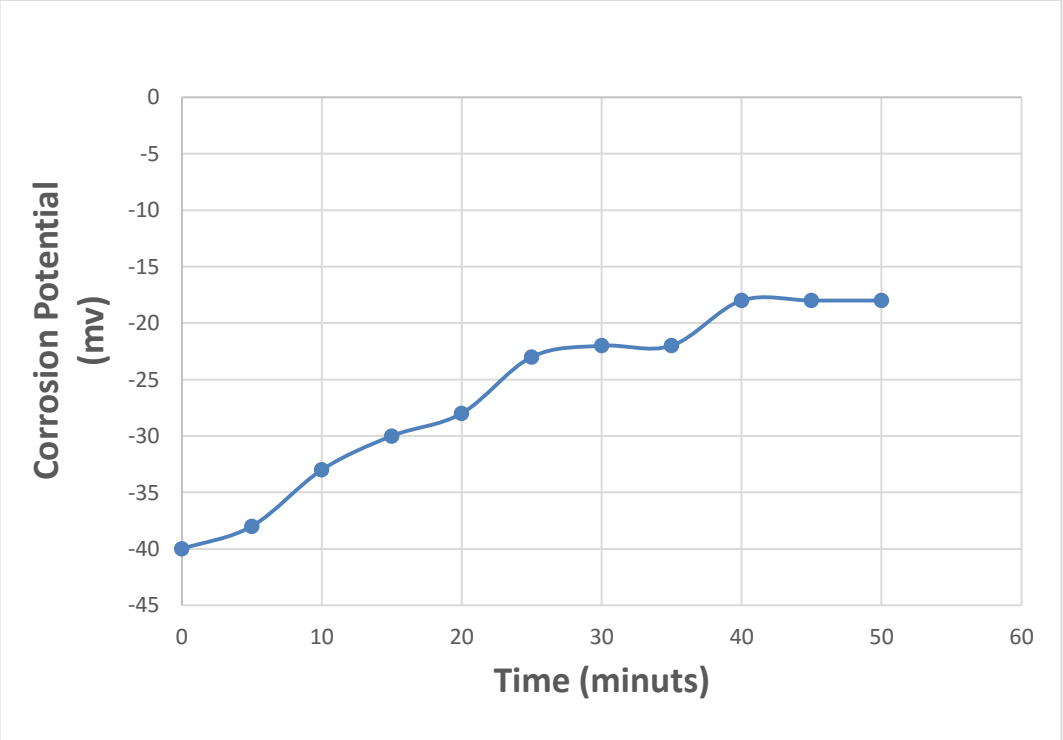

Figure (4.53): The corrosion potential Vs time for (Nb-1%Zr-2.5%Ge) Alloy for Saliva.

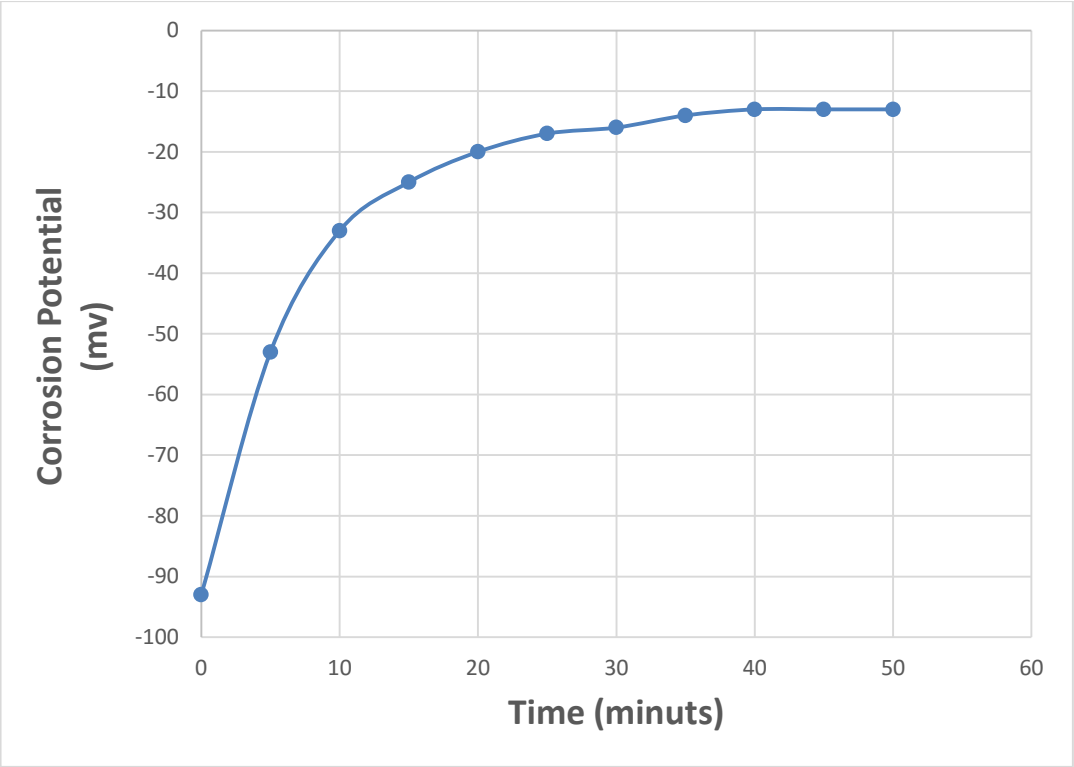

Figure (4.54): The corrosion potential Vs time for (Nb-1%Zr-3%Ge) Alloy for Saliva.

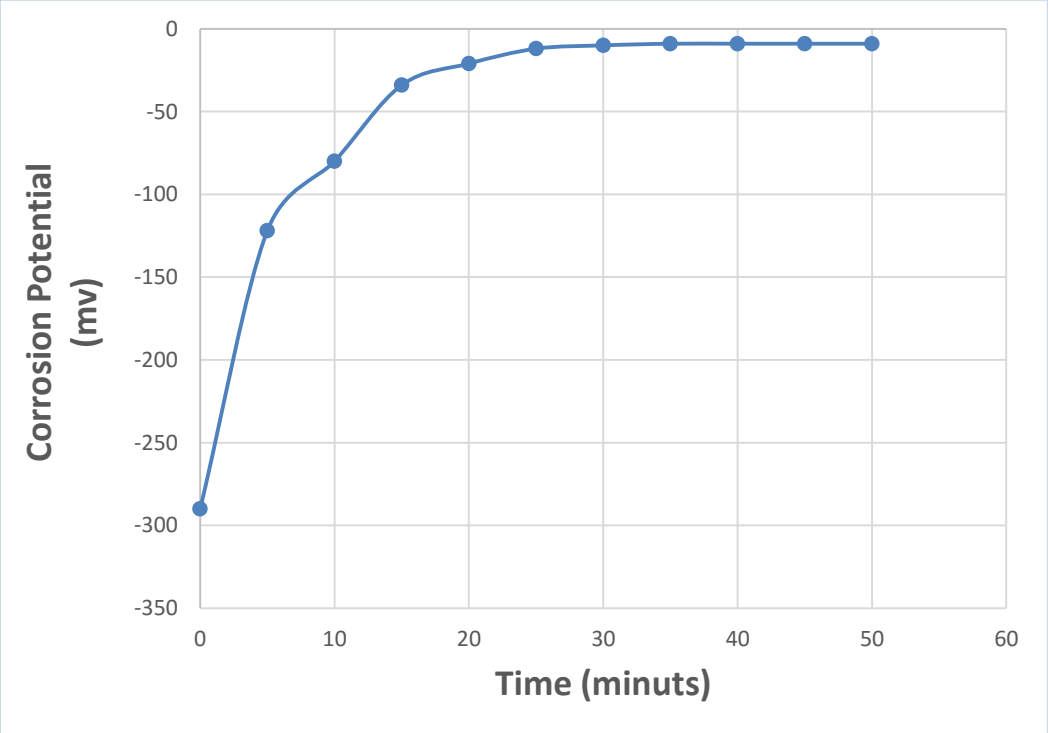

Figure (4.55): The corrosion potential Vs time for (Nb-1%Zr-3.5%Ge) Alloy for Saliva.

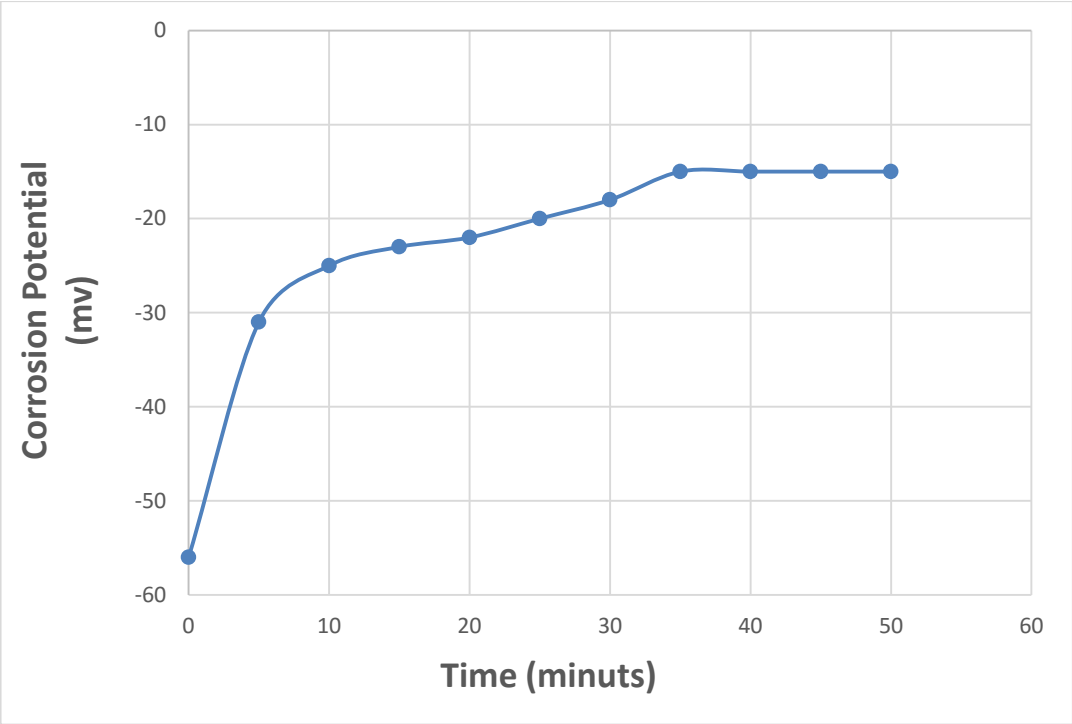

Figure (4.56): The corrosion potential Vs time for (Nb-1%Zr-4%Ge) Alloy for Saliva.

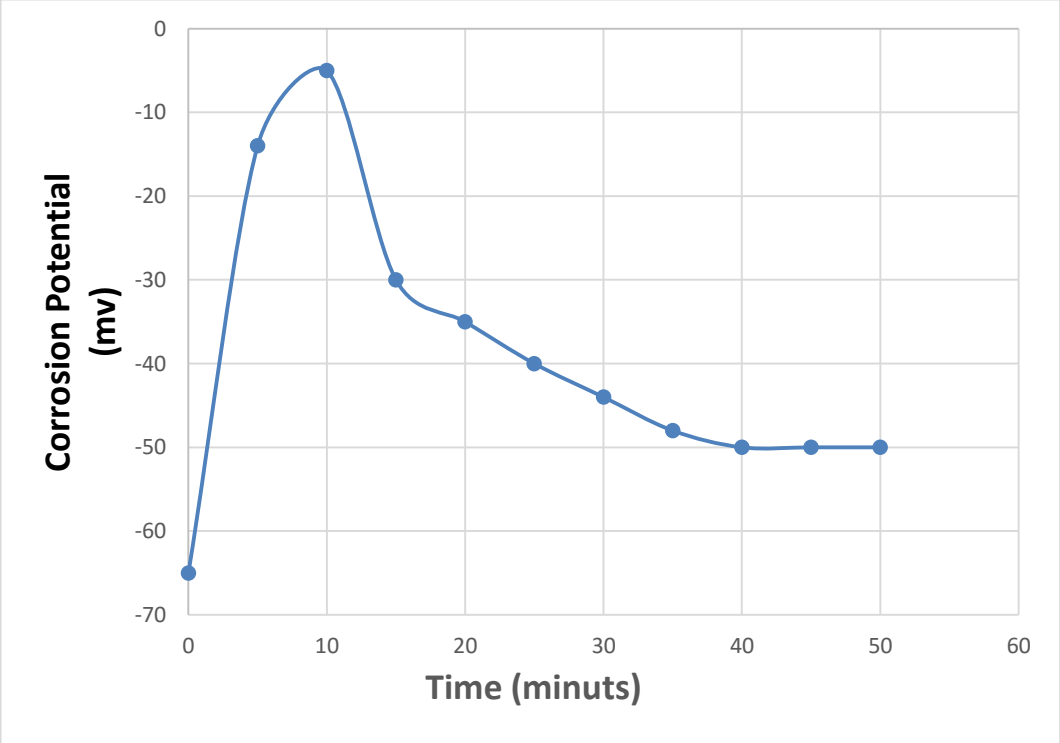

Figure (4.57): The corrosion potential Vs time for (Nb-1%Zr-4.5%Ge) Alloy for Saliva.

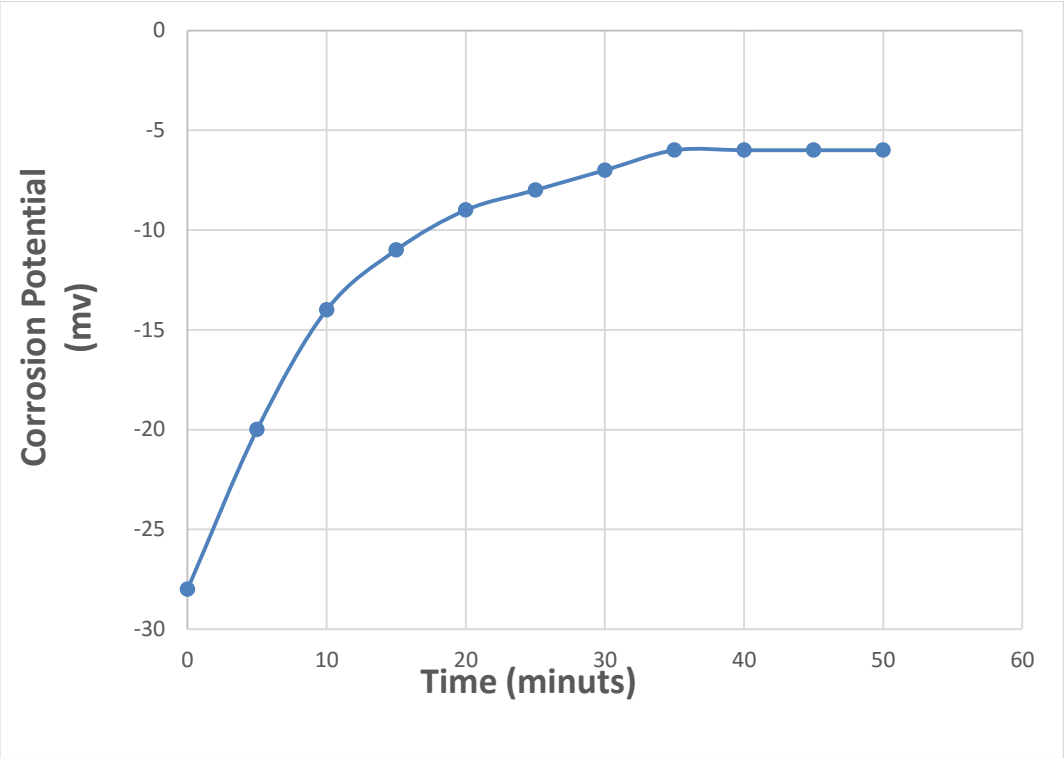

Figure (4.58): The corrosion potential Vs time for (Nb-1%Zr-5%Ge) Alloy for Saliva.

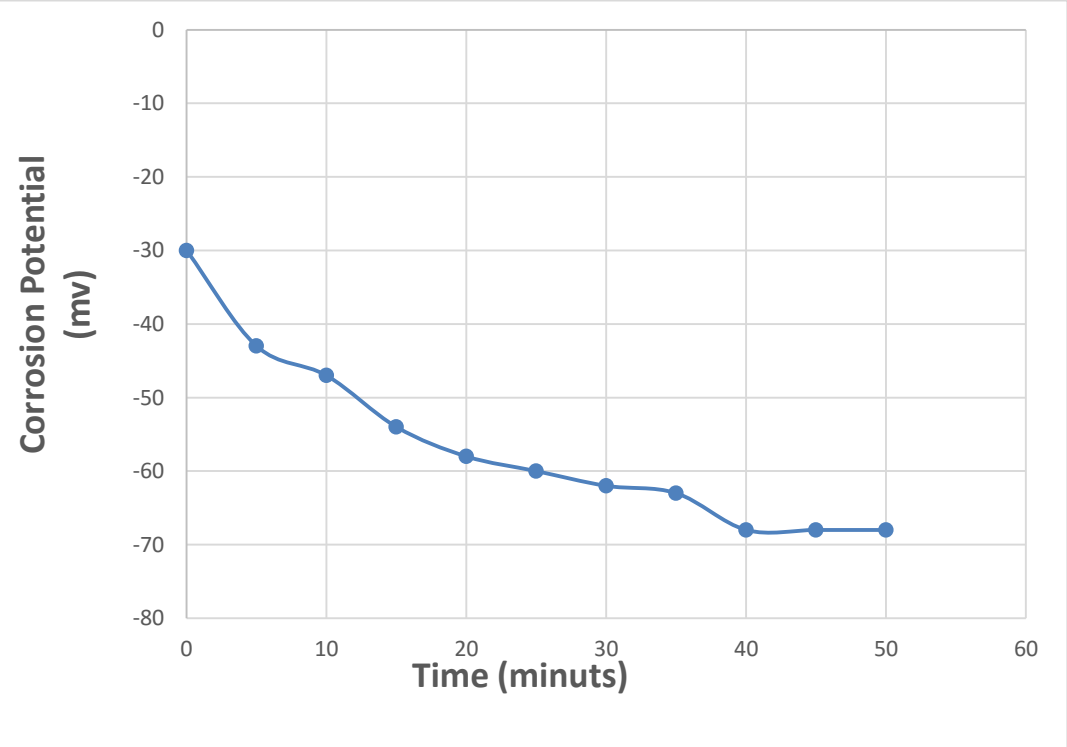

Figure (4.59): The corrosion potential Vs time for (Nb-1%Zr-5.5%Ge) Alloy for Saliva.

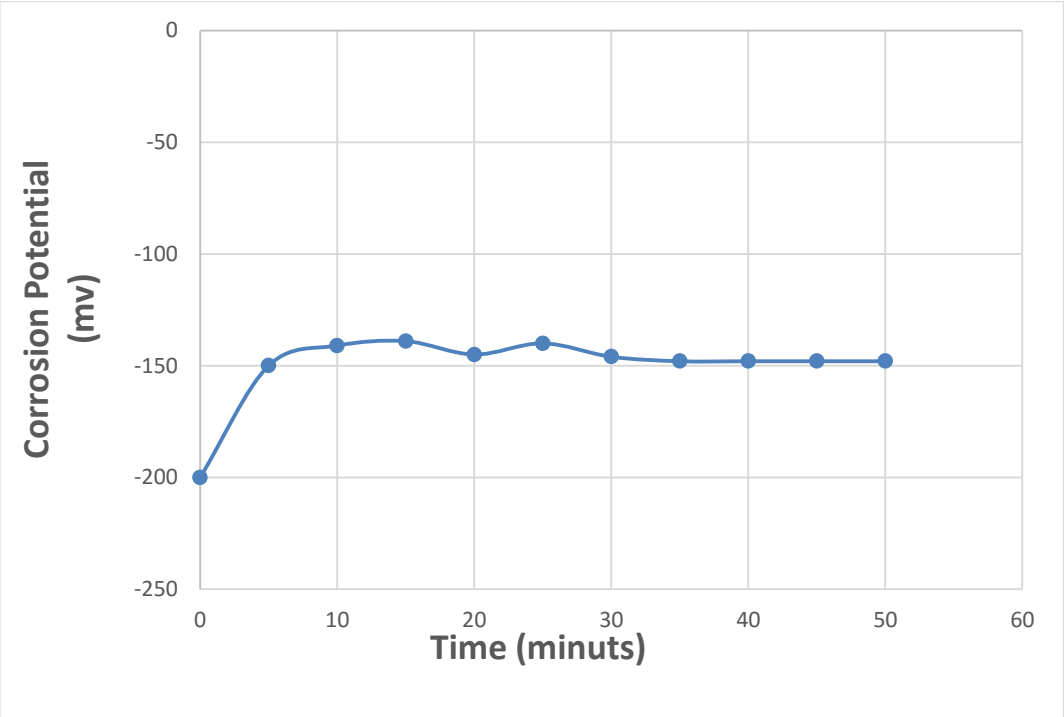

Figure (4.60): The corrosion potential Vs time for (Nb-1%Zr-6%Ge) Alloy for Saliva.

4.7.2 Potentiodynamic Polarization

The corrosion behavior of all alloys in Hank's solution and artificial saliva has been studied.

The corrosion parameters are corrosion current density ($i_{corr.}$), corrosion potential (Ecorr.) and corrosion rate (C.R.) resulted from corrosion test for spesimens in Hank's solution" and artificial saliva at 37±1 ºC were illustrated in table (4.5) and (4.6). It is obvious there is an increment in improvement percentage with increasing Ge content due to the formation of thin layer from metal oxide a round the surface.

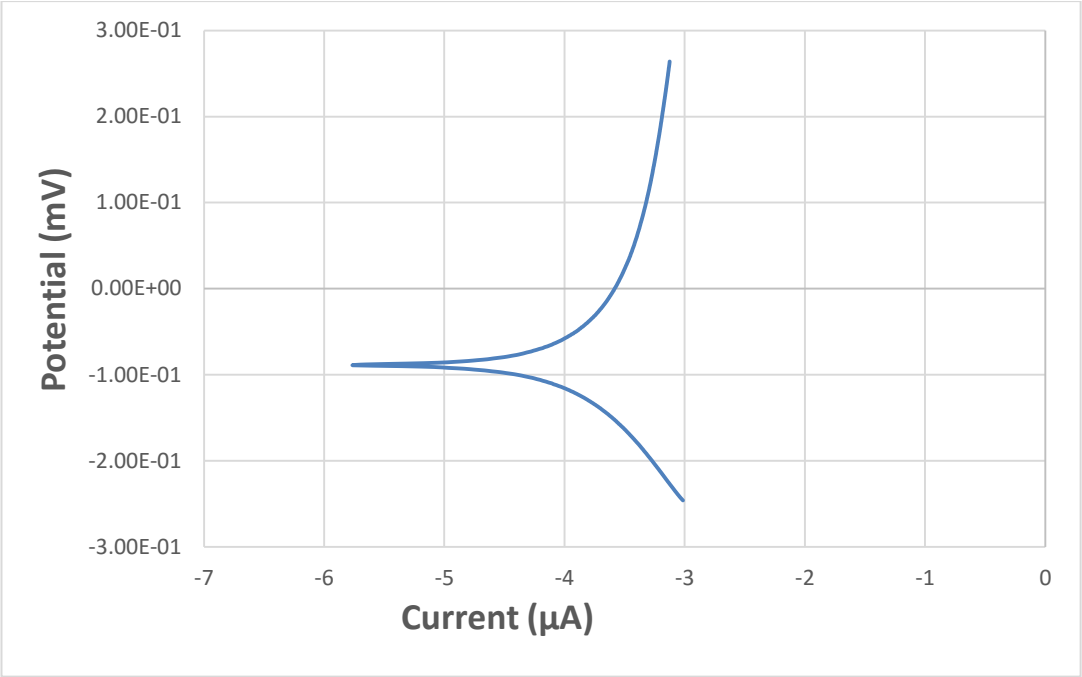

Figure (4.61): The Potential (mV) Vs Current (µA) for (Nb-1%Zr) Alloy for Artificial saliva.

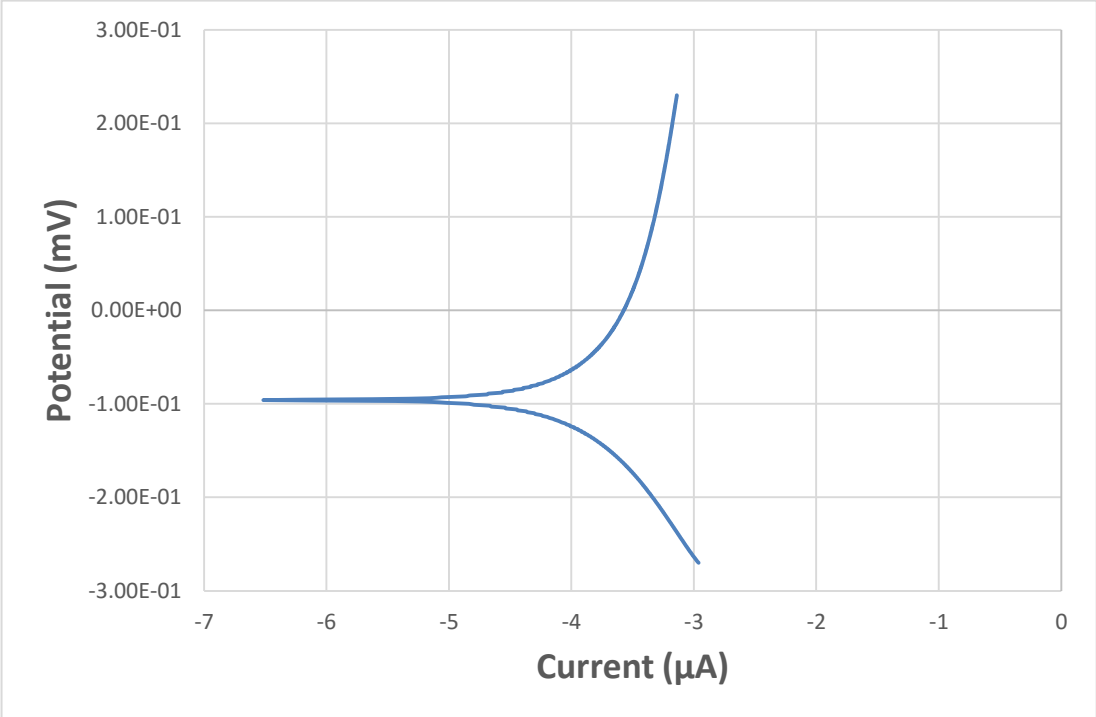

Figure (4.62): The corrosion potential Vs Current Density(µA) for (Nb-1%Zr-0.5%Ge) Alloy for Artificial saliva.

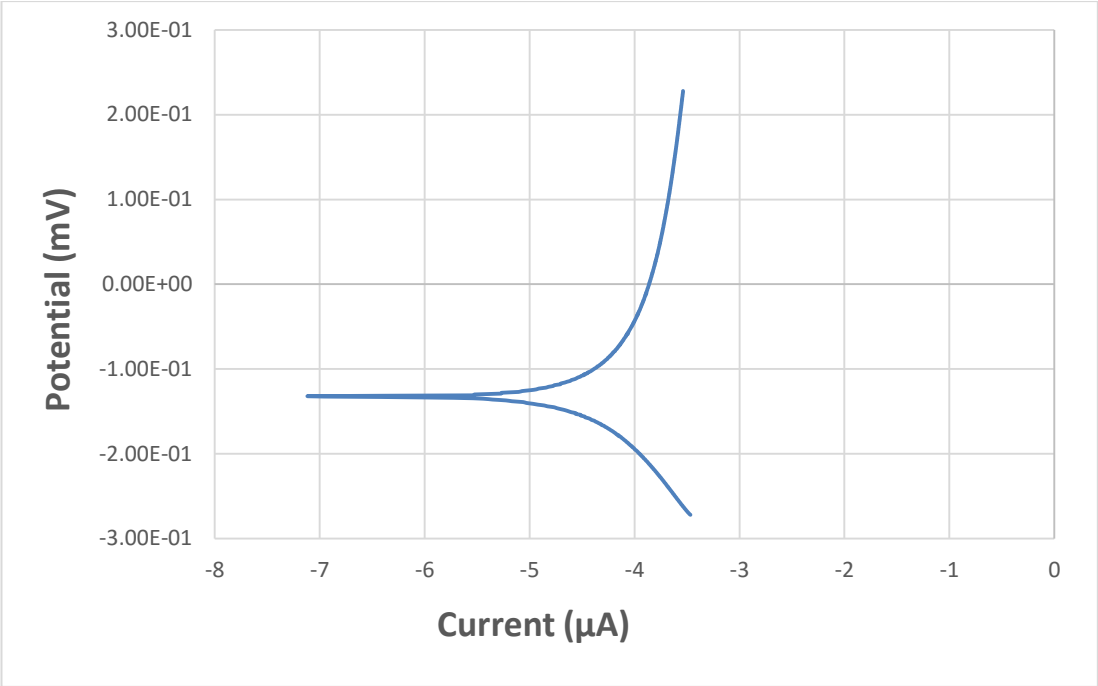

Figure (4.63): The corrosion potential Vs Current Density(µA) for (Nb-1%Zr-1%Ge) Alloy for Artificial saliva.

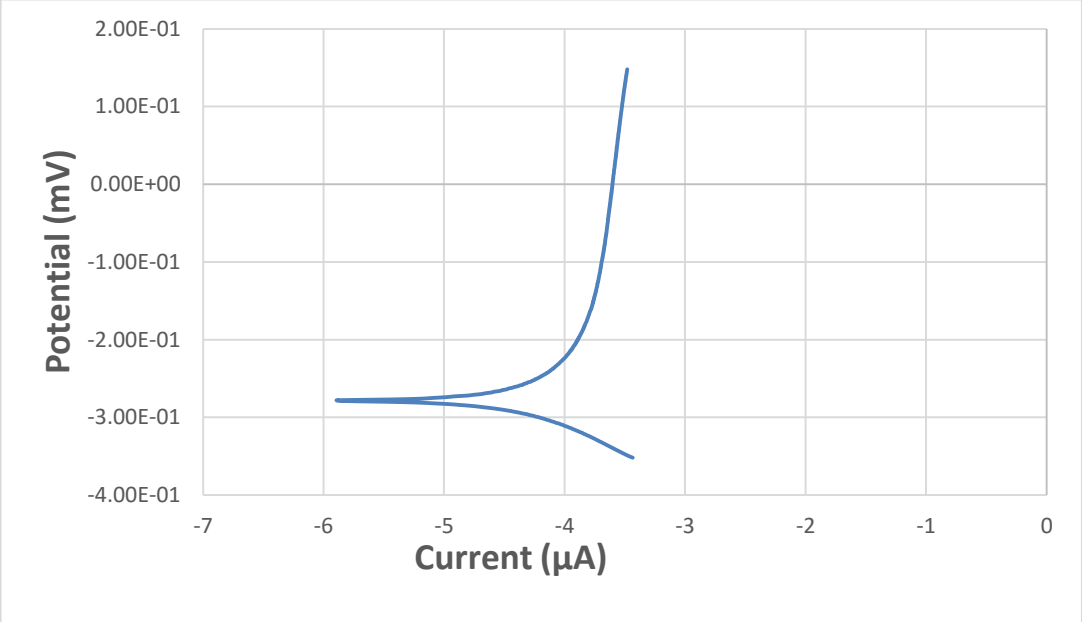

Figure (4.64): The corrosion potential Vs Current Density(µA) for (Nb-1%Zr-1.5%Ge) Alloy for Artificial saliva.

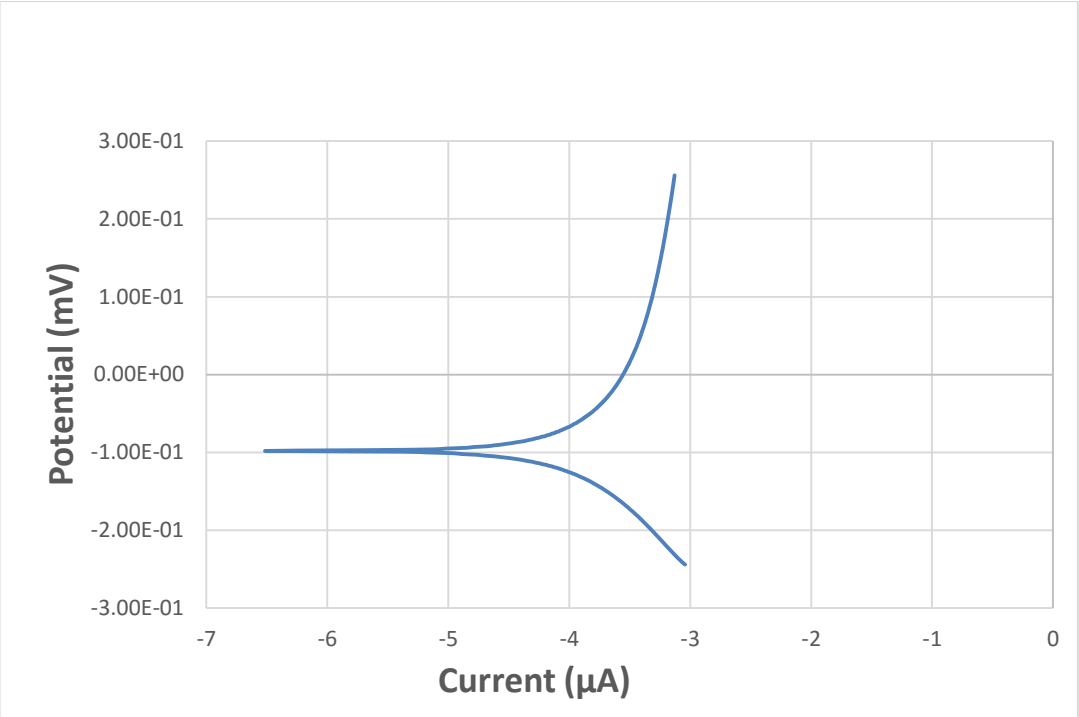

Figure (4.65): The corrosion potential Vs Current Density(µA) for (Nb-1%Zr-2%Ge) Alloy for Artificial saliva.

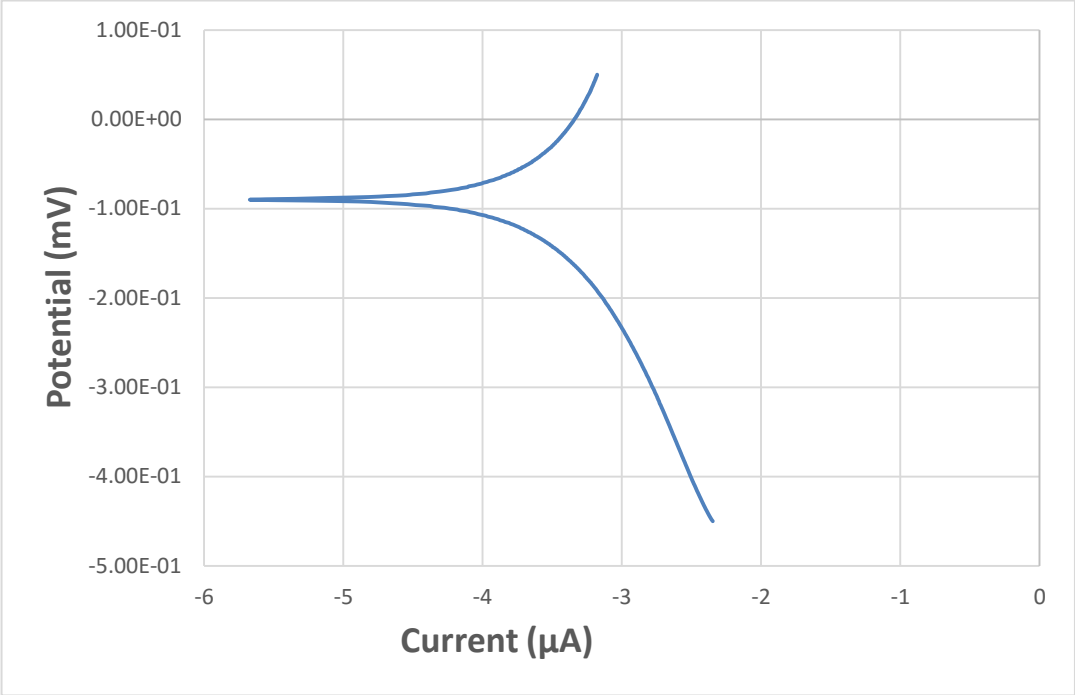

Figure (4.66): The corrosion potential Vs Current Density(µA) for (Nb-1%Zr-2.5%Ge) Alloy for Artificial saliva.

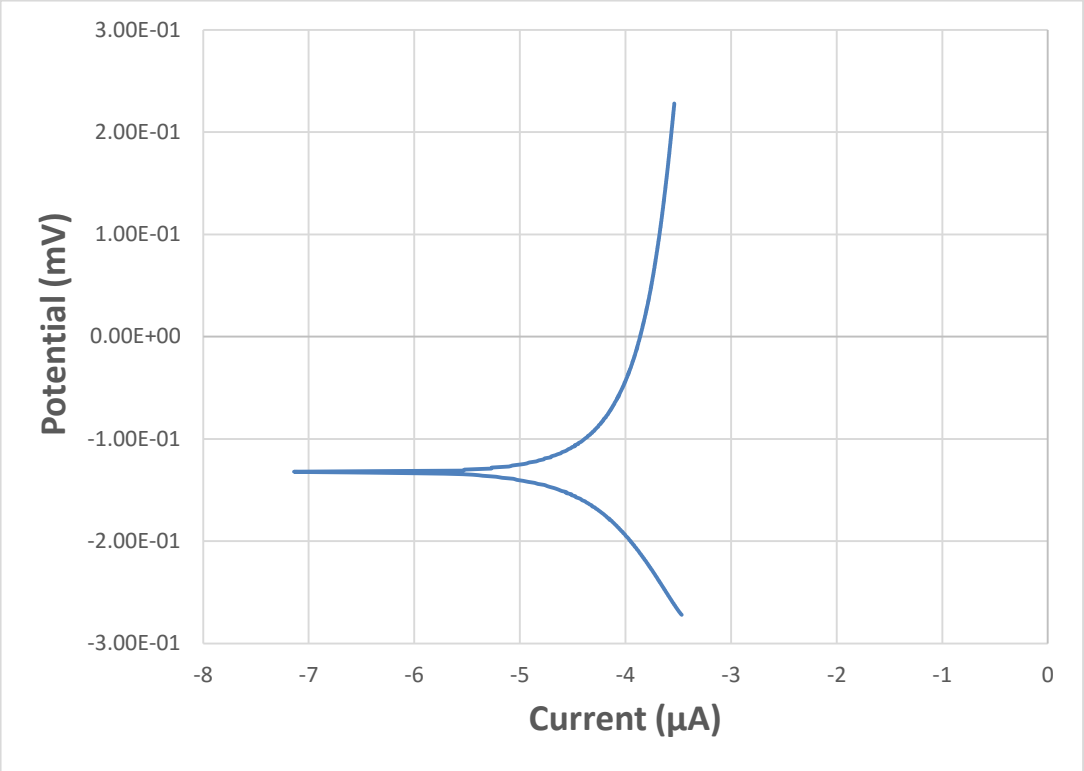

Figure (4.67): The corrosion potential Vs Current Density(µA) for (Nb-1%Zr-3%Ge) Alloy for Artificial saliva.

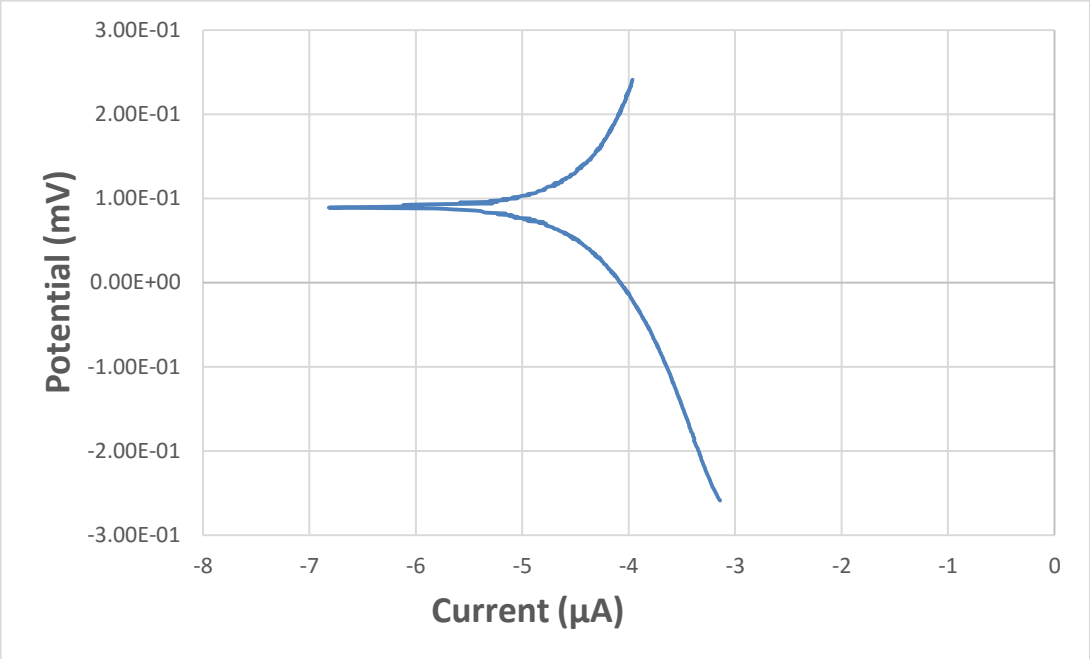

Figure (4.68): The corrosion potential Vs Current Density(µA) for (Nb-1%Zr-3.5%Ge) Alloy for Artificial saliva.

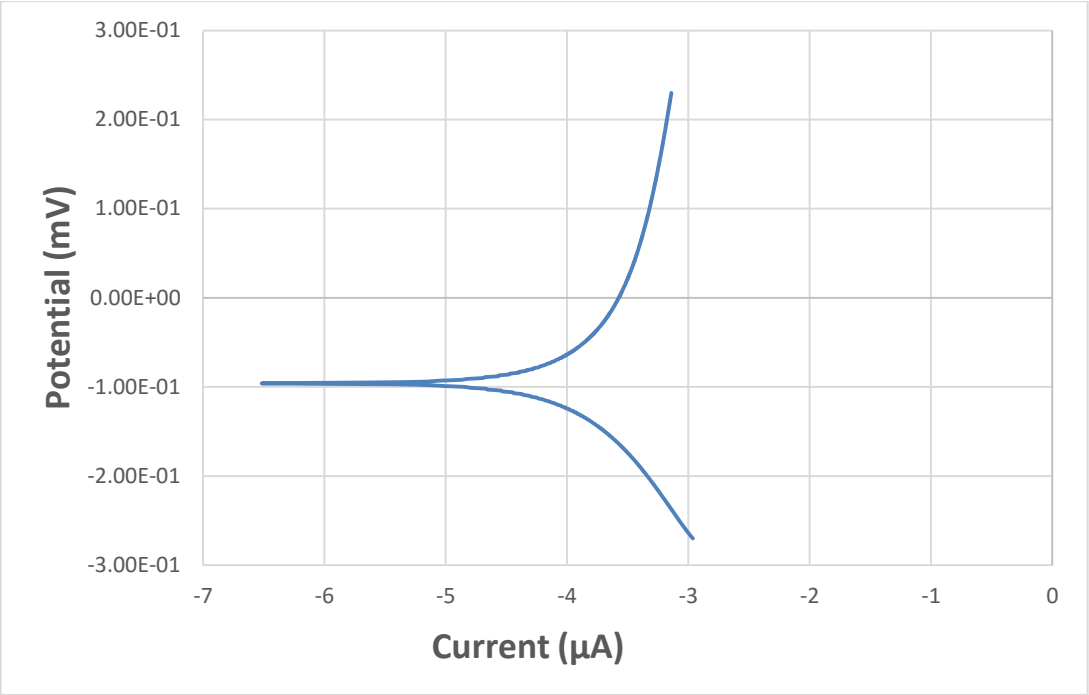

Figure (4.69): The corrosion potential Vs Current Density(µA) for (Nb-1%Zr-4%Ge) Alloy for Artificial saliva.

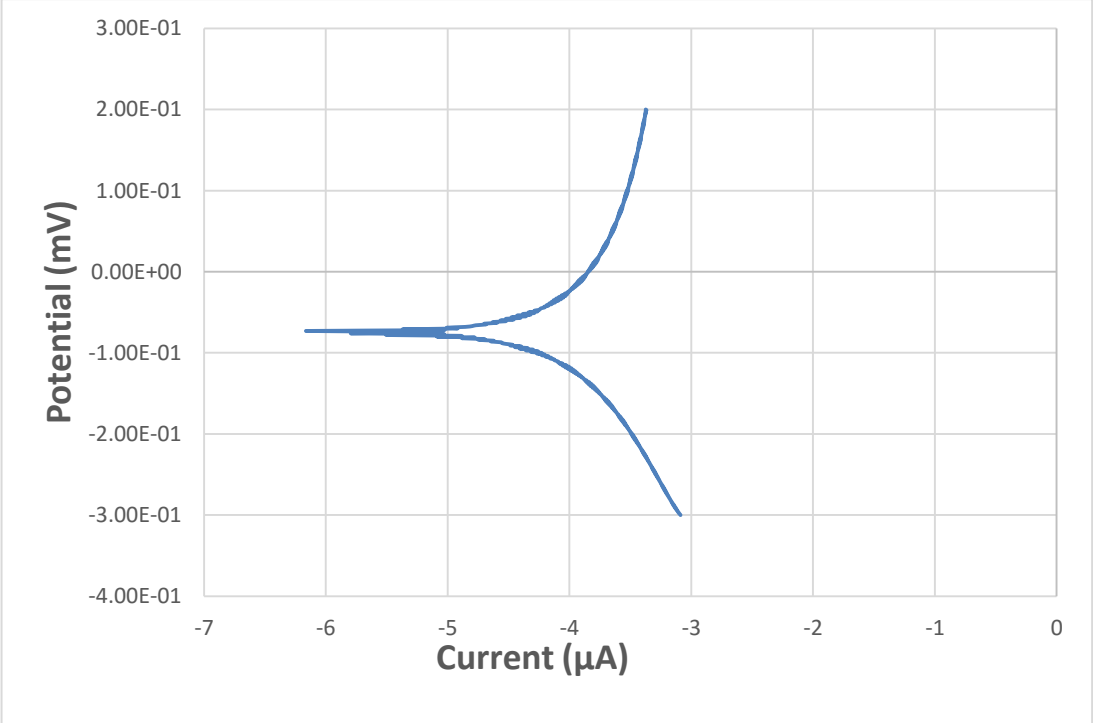

Figure (4.70): The corrosion potential Vs Current Density(µA) for (Nb-1%Zr-4.5%Ge) Alloy for Artificial saliva.

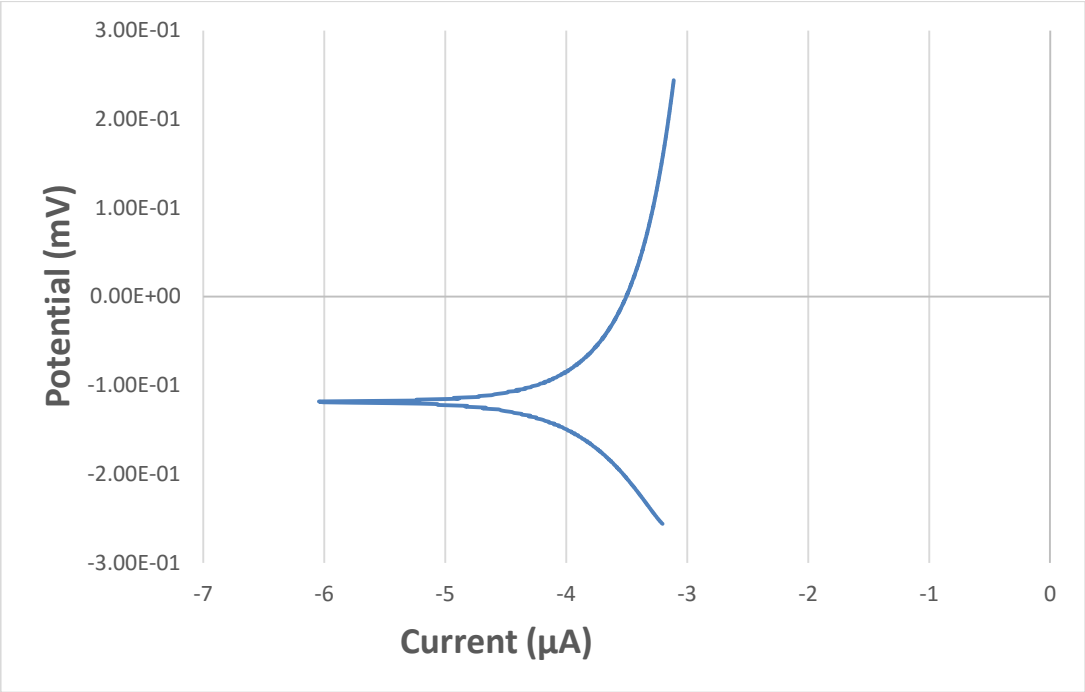

Figure (4.71): The corrosion potential Vs Current Density(µA) for (Nb-1%Zr-5%Ge) Alloy for Artificial saliva.

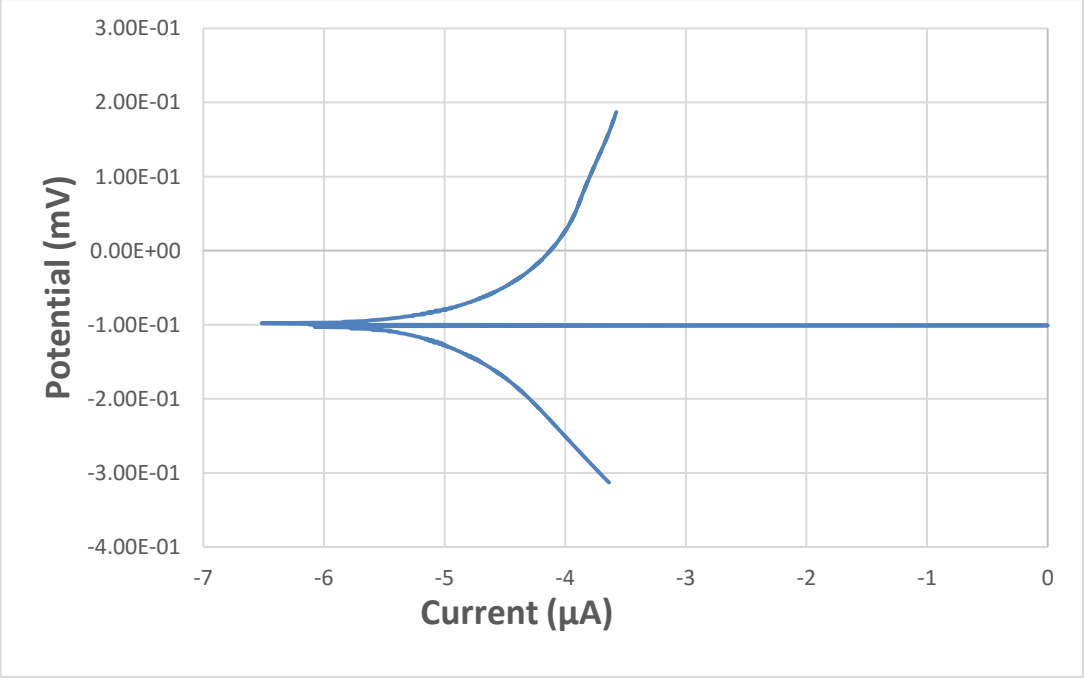

Figure (4.72): The corrosion potential Vs Current Density(µA) for (Nb-1%Zr-5.5%Ge) Alloy for Artificial saliva.

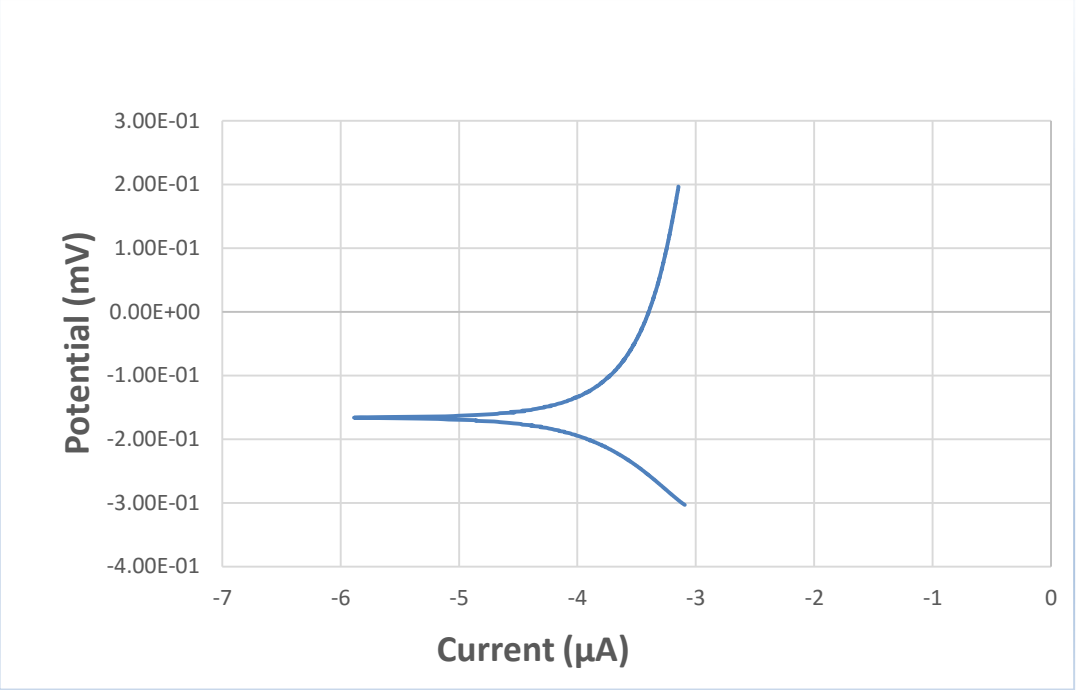

Figure (4.73): The corrosion potential Vs Current (µA) for (Nb-1%Zr-6%Ge) Alloy for Artificial saliva.

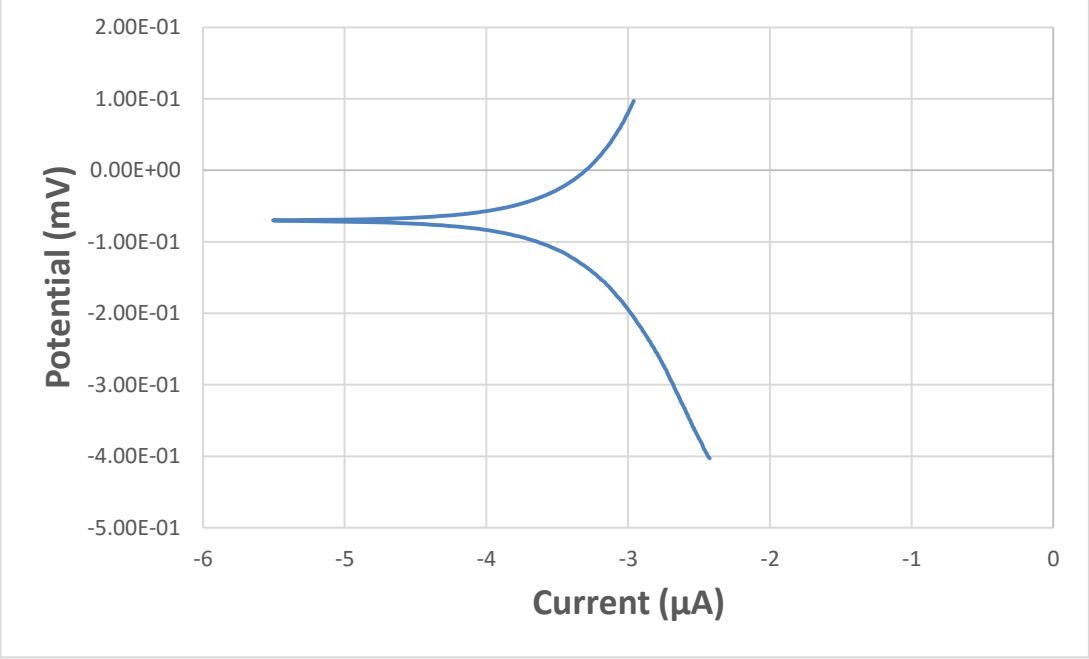

Figure (4.74): The corrosion potential Vs Current (µA) for (Nb-1%Zr) Alloy for Hank's solution.

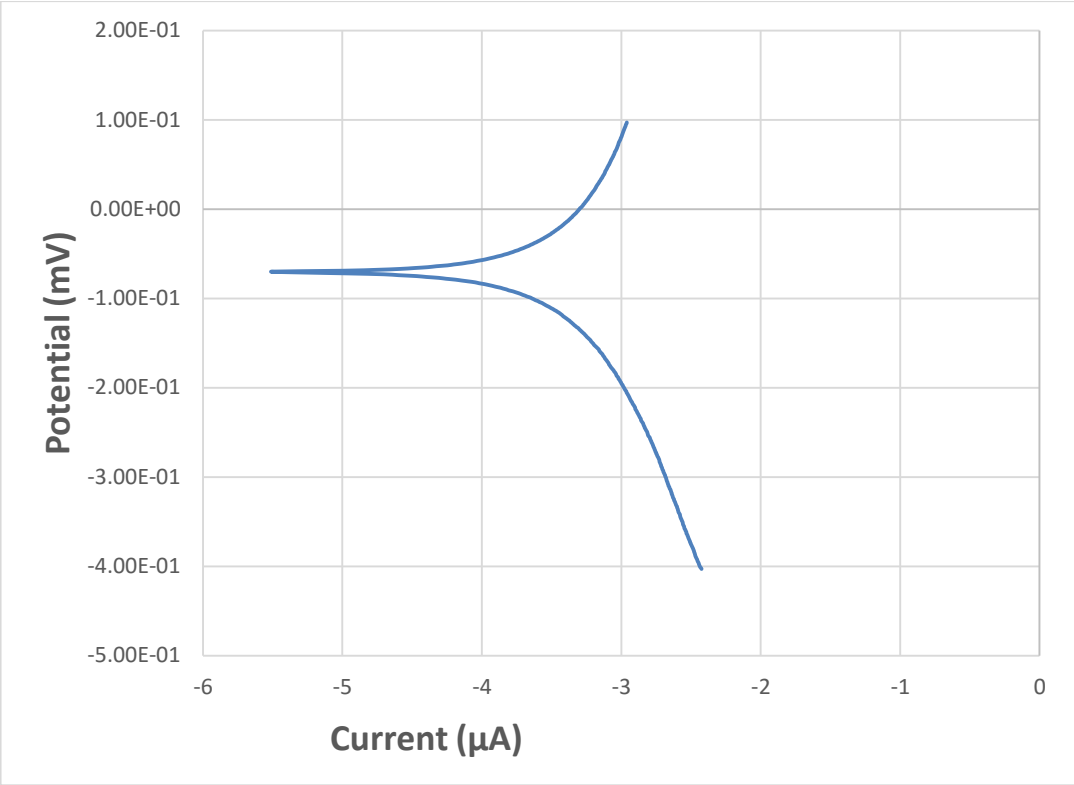

Figure (4.75): The corrosion potential Vs Current (µA) for (Nb-1%Zr-0.5%Ge) Alloy for Hank's solution.

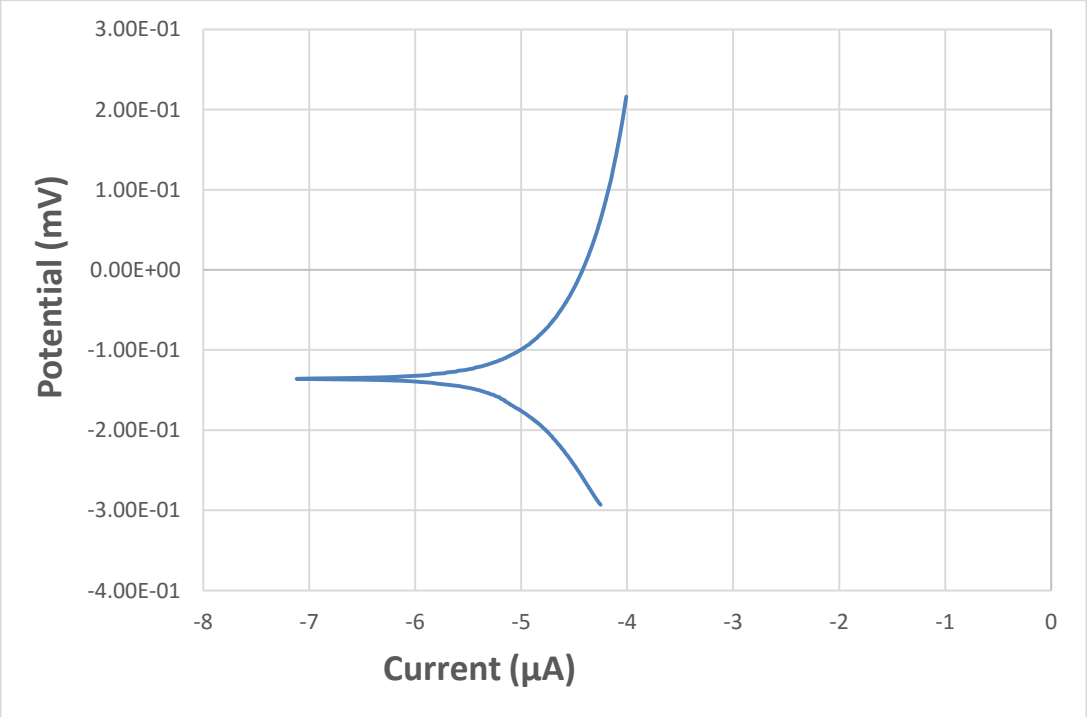

Figure (4.76): The corrosion potential Vs Current (µA) for (Nb-1%Zr-1%Ge) Alloy for Hank's solution.

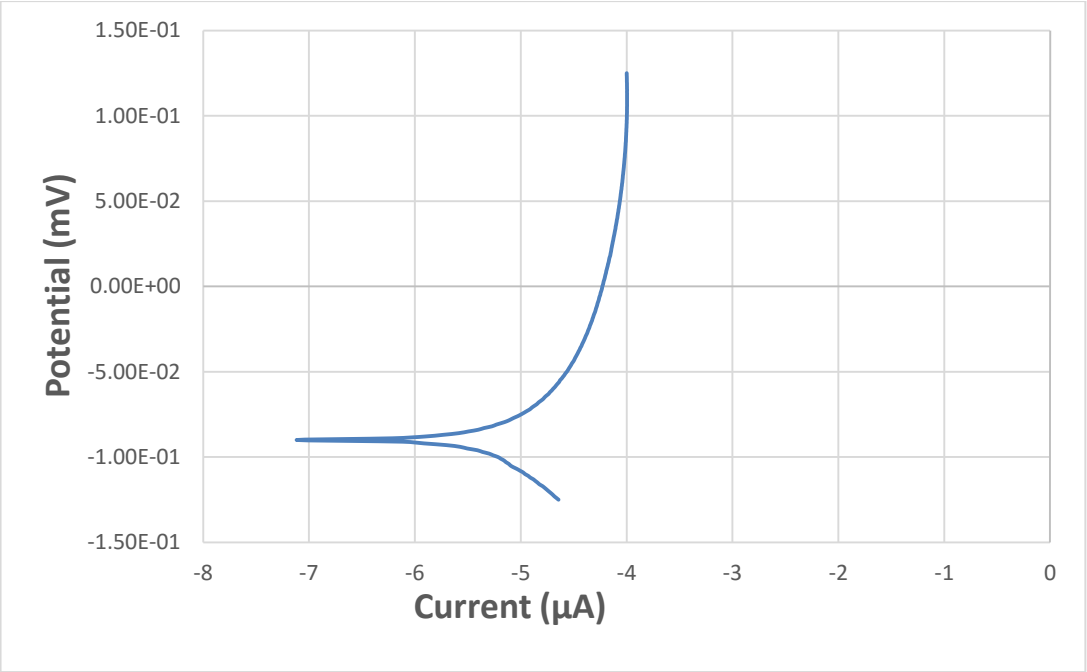

Figure (4.77): The corrosion potential Vs Current (µA) for (Nb-1%Zr-1.5%Ge) Alloy for Hank's solution.

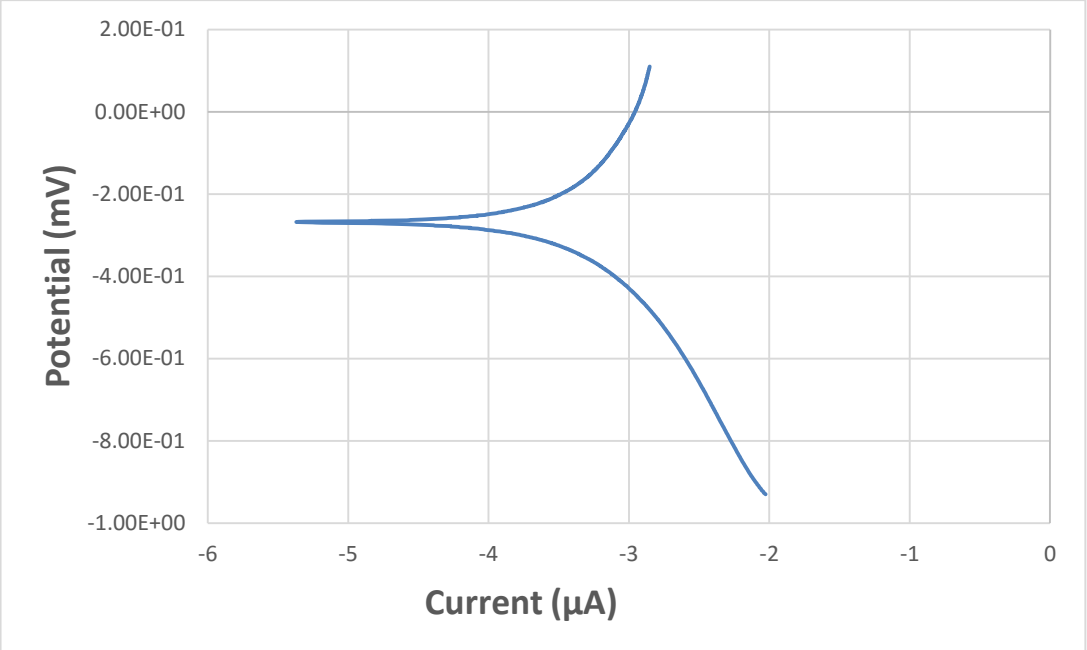

Figure (4.78): The corrosion potential Vs Current (µA) for (Nb-1%Zr-2%Ge) Alloy for Hank's solution.

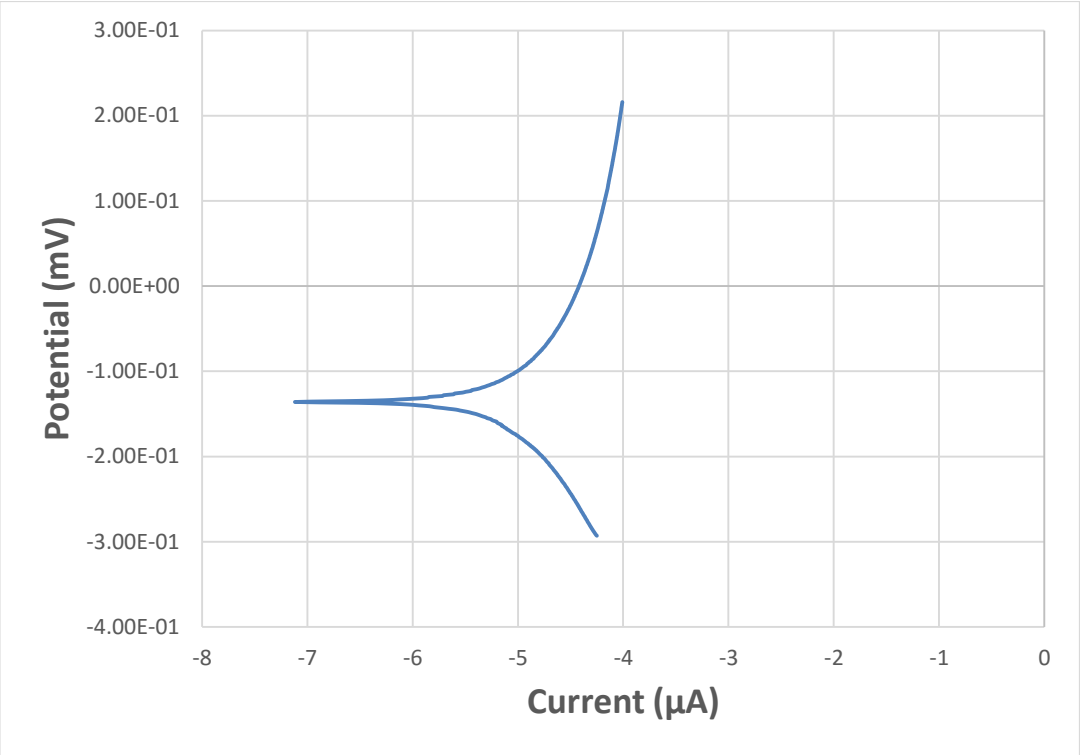

Figure (4.79): The corrosion potential Vs Current (µA) for (Nb-1%Zr-3%Ge) Alloy for Hank's solution.

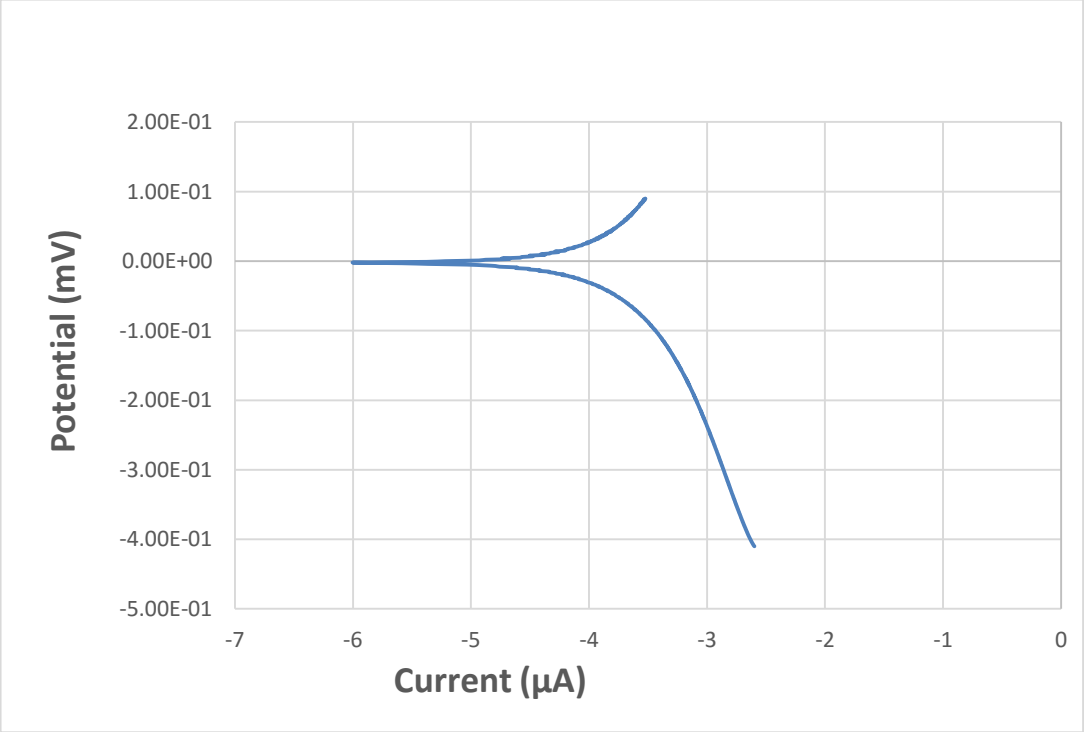

Figure (4.80): The corrosion potential Vs Current (µA) for (Nb-1%Zr-3.5%Ge) Alloy for Hank's solution.

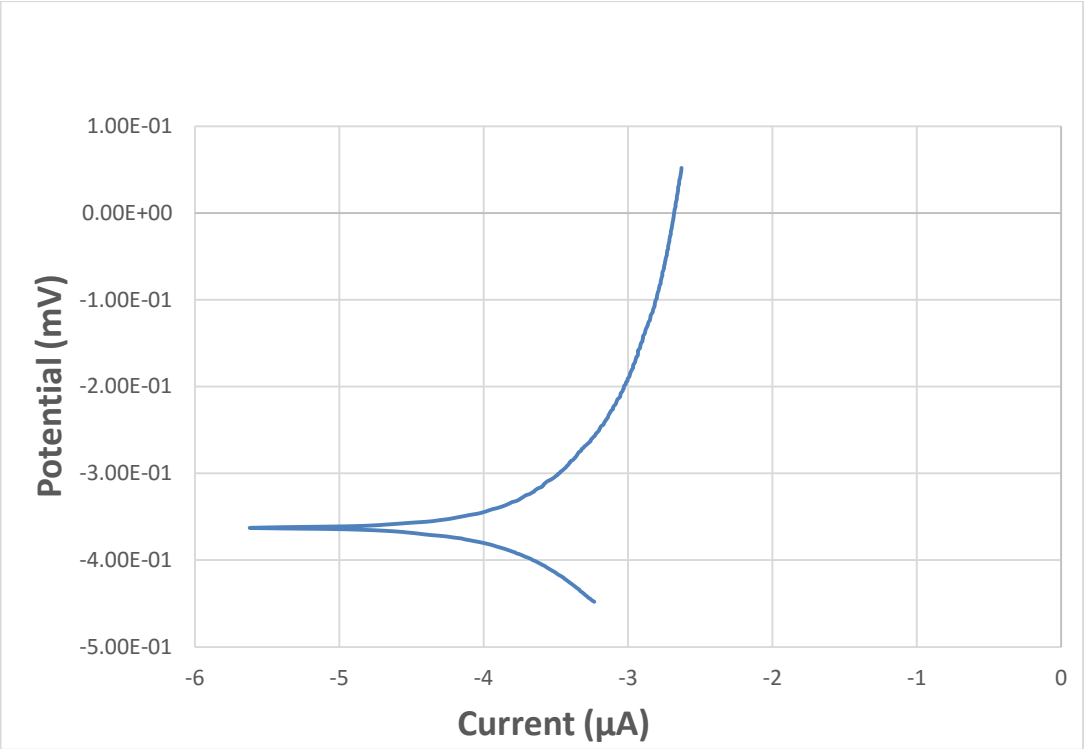

Figure (4.81): The corrosion potential Vs Current (µA) for (Nb-1%Zr-4%Ge) Alloy for Hank's solution.

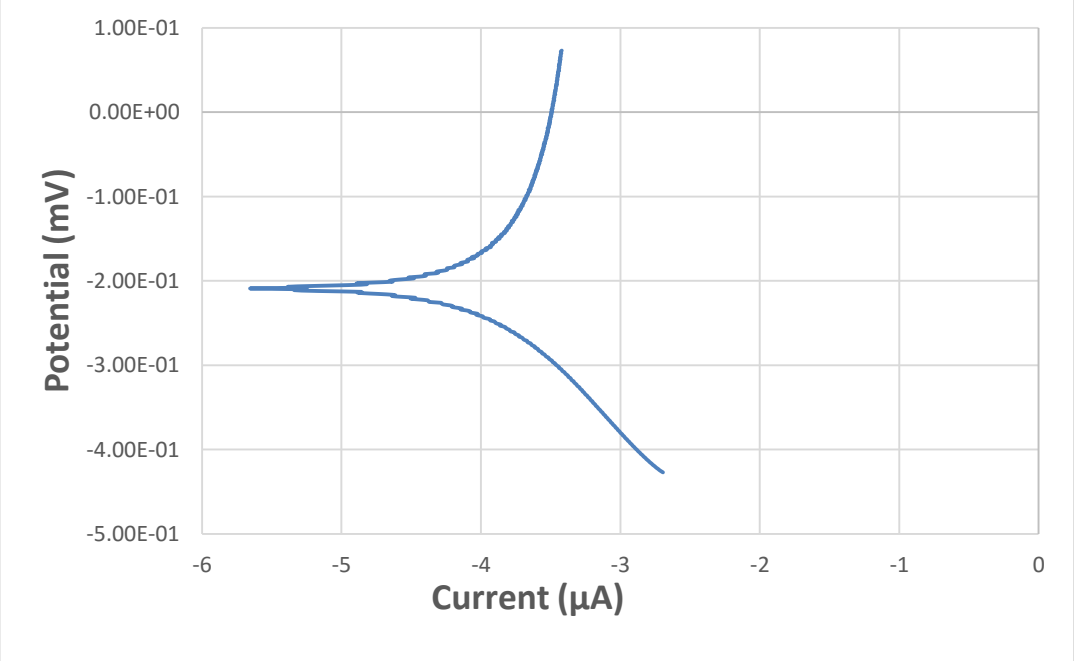

Figure (4.82): The corrosion potential Vs Current (µA) for (Nb-1%Zr-4.5%Ge) Alloy for Hank's solution.

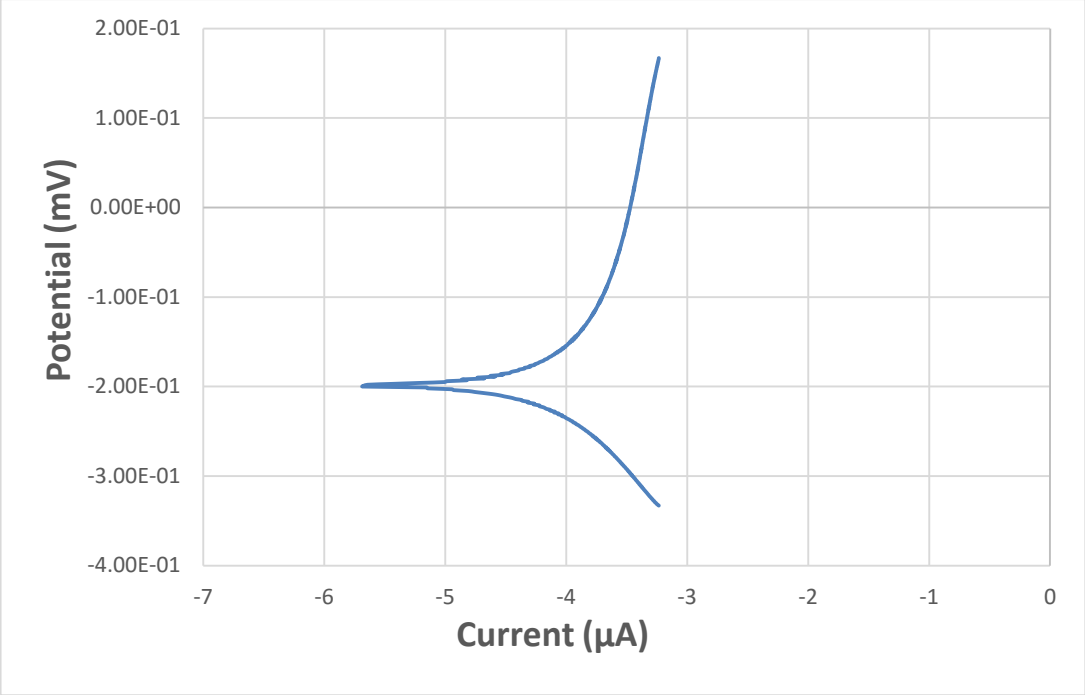

Figure (4.83): The corrosion potential Vs Current (µA) for (Nb-1%Zr-5%Ge) Alloy for Hank's solution.

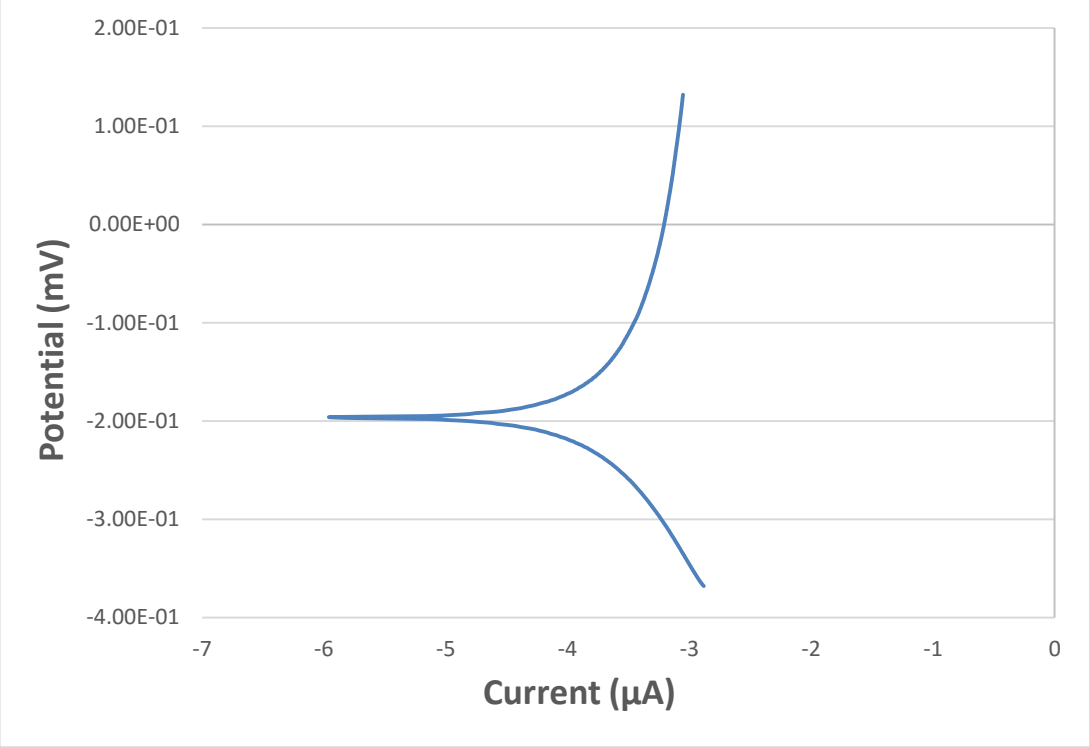

Figure (4.84): The corrosion potential Vs Current (µA) for (Nb-1%Zr-5.5%Ge) Alloy for Hank's solution.

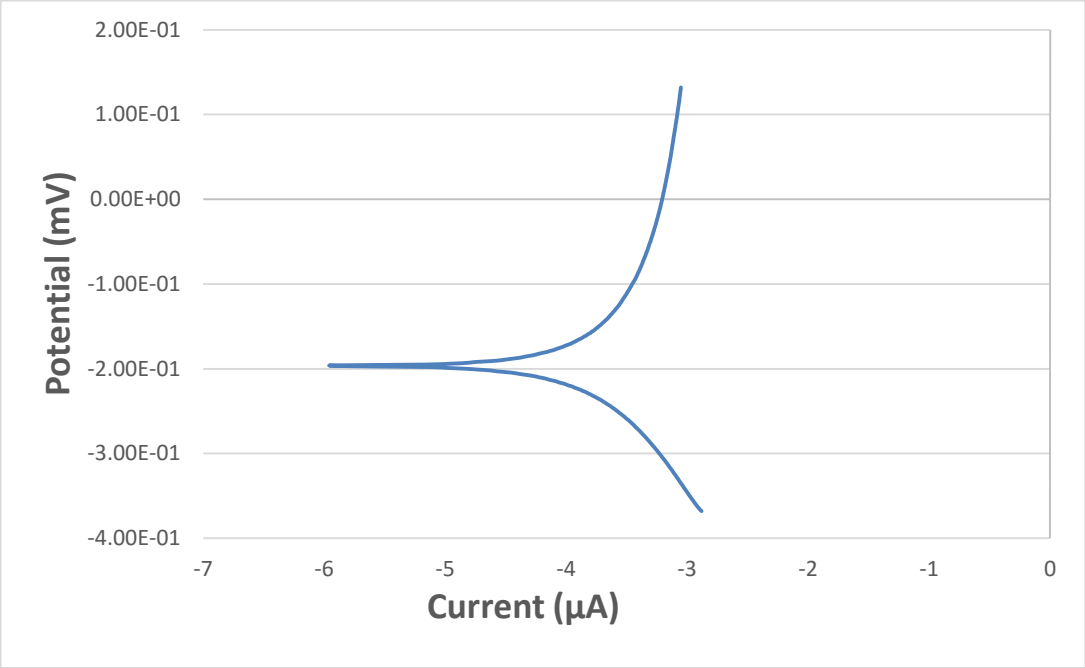

Figure (4.85): The corrosion potential Vs Current (µA) for (Nb-1%Zr-6%Ge) Alloy for Hank's solution.

Table (4.9): The Corrosion Current ($i_{corr.}$), Corrosion Potential ($E_{corr.}$) and Corrosion Rate (C.R.) for All Alloys in Hank's Solution at 37±1º.

Ge%	Ecorr (mV)	Icorr (µA)	C.R.mpy	Improvement percentage %
0	-47	8.619	0.1411	/
0.5	-58	7.8	0.1057	25.03
1	-136	6.921	0.0964	31.65
1.5	-197	5.11	0.0636	54.86
2	-50	4.575	0.0712	49.51
2.5	-102	2.54	0.0317	77.49
3	-54	2.046	0.0256	81.81
3.5	-70	1.92	0.0252	82.13
4	-132	1.54	0.0251	82.14
4.5	-90	1.436	0.0164	88.37
5	-363	1.419	0.0133	90.55
5.5	-268	1.329	0.0162	88.47
6	-196	1.101	0.0132	90.57

Table (4.10): The Corrosion Current ($I_{corr.}$), Corrosion Potential ($E_{corr.}$) and Corrosion Rate (C.R.) for All Alloys in Artificial Saliva at 37±1º

Alloy	Ecorr (mV)	Icorr. (µA)	C.R.mpy	Improvement percentage %
1	-89	87.0	0.14245	/
2	-96	84.7	0.1055	25.93
3	-118	78.9	0.10511	26.21
4	-278	61.77	0.086	39.62
5	-95	5.772	0.08988	36.90
6	-73	53.09	0.06637	53.40
7	-88	41.23	0.05171	63.69
8	-34	32.18	0.04225	70.34
9	-38	24.57	0.0402	71.77
10	-57	23.27	0.0265	81.39
11	-89	19.84	0.0186	86.94
12	-97	12.82	0.01568	88.99
13	-101	10.7	0.0129	90.94

From Table (4.9), it can be noted that there is a significant improvements in corrosion resistance of the alloys with different additives of Ge (0.5-6) wt%, $i_{corr.}$ for specimens is ranged from (8.619 µA) for (Nb-1%Zr) alloy to (1.101µA) for (Nb-1%Zr-6%Ge) alloy which are lower than i_{corr}. for B alloys. The $E_{corr.}$ is ranged from (-47 mV) for (Nb-1%Zr) alloy to (-196mV) for ((Nb-1%Zr-6%Ge) alloy which are lower than E_{corr}. For B alloy.

Also from Table (4.10), it can be noted that there is a significant improvement in corrosion resistance of the alloys with different addition of Germanium.

From Table (4.10), it can be noted that there is an improvement in corrosion resistance of (Nb-1%Zr) alloy with different additives of Ge (0.5-6) wt.% in artificial saliva , $i_{corr.}$ for (Nb-1%Zr) alloys is graded from (8.7 µA) for B alloy to (1.07µA) for ((Nb-1%Zr-6%Ge) alloy which are lower than i_{corr} and $E_{corr.}$ for (Nb-1%Zr) alloys is graded from (-98 mV) for (Nb-1%Zr) alloy to (-34mV) for ((Nb-1%Zr-3.5%Ge) alloy

which are higher than E_{corr} ,thus ((Nb-1%Zr-3.5%Ge) alloys are more noble than ((Nb-1%Zr) alloy.

From Tables (4.9) & (4.10) it can be seen that the values of corrosion current density and corrosion rate in Hank's solution are higher than in artificial saliva, which indicates that the Hank's solution is more aggressive than the artificial saliva.

Tables (4.9) and (4.10) show improvement in corrosion resistance of (Nb-1%Zr) alloy with different additives of Ge in two corrode solutions as compared with (Nb-1%Zr) alloy. So corrosion rate decreases with increasing Ge content as shown in table (4.9) and (4.10), where the maximum improvement percentage was (90.57% & 90.94%) for 6% Germanium in Hank solution and synthetic Sliva respectively.

The corrosion resistance increases as the Ge content increase, this can be attributed to the collective effect of Ge, such as passivity, oxide film, and sold solution which will lead to a protection corrosion in the surface layer.

From the figures **[(**4.61)-(4.85)], the addition of Germanium leads to an increase in the corrosion resistance of the alloys. The points of curves approach to the positive direction and stabilized at the end due to the formation of thin layer from the metal oxide. There is a significant increase in the improvement percentage of corrosion resistance.

4.7.3 Ion release:

It was found through the test that there is no ion release dected for Nb,Ge in all specimens rested , and there were released ions for of the element (zirconium**)** decreases with increasing in the percentage of germanium addition which indicate to increasing corrosion resistance of all Ge addition, and that agree with the polarization test results, where

the least zerconium ion release is for (6% Ge alloy) which has the best corrosion resistance improvement (90.57%).

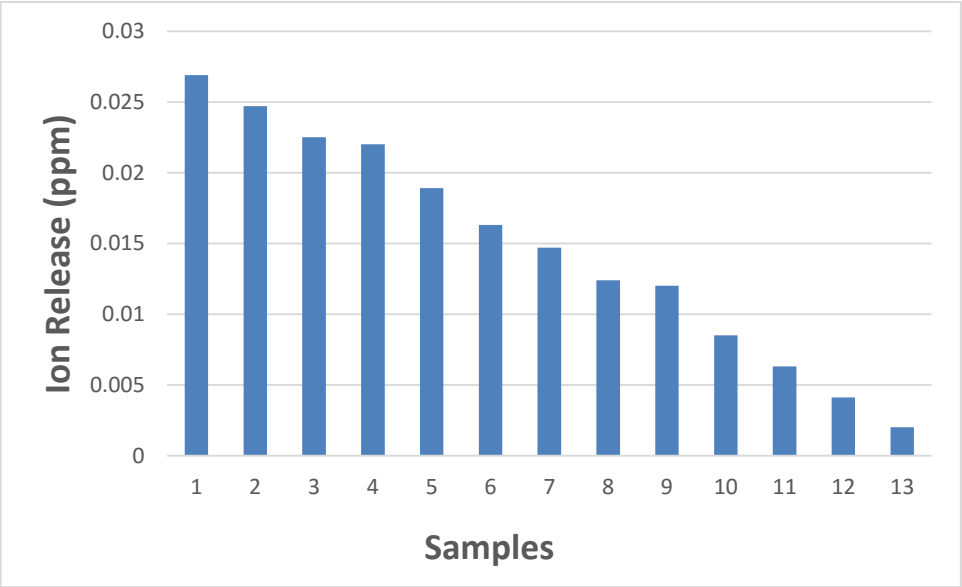

Figure (4.86): Quantity of metal (Zr) ion release in artificial saliva and hank for 30 days at 37°C.

4.8 Scanning Electron Microscope (SEM)

SEM images of etched alloys showed cracks and pores in different sizes. Figures (4.87), (4.88), & (4.89) show the effects of (Open circuit potential (OCP) and polarizayion) on the surface of alloys (Nb-1%Zr, Nb-1%Zr-3Ge, & Nb-1%Zr-6%Ge) respectively with different magnification.

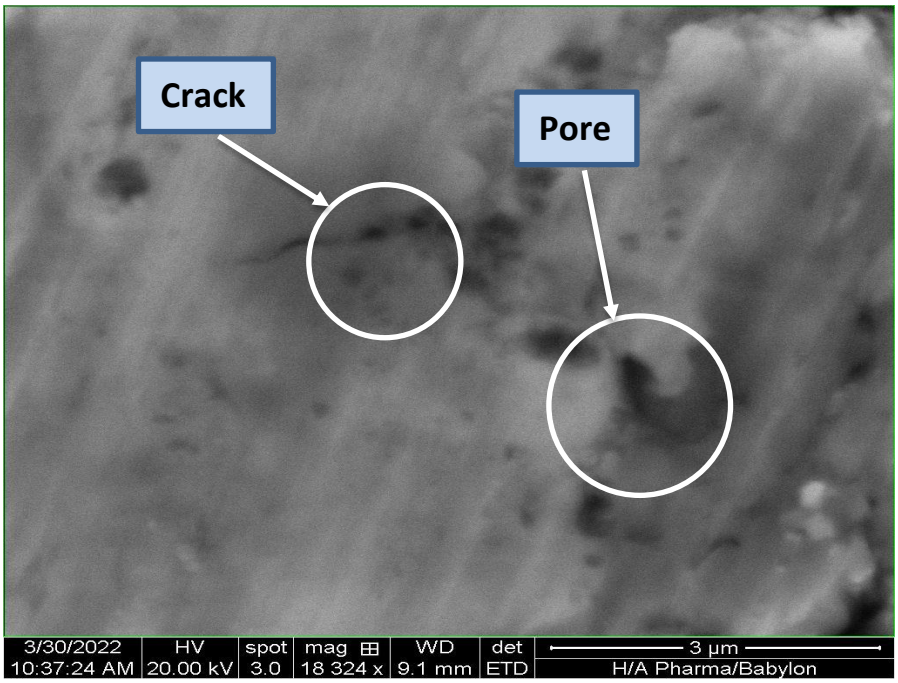

Figure (4.87):. SEM image for (Nb-1%Zr) Alloy.

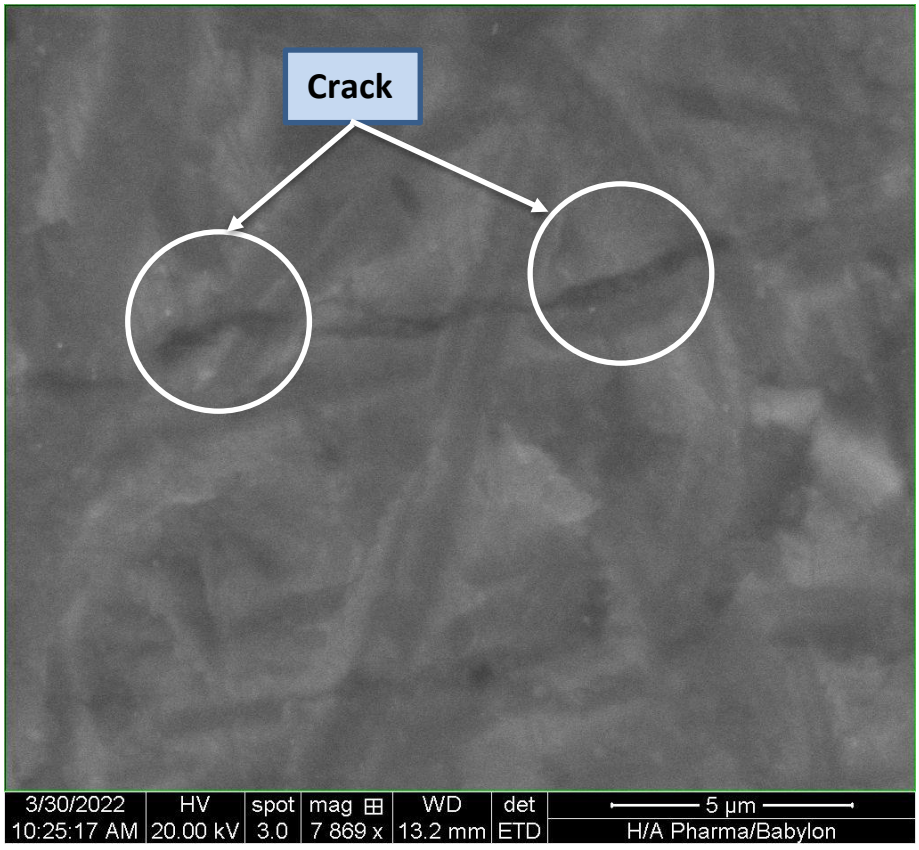

Figure (4.88):. SEM image for (Nb-1%Zr-3%Ge) Alloy

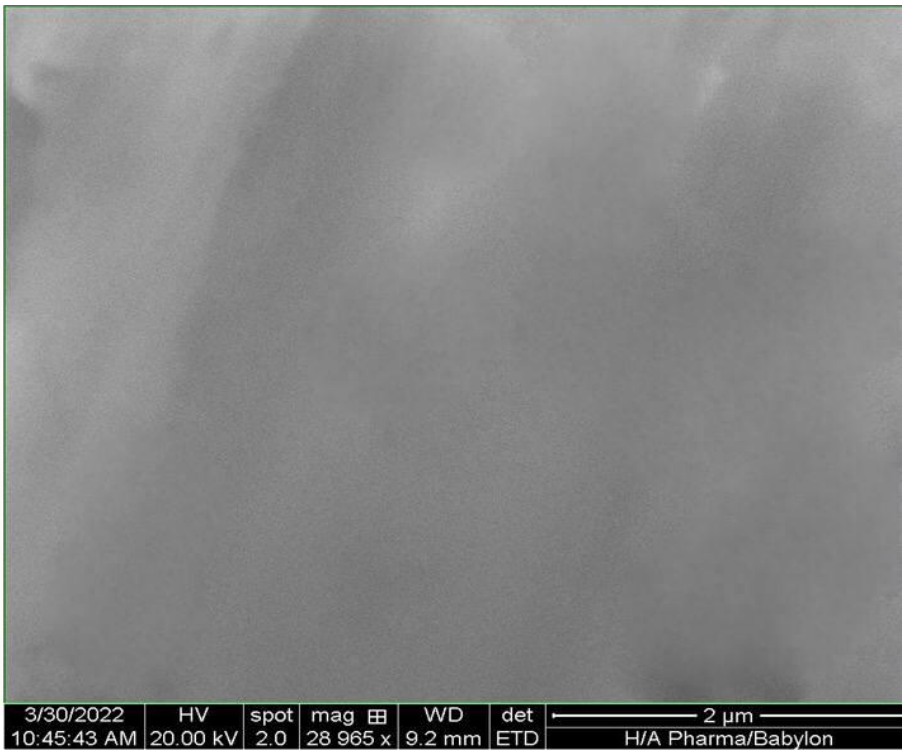

Figure (4.89):. SEM image for (Nb-1%Zr-6%Ge) Alloy

4.9 Biological tests

4.9.1 Antibacterial

Figure (4.90) represents results of the antibacterial test of control specimens. Firstly, the specimens washed with a solution of 1ml normal saline for five minutes, afterthen, adding Neutrient Agar to 0.5ml from the result solution in clean plate. After solidification of the medium, the plates were placed in the icubater for 24 hours. Finally, the plates taken out from the incubator and the results were recorded, the spesimens have no bacteria.

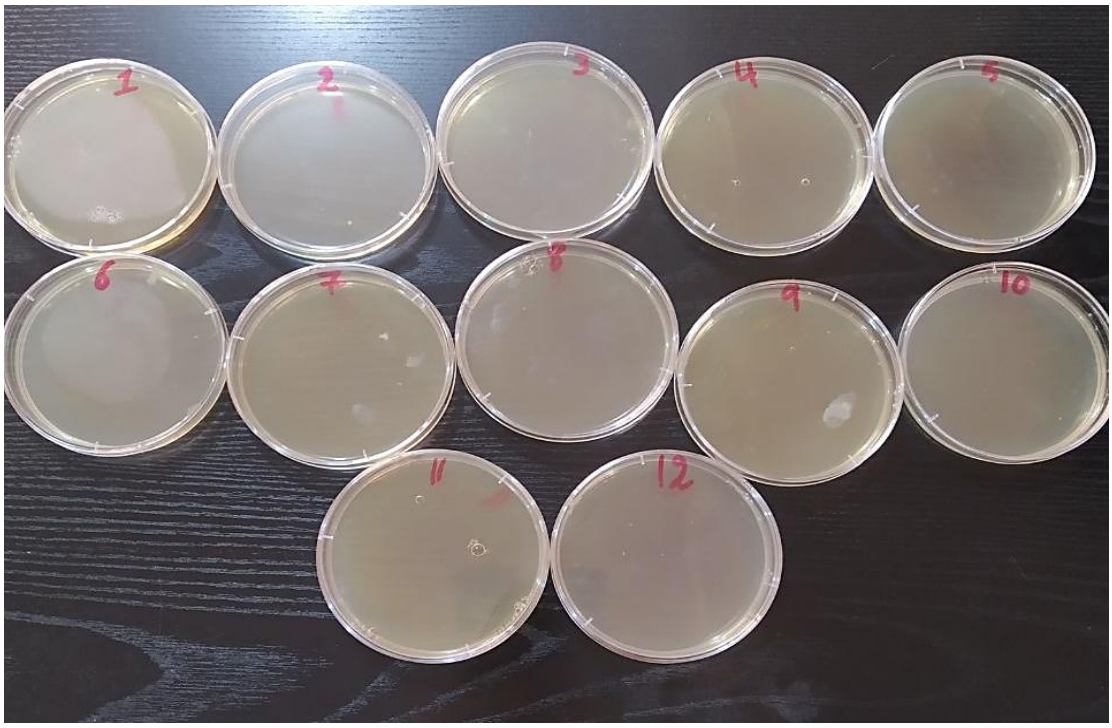

Figure (4.90): Results of the antibacterial test.

4.9.2 MTT Test :

This test calculates the percentage of cell viability of base Neobium alloy and that of Germanium addition. The base alloy (Nb-1%Zr) (control) had the viability percentage of cell as 100%. Germanium addition with (0.5, 3, & 6) wt.% was examided. The cell viability of the tested alloys are (87.1, 90.87, & 100)% respectively as shown in figure (4.91).

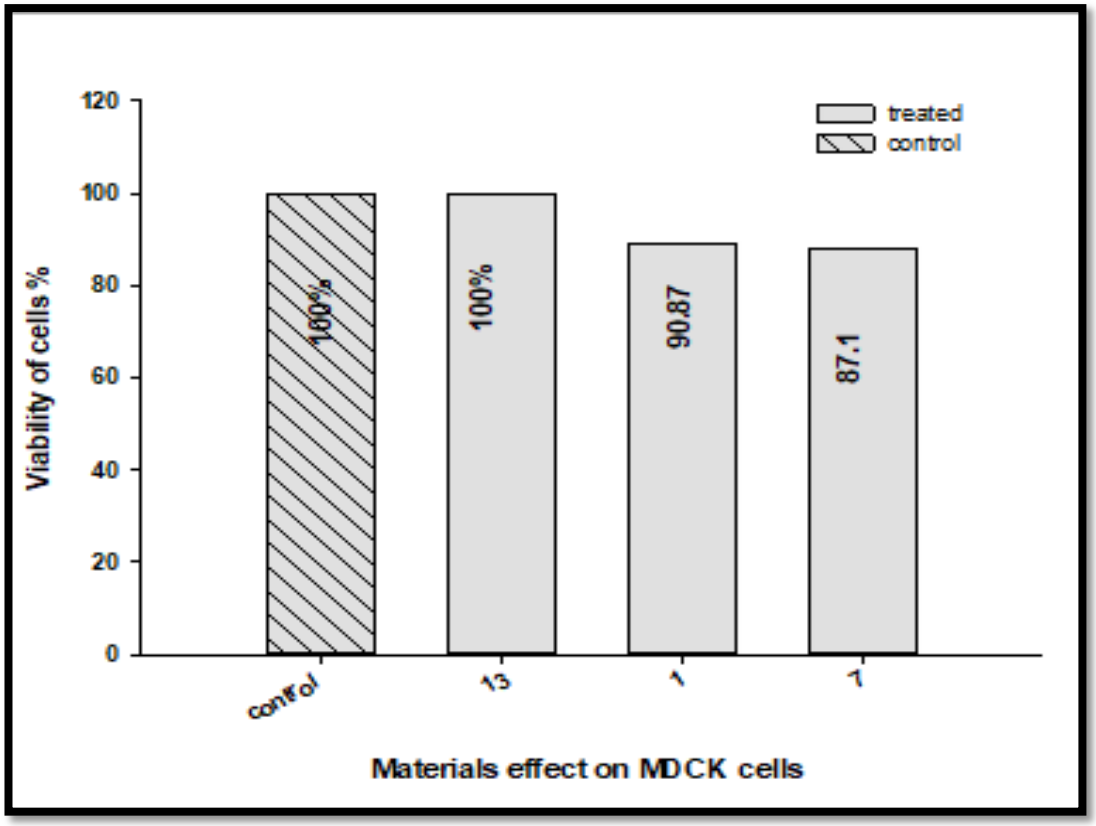

Figure (4.91): The effect of (Nb-1%Zr-xGe)of different conditions on MDCK cell line (after incubation for 24 hours) versus control group.

The appearance of cells after 24 hours as incubation time are shown in Figures (4.92). By comparing the appearance of cells for control with (Nb-1%Zr-xGe) large number of cells still alive under microscope.

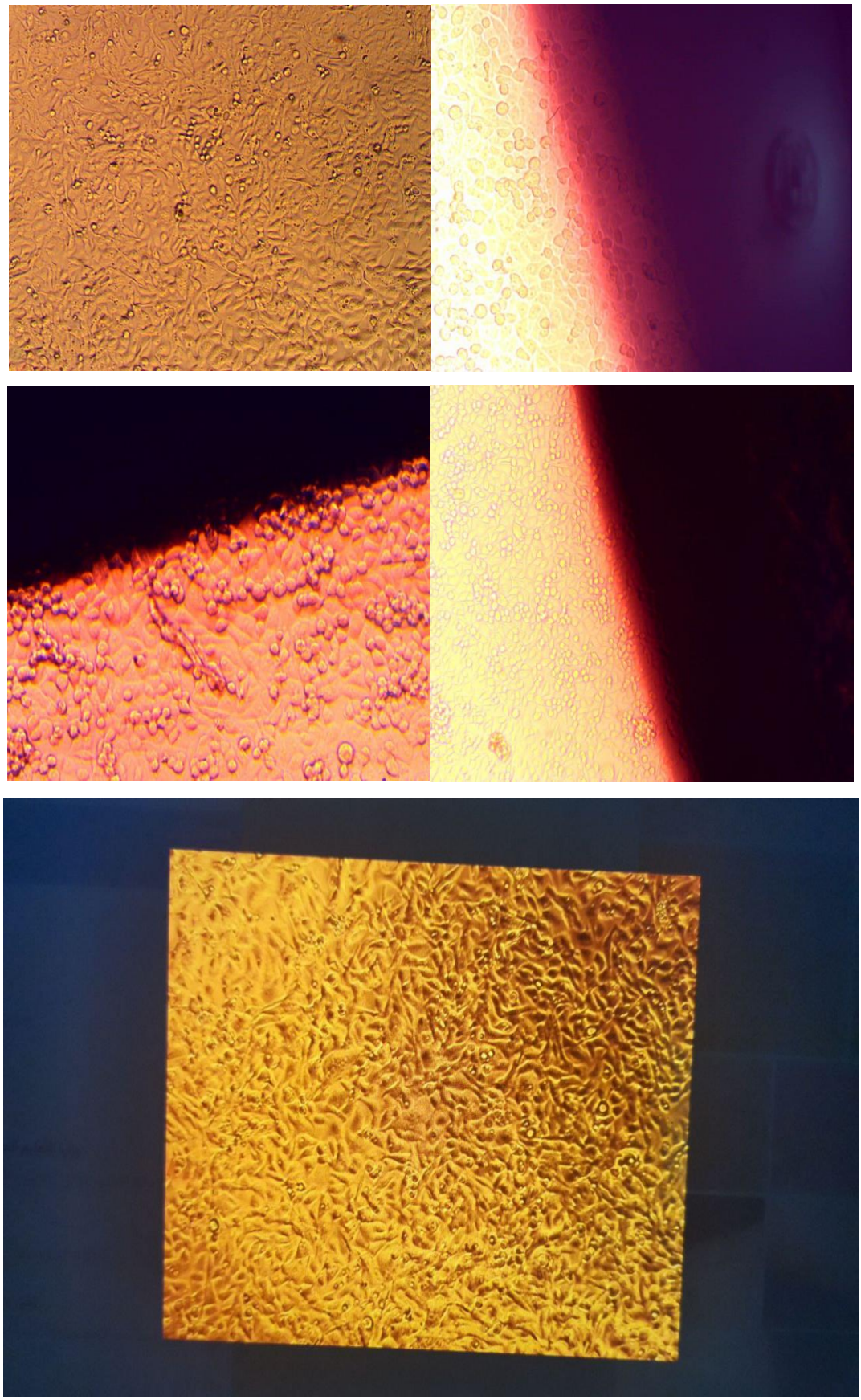

Figure (4.92): The appearance of MDCK cells after 24 hours of incubation.

4.9.3 Simulated body fluid:

The formation of (hydroxyapatite)[$(Ca_{10}(Po_4)_6(oH)_2$]is observed. (HAP), which represents the bone material in the body and is considered an examination in place to prove the connection and bone structure between the layer of paint and metal with the components of the body.

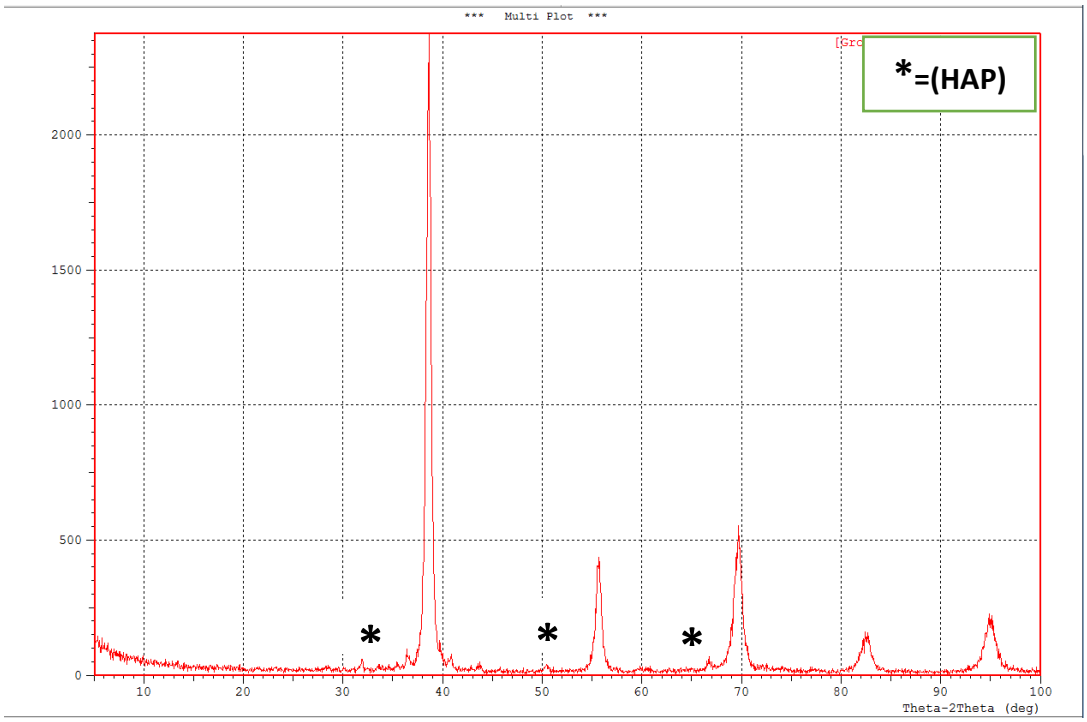

Figure (4.93): XRD Patterns for Alloy (Nb-1%Zr-6%Ge) After Simulated body fluid.

Chapter Five…Conclusion and Recomendation

5.1 Conclusions

Based on the obtained results, the following conclusions are made:

1. The sintering at 1200°C for 5hr of samples (with and without additives) is able to complete the transformation process of Nb, Zr, and Ge to alloy structure.

2. At room temperature, solid solution structure appears in all alloys with the addition of germanium.

3. The addition of Ge with (0.5 – 6) wt. % to Nb-1%Zr alloy decreases the porosity compared to base alloy without Ge.

4. The alloys with Ge additives (0.5 – 6) wt. % have hardness values higher than that for Nb-1%Zr alloy without Ge additives.

5. The addition of Ge with (0.5 – 6) wt. % to Nb-1%Zr alloy increases the wear resistance of these alloys and the wear rate decreases as Ge content increase.

6. The addition of Ge with (0.5-6)wt.% to Nb-1%Zr alloy increases the corrosion resistance of Nb-1%Zr alloy.

7. Germanium addition led to increasing of (Nb-1%Zr)alloy hardness.

8. Germanium addition donot change the anti bacterial effect of the base alloy (still antibacterial).

9. Germanium addition improvement the cell viability of the(Nb-1%Zr) alloy .

10.The formation of HA on Germanium containg alloys is an indication to improvement the osteointegration of the base alloy (Nb-1%Zr).

5.2 Recommendations

For future work, the following items are suggested:

1. Adding other alloying elements like Te, In and Sn and study the effect of these elements on the mechanical, electrochemical and biological properties of Nb-1%Zr alloy in vitro.

2. Using surface coating treatment to modify the surface properties of Nb-1%Zr and study the effect of the surface treatment on the corrosion resistance of these alloys in animal's bodies (in vivo).

3. Studying the effect of heat treatment on the wear resistance Nb-1%Zr alloys.

References

[1]. T. Duerig, A. Pelton, and D. Stöckel: **An overview of nitinol medical applications**. Mater. Sci. Eng., A 273–275, 149 (1999).

[2]. R.Z. Valiev, I.P. Semenova, E. Jakushina, V.V. Latysh, H. Rack, T.C. Lowe, J. Petruzelka, L. Dluhos, D. Hrusak, and J. Sochova: Nanostructured SPD processed titanium for medical implants. Mater. Sci. Forum 584–586, 49 (2008).

[3]. S.M. Toker, D. Canadinc, H.J. Maier, and O. Birer: Evaluation of passive oxide layer formation – biocompatibility relationship in NiTi shape memory alloys. Mater. Sci. Eng., C 36, 118 (2014).

[4]. A.Y. Imam, B.Yilmaz, T.B. Özçelik, and E.McGlumphy: **Salvaging an angled implant abutmentwith damaged internal threads**:A clinical report. J. Prosthet. Dent. 109, 287 (2013).

[5]. F. Zarrone, R. Sorrentino, T. Traini, D. Di lorio, and S. Caputi: Fracture resistance of implant-supported screw- vs cement-retained porcelain fused to metal single crowns: SEM fractographic analysis. D6.

[6]. C.H. Li and C.T. Chou: Bone sparing implant removal without terephine via internal separation of the titanium body with a carbide bur. Int. J. Oral Maxillofac. Surg. 43(2), 248–250 (2014).

[7]. N.J. Hallab, S. Anderson, M. Caicedo, and J.J. Jacobs: Zirconium and niobium affect human osteoblasts, fibroblasts, and lymphocytes in a similar manner to more traditional implant alloymetals. J. ASTM. Int. 3, 248–259 (2006). JAI12817.

[8]. H. Matsuno, A. Yokoyama, F. Watari, M. Uo, and T. Kawasaki: Biocompatibility and osteogenesis of refractory metal implants, titanium, hafnium, niobium, tantalum and rhenium. Biomaterials 22, 1253 (2001).

[9]. H.G. Kim, S.Y. Park, M.H. Lee, Y.H. Jeong, and S.D. Kim: Corrosion and microstructural characteristics of Zr–Nb alloys with different Nb contents. J. Nucl. Mater. 373, 429 (2008).

References

[10]. F. Rubitschek, T. Niendorf, I. Karaman, and H.J. Maier: Corrosion fatigue behavior of a biocompatible ultrafine-grained niobium alloy in simulated body fluid. J. Mech. Behav. Biomed. Mater. 5, 181 (2012).

[11]. T. Niendorf, D. Canadinc, H.J. Maier, I. Karaman, and G.G. Yapici: Microstructure – mechanical property relationships in ultrafinegrained NbZr. Acta Mater. 55, 6596 (2007).

[12]. T. Niendorf, H.J. Maier, D. Canadinc, G.G. Yapici, and I. Karaman: Improvement of the fatigue performance of ultrafine-grained Nb-Zr alloy by nano-sized precipitates formed by internal oxidation. Scripta Mater. 58, 571 (2008).

[13]. S.M. Toker, F. Rubitschek, T. Niendorf, D. Canadinc, and H.J. Maier: Anisotropy of ultrafine-grained alloys under impact loading: The case of biomedical niobium–zirconium. Scripta Mater. 66, 435 (2012).

[14]. M. Cehreli, S. Sahin, and K. Akca: Role of mechanical environment and implant design on bone tissue differentiation: Current knowledge and future contexts. J. Dent. 32, 123 (2004).

[15]. C. Anunmanaa, K.J. Anusavicea, Jr., and J.J. Mecholsky: Interfacial toughness of bilayer dental ceramics based on a short-bar, chevronnotch test. Dent. Mater. 26, 111 (2010).

[16]. H.S. Gupta and P. Zioupos: Fracture of bone tissue: The ‘hows’ and the ‘whys’. Med. Eng. Phys. 30, 1209 (2008).

[17]. M. Moazen, A.C. Jones, Z. Jin, R.K. Wilcox, and E. Tsiridis: Periprosthetic fracture fixation of the femur following total hip arthroplasty: A review of biomechanical testing. Clin. Biomech. 26, 13 (2011).

[18]. P. Kannus, J. Parkkar, and J. Poutala: Comparison of force attenuation properties of four different hip protectors under simulated falling conditions in the elderly: An in vitro biomechanical study. Bone 25, 229 (1999).

References

[19]. Y. Fukuda, S. Takai, N. Yoshino, K. Murase, S. Tsutsumi, K. Ikeuchi, and Y. Hirasawa: Impact load transmission of the knee joint-influence of leg alignment and the role of meniscus and articular cartilage. Clin. Biomech. 15, 516 (2000).

[20]. A. Verteramo and B.B. Seedhom: Effect of a single impact loading on the structure and mechanical properties of articular cartilage. J. Biomec. 40, 3580 (2007).

[21]. N. Wakaoa, A. Harada, Y. Matsui, M. Takemura, H. Shimokata, M. Mizuno, M. Itod, Y. Matsuyamaa, and N. Ishiguro: The effect of impact direction on the fracture load of osteoporotic proximal femurs. Med. Eng. Phys. 31, 1134 (2009).

[22]. T.P. Pinilla, K.C. Boardman, M.L. Bouxsein, E.R. Myers, and W.C. Hayes: Impact direction from a fall influences the failure load of the proximal femur as much as age-related bone loss. Calcif. Tissue Int. 58, 231 (1996).

[23]. Malegowd, Gownolla, Kokkarachedu Varaprasad, and Tippabattini Jayaramudu. 2015. "Biomaterials: Design, Development and Biomedical Applications." In *Nanotechnology Applications for Tissue Engineering*. Edited by S. Thomas, Y. Grohens, and N. Ninan, Elsevier.

[24]. Stanisławska, A. 2014. "Biomaterials and Implants Cardiac and Vascular Surgery: Review." *Advances in Materials Science*, Vol.14, No.3.

[25]. Dahman, Yaser. 2019. *Biomaterials Science and Technology: Fundamentals and Developments.* Boca Raton, Taylor & Francis Group, LLC.

[26]. Park, B. , and Young Kon Kim. 2007. "Metallic Biomaterials." I*n Biomaterials.* Edited by Joyce Y. Wong & Joseph D. Bronzino, Taylor and Francis Group, CRC Press.

References

[27]. Ramsden, J., D.M. Allen, D. J. Stephenson ,et al. 2007. "The Design and Manufacture of Biomedical Surfaces." *Crip Annals-Manufacturing Technology*, Vol.56, No.2, pp.687-711.

[28]. J.W. Morris, Jr.: Stronger, tougher steels. Science 320, 1022 (2008).

[29]. R. Song, D. Ponge, and D. Raabe: Mechanical properties of an ultrafine grained C–Mn steel processed by warm deformation and annealing. Acta Mater. 53, 4881 (2005).ent. Mater. 23, 296 (2007).

[30]. Y. Kimura, T. Inoue, F. Yin, and K. Tsuzaki: Inverse temperature dependence of toughness in an ultrafine grain-structure steel. Science 320, 1057 (2008).

[31]. P. Gabor, D. Canadinc, H.J. Maier, R.J. Hellmig, Z. Zuberova, and J. Estrin: The influence of zirconium on the low-cycle fatigue response of ultrafine-grained copper. Metall. Mater. Trans. A 38, 1916 (2007).

[32]. D. Canadinc, H.J. Maier, M. Haouaoui, and I. Karaman: **On the cyclic stability of nanocrystalline copper obtained by powder consolidation at room temperature**. Scripta Mater. 58, 307 (2008).

[33]. T. Niendorf, D. Canadinc, H.J. Maier, I. Karaman, and S.G. Sutter: On the Fatigue Behavior of Ultrafine-Grained IF Steel. Int. J. Mater. Res. 97, 1328 (2006).

[34]. Wen, Chunsheng, Xiaojiao Yu, Wei Zeng, et al. 2018. "Mechanical Behaviors and Biomedical Applications of Shape Memory Materials: A Review." AIMS Materials Science ,Vol.5, No.4, pp.559–590.

[35]. Davis, J. 2001. Surface Engineering for Corrosion and Wear Resistance. USA: The Materials Information Society, ASM, Institute of Materials.

[36]. Chu ,Paul . 2007. "Enhancement of Surface Properties of Biomaterials using Plasma-based Technologies.", Surface & Coatings Technology, Vol. 201 ,pp.8076–8082.

References

[37]. Jurczyk Mieczyslaw and Karolina Jurczyk. 2013. In Bionanomaterials for Dental Applications. Edited by Mieczyslaw Jurczyk, USA: Pan Stanford Publishing Pte. Ltd.

[38]. Jakubowics Jaroslaw,. 2013. "Carbon Materials." In Bionanomaterials for Dental Applications. Edited by Mieczyslaw Jurczyk, USA: Pan Stanford Publishing Pte. Ltd.

[39]. E.M. Viatkina, W.A.M. Brekelmans, and M.G.D. Geers: The role of plastic slip anisotropy in the modelling of strain path change effects. J. Mat. Proc. Tech. 209, 186 (2009).

[40]. I.J. Beyerlein and L.S. Tóth: Texture evolution in equal-channel angular extrusion. Prog. Mater. Sci. 54, 427 (2009).

[41]. M.R. Bache and W.J. Evans: Impact of texture on mechanical properties in an advanced titanium alloy. Mater. Sci. Eng., A 319–321, 409 (2001).

[42]. B.B. Martin, D.B. Burr, and N.A. Sharkey: Skeletal Tissue Mechanics (Springer-Verlag, New York, 1998).

[43]. J.Y. Rho, L. Kuhn-Spearing, and P. Zioupos: Mechanical properties and the hierarchical structure of bone. Med. Eng. Phys. 20, 92 (1998).

[44]. Grill R and Gnadenberger A. Niobium as mint metal: production: properties: processing. International Journal of Refractory Metals & Hard Materials. 2006; 24(4):275-282. http://dx.doi.org/10.1016/j.ijrmhm.2005.10.008.

[45]. Grill R. Niobium for coins. TIC Tantalum: Niobium. International Study Center-Bulletin. 2007; 129:6-8.

[46]. Ayanda OS and Adekola FA. A review of niobium-tantalum separation in Hydrometallurgy. Journal of Minerals & Materials Characterization & Engineering. 2011; 10:245-256.

References

[47]. ASM International. Properties and selection of the metals. 8th ed. Ohio; 1961. ASM Handbook 1.

[48]. ASM International. Properties and selection: nonferrous alloys and special-purpose materials. 10th ed. Ohio; 1990. ASM Handbook 2.

[49]. Kepert DL. The early transition metals. London: Academic Press; 1972. 142 p.

[50]. A. Biesiekierski, J. Wang, M.A. Gepreel, C. Wen, A new look at biomedical Tibased shape memory alloys, Acta Biomater. 8 (2012) 1661–1669.

[51]. F.Y. Zhou, B.L. Wang, K.J. Qiu, W.J. Lin, L. Li, Y.B. Wang, F.L. Nie, Y.F. Zheng, Microstructure, corrosion behavior and cytotoxicity of Zr–Nb alloys for biomedical application, Mater. Sci. Eng. C 32 (2012) 851–857.

[52]. G. Purcek, O. Saray, F. Rubitschek, T. Niendorf, H.J. Maier, I. Karaman, Effect of internal oxidation on wear behavior of ultrafine-grained Nb–Zr, Acta Mater. 59 (2011) 7683–7694.

[53]. O. Jin, Z.J. Zhang, B.X. Liu, Z.J. Zhang, B.X. Liua, Alloying behavior of formation induced by ion mixing in a system with positive heat, J. Appl. Phys. 78 (1995) 149–154.

[54]. T.L. Wang, S.H. Liang, J.H. Li, K.P. Tai, B.X. Liu, Abnormal alloying behavior observed in an immiscible Zr–Nb system, J. Phys. D: Appl. Phys. 41 (2008) 095310–095316.

[55]. C. Suryanarayana, J. Liu, Processing and characterization of mechanically alloyed immiscible metals, Int. J. Mater. Res. 103 (2012) 1125–1129.

[56]. H.H. Liebermann, Rapidly Solidified Alloys, Marcel Dekker, New York, 1993.

[57]. C. Suryanarayana, N. Al-Aqeeli, Mechanically alloyed nanocomposites, Prog. Mater. Sci. 58 (2013) 383–502.

References

[58]. H. Ahn, D. Lee, C.-W. Moon, K.-M. Lee, K. Lee, A study about the biocompatibility of Ti–8Ta–3Nb alloys with surface modification, Surf. Coat. Technol. 202 (2008) 5779–5783.

[59]. X.J. Wang, Y.C. Li, J.Y. Xiong, P.D. Hodgson, C.E. Wen, Porous TiNbZr alloy scaffolds for biomedical applications, Acta Biomater. 5 (2009) 3616–3624.

[60]. Shibo Guo, Aimin Chu, Haijiang Wu, Chunbo Cai, Xuanhui Qu, Effect of sintering processing on microstructure, mechanical properties and corrosion resistance of Ti–24Nb–4Zr–7.9Sn alloy for biomedical applications, J. Alloys Compd. 597 (2014) 211–216.

[61] C. Camurri, M. Ortiz, C. Carrasco, Hot consolidation of Cu–Li powder alloys: a first approach to characterization, Mater. Charact. 51 (2003) 171–176.

[62] C.Y. Xu, S.S. Jia, Z.Y. Cao, Synthesis of Al−Mn−Ce alloy by the spark plasma sintering, Mater. Charact. 54 (2005) 394−398.

[63] A. Biesiekierski, J. Wang, M.A. Gepreel, C. Wen, A new look at biomedical Tibased shape memory alloys, Acta Biomater. 8 (2012) 1661–1669.

[64] F.Y. Zhou, B.L. Wang, K.J. Qiu, W.J. Lin, L. Li, Y.B. Wang, F.L. Nie, Y.F. Zheng, Microstructure, corrosion behavior and cytotoxicity of Zr–Nb alloys for biomedical application, Mater. Sci. Eng. C 32 (2012) 851–857.

[65] G. Purcek, O. Saray, F. Rubitschek, T. Niendorf, H.J. Maier, I. Karaman, Effect of internal oxidation on wear behavior of ultrafine-grained Nb–Zr, Acta Mater. 59 (2011) 7683–7694.

References

[66] O. Jin, Z.J. Zhang, B.X. Liu, Z.J. Zhang, B.X. Liua, Alloying behavior of formation induced by ion mixing in a system with positive heat, J. Appl. Phys. 78 (1995)149–154.

[67] T.L. Wang, S.H. Liang, J.H. Li, K.P. Tai, B.X. Liu, Abnormal alloying behavior observed in an immiscible Zr–Nb system, J. Phys. D: Appl. Phys. 41 (2008) 095310–095316.

[68] C. Suryanarayana, J. Liu, Processing and characterization of mechanically alloyed immiscible metals, Int. J. Mater. Res. 103 (2012) 1125–1129.

[69] H.H. Liebermann, Rapidly Solidified Alloys, Marcel Dekker, New York, 1993.

[70] C. Suryanarayana, N. Al-Aqeeli, Mechanically alloyed nanocomposites, Prog. Mater. Sci. 58 (2013) 383–502.

[71]. M.A. Hussein a,b, C. Suryanarayana c, et. al, "Effect of sintering parameters on microstructure, mechanical properties and electrochemical behavior of Nb–Zr alloy for biomedical applications", Materials & Design. 0264-1275/© 2015 Elsevier Ltd. All rights reserved.

[72]. ASM Metals Handbook. Alloy Phase Diagrams, Vol.3 Binary.

[73]. William D. Callister, Jr., **Materials Science and Engineering,** Seventh Edition.

[74]. JOON B. PARK, Biomaterials – Principles and applications.

[75]. Sever Sontea, et.al**.,** ***Introduction to Powder Metallurgy,*** Raducanu Liviu engineer of S.C. Carmesin S. A Bucuresti, 2002.

[76]. Wiley John and Sons, **Fundamentals of Modern Manufacturing 2/e**, 2002.

[77]. Das S., et.al., **Experimental Investigation on the Effect of Reinforcement Particles on the Forge ability and the Mechanical**

References

Properties of Aluminum Metal Matrix Composites, materials sciences and applications, pp.310-316, 2010.

[78]. Sinka I.C.**, Modelling Powder Compaction,** Department of Engineering, University of Leicester, KONA No.25 (2007).

[79]. Meluch Ľubos**, Warm Compaction of Aluminum Alloy Alumix *123,*** September 2009**.**

[80]. Hemant Kumar Bansal, and Devesh Mahor, **Behavioral Modeling of Genetic Algorithm Processor using Model Sim**, International Journal of Advanced Research in Computer Science and Software Engineering, ISSN: 2277 128X, Vol. 4, Issue 1, January 2014.

[81]. B. Verlinden, **Aluminium Powder Metallurgy,** pp.5-7, Date of Issue: 1994, EAA-European Aluminium Association.

[82]. Jones, D.A. (1996) Principles and Prevention of Corrosion, 2nd Edition, Prentice Hall, Upper Saddle River, NJ.

[83]. Schultz, M.P. (1997) "OCE-4518 Protection of Marine Materials Class Notes", Florida Institute of Technology.

[84]. Swain, G.W. (1996) "OCE-4518 Protection of Marine Materials Class Notes", Florida Institute of Technology.

[85]. Dawson, T. (1993) "EN380 Engineering Aspects of Materials Class Notes", United States Naval Academy.

[86] A. Biesiekierski, J. Wang, M.A. Gepreel, C. Wen, A new look at biomedical Tibased shape memory alloys, Acta Biomater. 8 (2012) 1661–1669.

[87] F.Y. Zhou, B.L. Wang, K.J. Qiu, W.J. Lin, L. Li, Y.B. Wang, F.L. Nie, Y.F. Zheng, Microstructure, corrosion behavior and cytotoxicity of Zr–Nb alloys for biomedical application, Mater. Sci. Eng. C 32 (2012) 851–857.

[88]. T. Duerig, A. Pelton, and D. Stöckel: An overview of nitinol medical applications. Mater. Sci. Eng., A 273–275, 149 (1999).

References

[89]. R.Z. Valiev, I.P. Semenova, E. Jakushina, V.V. Latysh, H. Rack, T.C. Lowe, J. Petruzelka, L. Dluhos, D. Hrusak, and J. Sochova: Nanostructured SPD processed titanium for medical implants.

Mater. Sci. Forum 584–586, 49 (2008).

[90]. S.M. Toker, D. Canadinc, H.J. Maier, and O. Birer: Evaluation of passive oxide layer formation – biocompatibility relationship in NiTi shape memory alloys. Mater. Sci. Eng., C 36, 118 (2014).

[91]. A.Y. Imam, B.Yilmaz, T.B. Özçelik, and E.McGlumphy: Salvaging an angled implant abutmentwith damaged internal threads:A clinical report. J. Prosthet. Dent. 109, 287 (2013).

[92]. F. Zarrone, R. Sorrentino, T. Traini, D. Di lorio, and S. Caputi: Fracture resistance of implant-supported screw- vs cement-retained porcelain fused to metal single crowns: SEM fractographic analysis. Dent. Mater. 23, 296 (2007).

[93]. C.H. Li and C.T. Chou: Bone sparing implant removal without terephine via internal separation of the titanium body with a carbide bur. Int. J. Oral Maxillofac. Surg. 43(2), 248–250 (2014).

[94]. N.J. Hallab, S. Anderson, M. Caicedo, and J.J. Jacobs: Zirconium and niobium affect human osteoblasts, fibroblasts, and lymphocytes in a similar manner to more traditional implant alloymetals. J. ASTM. Int. 3, 248–259 (2006). JAI12817.

[95]. H. Matsuno, A. Yokoyama, F. Watari, M. Uo, and T. Kawasaki: Biocompatibility and osteogenesis of refractory metal implants, titanium, hafnium, niobium, tantalum and rhenium. Biomaterials 22, 1253 (2001).

[96]. H.G. Kim, S.Y. Park, M.H. Lee, Y.H. Jeong, and S.D. Kim: Corrosion and microstructural characteristics of Zr–Nb alloys with different Nb contents. J. Nucl. Mater. 373, 429 (2008).

References

[97]. Burakowski, T, and Wier zchon, T., Surface Engineering: Principles Technologies, CRC Press 1998.

[98]. Koji Kato, Wear in relation to friction - a review, Laboratory of Tribology, School of Mechanical Engineering, Tohoku University, Sendai 980-8579, Japan, Wear 241 -2000. 151-157.

[99]. K.N. Prabhu, P. Fernandes, G. Kumar, Mater. Des. 2, 297 (2009)

[100]. X. Zhao, M.J. Blunta, J.J. Yao, Pet. Sci. Technol. Eng. 71, 169 (2010)

[101]. Y.Q.Wang, H.F. Yang, Q.G. Hang, L. Fang, S.R. Ge, Adv.Mater. Res. 154–155, 1019 (2010)

[102]. M. Sakai, T. Yanagisawa, A. Nakajima, Y. Kameshima, K. Okada, Langmuir 25, 13 (2009)

[103]. Y. Son, C. Kim, D.H. Yang, D.J. Ahn, Langmuir 24, 2900 (2008)

[104]. J. Perelaer, C.E. Hendriks, A.W.M. de Laat, U.S. Schubert, Nanotechnology 20, 165303

(2009)

[105]. H. Yang, P. Jiang, Langmuir 26, 12598 (2010)

[106]. B. Bhushan, Y.C. Jung, K. Koch, Langmuir 25, 3240 (2009)

[107]. M. Rauscher, S. Dietrich, Annu. Rev. Mater. Sci. 38, 143 (2008)

[108]. K. Fei, C.P. Chiu, C.W. Hong, Microfluid. Nanofluid. 4, 321 (2008)

[109]. Z. Keshavarz-Motamed, L. Kadem, A. Dolatabadi, Microfluid. Nanofluid. 8, 47 (2010)

References

[110]. Y.S. Nanayakkara, S. Perera, S. Bindiganavale, E.Wanigasekara, H. Moon, D.W. Armstrong, Anal. Chem. 82, 3146 (2010).

[111]. Rho JY, Hobatho MC, Ashman RB. Relations of mechanical properties CT numbers in human bone. Med Eng Phys. 1995;17(5):347–55.

[112]. Lotz JC, Gerhart TN, Hayes WC. Mechanical properties of metaphyseal bone in the proximal femur. J Biomech. 1991;24(5): 317–29.

[113]. Martin RB, Boardman DL. The effects of collagen fiber orientation, porosity, density, and mineralization on bovine cortical bone bending properties. J Biomech. 1993;26(9):1047–54.

[114]. Schaffler MB, Burr DB. Stiffness of compact bone: effects of porosity and density. J Biomech. 1988;21(1):13–6.

[115]. Sjögren G, Sletten G, Dahl JE (2000) Cytotoxicity of dental alloys, metals, and ceramics assessed by Millipore filter, agar overlay, and MTT tests. J Prosthet Dent 84:229–236

[116]. James A. Davidson, Germantown, TN (US); Lee H. Tuneberg, Sheboygan, WI (US), **Niobium-Titanium-Zirconium- Molybdenum (Nbtizrmo) Alloys Fordental and Other Medical Device Applications,** US 6,238,491 B1, May 29, 2001.

[117]. Carlos Kleber Z. Andrade* and Rafael O. Rocha, **Recent Applications of Niobium Catalysts in Organic Synthesis,** Mini-Reviews in Organic Chemistry, 2006, 3, 271-280.

[118]. G. Zorn Æ I. Gotman Æ E. Y. Gutmanas Æ R. Adadi Æ C. N. Sukenik, Surface modification of Ti45Nb alloy by immobilization of

References

RGD peptide via self-assembled monolayer, Springer Science Business Media, LLC 2007

[119]. René Olivares-Navarrete 1, Jhon Jairo Olaya 2, Claudia Ramírez 3 and Sandra Elizabeth Rodil 3, *, **Biocompatibility of Niobium Coatings,** Coatings 2011, 1, 72-87; doi:10.3390/coatings1010072.

[120]. Qiang Li, Mitsuo Niinomi, Junko Hieda ⇑, Masaaki Nakai, Ken Cho, **Deformation-induced x phase in modified Ti–29Nb–13Ta–4.6Zr alloy by Cr addition**, 2013 Acta Materialia Inc. Published by Elsevier Ltd. All rights reserved.

[121]. Rodrigo Sacramento da Silva, Alexandre Antunes Ribeiro, **Characterization of Ti-35Nb alloy surface modified by controlled chemical oxidation for surgical implant applications**, 2019, Matéria (Rio de Janeiro).

[122]. Oleg Mishchenko , Oleksandr Ovchynnykov, Oleksii Kapustian, Maksym Pogorielov, **New Zr-Ti-Nb Alloy for Medical Application: Development, Chemical and Mechanical Properties, and Biocompatibility,** Materials (Basel). 2020 Mar 13;13(6):1306. doi: 10.3390/ma13061306.

[123]. Lee, S. H., Nomura, N., & Chiba, A. (2008) 'Significant improvement in mechanical properties of biomedical Co-Cr-Mo alloys with combination of N addition and Cr-enrichment', Materials transactions, Vol. 49, pp. 260264 .

[124]. Oksiuta, Z., Dabrowski, J. R., and Olszyna, A. (2009) 'Co–Cr–Mobased composite reinforced with bioactive glass', journal of materials processing technology, Vol. 209, pp. 978-985 .

[125]. Krishna, B. V., Xue, W., Bose, S., and Bandyopadhyay, A. (2008) 'Functionally graded Co–Cr–Mo coating on Ti–6Al–4V alloy structures', Acta biomaterialia, Vol. 4, pp. 697-706 .

References

[126]. Dourandish, M., Godlinski, D., Simchi, A., and Firouzdor, V. (2008) 'Sintering of biocompatible P/M Co–Cr–Mo alloy (F-75) for fabrication of porosity-graded composite structures', Materials Science and Engineering: A, Vol. 472, pp. 338-346.

[127]. Songür, M., Çelikkan, H., Gökmeşe, F., Şimşek, S. A., Altun, N. Ş., and Aksu, M. L. (2009) 'Electrochemical corrosion properties of metal alloys used in orthopaedic implants', Journal of Applied .Electrochemistry, Vol. 39, pp. 1259-1265

[128]. Giacchi, J. V., Morando, C. N., Fornaro, O., and Palacio, H. A. (2011) 'Microstructural characterization of as-cast biocompatible Co– .Cr–Mo alloys', Materials Characterization, Vol. 62, pp. 53-61

[129].Kamardan, M. G., Zaidi, N. H. A., Dalimin, M. N., Zaidi, A. M. A., Jamaludin, S. B., and Jamil, M. M. A. (2010) 'The sintering temperature effect on the shrinkage behavior of cobalt chromium alloy', .American Journal of Applied Sciences, Vol. 7, pp. 1443-1448

[130]. Rodrigues, W. C., Broilo, L. R., Schaeffer, L., Knörnschild, G., and Espinoza, F. R. M. (2011) 'Powder metallurgical processing of Co– 28% Cr–6% Mo for dental implants: Physical, mechanical and .electrochemical properties', Powder Technology, Vol. 206, pp. 233-238

[131]. Dobrzański, L. A. (2011) 'Influence of Cr and Co on [77] hardness and corrosion resistance CoCrMo alloys used on dentures', Journal of Achievements in Materials and Manufacturing Engineering, .Vol. 49, pp. 193-199

[132]. Adzali, N. M. S., Jamaludin, S. B., and Derman, M. N. (2012) 'Mechanical Properties, Corrosion Behavior, and Bioactivity of Composite Metal Alloys Added with Ceramic for Biomedical

References

Applications', Reviews of Advanced Materials Science, Vol. 30, pp. .262-266

[133]. Patel, B., Favaro, G., Inam, F., Reece, M. J., Angadji, A., Bonfield, W., ... and Edirisinghe, M. (2012) 'Cobalt-based orthopaedic alloys: relationship between forming route, microstructure and tribological

performance', Materials Science
.and Engineering: C, Vol. 32, pp. 12221229

[134]. Mischler, S., and Munoz, A. I. (2013) 'Wear of CoCrMo alloys used in metal-on-metal hip joints: a tribocorrosion appraisal', Elsevier, .Vol. 297, pp. 1081-1094

[135]. Liu, R., Li, X., Hu, X., and Dong, H. (2013) 'Surface modification of a medical grade Co-Cr-Mo alloy by low-temperature plasma surface alloying with nitrogen and carbon', Surface and Coatings Technology, .Vol. 232, pp. 906-911

[136]. Daud, Z. C., Jamaludin, S. B., Derman, M. N., & Wahab, J. A. (2013) 'The corrosion studies of powder metallurgy Co-Cr-Mo (F-75) .alloy', Advances in Environmental Biology, Vol. 7, pp. 3716-3719

[137]Muna, K. A., Sami, A. A. and Haitham M. W.(2014) 'Study of corrosion resistance of Co-Cr-Mo surgical implants alloy in artificial .saliva', Engineering and technology journal, Vol. 32, No. 10

[138].Mantrala, K. M., Das, M., Balla, V. K., Rao, C., and Kesava Rao, V. V. S. (2015) 'Additive manufacturing of Co-Cr-Mo alloy: Influence of heat treatment on microstructure, tribological, and electrochemical .properties', Frontiers in Mechanical Engineering, Vol. 1

References

[139] Sabine, W. and Bojan, M. (2015) ‘Microstructure and deformation of cornorary stentsfrom Co Cr –alloys with different designs. Multidisciplinary digital’, Publishing Institute Journal, Vol. 8, pp. 24672479.

وزارة التخطيط
الجهاز المركزي للتقييس والسيطرة النوعية
مديرية براءات الأختراع والنماذج الصناعية
القسم الأداري / شعبة الأستلام

مرامي

وصل أستلام طلب براءة أختراع

Nº 000058

رقم الطلب : ٢٣٤ / ٢٠٢٤ ص ص

أسم مقدم الطلب : صباح جواد عمر

عنوانه : بابل - الحلة - اليوسفية

عنوان الأختراع (تحسين مواصفات سيكة البيوبوم)

تاريخ الأستلام : ١ / ٦ / ٢٠٢٤

الصنف : كيمياوي

ع / مسجل براءة الأختراع والنماذج الصناعية

ترسيب جواد

ملاحظة :

١ ـ عملا بأحكام الفقرة ٣ من المادة الثانية من نظام براءة الأختراع والنماذج الصناعية رقم ٢١ لسنة ١٩٧٠

٢ ـ لا يعتبر هذا الوصل دلالة على قبول الطلب وصدور الشهادة

وزارة التخطيط
الجهاز المركزي للتقييس والسيطرة النوعية
مديرية براءات الأختراع والنماذج الصناعية
القسم الأداري / شعبة الأستلام

وصل أستلام طلب براءة أختراع

Nº 000058

رقم الطلب : ٤٣٤ / cc

أسم مقدم الطلب : صباح جواد عمر

عنوانه : بابل - الحلة - الميوناقع

عنوان الأختراع (تحسين خواص سيكة البيوبوم)

تاريخ الأستلام : ١ / ٦ / ٢٠٢٤

الصنف : كيمياوي

ع / مسجل براءة الأختراع والنماذج الصناعية

ترتيب جواد

ملاحظة :

١ ـ عملا بأحكام الفقرة ٣ من المادة الثانية من نظام براءة الأختراع والنماذج الصناعية رقم ٢١ لسنة ١٩٧٠

٢ ـ لا يعتبر هذا الوصل دلالة على قبول الطلب وصدور الشهادة

Appendix A

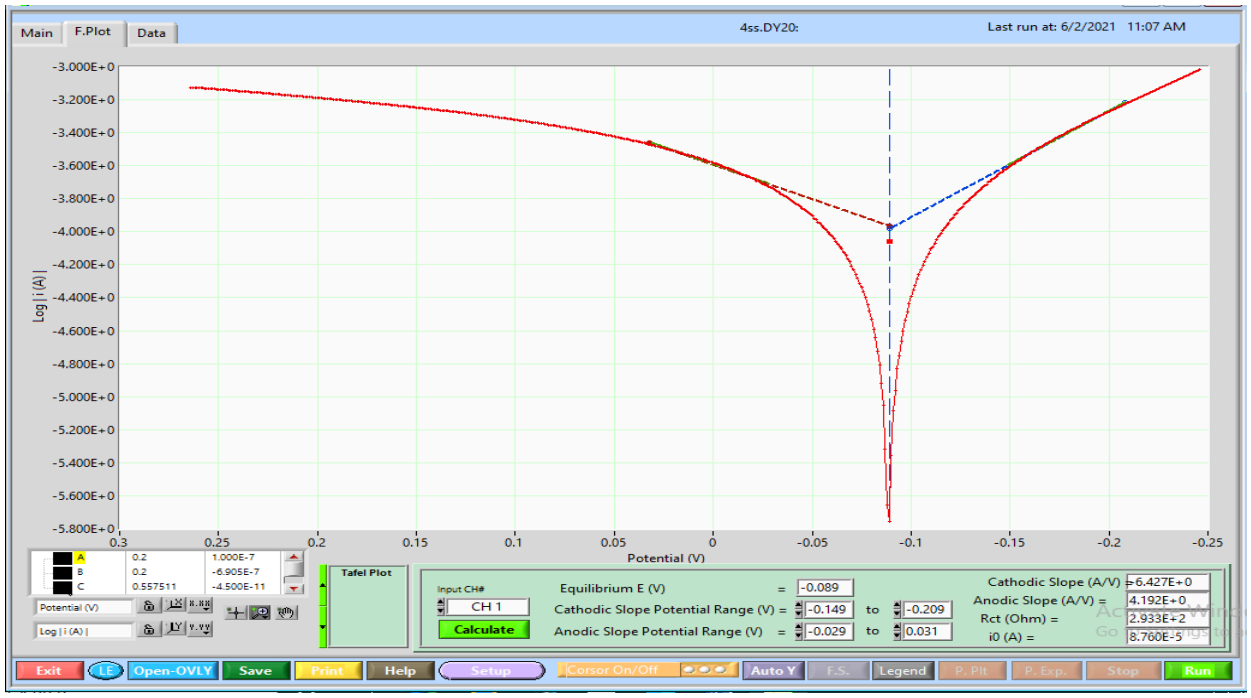

A1/ Potentiodynamic Polarization for Alloy in Artificial Saliva.

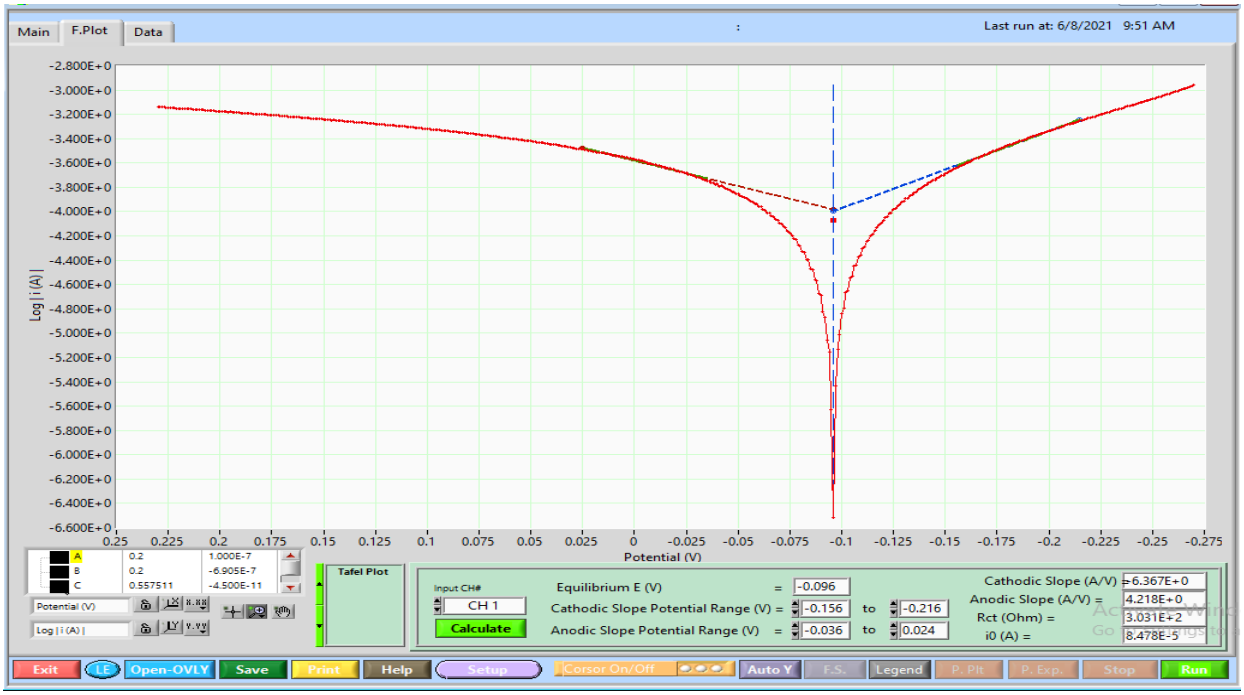

A2/ Potentiodynamic Polarization for B2 Alloy in Artificial Saliva

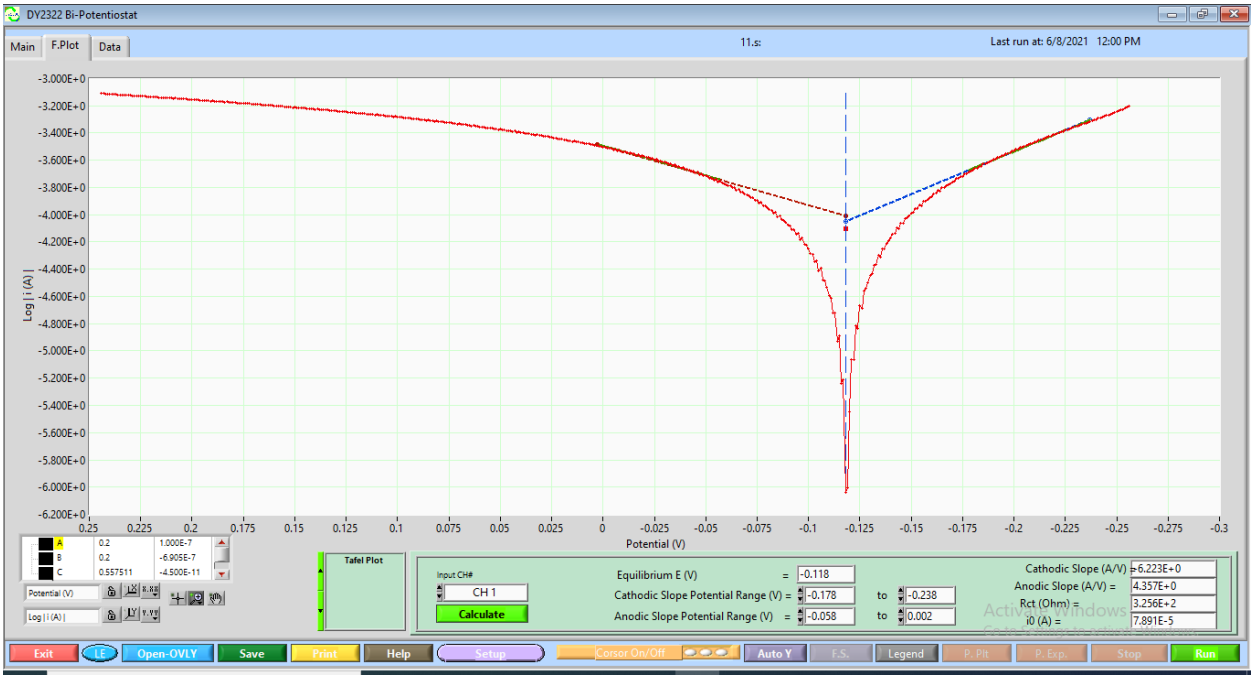

A3/ Potentiodynamic Polarization for Alloy in Artificial Saliva

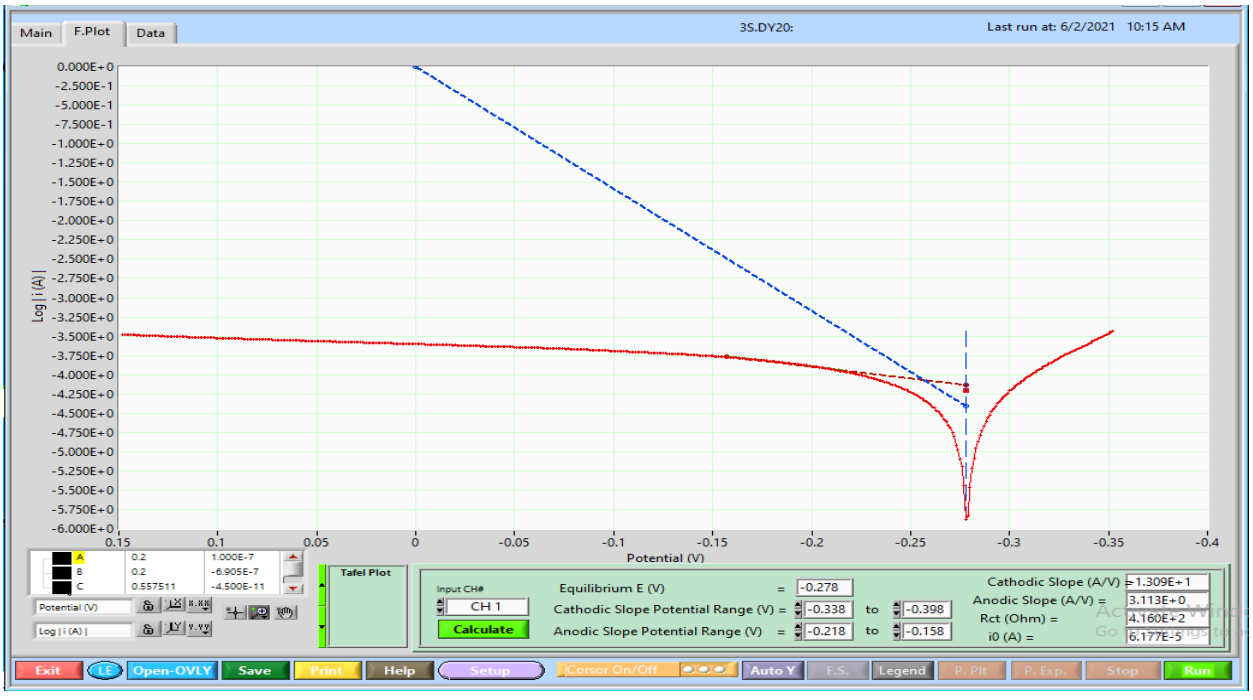

A4/ Potentiodynamic Polarization for Alloy in Artificial Saliva

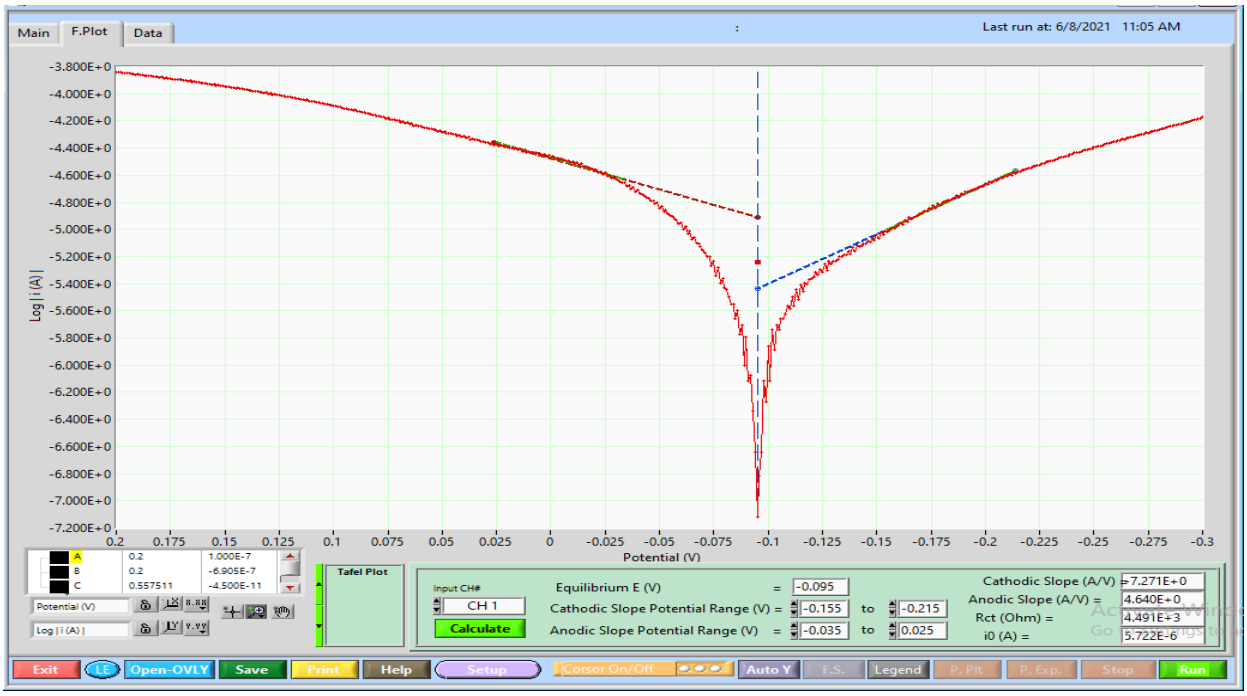

A5/ Potentiodynamic Polarization for Alloy in Artificial Saliva

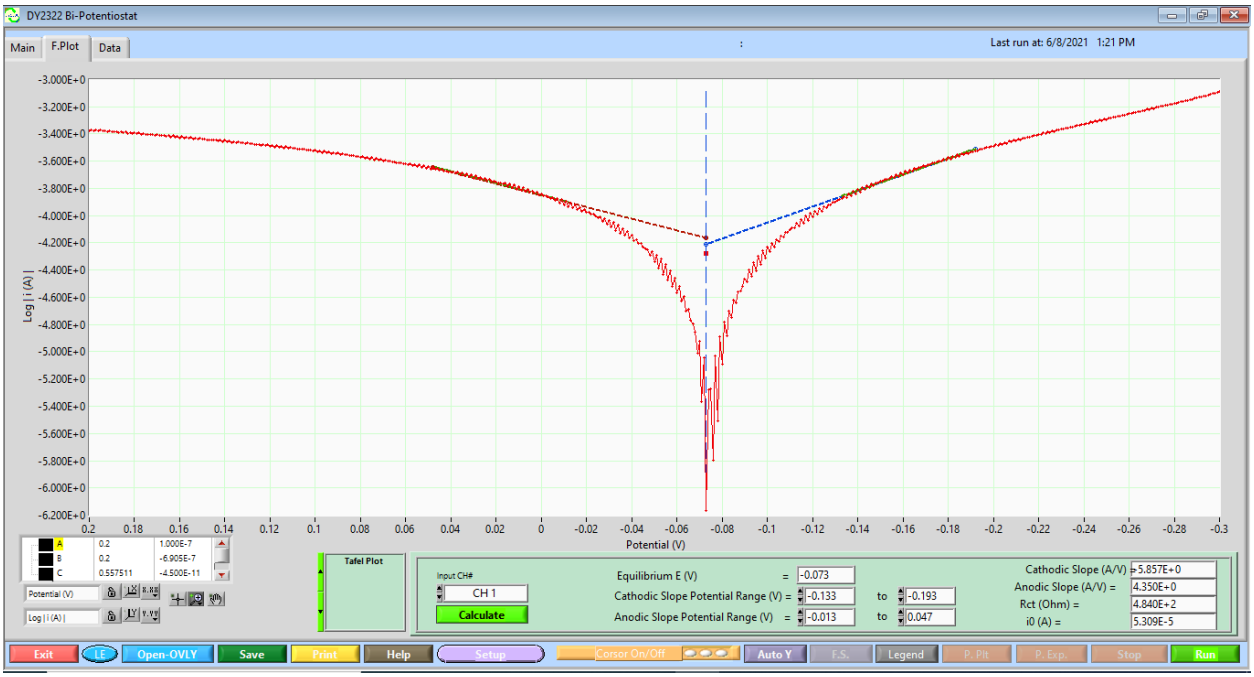

A6/ Potentiodynamic Polarization for Alloy in Artificial Saliva

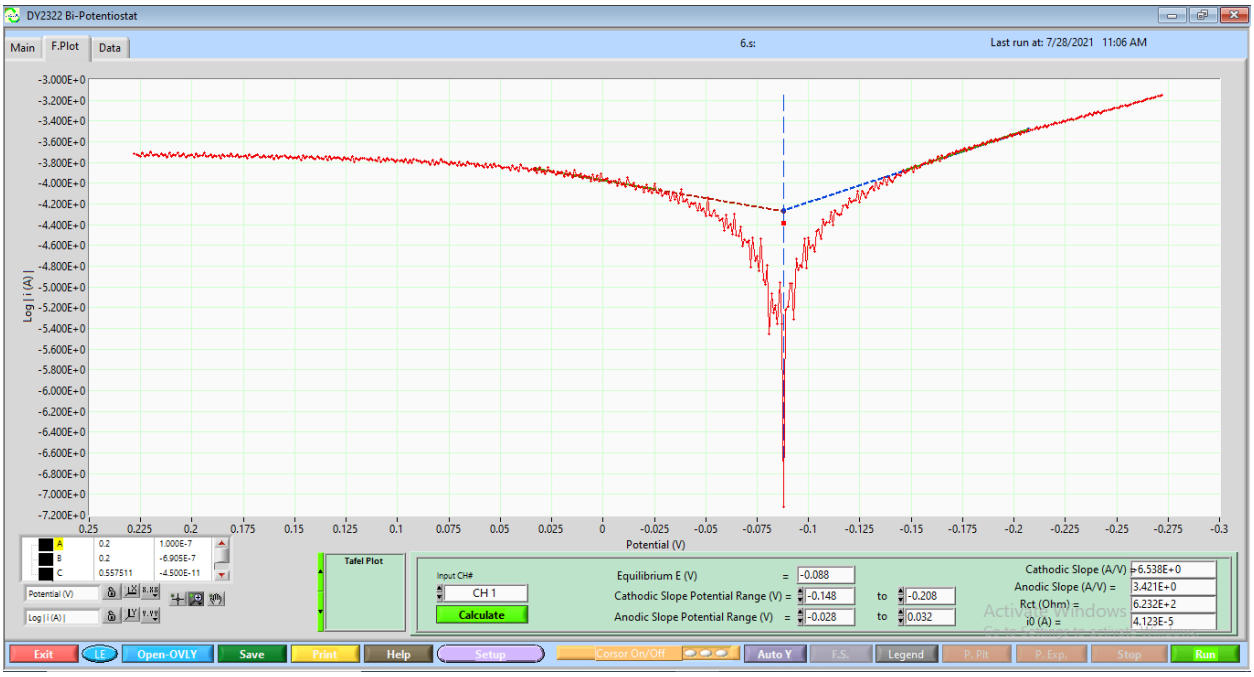

A7/ Potentiodynamic Polarization for Alloy in Artificial Saliva

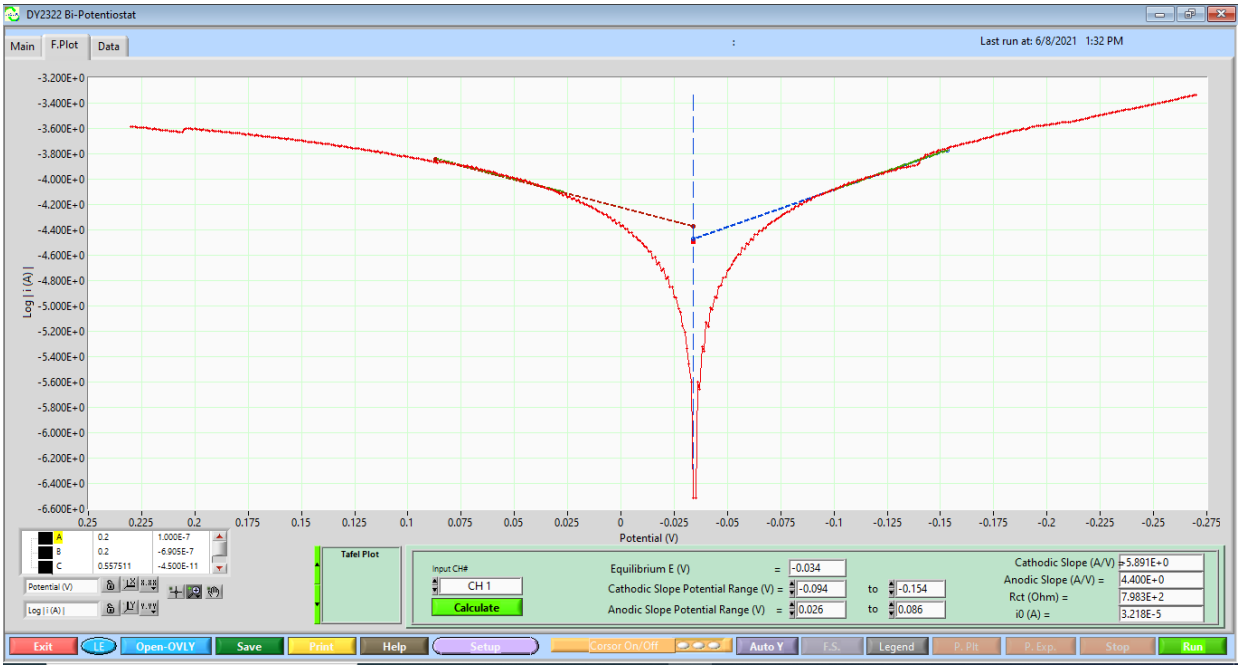

A8/ Potentiodynamic Polarization for Alloy in Artificial Saliva

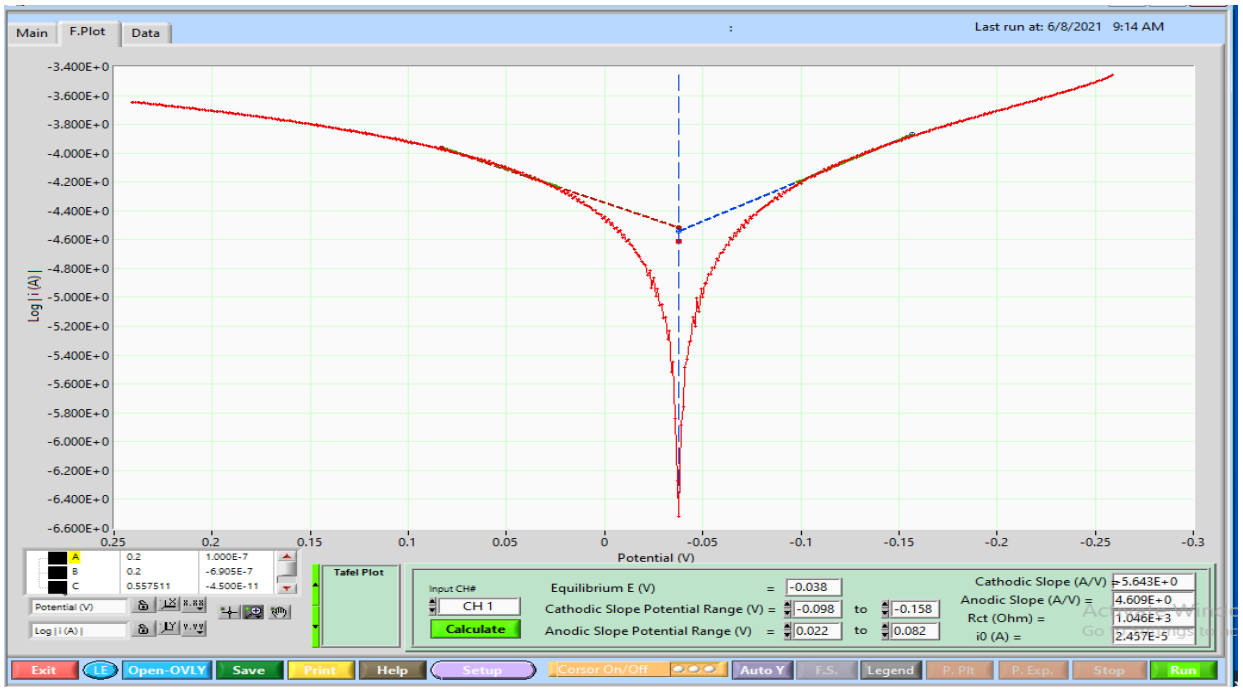

A9/ Potentiodynamic Polarization for Alloy in Artificial Saliva

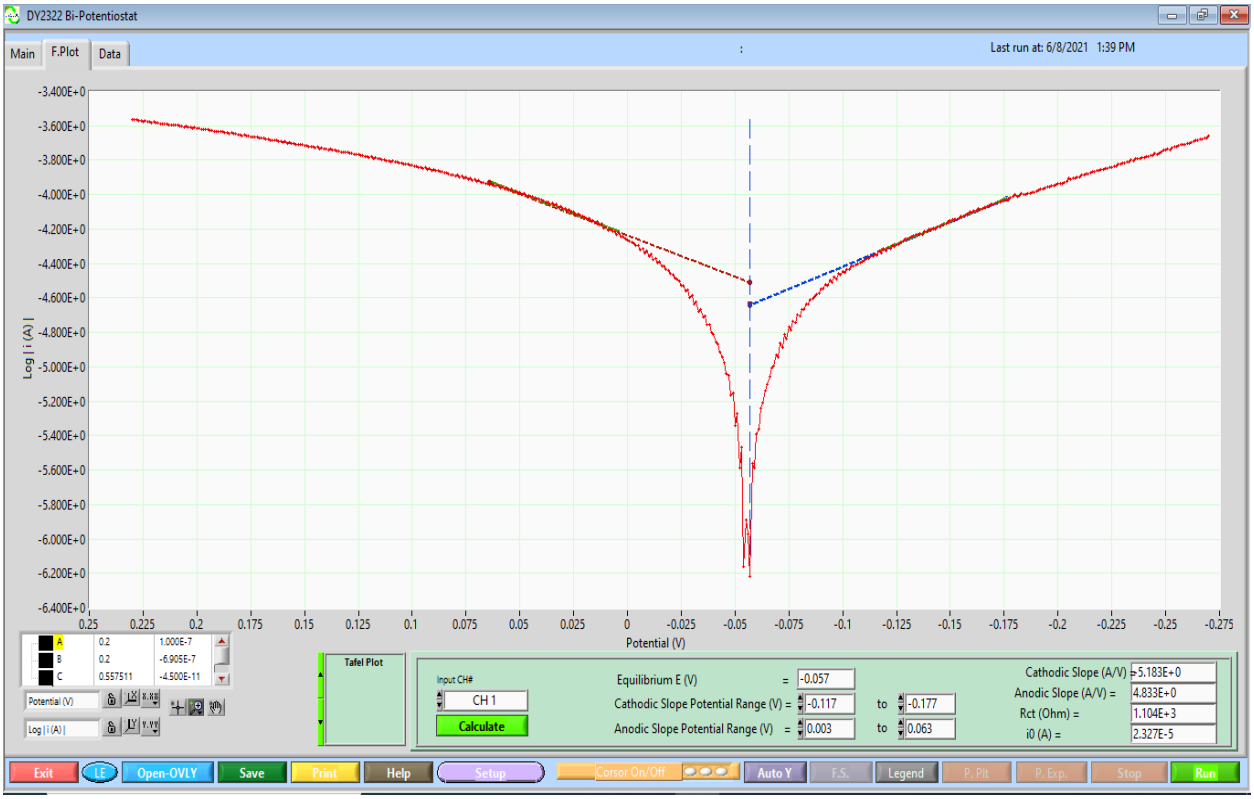

A10/ Potentiodynamic Polarization for Alloy in Artificial Saliva

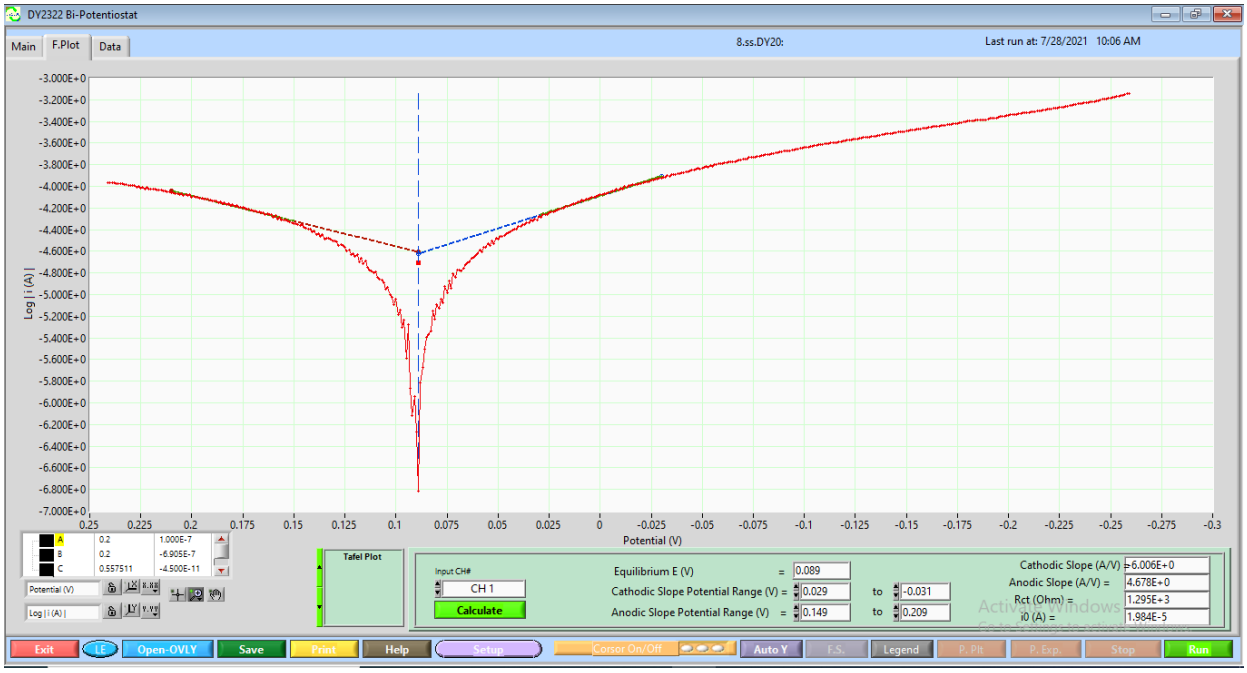

A11/ Potentiodynamic Polarization for Alloy in Artificial Saliva

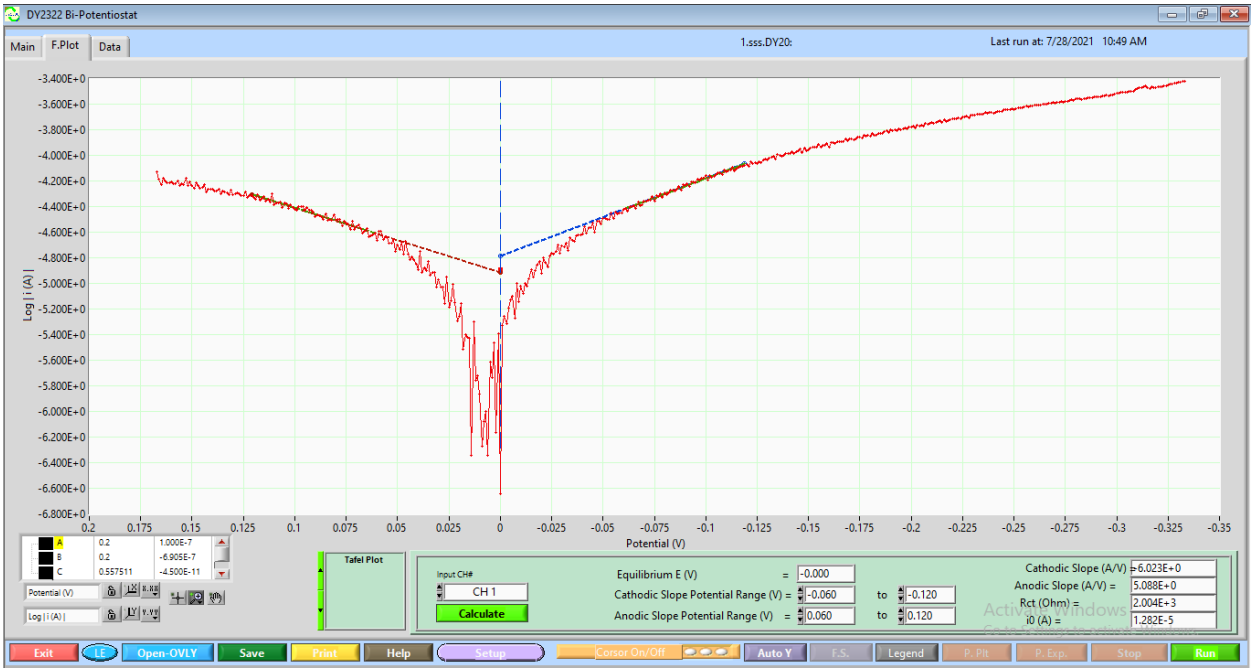

A12/ Potentiodynamic Polarization for Alloy in Artificial Saliva

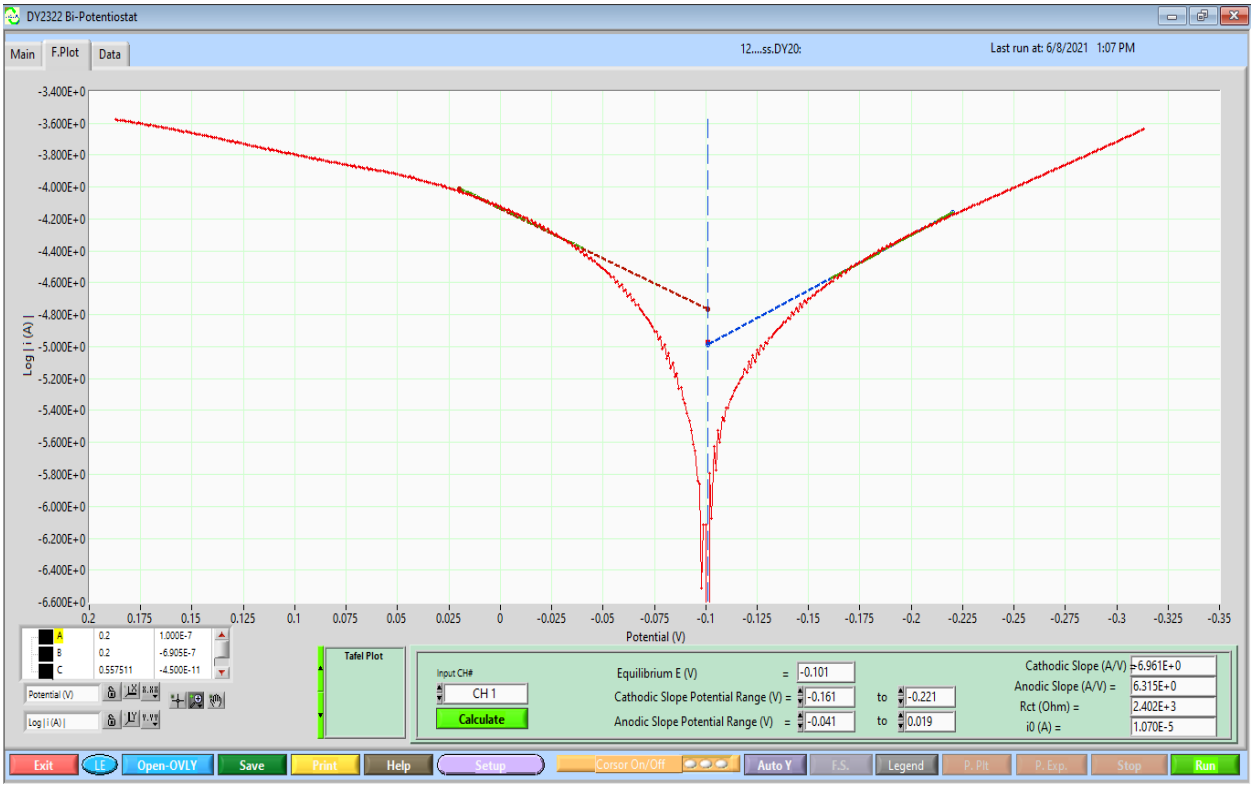

A13/ Potentiodynamic Polarization for Alloy in Artificial Saliva

Appendix B

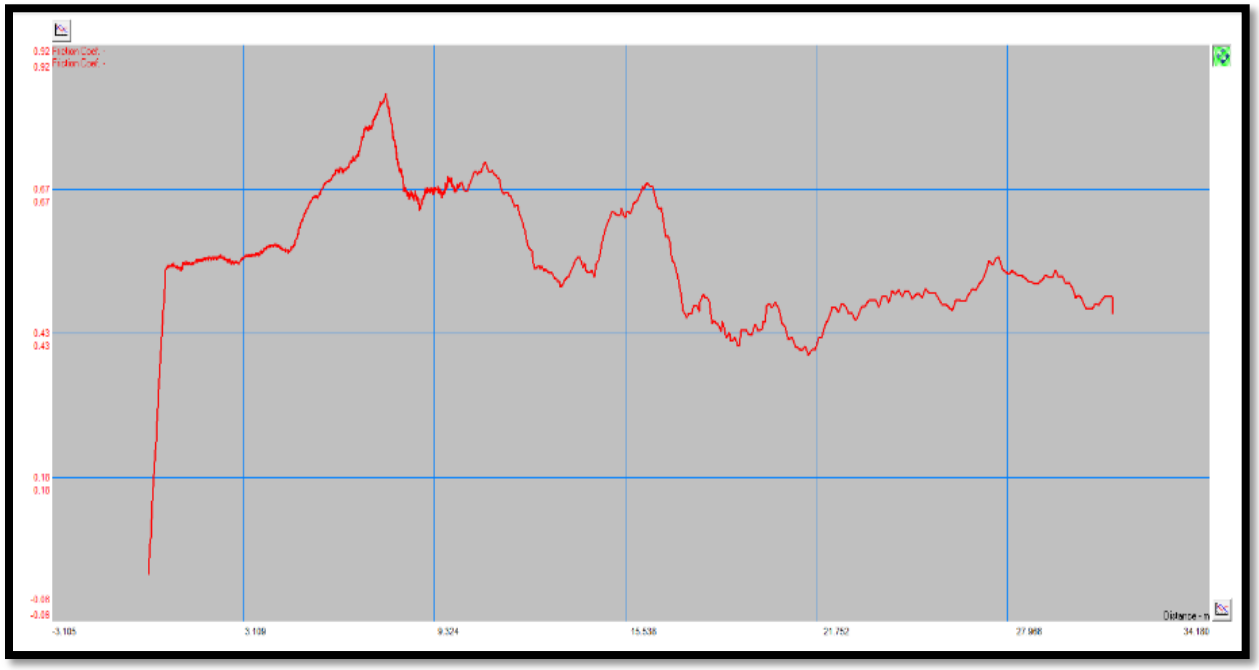

B1: Friction coefficient v's sliding distance in wear test at 5 min.

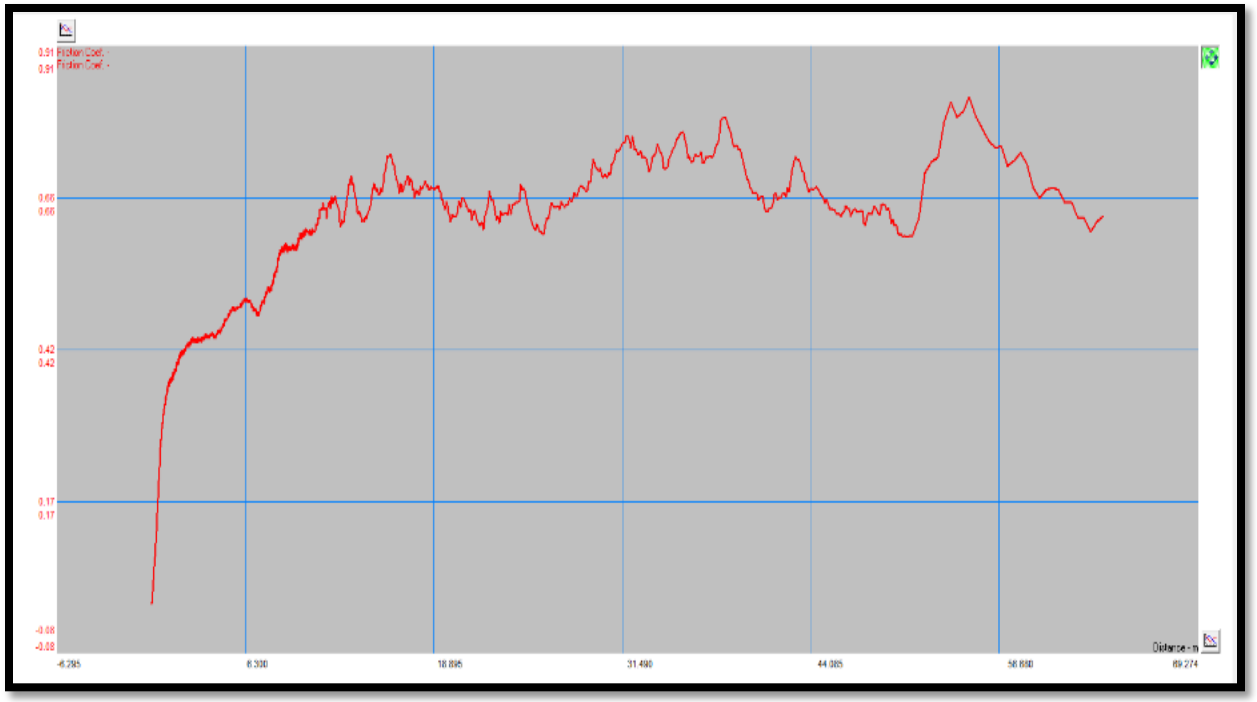

B2: Friction coefficient v's sliding distance in wear test at 10 min.

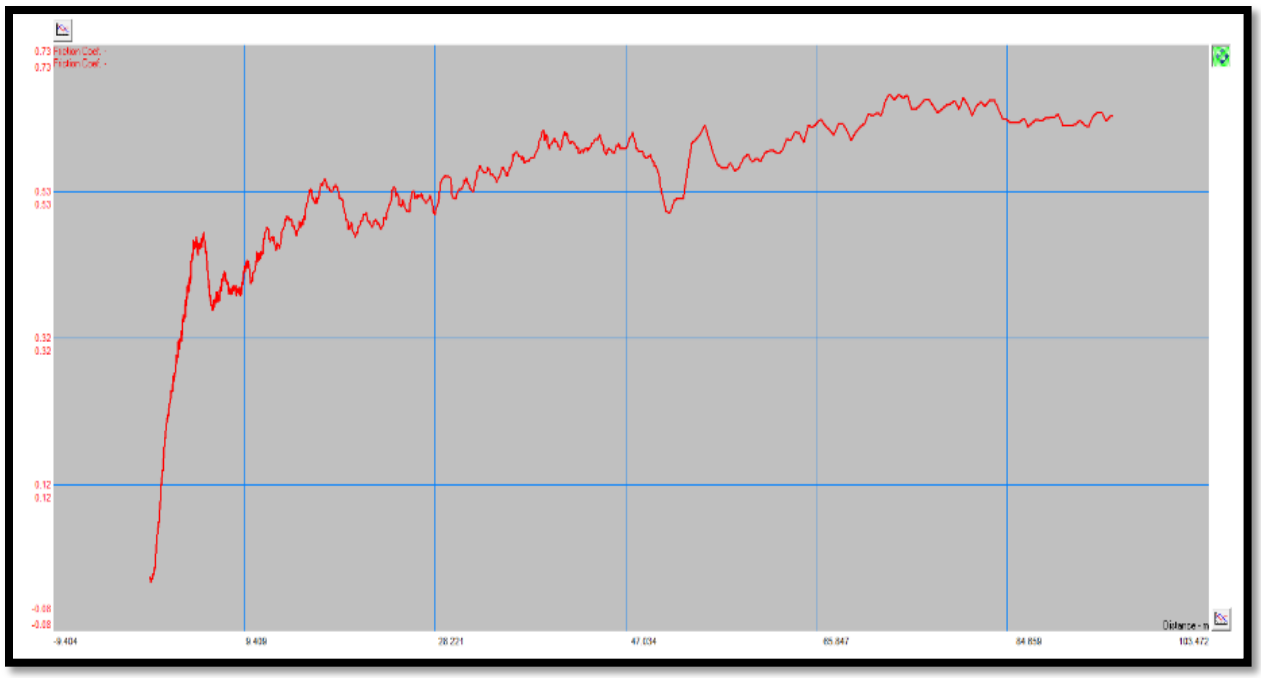

B3: Friction coefficient v's sliding distance in wear test at 15 min.

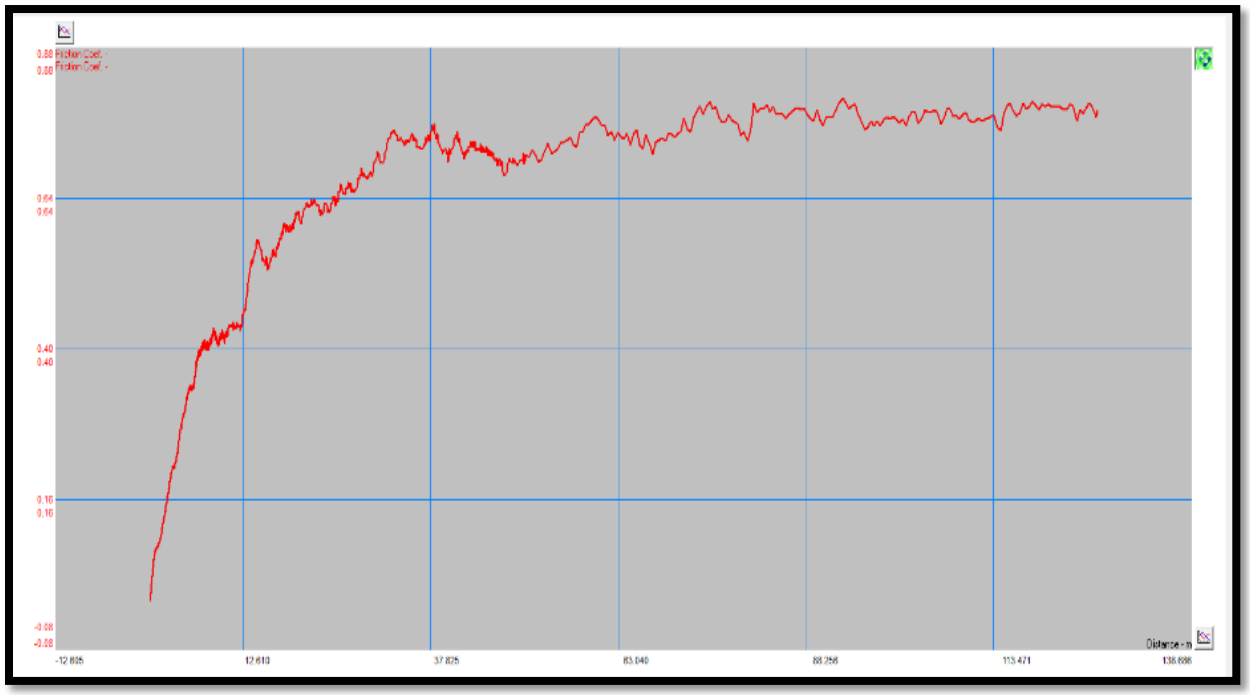

B4: Friction coefficient v's sliding distance in wear test at 20 min.

Appendix C

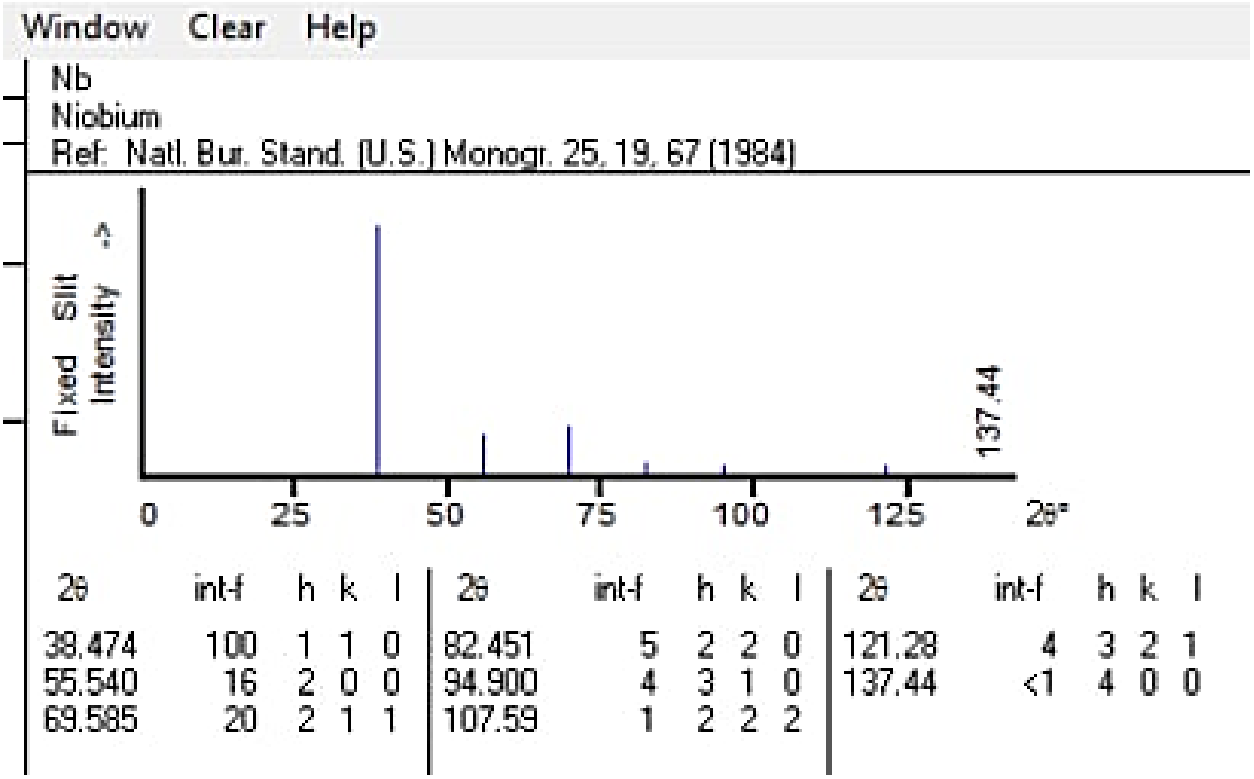

2θ	int-f	h	k	l	2θ	int-f	h	k	l	2θ	int-f	h	k	l
38.474	100	1	1	0	82.451	5	2	2	0	121.28	4	3	2	1
55.540	16	2	0	0	94.900	4	3	1	0	137.44	<1	4	0	0
69.585	20	2	1	1	107.59	1	2	2	2					

C1/ XRD Chart for Pure Niobium

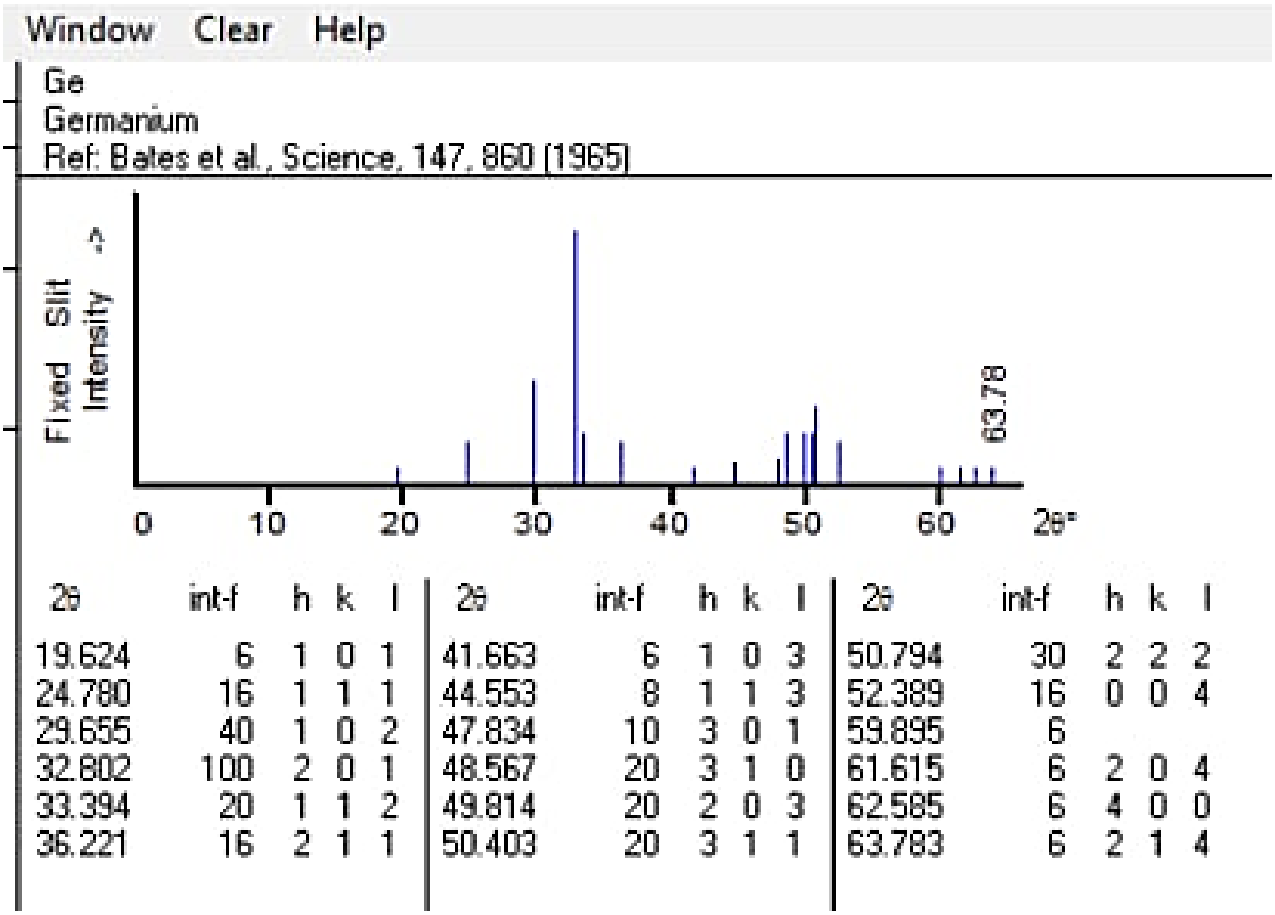

2θ	int-f	h	k	l	2θ	int-f	h	k	l	2θ	int-f	h	k	l
19.624	6	1	0	1	41.663	6	1	0	3	50.794	30	2	2	2
24.780	16	1	1	1	44.553	8	1	1	3	52.389	16	0	0	4
29.655	40	1	0	2	47.834	10	3	0	1	59.895	6			
32.802	100	2	0	1	48.567	20	3	1	0	61.615	6	2	0	4
33.394	20	1	1	2	49.814	20	2	0	3	62.585	6	4	0	0
36.221	16	2	1	1	50.403	20	3	1	1	63.783	6	2	1	4

C2/ XRD Chart for Pure Germanium

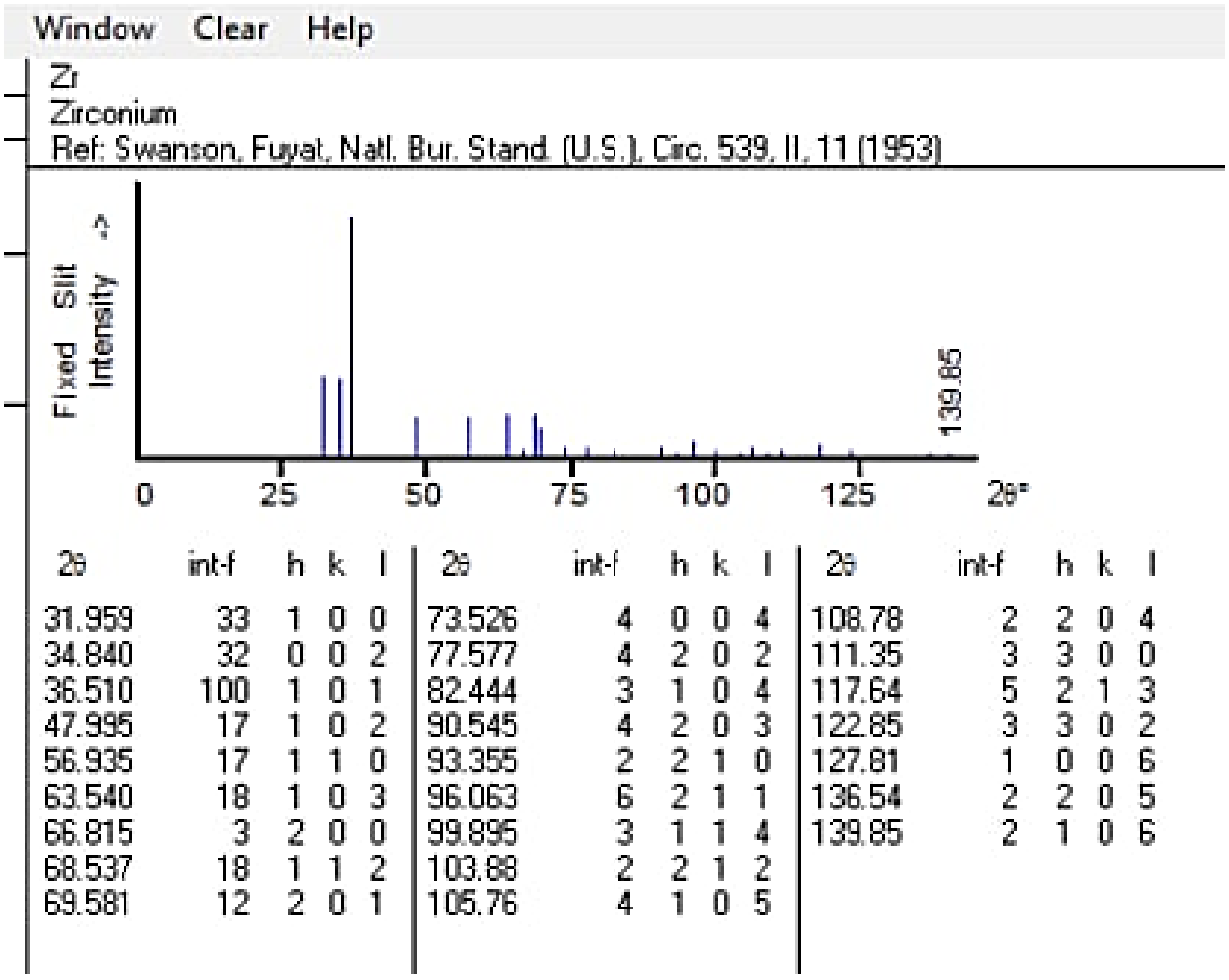

2θ	int-f	h	k	l	2θ	int-f	h	k	l	2θ	int-f	h	k	l
31.959	33	1	0	0	73.526	4	0	0	4	108.78	2	2	0	4
34.840	32	0	0	2	77.577	4	2	0	2	111.35	3	3	0	0
36.510	100	1	0	1	82.444	3	1	0	4	117.64	5	2	1	3
47.995	17	1	0	2	90.545	4	2	0	3	122.85	3	3	0	2
56.935	17	1	1	0	93.355	2	2	1	0	127.81	1	0	0	6
63.540	18	1	0	3	96.063	6	2	1	1	136.54	2	2	0	5
66.815	3	2	0	0	99.895	3	1	1	4	139.85	2	1	0	6
68.537	18	1	1	2	103.88	2	2	1	2					
69.581	12	2	0	1	105.76	4	1	0	5					

C3/ XRD Chart for Pure Zerconium

Window Clear Help

Ca5 (P O4)3 (O H)
Calcium Phosphate Hydroxide
Ref: de Wolff, P., Technisch Physische Dienst, Delft, The Netherlands, ICDD Grant-in-Aid

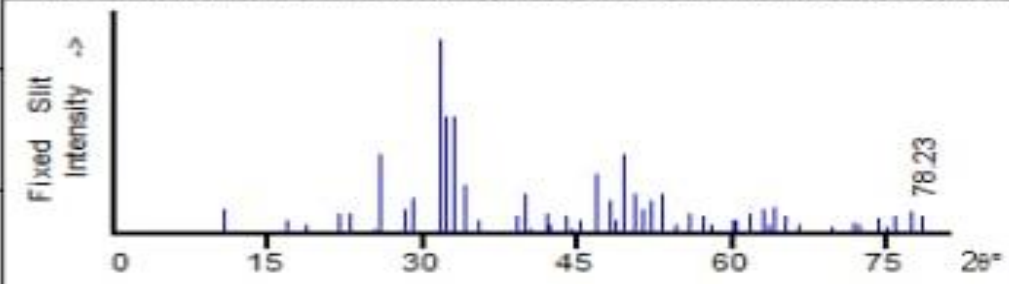

2θ	int-f	h	k	l	2θ	int-f	h	k	l	2θ	int-f	h	k	l
10.820	12	1	0	0	43.804	8	1	1	3	63.443	4	5	1	0
16.841	6	1	0	1	44.369	2	4	0	0	64.078	13	3	0	4
18.785	4	1	1	0	45.305	6	2	0	3	64.078	13	3	2	3
21.819	10	2	0	0	46.711	30	2	2	2	65.031	9	5	1	1
22.902	10	1	1	1	48.103	16	3	1	2	66.386	4	4	2	2
25.354	2	2	0	1	48.623	6	3	2	0	66.386	4	4	1	3
25.879	40	0	0	2	49.468	40	2	1	3	69.699	3	5	1	2
28.126	12	1	0	2	50.493	20	3	2	1	71.651	5	4	3	1
28.966	18	2	1	0	51.283	12	4	1	0	71.651	5	4	0	4
31.773	100	2	1	1	52.100	16	4	0	2	72.286	4	5	2	0
32.196	60	1	1	2	53.143	20	0	0	4	72.286	4	2	0	5
32.902	60	3	0	0	54.440	4	1	0	4	73.995	7	4	2	3
34.048	25	2	0	2	55.879	10	3	2	2	75.022	3	3	2	4
35.480	6	3	0	1	57.128	8	3	1	3	75.022	3	6	0	2
39.204	8	2	1	2	58.073	4	5	0	1	75.583	9	2	1	5
39.818	20	3	1	0	59.938	6	4	2	0	76.154	1	4	3	2
40.452	2	2	2	1	60.457	6	3	3	1	77.175	11	5	1	3
42.029	10	3	1	1	61.660	10	2	1	4	78.227	9	5	2	2
42.318	4	3	0	2	63.011	12	5	0	2					

C4/ Simulated Body Fluid